Kinetic description and study of heterogeneous catalytic reactions

A DISSERTATION
SUBMITTED TO THE FACULTY OF THE
UNIVERSITY OF MINNESOTA
BY

Neil Kanth Razdan

IN PARTIAL FULFILLMENT OF THE REQUIREMENTS
FOR THE DEGREE OF
DOCTOR OF PHILOSOPHY

Advised by Professor Aditya Bhan

June 2022

Acknowledgements

I foremost thank my advisor, Aditya Bhan, for his tutelage, patience, and trust. Ours has been the most productive and enjoyable professional relationship of my life. I moreover thank all members of the Bhan group, past and present, for maintaining an engaging, collaborative research environment, and, in particular, Anurag Kumar for his mentorship and for his company at many much-needed lunch and coffee breaks.

I am grateful to Brandon Foley, David Koshy, Zhichen Shi, Andrew Hwang, and Linh Bui for technical conversations and scrutiny which have materially contributed to the research described hereinafter. Perhaps most importantly, I thank Brandon for encouraging my interest in applied mathematics, and I thank David for discouraging my obsession with pure mathematics.

My enjoyment of graduate school — and my sanity — is indebted to, among others, (i) Matthew Palys, Wyatt Curtis, Daniel Tresnak, and Andreas Mueller for forcing me out of the lab in the earlier, more exacting years of my PhD and (ii) Olivia Flood-Wylie, Andrea Rose, and Eszternora Toth for supplying me with steadfast support and friendship.

I am singularly thankful for my best friend and partner, Savindie Liyanagamage, without whom the quality of my life, work, and the balance thereof, suffers. I feel fortunate to share my life with such a caring and thoughtful companion.

I reserve my final acknowledgement for my family, who warrant more gratitude than I am able to express. I thank my brother, Nikhil Shub Razdan, for being my oldest friend and most trusted confidant. I thank my parents, Ashutosh and Preeti Kusum Razdan, for their inexhaustible devotion and for giving me everything. My every success is owed to them. I thank my grandparents, Kameshwar and Raj Razdan, Autar Krishen Mandloo, and Sheela Saproo for their love, sacrifice, affection, and rogan josh.

Dedicated to Professors John M. Prausnitz and Kameshwar Razdan, from whose example I draw inspiration

Table of Contents

List of Tables

List of Figures

List of Schemes

1 An introduction to methane dehydroaromatization and the microkinetic description of heterogeneously-catalyzed reactions

1.1 Thermochemical methane dehydroaromatization catalyzed by metal-modified zeolite catalysts

Thermochemical valorization of methane is hindered by strong, apolar C-H bonds which confer onerous kinetic and thermodynamic barriers to selective CH_4 conversion. Oxidative strategies attempt to overcome these challenges by coupling C-H cleavage with O-H bond formation, but commonly fail to control the fate of intermediate oxygenate species and, instead, yield large quantities of undesired CO and CO_2 (*1*, *2*). Non-oxidative routes, such as catalytic dehydroaromatization (DHA), eliminate the possibility of C-O formation and proffer opportunities for direct conversion of methane to high-value hydrocarbon and dihydrogen products.

Mo-modified MFI zeolites (Mo/H-ZSM-5) catalyze methane dehydroaromatization with high benzene (~70%) and aromatic selectivity (~95%) at conversions near the equilibrium limit (~10%) at elevated reaction temperatures (~950 K) and ambient pressure (Figure 1.1) (*1–11*). Mo/H-ZSM-5 catalysts are synthesized at catalytic conditions (e.g. CH_4, 973 K) by reduction and carburization of MoO_x/H-ZSM-5 "pre-catalysts" which contain MoO_x precursors encapsulated within MFI zeolites by either (i) aqueous impregnation or (ii) stoichiometric exchange of Mo cations with proximate pairs of zeolitic Brønsted acid sites. Upon exposure to CH_4 at 973 K, oxygen from MoO_x moieties is removed in the form of gaseous CO, H_2O, and CO_2, and carbon is abstracted from CH_4 to form 0.6-1.5 nm MoC_x aggregates responsible for catalytic activation of methane (*12–18*).

Carbidic Mo species required for DHA catalysis co-exist with framework Brønsted acid sites which are native to H-ZSM-5 materials and are regenerated during detachment

of MoO_x from cation exchange sites during the induction period (*19*, *20*). Brønsted acid sites in H-ZSM-5 are well-known to catalyze olefin oligomerization at DHA-relevant temperatures (*19*, *21–24*) and; therefore, prevalent mechanistic postulates propose that Mo/H-ZSM-5 materials execute DHA through bifunctional reaction pathways in which (i) MoC_x catalyze initial C-C coupling events and (ii) H^+ sites scavenge C_2H_x intermediates to form aromatic products. Direct evidence of coupling between metallic and acidic catalytic functions, however, is scarce (*25*, *26*).

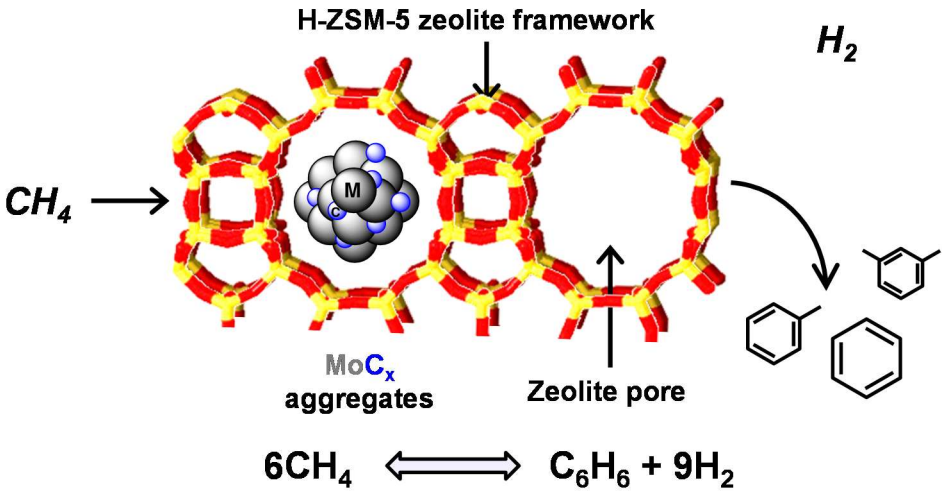

Figure 1.1: Methane DHA on Mo-modified H-ZSM-5 zeolite catalysts.

Scrutiny of the catalytic relevance of MoC_x and H^+ functions is complicated, not only by limited spectroscopic access at elevated reaction temperatures (*27*), but also by the highly-reversible nature of endothermic methane dehydroaromatization (e.g. ΔH_r^0 = 531 kJ/mol for $6CH_4 \rightleftharpoons C_6H_6 + 9H_2$; Figure 1.1) (*17*). Reverse aromatization reactions (e.g. benzene hydrogenation to methane; Figure 1.1) corrupt kinetic measurements and, consequently, obfuscate elementary-step details of methane activation, coupling, and dehydrocyclization. To this end, Chapter 3 of this dissertation is focused on developing a

methodology to quantitatively deconvolute kinetic and thermodynamic contributions to aromatic synthesis in order to enable judicious assessment of the distinct catalytic roles of metallic (MoC_x) and acidic (H^+) active sites. The deconvolution of CH_4 DHA kinetics and thermodynamics is achieved by application and development of fundamental thermochemical formalisms which (i) unravel connectivity of the DHA reaction network, (ii) identify rate- and reversibility-controlling elementary steps, and (iii) calculate the forward rate of methane aromatization — the kinetic assessor of intrinsic catalyst activity.

The learnings established in Chapter 3 are critically enabling for the systematic assessment of MoC_x and H^+ catalytic function detailed in Chapter 4. Measurement of DHA selectivity, reversibility, and rate on Mo/H-ZSM-5 catalysts of systematically-varied Mo-to-H^+ ratio demonstrated that (i) product distribution is unaffected by the ratio of metallic and acidic sites and (ii) forward rates consistently normalize by Mo-content irrespective of acid site density. The congruence of Mo-normalized forward rate among all Mo/H-ZSM-5 catalysts is corroborated by transient chemical titration and probe reaction experiments which verify that carbidic Mo moieties are the sole kinetically-relevant active site and that the only role of Brønsted acid sites is to anchor and disperse Mo during synthesis of MoO_x/H-ZSM-5 “pre-catalysts”.

Preceding mechanistic investigations in Chapters 3 and 4, Chapter 2 details polyfunctional strategies to circumvent equilibrium limits to dehydroaromatization by *in situ* scavenging of byproduct H_2 via formation of bulk metal hydrides stable at reaction conditions (e.g. $ZrH_{1.75}$). The described approach is agnostic to identity of DHA catalyst and, therefore, is conceptually-distinct from the research efforts of Chapters 3 and 4. Chapter 2 is not focused on scrutiny of Mo/H-ZSM-5 materials or DHA mechanism, but,

rather, on development and validation of reaction-transport formalisms that quantitatively describe synergy of spatially- and functionally-distinct active centers. Measurement of gas-phase dihydrogen diffusion coefficients and simulation of reaction-transport models elucidate the critical role of dispersive H_2 transport in determining efficacy of catalyst-absorbent interaction and prescribe strategies to maximize supra-equilibrium methane conversion without detriment to aromatic selectivity.

1.2 Catalytic consequences of multi-site requirements of elementary steps and surface intermediates

Reactions catalyzed on regularly-structured surfaces (e.g. low-index metal facets) are distinguished from homogeneous reactions by the population of intermediates on discrete adsorption/reaction sites which proscribe description of surface-catalyzed reactions in the context of continuum mechanics. That is to say that the distribution, interaction, and movement of surface-bound species cannot be described by constitutive laws of mass transport or theories of solution thermodynamics which govern the dynamics of fluid-phase reactants and intermediates. Consequently, the kinetic, thermodynamic, and mass transport formalisms employed to study methane dehydroaromatization in flow reactors (Chapters 2–4) are incapable of describing the molecular-level dynamics of surface-bound intermediates in multi-site, multi-step catalytic reactions. The formalisms discussed therein must be supplemented and, in some cases, reinterpreted by mathematical methodologies which account for the discrete adjacency requirements of multi-site elementary steps, adsorbate hopping (i.e. surface diffusion), and multi-body energetic interactions between adspecies. Rigorous treatment of each of these phenomena requires new rate terms that explicitly consider the contiguous ensemble of sites on which the concerned reaction or interaction occurs.

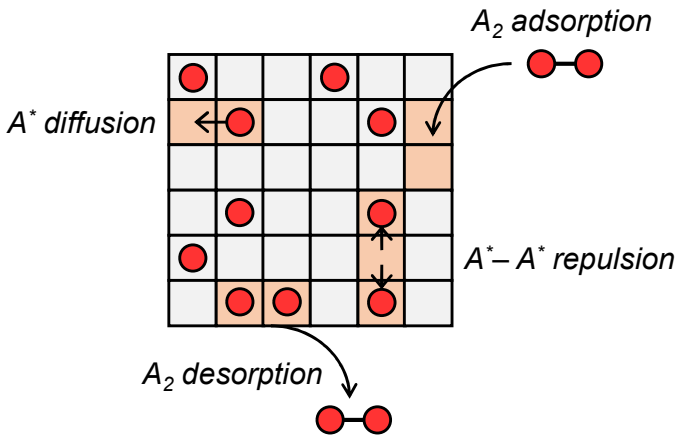

Figure 1.2: Schematic depiction of a square lattice populated by $\boldsymbol{A^*}$ adspecies (●) involved in multi-site elementary steps (Eqs. **1.1**-**1.2**) and multi-body interactions (Eq. **1.3**).

Consider, for example, a catalytic surface with adsorption/reaction active sites arranged in a regular square lattice and populated by adspecies A^* and vacant sites, $*$ (Figure 1.2). The description of (i) generation and elimination of A^* intermediates by reversible adsorption of fluid-phase species A_2,

$$A_2 + * - * \rightleftharpoons A^* - A^* \qquad \textbf{[1.1]}$$

(ii) diffusion of A^* species,

$$A^* - * \rightleftharpoons * - A^* \qquad \textbf{[1.2]}$$

and (iii) repulsive energetic interaction between neighboring A^* species, quantified by

$$\epsilon_{A^*-A^*} \equiv G^0_{A^*-A^*} - 2G^0_{A^*} \qquad \textbf{[1.3]}$$

each necessitate enumeration of $A^* - A^*$, $A^* - *$, and $* - *$ site pairs. Governing equations of continuum mechanics apropos for fluid-phase species are unable to inventory site-pair populations without assuming the distribution of adsorbates conforms to the mean-field approximation, or some variant thereof. Consequently, prevalent analytical treatments such as the Langmuir-Hinshelwood description (*28*, *29*), Bragg-Williams approximation (*30*, *31*), and quasi-chemical approximation (*32–36*) are limited to a finite range of relevance which requires that either (i) all elementary steps occur on a single site and all adspecies

are thermodynamically-ideal (i.e. there are no multi-site requirements or multi-body interactions) or (ii) surface diffusion (e.g. A^* diffusion in Eq. **1.2**) is sufficiently fast to randomize, or equilibrate, the adspecies distribution at steady state.

Chapters 5 and 6 of this dissertation are focused on redressing the shortcomings of mean-field approaches outside of these conditions. Chapter 5 formulates an analytical method which, in essence, expands the spatial scope of the mean-field approximation to explicitly describe the dynamics of ensembles of any shape and size. The presented formalism captures the clustering and partitioning of surface-bound intermediates inherently engendered by multi-site elementary steps with the same fidelity as stochastic-computational kinetic Monte Carlo (kMC) simulation and is robust to inclusion of lateral adsorbate interactions (e.g. Eq. **1.3**) and surface diffusion events (e.g. Eq. **1.2**). Examination of both simple reactions, such as $A + A \rightarrow A_2$, and industrially-relevant reactions, such as ammonia synthesis, reveals that mean-field methods (i) profoundly miscalculate rates and reversibilities, (ii) misidentify rate-determining steps, and (iii) fundamentally misinterpret consequences of the quasi-equilibrium approximation. Chapter 6 builds on these learnings by examination of the consequences of ensemble site requirements for (i) selectivity between reaction pathways proceeding through ensembles of disparate size, (ii) interpretation of observed reaction rates in terms of transition state theory, and (iii) description of reactions involving multi-site-occupying intermediates (e.g. two-site-occupying ${}^*C_2H_4^*$ during catalytic ethylene hydrogenation).

1.3 Kinetic description of electrochemical reactions

Chapter 7 of this dissertation is tangential to Chapters 2-6 and describes the application of the formalisms of transition state theory and degree of rate control to electrochemical

systems. Foundations in each of these concepts, established in research efforts described in Chapters 2-6, are exploited to formulate a mathematical framework which resolves long-standing questions in the field of electrochemical kinetics. In particular, synergies between transition state theory, the concept of degree of rate control, and De Donder relations are leveraged to (i) expand the descriptive scope of the ubiquitous Butler-Volmer equation, (ii) quantitatively explain the recurrent observation of cardinal Tafel slopes at large overpotential, and (iii) prescribe methods to deconvolute unidirectional contributions to macroscopic kinetic descriptors (e.g. Tafel slope, reaction order). The utility of these developments is demonstrated by application to the reversible hydrogen oxidation/evolution reaction for which observed kinetic behavior is rationalized with microscopic detail.

2 Controlling kinetic and diffusive length-scales during absorptive hydrogen removal in methane dehydroaromatization on MoC_x/H-ZSM-5 catalysts

*Contents herein are adapted with permission from Razdan, N. K., Kumar, A., Bhan, A. Controlling kinetic and diffusive length-scales during absorptive hydrogen removal in methane dehydroaromatization on MoC_x/H-ZSM-5 catalysts. *Journal of Catalysis*. **2019**, *372*, 370–381. https://doi.org/10.1016/j.jcat.2019.03.016.

2.1 Background

Dehydroaromatization (DHA) of methane to benzene ($6CH_4 \rightarrow C_6H_6 + 9H_2$) is highly endothermic and requires reaction temperatures $\gtrsim$ 950K to achieve ~10% equilibrium conversion at ambient pressure. Carbidic forms of Mo encapsulated in medium-pore MFI zeolites catalyze methane DHA with high benzene selectivity ($\gtrsim$ 70%) at conversions near the thermodynamic limit (*1–11*). Oxidic Mo precursors, deposited either by aqueous impregnation or stoichiometric exchange with zeolitic H^+ pairs, reduce and carburize upon exposure to CH_4 at high temperatures ($\gtrsim$ 950 K) to form molecular-size MoC_x clusters (0.6-1.5 nm) which activate C-H bonds in methane to initiate C-C coupling reactions that

lead to aromatics (*3*, *14*, *18*, *19*, *37–40*). Oxygen removed (2.44 ± 0.1 O:Mo) in the form of H_2O, CO, and CO_2 during reduction/carburization procedures corroborates formation of putative $(Mo_2O_5)^{2+}$ dimers which anchor to proximal Al site pairs on MoO_x/H-ZSM-5 materials prepared by solid-state stoichiometric exchange (*14*, *39–42*). Carbon deposition of ~9 C:Mo concurrent with oxygen evolution during catalyst reduction/carburization is the predominant source of coke formation on materials with ~3 wt% Mo (*18*, *39*, *43*).

H_2 formed during dehydrogenation and cyclization events on Mo/H-ZSM-5 inhibits net synthesis rates during methane pyrolysis; in-situ removal of hydrogen from catalyst proximity is virtuous in overcoming thermodynamic barriers of methane DHA set by reaction endothermicity (*44–46*). Liu et al. (*44*) demonstrate permselective membrane walls integrated into CH_4 DHA flow reactors effectively scavenge liberated hydrogen, modestly enhancing methane conversion from ~10% to ~12%. However, improvement in methane pyrolysis rates is principally owed to increased formation of entrained C_{12+} polynuclear aromatics as product distribution shifts to higher molecular weight unsaturated hydrocarbons which benefit most from hydrogen removal (*44–46*). The accumulation of large polycyclic aromatics congests zeolite pores and leads to a more rapid decrease in instantaneous conversion – first-order deactivation rate constants increase from 0.044 h^{-1} to 0.059 h^{-1} upon integration of permselective membrane walls.

Bhan and coworkers (*18*) recently demonstrated that in-situ hydrogen removal can be achieved by introduction of a selective hydrogen absorbent, zirconium metal. Addition of Zr metal particles to MoC_x/ZSM-5 in interpellet mixtures resulted in a 2.7× increase in methane converted and concurrent 1.4, 2.1, 2.6, and 5.6-fold increase in effluent benzene, naphthalene, toluene, and C_{10}^+ yields, respectively, in reference to a conventional

MoC_x/ZSM-5 catalyst at equivalent time-on-stream (8.7 ks). The maximum methane conversion on interpellet mixtures exceeded 27% – in significant excess of ~10% equilibrium-prescribed conversion at these reaction conditions – demonstrating that thermodynamic limitations encountered in methane dehydroaromatization on MoC_x/ZSM-5 are circumvented by addition of Zr as a hydrogen absorbent.

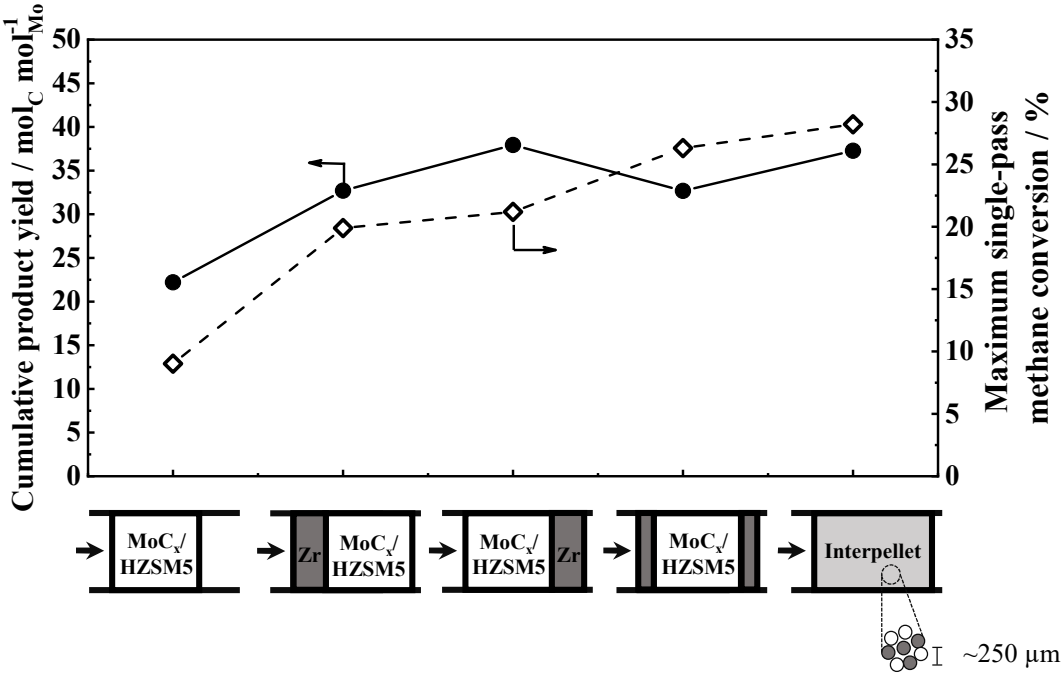

Figure 2.1: Maximum single-pass methane conversion (right axis) and cumulative product yield at 10.2 ks time-on-stream (left axis) on MoC_x/H-ZSM-5 and Zr catalyst beds configured with (i) MoC_x/H-ZSM-5 only, (ii) Zr packed upstream of MoC_x/H-ZSM-5, (iii) Zr packed downstream of MoC_x/H-ZSM-5, (iv) Zr packed both upstream and downstream of MoC_x/H-ZSM-5, and (v) an interpellet physical mixture of Zr and MoC_x/H-ZSM-5. Lines are to guide the eye. Reaction conditions: 973 K, MoC_x/H-ZSM-5 ≈ 1.2 g, Zr ≈ 2.4 g, feed flow rate ≈ 0.21 cm^3 s^{-1} (90 vol% CH_4).

Subsequent to these reports, Bhan and coworkers (*47*) demonstrated that staging of Zr metal upstream and/or downstream of MoC_x/ZSM-5 catalyst achieves enhancements to aromatic yield comparable to interpellet mixtures, indicating that polyfunctional MoC_x/ZSM-5 + Zr formulations competently couple spatially-separate catalytic and

absorptive functions (Figure 2.1). The coupling of absorptive and catalytic functions on ~1 cm reactor length scales signifies that polyfunctional DHA flow reactors must be significantly axially-dispersed; the observed influence of spatially-separate Zr is impossible in ideal plug-flow reactors wherein bulk convection is the sole form of mass transport. To this end, supra-equilibrium enrichments in aromatic production must be rationalized in terms of (i) quantitative measures of hydrogen diffusion and (ii) detailed reaction-transport formalisms which ally measurements of reaction kinetics and intermediate transport to predict and explain the capacity of staged and layered beds to reproduce the efficacy of interpellet mixtures.

Hereinafter, I discuss my particular contributions to the reports of Bhan and coworkers (*47*) in examining the critical role of catalyst-absorbent proximity and reactor hydrodynamics in determining efficacy of polyfunctional mixtures. Detail of reaction rate measurements and constitution of polyfunctional reactors are omitted; these efforts are entirely attributed to Dr. Anurag Kumar. Instead, I discuss (i) the measurement of dispersion coefficients by H_2 tracer studies with impulse and step-change inputs to flow vessels charged with inert catalyst proxies and (ii) the formulation and simulation of detailed reaction-transport models used to describe DHA reactions with and without Zr addition. Evaluation of reaction-transport models compares simulation results with experiment; however, I emphasize that all experimental reaction data was collected by Dr. Anurag Kumar.

2.2 Materials and Methods

2.2.1 Measurement of axial H_2 diffusion coefficient in packed-bed flow reactors

Inert H_2 tracer experiments were performed on beds of 180 – 425 μm quartz sand aggregates packed to 2.7 cm, an identical length as 1.2 g of 180 – 425 μm MoC_x/H-ZSM-

5 aggregates in a 1.05 cm ID tubular quartz reactor. Quartz sand was heated to 973 K in inert (He or Ar) flow (ca. 1 cm^3 s^{-1}). For pulse tracer experiments, a sample of H_2 (ca. 1 cm^3) was introduced to a stable reactor feed flow of CH_4 using an electronic six-way valve (ED66UWE, VICI Valco 6-port valve). In step-change experiments, reactor feed flow was switched from Ar to an Ar and H_2 gas mixture (5 vol % H_2/balance Ar). Reactor effluent was monitored using an online mass spectrometer (MS) (MKS Cirrus 200 Quadrupole MS system).

2.3 Results and Discussion

2.3.1 Measurement and Calculation of Péclet Number, Pe

The observed effects of catalyst-absorbent proximity on aromatic synthesis rates during methane DHA reactions, particularly those noted upon introduction of Zr upstream and/or downstream of the catalyst bed, highlight the critical role of dispersive H_2 transport in polyfunctional configurations. Efficacy of staged Zr beds to enhance aromatic yields to a similar degree as in interpellet mixtures demonstrates gas-phase H_2 generated over Mo/H-ZSM-5 catalysts is capable of bed-scale transport both co- and counter-current to bulk advection. Relative contributions of diffusive/dispersive and convective transport in tubular flow reactors can be assessed based on a Péclet number

$$Pe = uL/D_{eff} = \left(\frac{u_s}{\varepsilon}\right)L/D_{eff} \qquad \textbf{[2.1]}$$

which is the non-dimensional ratio of characteristic rates of diffusive and convective gas-phase transport in tubular flow reactors. Pe provides a useful metric to evaluate significance of axial dispersion considerations in terms of catalyst bed-length, L, effective diffusion coefficient, D_{eff}, and total linear flow velocity, u, or superficial linear flow velocity, u_s, and catalyst bed void fraction, ε. Ideal plug-flow reactors (PFRs) operate in the limit of Pe →

∞ wherein unidirectional bulk advection is the sole mechanism of mass transport, thereby rendering neighboring axial fluid-elements incapable of exchanging matter. Axial dispersion becomes relevant for Pe $\lesssim$ 10 which permit bed-scale molecular transport in response to concentration gradients arising from chemical reaction and/or absorption rate processes either (pseudo)-homogenously or at reactor bounds (*48*).

Introduction of catalyst or absorbent packed-beds in tubular flow reactors obstruct molecular movement, thereby shortening mean-free path and dampening diffusional motion. Consequently, effective bulk gas-phase diffusion coefficients, D_{eff}, decrease compared to the molecular limit, D, which defines proportionality between diffusive flux and species concentration gradients in an unobstructed fluid medium (*48*). Substitution of D for D_{eff} into Eq. **2.1** provides an absolute lower-bound on Pe. We evaluate D_{eff}, and Pe by theoretical and experimental means to corroborate observations of bed-scale hydrogen diffusion during methane dehydroaromatization reactions in polyfunctional catalyst-absorbent formulations.

Levenspiel details systematic procedures for approximation of Péclet number for conditions which deviate from the ideal plug-flow reactor (*48*). Calculation of Bodenstein number,

$$Bo = ud/D \qquad \textbf{[2.2]}$$

and catalyst-bed aspect-ratio,

$$A = L/d \qquad \textbf{[2.3]}$$

where d is reactor diameter, give Bo = 0.12 and A = 2.57 and suggest reactor configurations discussed in this investigation are neither ideally-dispersed nor convectively-controlled and thus prohibit calculation of Pe by asymptotic, closed-form solution of the Navier-

Stokes equation (*48*). Application of Darcy's law (*49*) and Poiseuille's law to a theoretical treatment of viscous fluid flow presented by Marshall (*50*) gives a simple relation between D, D_{eff}, and packed-bed porosity, ε

$$\frac{D_{eff}}{D} = \varepsilon^{\frac{3}{2}} \qquad \textbf{[2.4]}$$

Matsunanga et al., (*51*) report mutual diffusion coefficients for H_2 in a variety of gaseous mixtures measured by the Taylor dispersion method (*52*) and fit these data to power law models with coefficients similar to those predicted by the kinetic theory of gases (*53*). From reported correlations, we calculate D (973 K) = 6.3 ± 0.2 $cm^2\ s^{-1}$ giving, as an absolute lower-bound, Pe ≳ 0.3 using Eq. **2.1**. Taking $\varepsilon = 0.35$, a typical value for packed bed columns (*54*), we find Pe = 1.30 $\pm$ 0.2 under reactions conditions conforming with the balance of convective and diffusive time scales which the Bodenstein number and aspect ratio suggest (*48*).

To corroborate approximations of Pe from theoretical calculation, we measure Pe by both step-change and pulse input of H_2 through an inert bed of quartz sand particles sieved to identical size and packed to identical bed-length compared to 1.2 g MoC_x/H-ZSM-5 catalyst beds used in methane DHA reactions. Pulse and step-change tracer experiments were performed changing reactor diameter (0.68 – 1.05 cm), temperature (303 – 973 K), and total flow-rate (17.6 – 40 $cm^3\ s^{-1}$) to note dependence of D_{eff} solely on temperature. Following a formulism presented by Levenspiel (*48*), we calculate residence-time (exit-age) distribution, E, and mean residence time, t_{avg}, from effluent H_2 pressure histories for both pulse and step-change inputs. E is the distribution of exit-ages of fluid elements which elute from the flow vessel (packed-bed reactor) and is defined as a normalized quantity such that $\int_0^\infty Edt = 1$. Profiles of non-dimensional exit-age distribution

$$E_\theta = t_{avg}E \quad \textbf{[2.5]}$$

as a function of non-dimensional time elapsed from tracer entry

$$\theta = t/t_{avg} \quad \textbf{[2.6]}$$

are compared to analytical solutions of differential mole balances for a perfect pulse (i.e. Dirac-delta function) or perfect step-change (i.e. Heaviside function) of inert gas passing through an axially-dispersed tubular reactor with Pe fit by mean-square error minimization, as shown in Figure 2.2.

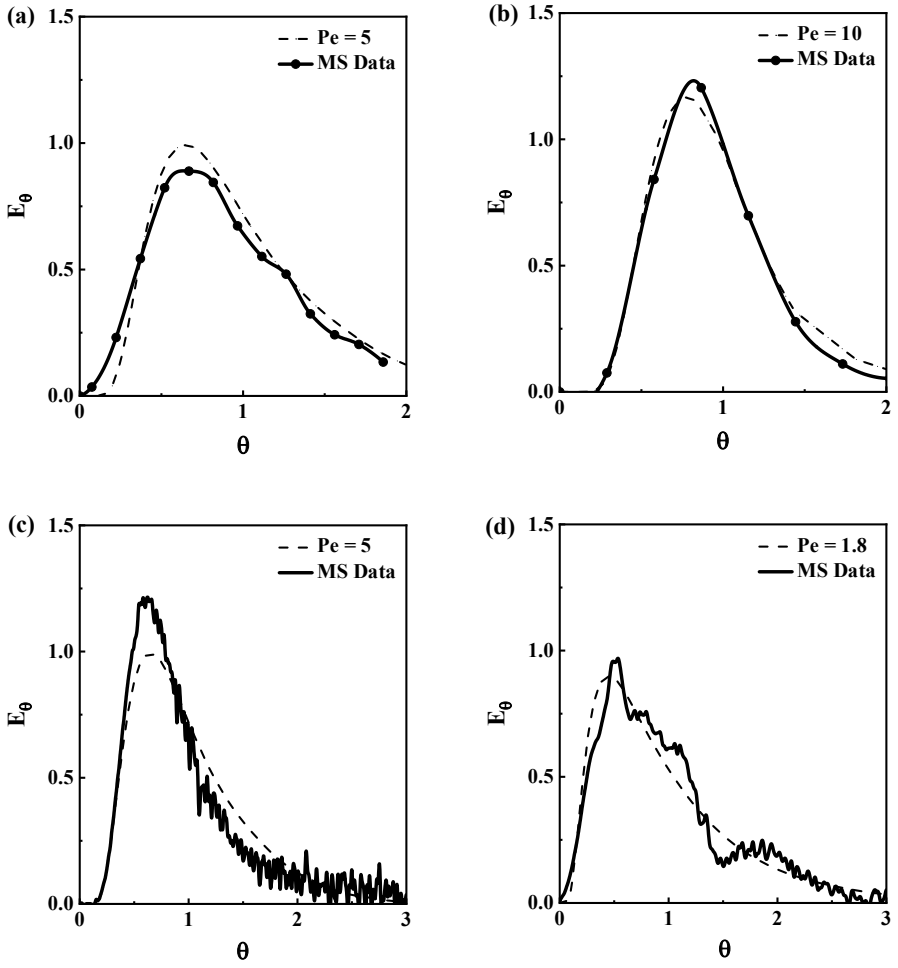

Figure 2.2: Non-dimensional tracer response curves (● or —) per effluent H_2 content monitored by online mass spectrometer and ideal response fit (---) upon introduction of H_2 by (a) impulse at 973 K with 0.33 cm^3 s^{-1} total flow and 0.68 cm reactor diameter, (b) impulse at 973 K with 0.66 cm^3 s^{-1} total flow and 0.68 cm reactor diameter, (c) step-change at 303 K with 0.29 cm^3 s^{-1} total flow and 1.05 cm reactor diameter, and (d) step-change at

973 K with 0.29 cm^3 s^{-1} total flow and 1.05 cm reactor diameter. Solid black lines in 3(a) and 3(b) are to guide the eye.

Table 2.1: Péclet number, Pe, and effective diffusion coefficients, D_{eff}, determined from fit to H_2 tracer responses using Eq. **2.5** and **2.6** and calculated from correlation (*51*) and Eq. **2.1** and **2.4**

Method [a]	Temperature [K]	Flow Rate [cm^3 s^{-1}]	Reactor Diameter [cm]	Pe [b]	D_{eff} [b] [cm^2 s^{-1}]
H_2 Pulse in CH_4 (Fig. 2.2a)	973	20.0	0.68	5.0	1.4
H_2 Pulse in CH_4 (Fig. 2.2b)	973	40.0	0.68	10	1.4
H_2 Step-Change in Ar (Fig. 2.2c)	303	17.6	1.05	5.0	0.5 (2.3[e])
H_2 Step-Change in Ar (Fig. 2.2d)	973	17.6	1.05	1.8	1.5
Equation **2.1** and **2.4** [c]	973[d]	13.0[d]	1.05[d]	1.3	1.5

[a] All experiments performed at 973 K
[b] Calculated taking $\varepsilon = 0.35$
[c] D taken from correlations given by Matsunaga et al. (*55*)
[d] Reaction conditions relevant to methane DHA reactions performed in this work
[e] Adjusted to 973 K assuming $D_{eff} \sim T^{3/2}$

Péclet numbers found from fit to experimental tracer response curves range from 1.8 to 10 depending on reactor diameter, total flow-rate, and bed temperature. D_{eff} calculated from Pe per Eq. **2.1**, 1.4-1.5 cm^2 s^{-1} at 973 K, agree well with theoretical value of 1.5 cm^2 s^{-1} from Eq. **2.4** using $\varepsilon = 0.35$. Taking an average experimental value D_{eff} = 1.43 cm^2 s^{-1} at 973 K gives Pe = 1.32 at temperature and flow-rate relevant to methane DHA reactions. Péclet numbers near unity dictate a balance of convective and diffusive mass transport in tubular flow reactors and demonstrate the presence of axial dispersion phenomena in studied polyfunctional reaction configurations.

2.3.2 Reaction-Transport Model

We present a 1-dimensional (1D) reaction-transport model for a steady-state axially-dispersed packed-bed reactor inclusive to all MoC_x/H-ZSM-5 + Zr formulations. Methane DHA reactions and H_2 absorption are treated as pseudo-homogenous processes in catalyst and absorbent beds, respectively. We consider methane conversion solely to benzene and naphthalene, which together constitute $\gtrsim$ 92% carbon selectivity. Benzene + naphthalene

(B+N) yield in reaction-transport simulations is thus identical to methane conversion and permits comparison to observed rates without complications conferred by methane conversion to entrained carbon and/or coke. Differential mole balance in the catalyst bed yields non-dimensional equations:

$$\frac{1}{\mathrm{Pe}}\frac{\mathrm{d}^2 y_M}{\mathrm{d}x^2} - \frac{\mathrm{d}y_M}{\mathrm{d}x} + \mathrm{Da_B} y_{CH_4}^{0.72}(1-\eta_B) + \mathrm{Da_N} y_{CH_4}^{0.74}(1-\eta_N) = 0 \quad \textbf{[2.7]}$$

$$\frac{1}{\mathrm{Pe}}\frac{\mathrm{d}^2 y_{H_2}}{\mathrm{d}x^2} - \frac{\mathrm{d}y_{H_2}}{\mathrm{d}x} - \frac{3}{2}\mathrm{Da_B} y_{CH_4}^{0.72}(1-\eta_B) - \frac{8}{5}\mathrm{Da_N} y_{CH_4}^{0.74}(1-\eta_N) + \mathrm{Da_{Zr}} y_{H_2} = 0 \quad \textbf{[2.8]}$$

$$\frac{1}{\mathrm{Pe}}\frac{\mathrm{d}^2 y_B}{\mathrm{d}x^2} - \frac{\mathrm{d}y_B}{\mathrm{d}x} - \frac{1}{6}\mathrm{Da_B} y_{CH_4}^{0.72}(1-\eta_B) = 0 \quad \textbf{[2.9]}$$

$$\frac{1}{\mathrm{Pe}}\frac{\mathrm{d}^2 y_N}{\mathrm{d}x^2} - \frac{\mathrm{d}y_N}{\mathrm{d}x} - \frac{1}{10}\mathrm{Da_N} y_{CH_4}^{0.74}(1-\eta_N) = 0 \quad \textbf{[2.10]}$$

where y_j is dimensionless gas-phase partial pressure, normalized by 1 bar, of component j, x is dimensionless length, and subscripts M, H_2, B, and N, refer to methane, hydrogen, benzene, and naphthalene respectively. Mole balance in the absorbent beds staged upstream and/or downstream of catalyst gives

$$\frac{1}{\mathrm{Pe_{Zr}}}\frac{\mathrm{d}^2 y_M}{\mathrm{d}x^2} - \frac{\mathrm{d}y_M}{\mathrm{d}x} = 0 \quad \textbf{[2.11]}$$

$$\frac{1}{\mathrm{Pe_{Zr}}}\frac{\mathrm{d}^2 y_M}{\mathrm{d}x^2} - \frac{\mathrm{d}y_M}{\mathrm{d}x} + \mathrm{Da_{Zr}} y_{H_2} = 0 \quad \textbf{[2.12]}$$

$$\frac{1}{Pe_{Zr}}\frac{d^2y_B}{dx^2} - \frac{dy_B}{dx} = 0 \qquad \textbf{[2.13]}$$

$$\frac{1}{Pe_{Zr}}\frac{d^2y_N}{dx^2} - \frac{dy_N}{dx} = 0 \qquad \textbf{[2.14]}$$

The final term in Eq. **2.8** is only included in interpellet mixtures wherein Eqs. **2.11** – **2.14** are unnecessary. Eqs. **2.7** – **2.14** collapse to those of an ideal PFR in the limit Pe → ∞ in which bulk convection is the dominant mode of mass transport (see Section A.1).

Non-dimensionalization of constitutive mass balance equations for a packed-bed reactor give rise to dimensionless parameters

$$Da_B = \frac{k_B L}{u} \qquad \textbf{[2.15]}$$

$$Da_N = \frac{k_N L}{u} \qquad \textbf{[2.16]}$$

$$Da_{Zr} = \frac{k_{Zr} L}{u} \qquad \textbf{[2.17]}$$

$$Pe = \frac{uL}{D_{eff}} \qquad \textbf{[2.18]}$$

$$Pe_{Zr} = \frac{uL}{D_{eff}} \qquad \textbf{[2.19]}$$

where u is linear velocity, L is the length of the catalyst bed, D_{eff} is effective diffusivity, and k_B, k_N, and k_{Zr} are 1st order rate constants for the benzene synthesis reaction, naphthalene synthesis reaction, and H_2 absorption, respectively.

Rate equations for forward rates of benzene and naphthalene synthesis are determined by kinetic measurements which rigorously account for influence of H_2, C_6H_6, and $C_{10}H_8$ partial pressures on reversibility of methane pyrolysis reactions (Section 2.3.1).

We assess axial changes in total molar flow-rate, arising from stoichiometric imbalance of aromatization reactions and in-situ removal of H_2, by alteration of total pressure, P; Da and Pe remain axially invariant. Axial changes in total pressure are, at maximum, 15% and are typically ~5-10% during methane DHA reactions as predicted by simulation and confirmed by GC analysis of reactor effluent.

Da and Pe^{-1} reflect ratios of the characteristic convective length-scale to kinetic and diffusive length-scales, respectively. Pe and Pe_{Zr} are Péclet numbers in the catalyst and Zr bed, calculated using D_{eff} measured by H_2 tracer pulse and step-change experiments (Section 2.3.2). Da_B and Da_N, both order unity, are Damköhler numbers for forward synthesis rates of benzene and naphthalene. H_2 removal by Zr is transport-limited under reaction-relevant process flow conditions, evidenced by breakthrough curves in H_2 uptake experiments which resemble Heaviside functions [30]. Thus, kinetic measurement of intrinsic first-order absorption rate constants, k_{Zr}, is inaccessible in current reactor configurations. $Da_{Zr} > 10^4$ give essentially invariant axial methane conversion and H_2 pressure profiles and are in quantitative agreement with net synthesis rates (Section 2.3.4). Terrani et al., (*55*) have reported activation energies and pre-exponential factors for first-order hydrogen absorption determined by dehydriding pressure-buildup experiments and

thermogravimetric studies which give $Da_{Zr} \sim 10^6$, conforming with $Da_{Zr} > 10^4$ per results of reaction-transport simulations.

Danckwerts boundary conditions are applied at both bounds of the catalyst and absorbent beds.

$$\frac{1}{Pe^+}\frac{dy_j}{dx}\Big|_{x^+_{entrance}} = y_j\left(x^+_{entrance}\right) - y_j\left(x^-_{entrance}\right) \quad \textbf{[2.20]}$$

$$\frac{1}{Pe}\frac{dy_j}{dx}\Big|_{x_{exit}} = 0 \quad \textbf{[2.21]}$$

$$y_j\left(x^-_{cat/abs}\right) = y_j\left(x^+_{cat/abs}\right) \quad \textbf{[2.22]}$$

$$\frac{1}{Pe^-}\frac{dy_j}{dx}\Big|_{x^-_{cat/abs}} = \frac{1}{Pe^+}\frac{dy_j}{dx}\Big|_{x^+_{cat/abs}} \quad \textbf{[2.23]}$$

where $x_{entrance}$ refers to inlet of the catalyst or absorbent bed furthest upstream, x_{exit} refers to outlet of the catalyst or absorbent bed furthest downstream, and $x_{cat/abs}$ refers to bounds between catalyst and absorbent. Eqs. **2.20** and **2.21**, generic "closed" Danckwerts boundary conditions (*56*), account for discontinuous change in dispersion length-scales between entrance and reaction/absorption sections and reaction/absorption and exit sections, respectively. We presume flow lines upstream and downstream of the reactor are dominated by convective flow such that Péclet numbers in entrance and exit sections far exceed those in reaction and absorption sections. Eqs. **2.22** and **2.23**, generic "open" Danckwerts boundary conditions, demand continuity of mass and of diffusive flux between

catalyst and absorbent beds which are of comparable length and thus are characterized by similar Péclet numbers.

Numerical simulation of the reaction-transport model, Eqs. **2.7** – **2.14**, with appropriate boundary conditions, Eqs. **2.20** – **2.23**, provides a useful tool to understand observed proximity effects in polyfunctional reaction configurations by inspection of axial product profiles otherwise unavailable by experimental means.

2.3.3 Measurement and Simulation of CH_4 aromatization with in-situ hydrogen abstraction

Figure 2.3 compares the results of the reaction-transport model with measured benzene + naphthalene (B+N) yield histories during methane DHA reactions in all five studied reactor configurations. Enhancement in instantaneous B+N yield upon zirconium addition mirrors improvements in methane conversion and cumulative aromatic yield shown in Figure 2.1; increase of B+N yield trends with proximity of Zr metal and MoC_x/H-ZSM-5 catalyst. Transient loss of activity in methane pyrolysis, evident by decreasing aromatic synthesis rates, arises from both MoC_x/H-ZSM-5 deactivation and zirconium saturation and is not treated in the steady-state transport model. Maximum instantaneous B+N yield coincides with a steady-state kinetic regime prior to onset of catalyst deactivation, as demonstrated by several previous investigations (*40*, *57*, *58*). Calculated B+N yield from steady-state reaction-transport simulations agree well with experimental maxima, demonstrating utility of Eqs. **2.7** – **2.14**.

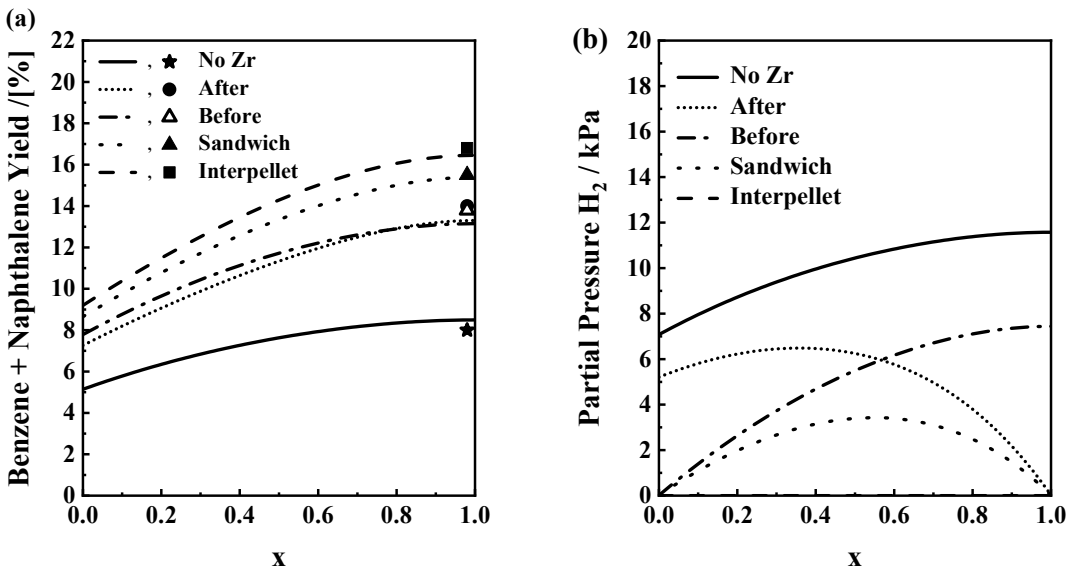

Figure 2.3: (a) Maximum single-pass (steady-state) (benzene + naphthalene) yield and (b) P_{H_2} along non-dimensional axial coordinate of catalyst bed, x, for all studied reaction configurations as predicted by simulation of the kinetic-transport model (lines) and quantified using the reactor effluent during methane DHA reactions (symbols). Reaction conditions: 973 K, MoC_x/H-ZSM-5 ≈ 1.2 g, Zr ≈ 2.4 g, feed flow rate ≈ 0.21 cm^3 s^{-1} (90 vol% CH_4).

Maximum possible single-pass B+N yield over MoC_x/H-ZSM-5 catalysts, henceforth referred to as the kinetic limit, is achieved in the complete absence of H_2 (i.e. $\eta \rightarrow 0$) and is limited solely by reaction kinetics and contact-time. The kinetic limit, ~17% for all configurations in Fig. 2.1, is determined by simulation of Eqs. **2.7** – **2.14** with $Da_B = 0.15$ and $Da_N = 0.03$ and $\eta = 0$ fixed for all reactions.

In all formulations, addition of Zr enhances methane conversion to benzene + naphthalene to near the kinetic limit, ~17%. Interpellet physical mixtures provide moderate improvements to maximum single-pass B+N yield compared to layered formulations, which yield similar aromatic production in either downstream or upstream packing of Zr. Similarity of effluent aromatic yield in staged configurations is reflected in symmetry of axial H_2 profiles; equivalent removal of H_2 at low or high contact times manifests

equivalent enhancement to aromatic synthesis. Partitioning zirconium in "sandwiched" configurations macroscopically mimics interpellet mixtures, improving B+N yield compared to singularly layered formulations; interpellet physical mixtures correspond to the limit of an infinite number of partitioned/stratified catalyst-absorbent layers.

Non-zero B+N yield and H_2 pressure at reactor inlet in certain configurations arises from "closed" Danckwerts boundary conditions, Eqs. **2.20** and **2.21**, which demand discontinuous change in species concentration from $x^-_{entrance}$ to $x^+_{entrance}$ as dispersion considerations become relevant upon transition from upstream flow lines, wherein $Pe \rightarrow \infty$, to the finite reaction and/or absorption section. Interpellet mixtures of zirconium and MoC_x/H-ZSM-5 beget near-complete removal of hydrogen owing to proximity of catalyst and absorbent. Response of H_2 axial profiles throughout the catalyst bed in staged configurations results from balance of convective and diffusive length scales ($Pe \sim 1$) which permits motility of gas-phase hydrogen in response to chemical potential gradients set by favorable thermodynamics of metal hydride formation. Axial H_2 pressures rise with distance from staged Zr beds as diffusional requirements rapidly increase ($L_{diffusion} \sim (\Delta x)^2$), preventing complete removal of hydrogen seen in interpellet mixtures. Staging zirconium before and after MoC_x/H-ZSM-5, at identical mass loading, shortens average separation between catalyst and absorbent and results in suppressed H_2 pressures throughout the catalyst bed. Ability of Zr upstream of MoC_x/H-ZSM-5 to scavenge H_2 is conferred by "open" Danckwerts boundary conditions, Eqs. **2.22** and **2.23**, which enables back-mixing into the absorbent bed.

Observed aromatization rates and simulated axial B+N yield and H_2 pressure profiles demonstrate synergistic interaction between MoC_x/H-ZSM-5 and Zr succeeds in

influencing reversibility of methane DHA reactions despite bed-scale separation of catalyst and absorbent in layered formulations, suggesting catalyst-absorbent proximity is crucial only to the extent that physical rate processes convey intermediates (e.g. H_2) between the absorbent and catalytic functions at time scales similar in magnitude to bulk advection and characteristic kinetic rates (i.e. $Pe \lesssim Da \approx 1$).

2.3.4 Control of Diffusive and Convective Length-Scales

We investigate the impact of convective and diffusive length-scales on methane conversion in the steady-state catalytic regime by (i) change of catalyst bed-length (equivalently catalyst mass loading) and (ii) change of linear velocity (equivalently total flow rate) in reactor configurations with Zr packed downstream of MoC_x/H-ZSM-5 at identical catalyst loading, reaction temperature, and reactor diameter. Systematic modification of Da and Pe^{-1}, by change of L (L/L_o = 0.2-1.6) and u (u/u_o = 1-8), provides a stringent test of the presented reaction-transport model and elucidates the key role of diffusive transport in polyfunctional staged-bed formulations. We assess direct influence of Da and Pe by use of the reaction-transport model; Figures A.2 and A.3 shows simulated surface plots of B+N yield as a function of Da and Pe with and without Zr packed downstream of catalyst.

Figure 2.4 compares measured maximum single-pass (i.e. steady-state) benzene + naphthalene yield during methane dehydroaromatization reactions with and without Zr packed downstream of MoC_x/H-ZSM-5 to those predicted by reaction simulations at varying total flow rate and catalyst loading. Data I in Fig. 2.4a and data II in Fig. 2.4b, single-pass B+N yield at $u/u_0 = 1$ and $L/L_0 = 1$, respectively, correspond to experimental measurements presented in Fig. 2.3.

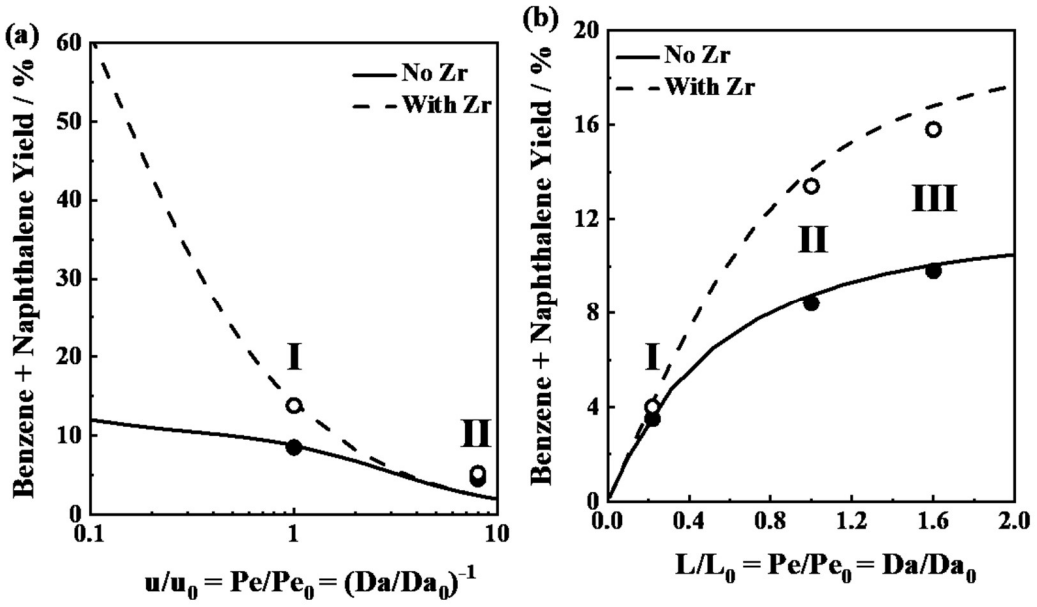

Figure 2.4: Maximum single-pass (benzene + naphthalene) yield with and without Zr packed downstream of MoC_x/H-ZSM-5 as measured (○,●) and predicted by simulation of the reaction-transport model (---, —), as a function of catalyst bed length, L, and linear feed velocity, u. Data labels I, II, and III refer to pairs of data at identical u/u_0 or L/L_0. Reaction conditions: 973 K, MoC_x/H-ZSM-5 ≈ (0.15 – 1.9) g, Zr ≈ 2.4 g, feed flow rate ≈ (0.21 – 2.00) $cm^3\ s^{-1}$, L_o ≈ 2.7 cm, u_o ≈ 0.71 cm s^{-1}

Decrease of u/u_0 from 8 to 1, data II to data I in Fig. 2.4a, enhances B+N yield from ~4% to 10% without Zr and 14% with Zr packed downstream of the catalyst. For $u/u_0 \gtrsim 4$, B+N yield is unchanged by Zr addition, as evidenced by data II, owing to characteristic convective rates dominating over both kinetic and diffusive rates (i.e., both Da and $Pe^{-1} \rightarrow 0$). Simulation of the reaction-transport model captures the observed trends and predicts most significant influence of Zr addition to occur as $u/u_0 \rightarrow 0$. Reduction of linear velocity, u, increases both Da and Pe^{-1}, simultaneously lifting kinetic and thermodynamic barriers to methane conversion in catalyst-absorbent mixtures. Enhancement to kinetic limits to aromatic production, determined by $Da = kL/u = k\tau$, results from elongated contact-times. Increase of $Pe^{-1} = D/(uL)$ with decreasing u reflects decrease in characteristic rates of axial convection and permits improved motility of gas-phase H_2 to the downstream absorbent

bed, thereby lifting thermodynamic limitations to methane DHA. Without staging of zirconium, decreasing flow rate modestly increases methane conversion until approach to the unchanged equilibrium limit (~10%); improved kinetic limits cannot be achieved without in-situ H_2 removal.

Data I-III in Fig. 2.4b demonstrate that, with and without a subsequent Zr bed, increasing catalyst bed-length/mass loading monotonically enhances B+N yield. Curves generated by simulation of the reaction-transport model follow data I-III and show increase of B+N yield with L/L_0 is roughly linear at low loadings and plateaus as $L/L_0 \rightarrow \infty$. Limits to B+N yield at $L/L_0 \rightarrow \infty$ are ~17% with downstream Zr and ~10%, the equilibrium limit, without Zr addition (Fig. S8). Difference in B+N yield with and without Zr grows with L/L_0 as net synthesis rates in monofunctional formulations become more limited with increasing methane conversion. Curvilinear dependence of B+N yield with respect to catalyst loading is similar to enhancement of methane conversion, X, in an ideal PFR wherein, for a 1st-order reaction, $X = (1+Da^{-1})^{-1}$. Congruence of conversion versus bed-length profiles with and without Zr is owed to converse dependence of Da and Pe^{-1} upon bed-length, L. The disproportionate dependence of contact-time ($\tau = L/u$) and characteristic diffusional time-scale (L^2/D) upon L dictates Pe^{-1} decreases with catalyst loading despite increase of τ and Da. Thus, systematic change of L results in a balance between kinetic and thermodynamic barriers: increasing bed-length imposes stricter limits on H_2 motility as kinetic maxima of methane conversion grow asymptotically with $Da = kL/u$.

2.3.5 Impacts of Catalyst-Absorbent Proximity on MoC_x/H-ZSM-5 Deactivation

Apparent loss of methane DHA activity in polyfunctional mixtures is complicated by conflation of dynamics attributable to catalytic CH_4 activation and stoichiometric absorption of H_2 into bulk Zr. As a metric for deactivation we consider decay in benzene

yield, concomitant with decrease in total methane conversion, which results from (i) a deactivation of the MoC_x/H-ZSM-5 catalyst and (ii) gradual saturation of Zr hydrogen absorption capacity. Ding et al., (*59*) have demonstrated the kinetics of deactivation on conventional $Mo(C_x)$/H-ZSM-5 catalysts are well-described by a 1st-order deactivation rate constant, which assumes decrease in activity arises solely from a loss of catalytic active sites, S, at a rate

$$\frac{dS}{dt} = -k_d S \qquad \textbf{[2.24]}$$

Figure 2.5 shows this simple model quantitatively captures decay of net benzene formation rates for MoC_x/H-ZSM-5 with or without Zr. Formulations wherein zirconium is either physically mixed with MoC_x/H-ZSM-5 or staged downstream of the catalyst show two distinct deactivation regimes whose transition coincides, in each case, with hydrogen breakthrough (i.e., complete saturation of ZrH_x) (*18*). Apparent deactivation due to Zr saturation during in-situ H_2 removal is more rapid in interpellet mixtures than in staged configurations owing to catalyst-absorbent intimacy increasing rates of both H_2 production by DHA reactions and absorption by proximate Zr. Following hydrogen breakthrough, net benzene rates in physical interpellet mixtures are significantly less than those intrinsic to MoC_x/H-ZSM-5 catalysts suggesting increased carbon deposition during in-situ H_2 removal (*18*) alters either the quantity or nature of catalytic active sites. In contrast, staging Zr downstream of MoC_x/H-ZSM-5 (Figure 2.5(b)) has little effect on benzene rates after zirconium saturation, demonstrating separation of catalyst and absorbent moderates coke formation during polyfunctional catalysis, preventing significant alteration to speciation and number of active sites. Further, 1st-order deactivation rate constants after hydrogen breakthrough in both interpellet and staged configurations are unchanged compared to

MoC_x/H-ZSM-5 catalysts under identical reaction conditions (Table 2.2), evincing in-situ H_2 removal in these formulations does not irreversibly alter kinetics of deactivation phenomena despite impacting carbon dynamics during enhanced methane conversion.

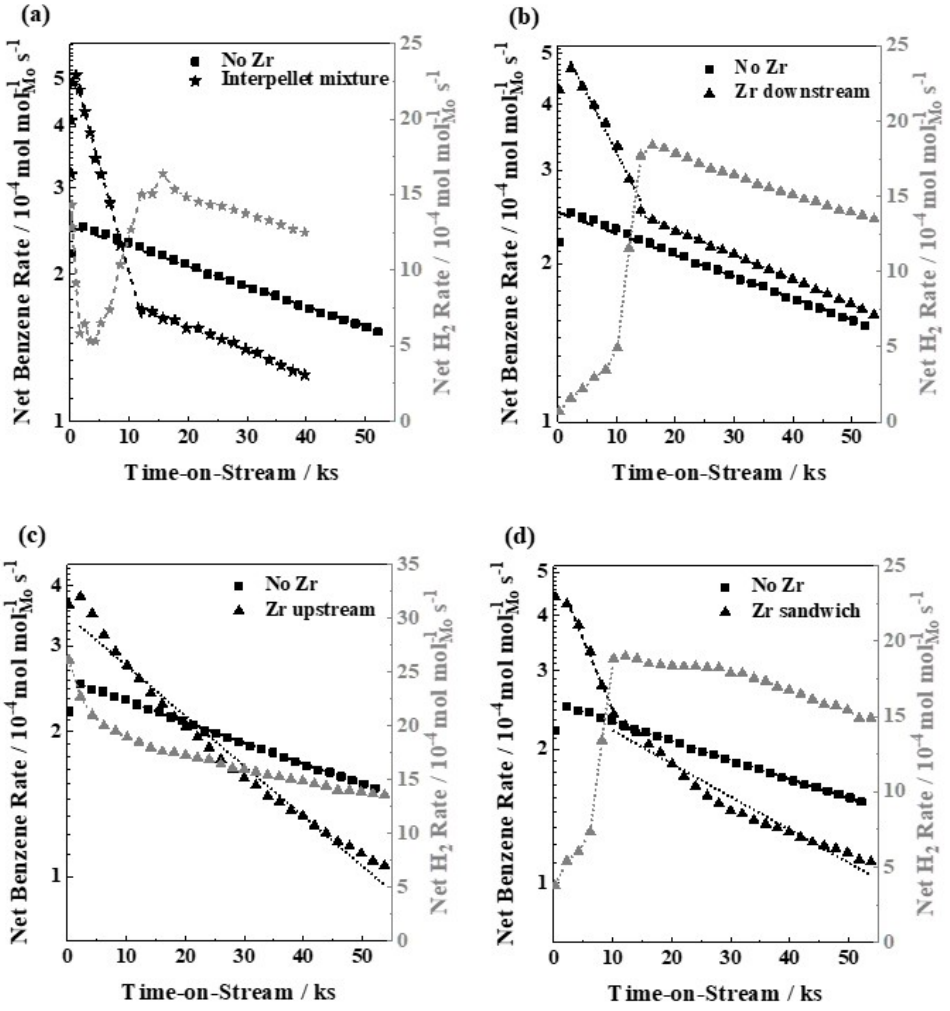

Figure 2.5: Instantaneous net benzene synthesis rate (left y-axes) and hydrogen effluent rate (right y-axes) as a function of time-on-stream during methane DHA reaction for (a) an interpellet physical mixture of Zr and MoC_x/H-ZSM-5, (b) Zr packed downstream of MoC_x/H-ZSM-5, (c) Zr packed upstream of MoC_x/H-ZSM-5, and (d) sandwich configuration, compared to MoC_x/H-ZSM-5 only in each case. Reaction conditions: 973 K, MoC_x/H-ZSM-5 ≈ 1.2 g, Zr ≈ 2.4 g, feed flow rate ≈ 0.21 $cm^3\ s^{-1}$ (90 vol% CH_4). Dashed lines are linear fits for the curves as discussed in text and corresponding data shown in Table 2.2.

Table 2.2: Summary of deactivation constants for benzene formation calculated using Eq. **2.24** for MoC_x/H-ZSM-5 and Zr in different fixed-bed configurations

Fixed-bed configuration	k_d before hydrogen breakthrough / s^{-1}	k_d after hydrogen breakthrough / s^{-1}
MoC_x/H-ZSM-5 only	NA	0.0094
Interpellet mixture [a]	0.1058	0.0113
Zr downstream [b]	0.0418	0.0109
Zr upstream [c]	NA	0.0243
Sandwich [d]	0.0733	0.0171

[a] Corresponding data shown in Figure 2.5(a)
[b] Corresponding data shown in Figure 2.5(b)
[c] Corresponding data shown in Figure 2.5(c)
[d] Corresponding data shown in Figure 2.5(d)

Figures 2.5(c) shows benzene net synthesis rate histories for Zr packed upstream of MoC_x/H-ZSM-5. Saturation of ZrH_x upstream of MoC_x/H-ZSM-5 catalyst demands H_2 transport opposite to convective flow, concomitantly eliminating both breakthrough behavior of H_2 elution curves and the two distinct deactivation regimes characteristic of polyfunctional formulations in Figure 2.5(a) and 2.5(b). Loss of activity in Figure 2.5(c) follows a 1^{st}-order deactivation profile throughout the lifetime of the catalyst and the absorbent with greater k_d than that intrinsic to MoC_x/H-ZSM-5 (Table 2.2). We posit that the high concentration of H_2 removal sites at low contact times is responsible for the rapid deactivation in these reactor configurations. MoC_x/H-ZSM-5 deactivation may, in part, result due to molecular moieties formed at low contact times (equivalently low

conversions) whose formation is promoted by removal of molecular hydrogen. At low conversions, H_2 abstraction may disproportionately enhance formation of graphitic carbon, $CH_4 \rightarrow C_{(s)} + 2H_2$, which provides an absolute upper-bound on H_2 liberated per carbon, and thus, if equilibrium limited, is most aided by hydrogen removal.

Figure 2.5(d) demonstrates H_2 breakthrough and benzene rate histories are complicated by partition of Zr upstream and downstream of the catalyst bed. We identify two deactivation regimes before and after H_2 breakthrough; however, the transition is not distinct as in Figure 2.5(a) and 2.5(b). Apparent breakthrough in Fig. 2.5(d) corresponds solely to complete saturation of Zr partitioned downstream of catalyst; saturation of Zr packed upstream of catalyst is not coincident with H_2 breakthrough, as evidenced by Fig. 2.5(c). In contrast to interpellet mixtures and formulations with Zr staged solely downstream of catalyst, 1^{st}-order deactivation rate constants after H_2 breakthrough for sandwich configurations are significantly larger than those without zirconium suggesting H_2 removal sites concentrated upstream of the catalyst bed continue to deleteriously impact stability of methane aromatization rates. Disparate impact of H_2 removal at low or high contact times on catalyst stability, even after Zr saturation, supports hypotheses that graphitic carbon is involved in deactivation of active sites in Mo/H-ZSM-5 catalysts.

2.4 Conclusion

Introduction of a continuous hydrogen scavenging functionality via interpellet and staged fixed-bed configurations of MoC_x/H-ZSM-5 and Zr metal circumvents intrinsic thermodynamic limitations of methane DHA at 973 K, thereby, increasing single-pass methane conversion to near the kinetic limit (~14% conversion to benzene and ~17% conversion to benzene + naphthalene), as dictated by forward synthesis rates. Zr metal beds staggered downstream and/or upstream of the MoC_x/H-ZSM-5 catalyst bed results in 1.5 –

1.7 fold enhancement in cumulative product yield due to transient hydrogen absorption by Zr accelerating methane conversion to aromatics. A reaction-transport model accounting for axial dispersion in packed bed reactors elucidates the underlying role of reactor hydrodynamics in lab-scale investigations. Simulated axial profiles of hydrogen and hydrocarbon partial pressure reveal Péclet number values near unity are required for efficacious removal of H_2 from the proximity of MoC_x/H-ZSM-5 catalyst by staged Zr. Inert H_2 tracer studies with impulse and step-change input measure effective H_2 dispersion coefficients, D_{eff} = 1.43 cm^2 s^{-1}, and Péclet number, Pe = 1.32, to confirm the significant role of axial dispersion at process conditions relevant to catalytic studies. Both reaction-transport simulations and kinetic measurements demonstrate control of diffusive and convective length scales by alteration of catalyst bed-length and total flow-rate systematically changes methane to benzene + naphthalene yield (3% – 17%), thereby explicating the critical influence of H_2 motility on efficacy of polyfunctional interaction between catalyst and absorbent. Impacts of in-situ H_2 removal on catalyst deactivation are observed to be most severe and sometimes irreversible in configurations with high concentrations of H_2 absorptive capacity at low contact times; interpellet mixtures or configurations with Zr packed solely downstream of MoC_x/H-ZSM-5 have mild and reversible effects on catalyst deactivation.

3 Influence of ethylene and acetylene on the rate and reversibility of methane dehydroaromatization on Mo/H-ZSM-5 catalysts

*Contents herein are reproduced with permission from Razdan, N. K., Kumar, A., Foley, B. L., Bhan, A. Influence of ethylene and acetylene on the rate and reversibility of methane dehydroaromatization on Mo/H-ZSM-5 catalysts. *Journal of Catalysis*. **2020**, *381*, 261–270. https://doi.org/10.1016/j.jcat.2019.11.004.

3.1 Conspectus

Acetylene is identified as a key intermediate in methane dehydroaromatization (DHA) reactions present in concentrations $\mathcal{O}(1)$ Pascal. The rank of acetylene and other C_2 hydrocarbon intermediates is determined by conversion-selectivity profiles collected from 0.01-8% methane conversion varied by extent of "non-selective" deactivation of Mo/H-ZSM-5 catalysts. Ethane is shown to be the sole primary product of methane pyrolysis and is sequentially dehydrogenated to ethylene and acetylene – which aromatizes to benzene with rates similar to direct acetylene aromatization measured in the absence of methane. The influence of C-H cleavage and C-C coupling events to control the rate and reversibility of DHA is assessed by the degree of reversibility control, introduced here for the first time, and the degree of rate control. The approach to equilibrium of the methane to benzene synthesis reaction is length averaged and affinity averaged by the degree of reversibility control of each intervening elementary step to rigorously calculate forward rates of benzene synthesis by use of De Donder relations. Forward rates are found to be invariant along the catalyst bed once the DHA network reaches a pseudo-steady state and methane, ethane, and ethylene form an equilibrated pool.

3.2 Introduction

Strong, apolar C-H bonds in methane confer significant thermodynamic and kinetic challenges in non-oxidative methane valorization (*8*, *60*). Mo-modified medium pore MFI zeolites (Mo/H-ZSM-5) reduce kinetic barriers to methane pyrolysis and catalyze

dehydroaromatization (DHA) reactions with high benzene (≳ 70%) and aromatic (≳ 95%) selectivity (*18*, *19*, *21*, *37*, *61*). Active Mo/H-ZSM-5 catalysts contain carbidic forms of Mo synthesized from high-temperature (~950 K) reduction and carburization of oxidic Mo precursors impregnated within ZSM-5 zeolite by either incipient wetness impregnation or vapor-phase cation exchange. Preparation of oxidic "pre-catalysts" by solid-state vapor-phase exchange of MoO_3 monomers with proximate pairs of zeolitic Brønsted acid sites in ZSM-5 anchors Mo cations to the zeolite framework as well-defined $(Mo_2O_5)^{2+}$ dimers (*38*, *42*). Impregnation of oxidic Mo, provenance of dimeric $(Mo_2O_5)^{2+}$, and evolution to carbidic Mo by carburization in methane is confirmed by Raman spectroscopy, infrared absorption (IR), X-ray absorption spectroscopy, ^{27}Al magic-angle-spinning (MAS) NMR, transmission electron microscopy, and chemical transients during dimer formation and subsequent carburization (*18*, *19*, *22*, *38*, *57*, *62*). These methods note evolution of $(Mo_2O_5)^{2+}$ to MoC_x, but do not probe stoichiometry or speciation of resultant carbidic Mo. Recent studies utilize ^{13}C MAS NMR, CO IR, and dynamic nuclear polarization surface enhanced NMR spectroscopy to show Mo speciation after carburization is diverse – including monomeric and dimeric (oxy)carbides and Mo_2C nanoparticles which may all play some catalytic role (*12*, *27*, *63*, *64*).

Even at high DHA reaction temperatures (~950 K), thermodynamic barriers to methane valorization persist, limiting equilibrium conversion to ~10% (*58*, *65–69*). Stringent thermodynamic constraints result in a highly reversible DHA reaction network with observed net benzene synthesis rates decreasing with catalyst contact time as reverse hydrogenation and cracking reactions become prominent (*19*). In this study we seek to evaluate the intrinsic kinetics of methane DHA on Mo/H-ZSM-5 by quantitatively

accounting for the influence of reverse reactions on observed net rates. We rigorously de-convolute thermodynamic and kinetic contributions to observed DHA rates in order to (i) elucidate the rate control of intervening dehydrogenation and oligomerization events, and (ii) isolate the forward rate of benzene formation on Mo/H-ZSM-5. Application of De Donder relations and concepts of microscopic reversibility shows methane, ethane, and ethylene form an equilibrated pool at early contact times corresponding to methane conversion ≥ 2.5%, congruent with existing reports (*39*, *70*), and reveals acetylene to be a key reactive intermediate in benzene formation, as suggested previously (*71*, *72*). Elucidation of the DHA reaction network informs calculation of forward rates by allowing for quantitative appraisal of the reversibility of the single-path methane to benzene series reaction in terms of approach to equilibrium of constituent elementary steps. Previous investigations attempt to account for reversibility of the DHA reaction network by quantifying solely the approach to equilibrium of the overall benzene synthesis reaction ($6CH_4 \rightleftarrows C_6H_6 + 9H_2$) (*19*, *40*); however, we demonstrate the hitherto unrecognized importance of averaging reaction reversibility by the affinity of all non-equilibrated intervening steps during methane DHA. Determination of elementary step reversibilities permits quantitative appraisal of kinetic and thermodynamic influence of dehydrogenation and oligomerization events in terms of the degree of rate control and the degree of reversibility control, defined herein for the first time. Finally, we outline and address the critical importance of formalisms of affinity averaging and spatial averaging to calculate forward rates in flow reactors. We rigorously affinity average and spatially average overall approach to equilibrium of benzene synthesis to demonstrate forward aromatization rates

are invariant once a pseudo-steady state is achieved upon equilibration of methane, ethane, and ethylene.

3.3 Materials and Methods

3.3.1 Catalyst synthesis and preparation

Mo/H-ZSM-5 catalysts were synthesized by exposure of MoO_x/H-ZSM-5 "pre-catalysts" to 0.21 cm^3 s^{-1} 90% CH_4 at 973 K and ~115 kPa total pressure, irrespective of catalyst loading or total flow rate during DHA reactions. MoO_x/H-ZSM-5 materials were prepared by methods detailed previously (*18*, *19*, *47*, *57*, *73*) and summarized in the following. In brief, H-ZSM-5 zeolite was synthesized from NH_4-ZSM-5 (Zeolyst International, Si/Al = 11.5, CBV 2314) treated in dry air (~1.67 cm^3 s^{-1}) to thermally decompose NH_4^+ to H^+ and NH_3(g) at 773 K (0.0165 K s^{-1}; 36 h hold). Oxidic Mo precursors, MoO_3 (Sigma-Aldrich, 99.9%), were physically mixed with H-ZSM-5 powders in an agate mortar and pestle for 15-30 min with nominally 3.3 wt% Mo (Mo/Al = 0.25). Intimate MoO_3 + H-ZSM-5 mixtures were heated from ambient temperature to 623 K (0.0167 K s^{-1}) and held for 15 h in dry air (0.67 cm^3 s^{-1}) to ensure removal of physisorbed water and dispersion of MoO_x oligomers on the external zeolite surface (*38*, *42*, *62*). Solid-state vapor-phase exchange of oxidic Mo with zeolitic Brønsted acid sites was achieved at 973 K (0.167 K s^{-1}; 10 h hold). The resultant MoO_x/H-ZSM-5 material was pressed, crushed, and sieved to obtain particle sizes between 180 and 425 μm (mesh 40 – 80) for activation to Mo/H-ZSM-5 and use in catalytic dehydroaromatization reactions.

3.3.2 Methane dehydroaromatization catalytic reactions

Methane dehydroaromatization reactions were performed in fixed-bed tubular quartz reactors (I.D. 10.5 mm). MoO_x/H-ZSM-5 materials were heated in inert He flow (~ 0.33 cm^3 s^{-1}, UHP, Minneapolis Oxygen) to 973K at 0.18 K s^{-1} in a resistively-heated furnace

(National Element FA120). Tubular reactors were encased in an annular Inconel cylinder to ensure gradientless conduction of heat between the furnace and quartz reactor. Catalyst-bed temperature was monitored by two thermocouples stationed diametrically on the outer wall of the tubular quartz reactor. Oxidic pre-catalysts were exposed to CH_4/Ar (90 vol% CH_4 and 10 vol% Ar, total feed flow rate 0.21 $cm^3\ s^{-1}$, UHP, Matheson Tri-Gas) at 973 K until carburization is complete – as indicated by closure of carbon balance. Illustrative data is shown in Section B.1. DHA reactions were either continued under 0.21 $cm^3\ s^{-1}$ total flow or were performed at identical composition, but varied flow range (0.21-2.1 $cm^3\ s^{-1}$), after ~30 minutes flush of reactor lines in He flow (~ 0.33 $cm^3\ s^{-1}$) as reaction feed flow stabilized. Entrance and exit flow lines were heated to > 450K via resistive-heating tapes to prevent condensation of aromatic products and water. The effluent composition was analyzed using a mass spectrometer (MKS Cirrus 200 Quadrupole MS system) and a gas chromatograph (Agilent 7890) equipped with a methyl-siloxane capillary column (HP-1, 50 m x 320 μm x 0.52 μm) connected to a flame ionization detector (FID) for detection of hydrocarbons and a GS-GasPro column (60 m x 0.320 mm) connected to a thermal conductivity detector (TCD) for detection of permanent gases (H_2, Ar, and CH_4).

3.4 Results and Discussion

Methane dehydroaromatization reactions were performed over 0.025-1.2 g of Mo/H-ZSM-5 (Mo/Al = 0.25, Si/Al = 11.5) catalysts at 973 K with 0.21-2.1 $cm^3\ s^{-1}$ total flow of 90% CH_4 and 10% Ar as an internal standard at ~115 kPa total pressure. All reported flow rates are at standard temperature and pressure (STP).

3.4.1 Methane DHA reaction pathway

Figure 3.1 shows selectivities of DHA products as a function of methane conversion over several Mo/H-ZSM-5 catalyst samples at 973 K. Changes in conversion for each

catalyst sample are achieved by allowing the catalyst to deactivate with time on stream (TOS). The coincidence of conversion-selectivity profiles for each product across three samples and 0.5-8% methane conversion, f, demonstrates that deactivation of Mo/H-ZSM-5 catalysts is "non-selective", or occurs without modification of the intrinsic chemical nature of catalytic sites (*46*, *62*, *74*). Thus, elucidation of the DHA reaction network by contact-time variation experiments at steady state can equivalently be performed by allowing Mo/H-ZSM-5 catalysts to deactivate with time on stream.

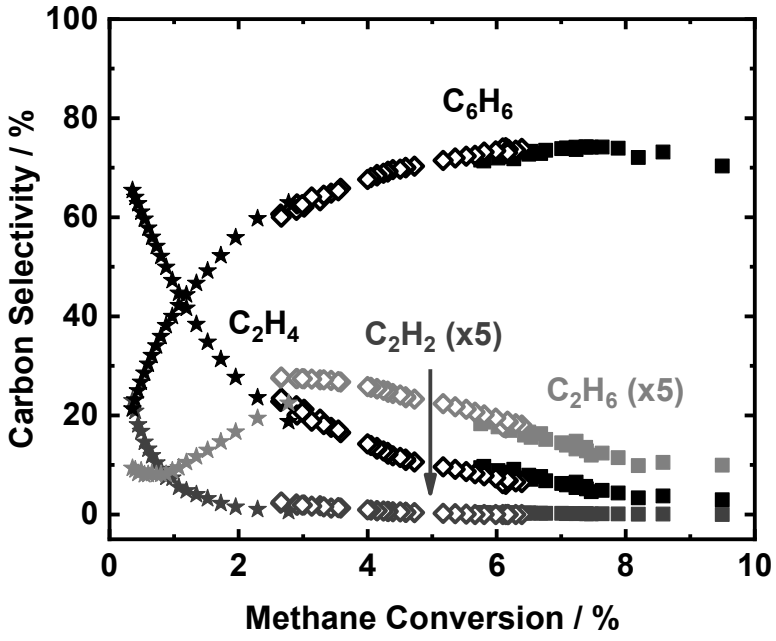

Figure 3.1: Carbon selectivity of DHA products as a function of methane conversion over three deactivating catalysts (Mo/Al = 0.25, Si/Al = 11.5). Reaction conditions: 973 K, ~115 kPa total pressure, 90% CH_4, 10% Ar. 1.2 g Mo/H-ZSM-5, 0.21 $cm^3\ s^{-1}$ (■); 1.0 g Mo/H-ZSM-5, 0.21 $cm^3\ s^{-1}$ (◊); 1.2 g Mo/H-ZSM-5, 2.1 $cm^3\ s^{-1}$ (★).

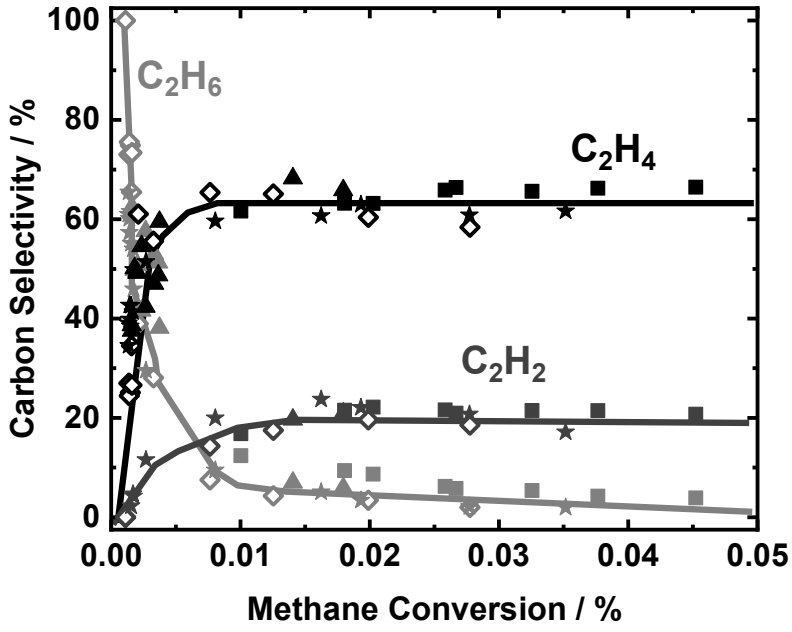

Figure 3.2: Carbon selectivity of DHA C_2 hydrocarbons at differential methane conversion over four deactivating catalysts (Mo/Al = 0.25, Si/Al = 11.5). Reaction conditions: 973 K, ~115 kPa total pressure, 90% CH_4, 10% Ar, 2.1 $cm^3\ s^{-1}$. 0.025 g Mo/H-ZSM-5 (◊); 0.025 g Mo/H-ZSM-5 (★); 0.250 g Mo/H-ZSM-5 (■); 0.100 g Mo/H-ZSM-5 (▲).

The selectivity of C_2 hydrocarbons as methane conversion, f, approaches zero (< 0.05%) is shown in Figure 3.2. The congruence of selectivity profiles for each C_2 across four catalyst samples again demonstrates deactivation is non-selective and evinces the reproducibility of the presented data. The asymptotic approach of C_2H_6 selectivity to 100% as $f \rightarrow 0$ in Figure 3.2 reveals ethane is the sole primary stable gas-phase product. Several investigations propose ethylene is the primary product of methane DHA per observations that (i) ethylene selectivity increases with space velocity (*24*, *37*, *42*), reaction time (i.e. extent of deactivation) (*24*, *37*, *42*), and reaction temperature (*75*); and (ii) ethylene aromatization over H-ZSM-5 gives similar product distribution to methane DHA on Mo/ZSM5 materials (*21*). Fig. 3.2 demonstrates ethylene and acetylene selectivities approach zero as methane conversion decreases from 0.05% to 0%; concurrently, ethane

selectivity approaches 100%. Zero initial selectivity of ethylene and acetylene eliminates the possibility of C_2H_4 or C_2H_2 formation from direct C-C coupling of CH_2 or CH fragments from methane (i.e. $2CH_4 \rightarrow 2CH_x + (2 - ½x)H_2 \rightarrow C_2H_{2x} + (2 - ½x)H_2$; x = 1, 2). Ethylene and acetylene are necessarily sequential pyrolysis products formed from dehydrogenation of ethane or coupling of ethane-derived surface fragments.

From conversion-selectivity profiles in Figs. 3.1 and 3.2 we propose methane DHA to benzene proceeds via a single-path series reaction depicted in Scheme 3.1.

Scheme 3.1: Proposed methane DHA reaction pathway

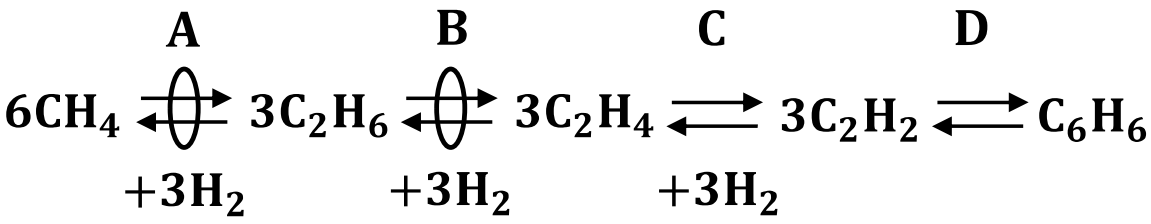

Methane, ethane, and ethylene form a quasi-equilibrated pool catalyzed by carbidic Mo sites for sufficient contact-times (> 7 mol_{Mo} s mol_{CH4}^{-1}). Subsequent ethylene dehydrogenation to acetylene is proposed to occur over carbidic Mo sites and acetylene aromatization to benzene may be catalyzed by Mo or zeolitic Brønsted acid sites.

The rank of ethane dehydrogenation products is evident in Fig. 3.3 which shows total approach to equilibrium, Z, of steps A-D (Scheme 3.1). Total approach to equilibrium for global gas-phase reaction or elementary step i in a series reaction is calculated as

$$Z_i = \frac{1}{K_{eq,i}} \prod_{j=species} P_j^{\nu_{ij}} \qquad \textbf{[3.1]}$$

where P_j is the partial pressure of species j divided by 1 bar (reference pressure), ν_{ij} is the stoichiometric coefficient of species j in step i, and $K_{eq,i}$ is the equilibrium constant of step i. By global gas-phase reaction we mean the interconversion between stable gas-phase species (e.g. $2CH_4 \rightleftharpoons C_2H_6 + H_2$) resultant from a sequence of elementary steps. In this

work we calculate Z_i on a six carbon atom basis (e.g. $Z = P_{C_6H_6} P_{H_2}^9 \left(P_{CH_4}^6 K_{eq}\right)^{-1}$ for overall reaction $6CH_4 \rightleftharpoons C_6H_6 + 9H_2$) (*76*). The precedent in the literature is to report Z on a one carbon atom basis (i.e. for overall reaction $CH_4 \rightleftharpoons 1/6\ C_6H_6 + 3/2\ H_2$) (*19*, *39*, *70*); however, this basis requires stoichiometric numbers of elementary steps to be less than unity to correctly calculate approach to equilibrium of elementary steps (*vida infra*) which we seek to avoid for sake of clarity.

Principles of thermodynamics dictate for each step in a series reaction $Z \leq 1$ (i.e. that each step is either thermodynamically downhill or equilibrated). Thus, $Z_C < 1$ for $C_2H_4 \rightleftharpoons C_2H_2 + H_2$ (see Fig. 3.3) suggests acetylene is a dehydrogenation product of ethylene and is consistent with a series reaction pathway wherein methane activation and C-C coupling to C_2H_6 is followed by sequential dehydrogenation to C_2H_4 and then C_2H_2 (Scheme 3.1).

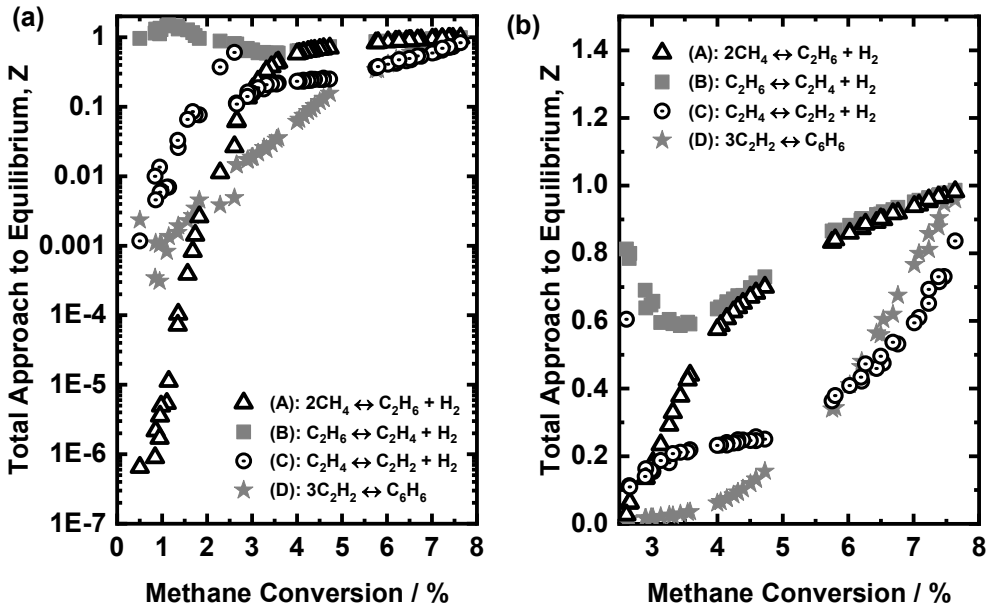

Figure 3.3: Total approach to equilibrium of global gas-phase DHA reactions, as listed in Scheme 3.1 on a one benzene molecule basis (i.e. overall reaction $6CH_4 \rightleftharpoons C_6H_6 + 9H_2$). Figure 3.3a and 3.3b are the same data shown on differently scaled axes. Reaction

conditions: 973 K, ~115 kPa total pressure, 90% CH_4, 10%Ar, 0.21-2.1 $cm^3\ s^{-1}$, 0.1-1.2 g Mo/H-ZSM-5.

The presence of acetylene in pseudo-steady state (PSS) quantities (*vida infra*) which deviate from $C_2H_4 \rightleftharpoons C_2H_2 + H_2$ equilibrium also implies acetylene must be consumed in subsequent oligomerization and cyclization steps. Acetylene consumption by coke formation is unlikely as carbon deposition during DHA catalysis is negligible after an initial induction period which corresponds to carburization of the pre-catalyst (*18*, *47*); less than 0.1 C/Mo is deposited after 8.52 ks time on stream on 1.2g pre-carburized MoC_x/H-ZSM-5 with 0.21 $cm^3\ s^{-1}$ 90% methane feed (*18*). Thus, $Z_C < 1$ suggests C_2H_2 is an intermediate in DHA catalysis, as has been proposed previously (*77–79*). Ha et al., (*78*) have demonstrated acetylene aromatization over H-ZSM-5, Mo/SiO_2, and Mo/H-ZSM-5 occurs with larger rates than either ethylene or methane aromatization at 923 K and hydrocarbon and H_2 partial pressures relevant to DHA catalysis. Acetylene aromatization rates (144 μmol $g^{-1}\ h^{-1}$) over Mo/H-ZSM-5 were 1.5 times larger than ethylene aromatization (97 μmol $g^{-1}\ h^{-1}$) and were comparable to methane aromatization rates (131 μmol $g^{-1}\ h^{-1}$), leading Ha et al., (*78*) to conclude benzene is formed via oligomerization of acetylene-derived vinyl cation intermediates. We also measure acetylene to benzene forward rates over Mo/H-ZSM-5 which show good agreement with forward rates of acetylene aromatization during CH_4 DHA catalysis calculated from De Donder relations (*vida infra*), shown in Section B.1.

Tsai et al., (*80*) have demonstrated acetylene aromatization over H-ZSM-5 occurs readily without H_2 co-feed at rates far exceeding ethylene aromatization and also propose acetylene oligomerization is initiated by formation of highly reactive vinyl cations. Production of benzene from acetylene in the absence of H_2, shown in Section B.1 and

reported by Tsai et al., (*80*) demonstrates C_2H_2 can aromatize without proceeding through an ethylcarbenium intermediate, as is proposed in existing kinetic models of DHA on Mo/H-ZSM-5 (*58*, *67*). Detailed kinetic models of methane pyrolysis developed by Dean (*81*) demonstrate production of aromatics likely proceeds through acetylene as (i) vinylic products of acetylene coupling are far more reactive than allylic species resultant from ethylene dimerization and (ii) benzene synthesis from acetylene benefits from high reaction exothermicity required to overcome entropic loss during cyclization.

From this body of evidence, we conclude acetylene is likely the immediate stable gas-phase precursor to benzene in the single-path methane DHA reaction sequence (Scheme 3.1). However, we cannot unequivocally eliminate the possibility that aromatization proceeds through ethylene oligomerization and therefore report results for the kinetic and thermodynamic analyses to follow under this presumption in Section B.2.

In what follows, we use De Donder relations to assess quantitatively the extent to which dehydrogenation and oligomerization/aromatization events in Scheme 3.1 control the rate and reversibility of methane DHA.

3.4.2 Concepts of rate- and reversibility-control of elementary steps in series reactions

3.4.2.1 The De Donder formalism for single-path catalytic reaction sequences

The net rate of an elementary step, r_i, is given by the difference of forward and reverse rates:

$$r_i = \vec{r}_i - \overleftarrow{r}_i \qquad \textbf{[3.2]}$$

The De Donder equation (*72*) relates the ratio of forward and reverse rates of elementary steps to measurable thermodynamic quantities

$$\frac{\overleftarrow{r}_i}{\vec{r}_i} = e^{-\frac{A_i}{RT}} = z_i \qquad \textbf{[3.3]}$$

where $A_i = -\Delta G_i$ is the affinity of step i at a particular extent of reaction and z_i is approach to equilibrium of the corresponding elementary step; z_i approaches zero for a fully irreversible reaction and unity for an equilibrated step. The total affinity of a global gas-phase reaction or elementary step per catalytic turnover is given by $A_{tot,i} = \sigma_i A_i$ where σ_i is the stoichiometric number of global gas-phase reaction or elementary step i. Thus, the total approach to equilibrium of global gas-phase reaction or elementary step i is related to its total affinity by

$$Z_i = e^{-\frac{A_{tot,i}}{RT}} \qquad \textbf{[3.4]}$$

The overall affinity of a series reaction is $A_{ov} = \sum_i \sigma_i A_i = \sum_i A_{tot,i}$ (*76*); therefore, the overall approach to equilibrium, z_{ov}, is a product of total approach to equilibrium of all elementary steps

$$z_{ov} = \prod_{i=steps} Z_i = \prod_{i=steps} z_i^{\sigma_i} \qquad \textbf{[3.5]}$$

Since reaction affinities are state functions, z_{ov} is also the product of total approach to equilibrium of all global gas-phase reactions; i.e. $z_{ov} = Z_A Z_B Z_C Z_D$ per Scheme 3.1.

Provided the concentration of all intermediates can be described by the pseudo-steady state hypothesis (PSSH), the forward rate of the overall reaction, $\vec{R}$, is related to the overall net rate, $R = r_i/\sigma_i$ for elementary steps, by

$$\vec{R} = \frac{R}{1 - \prod_i z_i} = \frac{R}{1 - z_{ov}^{1/\bar{\sigma}}} \qquad \textbf{[3.6]}$$

where

$$\bar{\sigma} = \frac{\sum_i \sigma_i A_i}{\sum_i A_i} = \frac{\sum_i \ln(Z_i)}{\sum_i \ln(z_i)} \quad \textbf{[3.7]}$$

is the affinity-averaged stoichiometric number where i is an index over all elementary steps (*82*).

The functional form of Eq. **3.6** communicates essential information regarding the manner by which elementary steps in a single-path reaction sequence affect the relationship between the overall net and forward rate.

Eq. **3.6** reveals the affinity-averaged stoichiometric number is critical in determining the effect of the overall reversibility, z_{ov}, to suppress overall net rates, R. Previous investigations, including our own (*19*), have implicitly assumed $\bar{\sigma} = 1$ in Eq. **3.6** without evidence or rationale. Forward rates calculated with $\bar{\sigma} = 1$ are serendipitously similar to those in this work if z_{ov} is also incorrectly length averaged, as described in Section 3.4.4 (*19*, *47*). We seek to directly calculate $\bar{\sigma}$ by Eq. **3.7** from 0-8% methane conversion in order to correctly account for reversibility of DHA reactions and utilize Eq. **3.6** to calculate the forward rate of methane DHA.

Eq. **3.6** also shows that a single-path reaction sequence behaves as if it were a single elementary step with a reversibility, $\overleftarrow{R}/\overrightarrow{R}$, equal to the product of the approach to equilibrium of all elementary steps

$$z_{eff} \equiv \frac{\overleftarrow{R}}{\overrightarrow{R}} = \prod_{i=steps} z_i = z_{ov}^{1/\bar{\sigma}}. \quad \textbf{[3.8]}$$

The effective reversibility, z_{eff}, is the approach to equilibrium of the overall process, z_{ov}, corrected by the affinity-averaged occurrences per turnover of all intervening elementary steps, $\bar{\sigma}$. In the case of a single, rate-determining step (rds) away from equilibrium, the overall reaction behaves as if it were an elementary step that occurs $\bar{\sigma} = \sigma_{rds}$ times per

turnover. Therefore, the extent to which each elementary step i exerts control on the effective approach to equilibrium, z_{eff}, is the degree of reversibility control,

$$X_{ZC,i} \equiv \left(\frac{\partial \ln \ln(z_{eff})}{\partial \ln \ln(z_i)}\right)_{z_j \neq i} = \frac{A_i}{\sum_j A_j} \quad \textbf{[3.9]}$$

where j is an index over all elementary steps. Section B.3 provides proof of the equivalence of the above expressions. Briefly, the first application of the natural logarithm converts z_{eff} from a product of z_i to a sum of $\ln(z_i)$, and the second application extracts the fractional influence of $\ln(z_i)$ on $\ln(z_{eff})$ and is analogous to the function of the natural logarithm in the definition of degree of rate control (*83*, *84*). The proposed definition of degree of reversibility control is a mathematical manifestation of a metric of rate-determining character suggested by Dumesic (*72*) where a step is rate-determining if $z_i \sim z_{eff}$ or $A_i \sim \sum_j A_j$. We posit that X_{ZC} is not a measure of degree of rate control, but, instead, a quantitative measure of the influence of each step to determine the apparent behavior of a series reaction as an elementary step, or, equivalently, the influence of each step to determine $z_{eff} \equiv \overleftarrow{R}/\overrightarrow{R}$. The result that $X_{ZC} = 0$ for a step with no rate control and $X_{ZC} = 1$ for a sole rate-determining step is a consequence of correlative, but not causal, relationship between rate control and reversibility control. In the following, we will demonstrate that X_{ZC} does not provide information about what steps control the rate, and that agreement between X_{ZC} and Campbell's definition of degree of rate control, X_{RC}, for bookend cases $X_{RC} = X_{ZC} = 0$ and $X_{RC} = X_{ZC} = 1$ is not reflected in intermediate values of X_{ZC} and X_{RC} where control of rate and apparent elementary step behavior of the overall reaction sequence are similar but not identical. In particular, the degree of reversibility control fails to capture a key principle of series reactions: for the same approach to equilibrium, steps

earlier in a single-path sequence exert more rate control than those later in the sequence. The nature of free energy as a state function manifests X_{ZC} be agnostic to the position of a step along the overall reaction coordinate, and, therefore, comparison solely of affinities of elementary steps is insufficient to evaluate rate control of each step.

3.4.2.2 The degree of rate control in single-path catalytic reaction sequences

Cortright and Dumesic (*85*) demonstrate that the degree of rate control of each elementary step i, defined as

$$X_{RC,i} \equiv \left(\frac{\partial \ln R}{\partial \ln \vec{k}_i}\right)_{K_i, k_{j\neq i}} \qquad \textbf{[3.10]}$$

where i and j are indices for elementary steps, in a single-path reaction sequence may be calculated from approach to equilibrium of elementary steps without need for any reaction rate constants, $\vec{k}_i$ or $\overleftarrow{k}_i$. In particular, the authors demonstrate, by example, that for a single-path sequence of fluid-phase elementary steps with one reactant and one product in each step,

$$X_{RC,i} \equiv \left(\frac{\partial \ln R}{\partial \ln \vec{k}_i}\right)_{K_i, k_{j\neq i}} = \sigma_i(1 - z_i) \prod_{j=1}^{j=i-1} z_j \Bigg/ \sum_{i=1}^{N} \left[\sigma_i(1 - z_i) \prod_{j=1}^{j=i-1} z_j\right]. \qquad \textbf{[3.11]}$$

where i and j are indices for elementary steps and N is the number of elementary steps in the reaction sequence (*83–85*). Eq. **3.11** is a generalization of particular cases investigated by Cortright and Dumesic (*85*). Per Eq. **3.11**, equilibrated steps ($z_i = 1$) have no rate-determining character and the rate-determining character of fully irreversible steps ($z_i = 0$) are limited by the deviation from equilibrium of all previous steps. X_{RC} thus captures the key principle of series reactions that is missed simply by inspection of z_i: steps earlier in a reaction sequence exhibit more rate control for the same approach to equilibrium than those

later in a reaction sequence – unless both steps are at equilibrium. Section 3.4.3 presents equations analogous to Eq. **3.11** which calculate degree of rate control of each step in the methane DHA reaction sequence while allowing for multiple reactants and/or products in each elementary step (e.g. unsaturated hydrocarbon and H_2 products in dehydrogenation reactions).

3.4.3 Rate- and reversibility-control of dehydrogenation and oligomerization in CH_4 DHA

Use of De Donder relations, degree of reversibility control, and degree of rate control is predicated on knowledge of the identity, standard Gibbs energy, and concentration of all species involved in the elementary steps which constitute the single-path methane to benzene series reaction. Coverages and energies of surface species are experimentally inaccessible; however, forward rates, X_{RC}, and X_{ZC}, may be calculated directly from thermodynamic properties, flow rates, and partial pressures of observable species provided each global gas-phase reaction contains only one rate-determining elementary step with an identifiable stoichiometric number, σ^*, as shown in Section B.3. The approach to equilibrium of the rate-determining elementary step, z_i^*, in a global gas-phase reaction i is related to the total approach to equilibrium of the global gas-phase reaction, Z_i by

$$z_i^* = Z_i^{1/\sigma_i^*} \qquad \textbf{[3.12]}$$

where all deviation from equilibrium in Z_i is attributed to z_i^*. Hence, z_i^* is the relevant thermodynamic bottleneck in each global gas-phase reaction i and σ_i^*, not σ_i, is the relevant stoichiometric number. For example, for global gas-phase reaction A, $\sigma_A^* = 6 \neq \sigma_A = 3$. Thus, if $Z_A = 0.90$, we impose $z_{A.2} = 1$, and calculate $z_{A.1} = z_A^* = Z_A^{1/6} = 0.98$. Identification of σ^* therefore permits calculation of approach to equilibrium for all non-equilibrated elementary steps in the overall series reaction and enables use of De Donder relations and

degree of rate control by Eqs. **3.6-3.13**. Fig. 3.4 shows approach to equilibrium, z_i^*, of rate-determining elementary steps listed in Scheme 3.2 within each global gas-phase reaction (A-D).

Scheme 3.2 posits a plausible sequence of pseudo-elementary steps consistent with Scheme 3.1 and the observations presented in Sections 3.4.1. The steps in Scheme 3.2 are not meant to faithfully represent the molecular events which occur during catalysis, but simply to enumerate the stoichiometric number of elementary steps which constitute gas-phase reactions A, B, C, and D in Scheme 3.1.

Scheme 3.2: Methane DHA reaction sequence with pseudo-elementary steps

	Reaction	**σ**	**σ***
(A.1)	**$CH_4 \rightleftharpoons CH_3 + ½\ H_2$**		**6**
(A.2)	$2CH_3 \rightleftharpoons C_2H_6$	3	
(A)	$2CH_4 \rightleftharpoons C_2H_6 + H_2$	3	
(B.1)	**$C_2H_6 \rightleftharpoons C_2H_5 + ½\ H_2$**		**3**
(B.2)	$C_2H_5 \rightleftharpoons C_2H_4 + ½\ H_2$	3	
(B)	$C_2H_6 \rightleftharpoons C_2H_4 + H_2$	3	
(C.1)	**$C_2H_4 \rightleftharpoons C_2H_3 + ½\ H_2$**		**3**
(C.2)	$C_2H_3 \rightleftharpoons C_2H_2 + ½\ H_2$	3	

(C)	$C_2H_4 \rightleftharpoons C_2H_2 + H_2$	3
(D.1)	**$2C_2H_2 \rightleftharpoons C_4H_4$**	**1.5**
(D.2)	$C_2H_2 + C_4H_4 \rightleftharpoons C_6H_6$	1
(D)	$3C_2H_2 \rightleftharpoons C_6H_6$	1
overall	$6CH_4 \rightleftharpoons C_6H_6 + 9H_2$	1

Bolded entries indicate rate-determining elementary steps within each gas-phase global reaction (A, B, C, and D). All σ^* are assigned on a one benzene molecule basis with overall reaction $6CH_4 \rightleftharpoons C_6H_6 + 9H_2$; σ^* for overall reaction $CH_4 \rightleftharpoons 1/6\ C_6H_6 + 3/2\ H_2$ are adjusted by a factor of 6.

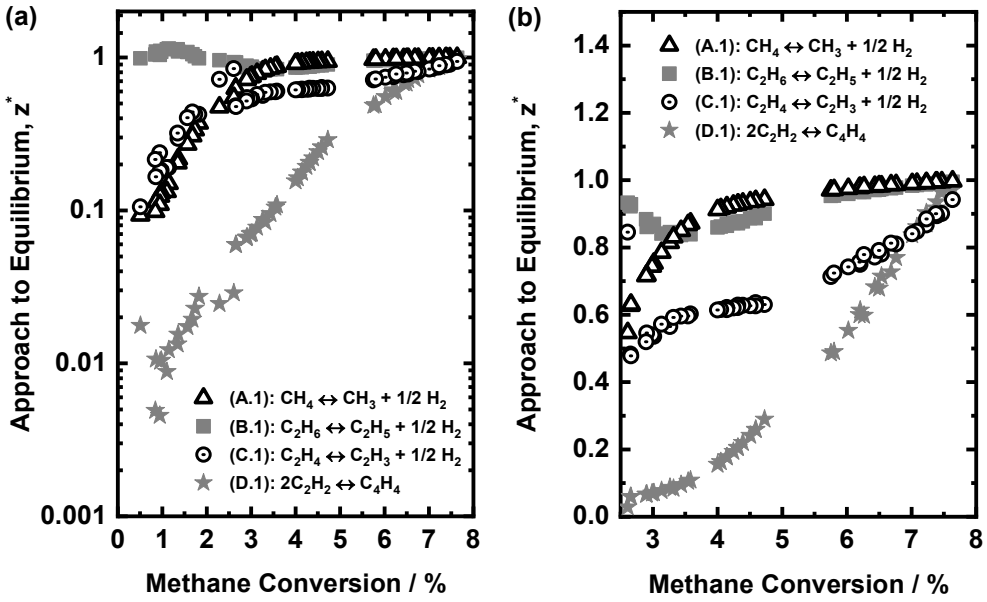

Figure 3.4: Approach to equilibrium of rate-determining elementary steps within each global gas-phase DHA reaction, as listed in Scheme 3.2. Figure 3.4a and 3.4b are the same data shown on differently scaled axes. Reaction conditions: 973 K, ~115 kPa total pressure, 90% CH_4, 10% Ar, 0.21-2.1 $cm^3\ s^{-1}$. 0.1-1.2 g Mo/H-ZSM-5

Identification of σ^* for reactions B and C is trivial; $\sigma^*_B = \sigma^*_C = 3$ since the stoichiometric number of all elementary steps in alkane and alkene dehydrogenation reactions are identical (*71*).

Carbon numbers of methane, ethane, acetylene, and benzene bound σ_A^* by 3 and 6, and σ_D^* by 1 and 1.5. We assign $\sigma_A^* = 6$ because of the well-documented difficulty of activating C-H bonds in methane in both homogenous and catalytic pyrolysis (*46*, *81*). Iglesia and co-workers (*65*) show ethylene formation is first order in methane for contact times where ethane and ethylene are equilibrated, demonstrating methane C-H bond scission is rate-determining in ethane formation. Microkinetic models of catalytic methane DHA developed by Wong et al., (*58*) and Karakaya et al., (*69*) reproduce experimentally-observed aromatization rates and product selectivities treating methane dimerization as a pseudo-elementary first-order process, again consistent with rate-determining methane activation in step A (*58*, *69*).

We assign $\sigma_D^* = 1.5$, consistent with observed second-order kinetics in acetylene and rate-determining formation of vinylacetylene as the sole primary product during acetylene pyrolysis at temperatures below 1200 K (*86*, *87*). We note that all σ^* are assigned on a one benzene molecule basis per Scheme 3.2; σ^* per a one carbon atom basis (i.e. overall reaction $CH_4 \rightleftharpoons 1/6\ C_6H_6 + 3/2\ H_2$) are simply adjusted by a factor of 6 to give the same elementary step reversibilities which must be agnostic to the choice of basis.

Assignment of σ_i^* and of the sequence of pseudo-elementary steps in Scheme 3.2 allows for derivation of X_{RC} (details in Section B.3) for rate-determining elementary steps within global gas-phase reactions A-D assuming the coverage of any $C_{1\text{-}4}$-derived surface intermediates is much less than unity

$$X_{RC,A} = \frac{\sigma_A^* \left(1 - z_A^*\right)}{\xi} \qquad \textbf{[3.13]}$$

$$X_{RC,B} = \frac{\sigma_B^* \, z_A^* \left(1 - z_B^*\right)}{\xi} \qquad \textbf{[3.14]}$$

$$X_{RC,C} = \frac{\sigma_C^* \, z_A^* z_B^* (1 - z_C^*)}{\xi} \qquad \textbf{[3.15]}$$

$$X_{RC,D} = \frac{\sigma_D^* \, z_A^* z_B^* z_C^* (1 - z_D^*) \left(1 + \frac{\sigma_C^*}{\sigma_D^*} z_D^*\right)^{-1}}{\xi} \qquad \textbf{[3.16]}$$

where ξ is the sum of the numerators in Eqs. **3.13**-**3.16** so that $\sum_i X_{RC,i} = 1$ (*88*). Eqs. **3.13**-**3.16** are similar to Eq. **3.11** with an additional, nearly quantitatively negligible term in the numerator of Eq. **3.16** to account for multiple steps (D.1 and D.2) which consume acetylene. X_{RC} values calculated by Eqs. **3.13**-**3.16** are relatively insensitive to choice of $\sigma_A^* = 3$ or 6 and $\sigma_D^* = 1$ or 1.5 because (i) methane and ethane equilibrate for methane conversion > 2.5%, and (ii) $Z_D \sim Z_D^{2/3}$ for methane conversions where step D exerts significant rate control.

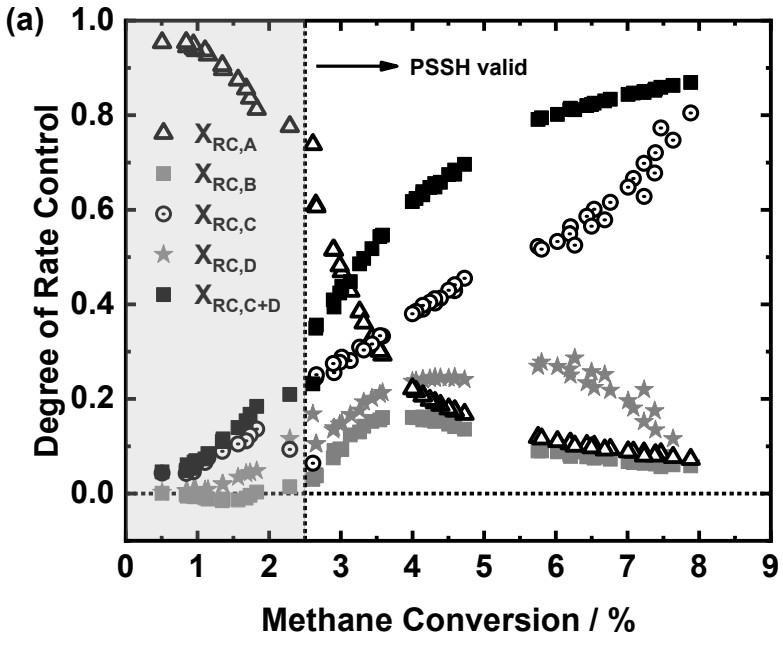

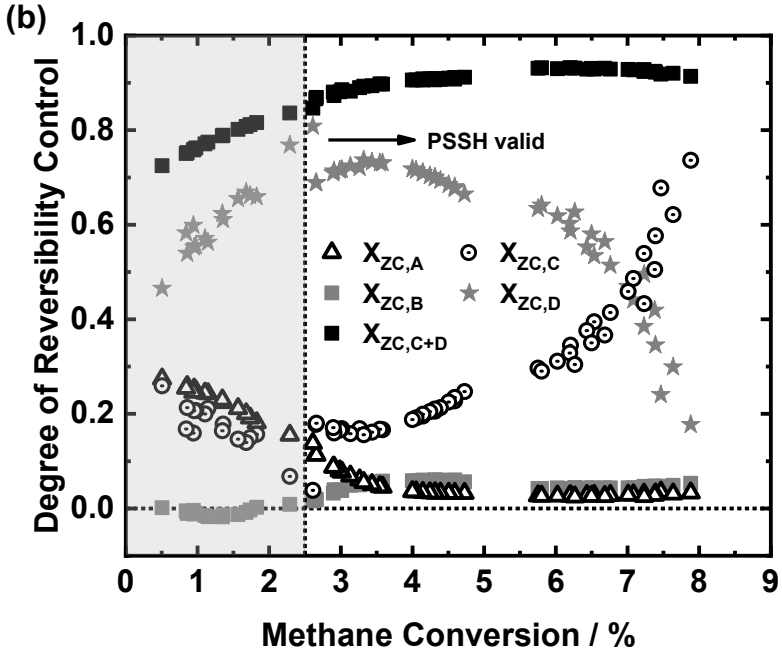

Figure 3.5: Degree of rate control (a) and reversibility control (b) of rate-determining elementary steps in global gas-phase reactions A-D from 0.5-8% methane conversion. Solid squares (■) are a sum of X_{ZC} or X_{RC} rate-determining elementary steps in global gas-phase reactions C and D.

Figure 3.5 shows X_{ZC} and X_{RC} for steps A-D calculated by Eqs. **3.9** and **3.13**-**3.16** using σ^* listed in Scheme 3.2. As we demonstrate in Section 3.4.4, the PSS hypothesis, from which Eqs. **3.13**-**3.16** are derived, is valid once $z_A^* \sim z_B^* \sim 1$ for $f > 2.5\%$ (see Fig. 3.4b). We report and assess X_{ZC} and X_{RC} for $f < 2.5\%$ as probes for rate and reversibility control of steps A-D, but stress that Eqs. **3.13**-**3.16** are not rigorously correct expressions for rate control until $f > 2.5\%$. There is a need for development of a mathematically-justified definition of transient degree of rate control which extends existing formalisms for calculation of X_{RC} (*84*, *85*, *88*) to regimes where single-path reactions have not yet achieved pseudo-steady state. Discrepancies between X_{ZC} and X_{RC} as calculated by Eqs. **3.9** and **3.13**-**3.16** are most apparent at low conversions where methane activation is yet to

equilibrate and therefore provide qualitative insight which is corroborated quantitatively by reversibility and rate data during pseudo-steady state ($f > 2.5\%$).

For conversions less than 2.5%, methane activation is rate-controlling ($X_{RC,A} > 0.7$), but exerts little reversibility control ($X_{ZC,A} < 0.3$) as methane coupling to ethane rapidly equilibrates ($0.1 \leq z_A^* \leq 1$ from 0.5% to 3% conversion). The significant rate control of methane activation at these low contact times, despite $z_A^* >> z_D^*$, demonstrates the disproportionate rate control of steps which occur earliest in a series reaction sequence. Once methane, ethane, and ethylene form a quasi-equilibrated pool (*39*, *70*), and therefore exert little control over rate or overall reversibility, both rate and reversibility controlling character shifts to steps involving acetylene (C and D) – suggesting steady-state DHA reactions are kinetically and thermodynamically controlled by steps between ethylene and benzene. Dominant reversibility control of steps involving acetylene is reflected by $X_{ZC,C} + X_{ZC,D} \sim 0.8$ for all contact times and manifests $\bar{\sigma}$ is essentially an affinity average of steps C and D – bounding $\bar{\sigma}$ by 2 and 3, as shown in Section B.3.

For $f > 2.5\%$, $z_A^* \sim z_B^* \sim 1$ and X_{ZC} and X_{RC} for steps C and D are semi-quantitatively similar – both steps are away from equilibrium and exert both rate and reversibility control, evincing the key role of acetylene during dehydroaromatization reactions. $X_{RC,D} < X_{ZC,D}$ and $X_{RC,C} \gtrsim X_{ZC,C}$ because ethylene dehydrogenation precedes and serves as a kinetic bottleneck to acetylene dimerization. Acetylene dimerization reversibility increases along the catalyst bed, effecting increase of z_{eff} during pseudo-steady state methane DHA. As z_D^* increases beyond z_C^*, ethylene dehydrogenation becomes rate-determining and is seemingly the last step to equilibrate.

Contrary to our observations, simulation of kinetic models of methane pyrolysis performed by Iglesia and co-workers (*45*, *65*) suggest ethylene dehydrogenation to acetylene rapidly equilibrates in homogenous or catalytic reaction pathways at 1038 K. Equilibration of $C_2H_4 \rightleftharpoons C_2H_2 + H_2$ at the onset of PSS in our catalytic studies would require a ~2x adjustment in $K_{eq,D}$, resulting a maximum value of $z_D^* \gtrsim 2$ (Fig. 3.4b) at the largest measured contact time – which is thermodynamically forbidden (*89*, *90*). We therefore suggest equilibrium of $C_2H_4 \rightleftharpoons C_2H_2 + H_2$ in simulation of kinetic methane pyrolysis models by Iglesia and co-workers results from lack of acetylene oligomerization pathways which kinetically couple C_2H_2 and reduce approach to equilibrium of ethylene dehydrogenation.

Crucially, the use of Eqs. **3.13**-**3.16** for the degree of rate control relies on the pseudo-steady state hypothesis – essentially that (i) the partial pressure of all carbon-containing intermediates (i.e. C_2H_x hydrocarbons) is determined arithmetically by the pressure of CH_4, H_2, and aromatic products, and (ii) forward rates are nearly invariant with methane conversion or contact time provided methane conversion is differential (i.e. <10%) and there is no kinetic product inhibition (e.g. competitive adsorption of H_2). The first condition amounts to requiring the instantaneous rate of all C_2H_x hydrocarbons be much less than the instantaneous rate of methane consumption, as we show is true once methane, ethane, and ethylene form an equilibrated pool at contact times >7 mol_{Mo} s $(mol_{CH4})^{-1}$ in Section B.4. To assess the validity of the second condition, we use Eq. **3.6** to calculate the overall forward rate of benzene synthesis, $\vec{R}$, from measured net rates and $\bar{\sigma}$. These calculations, however, are complicated by the nature with which effluent streams in flow reactors carry kinetic and thermodynamic information. Exit streams in flow reactors reflect spatially-

averaged net rates, but only effluent, or instantaneous, reversibilities. We address these limitations by collecting reversibility data as a function of contact time to rigorously affinity and length average z_{ov} and calculate forward benzene synthesis rates.

3.4.4 Affinity and length averaging in highly reversible CH_4 DHA flow reactors

Use of Eq. **3.6** from flow reactor data requires affinity averaging of z_{ov} by use of Eq. **3.7** and numerical integration of z_{ov} along the catalyst bed (i.e. spatial averaging). Spatial averaging of z_{ov} from flow reactor data is necessary because effluent flow rates inherently reflect length-averaged rates, $< R >$, while effluent partial pressures reflect instantaneous approach to equilibrium, Z. Therefore, measured effluent, instantaneous z_{ov} must be length-averaged to capture the same information as measured effluent flow rates, i.e. length-averaged reaction rates. The inherent length-averaging of reaction rates by flow reactors is best demonstrated by integration of the PFR mole balance. The effluent flow rate of a product j in a PFR normalized by the total number of active sites, F_j, is given by

$$F_j = \frac{1}{\int_0^X dx} \cdot \int_0^X \sum_i \nu_{ij} R_i \, dx = \sum_i \nu_{ij} < R_i > \qquad \textbf{[3.17]}$$

where index i refers to overall reactions, x is the contact time along the catalyst bed, and X is the total contact time. Eq. **3.17** clearly demonstrates effluent flow data measure length-averaged reaction rates in a PFR and also holds for a dispersed packed-bed reactor with closed-closed Danckwerts boundary conditions, as shown in Section B.4. The pseudo-steady state hypothesis, canonically a prerequisite of the De Donder analysis, dictates that the overall forward rate is nearly constant along the catalyst bed. Thus,

$$\vec{R}_i = \frac{< R_i >}{< 1 - z_{ov,i}^{1/\bar{\sigma},i} >} = \frac{1}{\nu_{ij}} \frac{F_j - \sum_{k \neq i} \nu_{kj} < R_k >}{< 1 - z_{ov,i}^{1/\bar{\sigma},i} >} \qquad \textbf{[3.18]}$$

where indices i and k refer to overall reactions and index j refers to species j. The term $\left[F_j - \sum_{k \neq i} \nu_{kj} < R_k >\right]$ in Eq. **3.18** generally accounts for all reactions which form or consume species j and is redacted to a simpler, particular form for the overall benzene synthesis reaction in Eq. **3.19**. Eq. **3.18** is a function of only measurable quantities: effluent flow rate, effluent overall approach to equilibrium, and effluent affinity-averaged stoichiometric number – provided the latter two are appropriately length-averaged. In the following, we calculate $\vec{R}$ for benzene production by a particular form of Eq. **3.18** and show, once methane activation equilibrates, the overall forward rate of methane DHA is indeed invariant with contact time, evincing the validity of PSSH. De Donder relations used to calculate forward rate make no assumption regarding the identity or distribution of catalytic active sites and therefore are agnostic to the role of MoC_x, Brønsted acid sites, or co-catalytic entrained carbon in each step. Calculation of rate and contact time to follow normalize by active Mo atoms, as is the precedent in the literature (*19*, *37*, *40*, *91*), but this assignment of active site has no effect on validity of the De Donder formalism or the PSSH.

We collect data for calculation of $\bar{\sigma}$ and z_{ov} as a function of contact time by leveraging the non-selective nature of Mo/H-ZSM-5 deactivation during methane DHA (see Fig. 3.1). Retention of the catalytic properties of active sites during deactivation implies methane conversion, f, is a one-to-one function of contact time, τ [=] mol_{Mo} s $(mol_{CH4})^{-1}$, provided inlet composition, reaction temperature, and total pressure are unchanged. We determine $f(\tau)$ by systematic change of contact time, or catalyst loading, during steady-state methane DHA reactions. Section B.4 discusses and demonstrates that f is a one-to-one function of τ in ideal plug-flow and axially dispersed flow reactors. Section B.4 shows $f(\tau)$ is a monotonic function which we fit by a piecewise polynomial expression. Determination of

f(τ) permits calculation of contact time, correctly normalized by *active* Mo atoms, during deactivation of Mo/H-ZSM-5 catalysts, and, in effect, enables calculation of turnover frequencies, R [=] mol/mol$_{\text{active Mo}}$/s, even as the catalyst deactivates.

Fig. 3.6 reports overall forward rates of benzene synthesis during methane DHA on Mo/H-ZSM-5 determined by variation of contact time both by (i) extent of catalyst deactivation and (ii) change of catalyst loading in a catalog of steady-state DHA reactions with identical total flow rate. We take the net rate of benzene synthesis to be the sum of benzene and naphthalene flow rates since naphthalene constitutes significant carbon selectivity and is presumed to be formed from a single benzene molecule and addition of smaller hydrocarbons. Explicitly, the forward rate of the methane to benzene single-path reaction sequence is

$$\vec{R} = \frac{< R >}{< 1 - z_{ov}^{1/\bar{\sigma}} >} = \frac{F_{C_6H_6} + F_{C_{10}H_8}}{< 1 - z_{ov}^{1/\bar{\sigma}} >} \qquad (19).$$

Fig. 3.6 shows forward rates reach a steady value at the same contact time as $z_A^* \sim z_B^* \sim 1$, evincing the validity of the PSSH and demonstrating the sole inhibiting effect of H_2 liberated in DHA reactions is thermodynamic in nature. Fortuitously, our previous calculations of constant forward benzene rates (*19*, *47*) are similar to those in this work due to a balance of incorrect length averaging and affinity averaging which overestimate and underestimate forward rates, respectively (see Section B.5). Section B.5 also shows deviation from PSSH for $\tau < 7$ mol$_{Mo}$ s (mol$_{CH4}$)$^{-1}$ has little influence on calculation of forward rates as, at these low contact times, $<z_{eff}> << 1$ and $R \sim \vec{R}$.

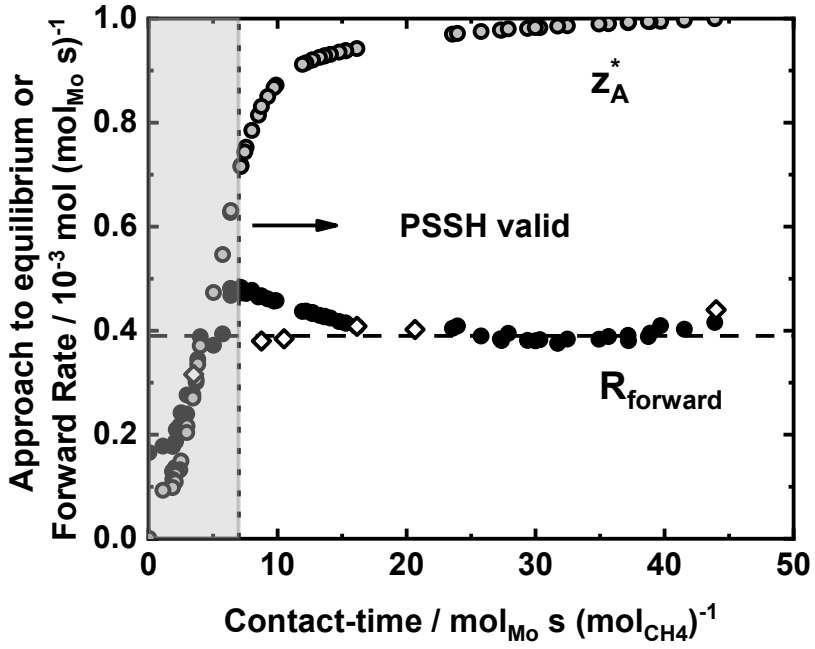

Figure 3.6: Approach to equilibrium of methane activation as a function of contact time varied by extent of deactivation (○; T = 973 K), and forward rates of benzene synthesis [=] $mol_{benzene}$ $(mol_{Mo}\ s)^{-1}$ as a function of contact time varied by extent of deactivation (●; T = 973 K) and catalyst loading during steady-state catalysis (◊; T = 973 K).

3.5 Conclusion

Mo-modified H-ZSM-5 catalyzes methane dehydroaromatization via a single-path series reaction wherein initial methane activation and C-C coupling to ethane is followed by sequential dehydrogenation to ethylene and acetylene, the immediate stable gas-phase intermediate to benzene formation. Elucidation of the DHA reaction network and quantification of reversibility of intervening dehydrogenation and oligomerization reactions is achieved by change of effective contact time by extent of "non-selective" deactivation. The "non-selective" nature of deactivation is confirmed by congruence of conversion-selectivity curves and permits probe of axial rate and reversibility profiles after determination of f(τ), the one-to-one function between methane conversion and contact

time. Methane, ethane, and ethylene form a quasi-equilibrated pool at contact times beyond 7 mol_{Mo} s $(mol_{CH4})^{-1}$, resulting in a pseudo-steady state methane aromatization pathway with both rate- and reversibility-determining steps, C_2H_4 dehydrogenation and C_2H_2 dimerization, involving acetylene – identified to be a key reactive intermediate in DHA.

Rate control and reversibility control of intervening steps is quantified by the degree of reversibility control, defined herein for the first time, and the degree of rate control which account for the stoichiometric number of rate-determining elementary steps within each global gas-phase reaction. The degree of reversibility control is necessary for rigorous affinity averaging of overall reversibility of the methane-to-benzene single-path reaction, but is insufficient to predict the rate-control of each step as reaction affinities are thermodynamically-determined state functions inherently limited in their ability to describe rates of path-dependent reaction sequences. Congruence of degree of rate control and degree of reversibility control for bookend cases is not reflected at intermediate contact times and highlights the need for the degree of rate control to identify rate-determining steps in reversible series reactions with multiple steps away from equilibrium. Axial degree of reversibility control profiles are nonetheless critically useful to determine the affinity-averaged stoichiometric number along the catalyst bed, as is necessary to calculate forward DHA rates.

Forward benzene rates determined from formalisms of affinity averaging and length averaging are invariant with contact-time once methane, ethane, and ethylene equilibrate and evince the validity of the pseudo-steady-state hypothesis upon which conventional definitions of degree of rate control and the De Donder formalism are predicated. Unchanged forward aromatization rates at contact times beyond 7 mol_{Mo} s $(mol_{CH4})^{-1}$ set

kinetic limits to methane aromatization on Mo/H-ZSM-5 catalysts and motivate investigations to (i) overcome thermodynamic barriers set by reaction endothermicity and (ii) identify and eliminate mechanisms of catalyst deactivation to progress technical development of direct methane valorization to ethylene and aromatics.

4 Carbidic Mo is the sole kinetically-relevant active site for catalytic methane dehydroaromatization on Mo/H-ZSM-5

*Contents herein are reproduced with permission from Razdan, N. K., Bhan, A. Carbidic Mo is the sole kinetically-relevant active site for catalytic methane dehydroaromatization on Mo/H-ZSM-5. *Journal of Catalysis*. **2020**, *389*, 667–676. https://doi.org/10.1016/j.jcat.2020.06.035.

4.1 Conspectus

Systematic variation of Mo/Al = {0.10, 0.25, 0.35} in Mo/H-ZSM-5 catalysts effects ~20x change of Mo-to-H^+ ratio during methane dehydroaromatization (DHA) reactions at steady state and on deactivating catalysts. Mo and Brønsted-acid site count, respectively enumerated by ethane hydrogenolysis probe reaction and dimethyl ether chemical titration, evolve disparately during DHA catalysis, indicating the two sites reduce in number by distinct mechanisms. The deactivation of Mo/H-ZSM-5 catalytic activity is uniquely attributed to the loss of active, or accessible, Mo sites, evinced by (i) the non-selective nature of deactivation (i.e. that deactivation occurs without modification of residual active sites), (ii) invariance in product distribution from Mo/H^+ = 0.10 – 2.1, and (iii) linear correspondence between Mo-catalyzed ethane hydrogenolysis rate and active site count during DHA on deactivating samples. DHA forward rate – the intrinsic kinetic descriptor of catalyst activity – normalizes by Mo content at steady state and on deactivating catalysts with Mo/Al = 0.10 – 0.35 for Mo-based contact times in the range τ_{Mo} = 0.79 – 44 mol_{Mo} s mol_C^{-1}, unequivocally establishing Mo aggregates as the sole kinetically-relevant active site on Mo/H-ZSM-5. Brønsted-acid site content over a ~40x range in τ_{H+} = 1.4 – 54 mol_{H+} s mol_C^{-1} has no discernable correlation with or effect on DHA rate, methane conversion, or product distribution – demonstrating H^+ does not catalyze any rate- or selectivity-determining steps in the benzene formation pathway and suggesting that the benefits of

zeolitic acid sites are only to disperse Mo during catalyst synthesis and, conceivably, to catalyze equilibrated reaction steps.

4.2 Introduction

Growing access to natural gas reserves motivates development of diverse thermochemical strategies for valorization of stranded methane as alternatives to on-site flaring (*60*, *92–94*). Mo-modified proton-form ZSM-5 zeolites (Mo/H-ZSM-5) catalyze non-oxidative dehydroaromatization (DHA) of methane with ≳95% aromatic selectivity at CH_4 conversions near the ~10% equilibrium limit at ~950 K. Endothermicity of methane pyrolysis imposes stringent thermodynamic barriers to aromatic formation which intensify with CH_4 conversion, resulting in a highly-reversible reaction network which renders ineffective differential kinetic analyses. De Donder relations and constitutive laws of mass transport are required to de-convolute kinetic and thermodynamic contributors to rate in flow reactors and calculate forward site-time yield, the intrinsic kinetic descriptor of catalyst activity (*82*, *95*).

Mo/H-ZSM-5 catalysts are synthesized *in situ* by introduction of methane at DHA reaction temperature to MoO_x/H-ZSM-5 pre-catalysts (*9*, *21*, *42*, *96*) to remove oxygen and form MoC_x/H-ZSM-5 active for DHA catalysis. Synthesis of pre-catalysts by solid-state vapor-phase exchange proceeds via thermal treatment of physical mixtures of MoO_3 and H-ZSM-5 in dry air to disperse MoO_3 oligomers on the external zeolite surface (773 K) and subsequently sublime oxidic Mo moieties which diffuse into the zeolite micropore structure and exchange with acid sites (973 K) (*18*, *19*, *38*, *39*, *42*, *62*). $MoO_{3(g)}$ monomers react with proximate pairs of zeolitic Brønsted-acid sites to liberate H_2O and form well-defined $[Mo_2O_5]^{2+}$ dimers anchored to the zeolite framework (*38*, *42*). X-ray absorption near edge and extended fine structure confirm and monitor evolution of Mo speciation from

MoO_3 to $[Mo_2O_5]^{2+}$ during pre-catalyst synthesis and are corroborated by Raman bands observed at 970 cm^{-1} corresponding to symmetric terminal Mo=O stretches in Mo dimers (*18*, *38*, *97*, *98*). Preparation of pre-catalysts by wetness impregnation techniques produce oxidic Mo of distinct and diverse speciation (e.g. $[Mo(=O)_2]^{2+}$, $[Mo(=O)_2OH]^{+}$) (*23*, *64*, *99*); however, identity of Mo in pre-catalysts does not influence rates or product distribution of DHA catalysis provided Mo is sufficiently dispersed and encapsulated within unperturbed ZSM-5 framework (*17*, *42*).

Introduction of methane at ~950 K reduces oxidic pre-catalysts, evolving 2.4 ± 0.1 O per Mo as CO, CO_2, and H_2O in samples prepared by solid-state vapor-phase exchange, consistent with the stoichiometry of $[Mo_2O_5]^{2+}$ (*18*, *40*, *100*). Methane and hydrocarbon products formed over reducing Mo centers deposit 9 – 44 C/Mo (*18*, *62*) and form MoC_x aggregates to initiate DHA catalysis. Dehydroaromatization is proposed to proceed via a bifunctional mechanism wherein carbidic Mo centers dehydrogenate CH_4 to C_2H_x intermediates which cyclize to aromatics over zeolitic Brønsted-acid sites well-known to catalyze olefin oligomerization (*19*, *21–24*). Kosinov et al. (*25*) challenge putative bifunctional reaction schemes and demonstrate that acid-free Mo/SiO_2 and Mo/1-Silicalite materials catalyze non-oxidative methane activation to benzene and higher aromatics, albeit with poor Mo-normalized rates and time-on-stream stability in comparison to Mo/H-ZSM-5 catalysts (*21*). H-ZSM-5-encapsulated carbidic Mo may plausibly catalyze DHA with higher aromatic production rates than Mo/SiO_2 and Mo/1-Silicalite due to (i) interception and aromatization of coke precursors by Brønsted-acid sites, (ii) enhanced Mo dispersion due to cation exchange with zeolitic protons, and/or (iii) MFI micropore

structure affording confining environments selective for formation of mono- and bicyclic aromatics capable of egressing from the zeolite.

In this study we seek to ascertain the catalytic roles of carbidic Mo and zeolitic Brønsted-acid sites using thermochemical kinetic analyses complemented by Mo and H^+ site-counting at steady state and during deactivation. Mo and H^+ sites are enumerated during deactivation by ethane hydrogenolysis probe reaction and dimethyl ether titration, respectively, to demonstrate that loss of catalytic activity, determined by instantaneous methane conversion, is uniquely attributable to the reduction in the number of active carbidic Mo moieties. Deactivation of Mo/H-ZSM-5 catalysts is therefore non-selective, or occurs without chemical modification of residual active sites and with product distribution unaffected by Mo-to-H^+ ratio, suggesting a single site catalyzes all rate-controlling steps during DHA. Non-selective deactivation is leveraged to instantaneously normalize DHA rates by the contemporaneous active Mo site count, giving site-time yields which agree quantitatively with those measured at steady state. Thermochemical-kinetic formalisms based on De Donder relations enable calculation of steady-state and transient forward turnover rates which normalize by Mo content over a ~20x range of Mo-to-H^+ ratio (0.10 – 2.1) and ~50x range of Mo-based contact time (0.79 – 44 mol_{Mo} s mol_C^{-1}). Brønsted-acid site densities do not influence aromatization rates or product distribution, confirming acid sites do not catalyze rate- or selectivity-determining steps.

4.3 Materials and Methods

4.3.1 MoO_x/H-ZSM-5 pre-catalyst synthesis

H-ZSM-5 was prepared by deamination of NH_4-ZSM-5 (Zeolyst International, Si/Al = 11.5, CBV 2314) in dry air (~1.67 cm^3 s^{-1}) at 773 K for 36 h (0.0165 K s^{-1}). MoO_3 (Sigma-Aldrich, 99.9%) and H-ZSM-5 powders were physically mixed in an agate mortar and

pestle for 25 min in quantities corresponding to Mo-to-Al ratios of 0.10, 0.25, and 0.35. Intimate physical mixtures of MoO_3 + H-ZSM-5 were heated in dry air to 623 K for 15 h (0.0167 K s^{-1}) and then to 973 K for 10 h (0.167 K s^{-1}) to form the MoO_x/H-ZSM-5 pre-catalyst which was pressed into pellets and sieved to retain particles between 180 and 425 μm in diameter for activation to Mo/H-ZSM-5 and use in catalytic dehydroaromatization reactions.

4.3.2 Catalytic methane dehydroaromatization reactions

MoO_x/H-ZSM-5 pre-catalysts (0.10 – 1.20 g) were held in place by quartz wool in fixed-bed tubular quartz reactors (I.D. 10.5 mm), heated to 973 K (0.18 K s^{-1}) in He flow (~ 0.33 cm^3 s^{-1}, UHP, Minneapolis Oxygen), and exposed to methane after reactor temperature was allowed to stabilize for 2 h. Tubular reactors were held in an annular Inconel casing to eliminate radial temperature gradients from the resistively-heated furnace (National Element FA120). Reactor temperature was monitored by two thermocouples diametrically-positioned across the catalyst bed on the exterior of the tubular quartz reactor. Carburization of pre-catalysts, initiated by introduction of CH_4/Ar (90 vol% CH_4 and 10 vol% Ar, total feed flow rate 0.21 cm^3 s^{-1}, UHP, Matheson Tri-Gas) at 973 K, proceeded for 5 – 15 ks depending on the Mo-to-Al ratio and mass of catalyst. Closure of carbon balance and onset of non-selective deactivation (*vida infra*) indicate the end of carburization and inception of DHA catalysis. Section C.1 shows illustrative data depicting the onset of DHA catalysis and steady-state aromatization rates and methane conversion. After carburization, DHA reactions were either continued under 0.21 cm^3 s^{-1} total flow or were performed at identical composition, but varied flow range (0.21-2.1 cm^3 s^{-1}), after flush of reactor lines in He flow (~ 0.33 cm^3 s^{-1}) as reaction feed flow stabilized. Transfer lines were heated to 393 – 453 K to ensure no condensation of aromatic products and water.

Reactor effluent composition was analyzed using a mass spectrometer (MKS Cirrus 200 Quadrupole MS system) and a gas chromatograph (Agilent 7890) equipped with a methyl-siloxane capillary column (HP-1, 50 m x 320 μm x 0.52 μm) using a flame ionization detector (FID) for detection of hydrocarbons and a GS-GasPro column (60 m x 0.320 mm) using a thermal conductivity detector (TCD) for detection of H_2, Ar, CO, and CH_4.

All reported volumetric flow rates are referenced to 1 bar and 298 K.

4.3.3 Dimethyl ether titration of zeolitic Brønsted-acid sites

Chemical titration of zeolitic Brønsted-acid sites were performed with dimethyl ether (DME) on Mo/H-ZSM-5 and H-ZSM-5 samples using the same equipment as in methane dehydroaromatization reactions. The number of accessible acid sites was determined according to the stoichiometric reaction between DME and acid sites to form two persistent methyl groups on framework oxygen bound to Al ($CH_3OCH_{3(g)} + 2[AlO^-H^+]_{(s)} \rightarrow 2[AlO^-CH_3^+]_{(s)} + H_2O_{(g)}$) (*101*). In preparation for DME titration, Mo-containing and Mo-free zeolite samples were either (i) cooled to 423 K in ~0.8 $cm^3\ s^{-1}$ He flow following different durations of DHA (3 – 100 ks) or (ii) heated from ambient to 773 K at 0.08 K s^{-1}, held at 773 K for >5 h to remove physisorbed water, and then cooled to 423 K in ~0.8 $cm^3\ s^{-1}$ He flow. Pulses of DME (0.25 or 1.00 cm^3) were introduced by 0.5 $cm^3\ s^{-1}$ flow of 96% He and balance Ar at regular intervals (120 or 240 s) until unreacted DME was observed in the effluent stream by MS. Samples were subsequently flushed in the same 0.5 $cm^3\ s^{-1}$ flow of 96% He and balance Ar for >3 h to remove physisorbed DME and H_2O. Section C.2 shows characteristic data for evolution of DME upon breakthrough (i.e. after all zeolitic protons have undergone stoichiometric exchange with methyl groups).

4.3.4 Steady-state ethane hydrogenolysis probe reactions

Steady-state rates of ethane hydrogenolysis were measured at differential C_2H_6 and H_2 conversion (<2%) to determine the relative number of active Mo atoms on Mo/H-ZSM-5 samples after different durations of CH_4 DHA (3 – 100 ks). Following DHA, samples were treated in ~0.8 cm^3 s^{-1} He at reaction temperature 973 K for >2 h to remove adsorbed hydrocarbons and then allowed to cool to 750 K in the same He flow. Reactor temperatures stabilized for >2 h prior to introduction of 0.49 cm^3 s^{-1} 46% C_2H_6/49% H_2/balance Ar to initiate ethane hydrogenolysis. Methane formation rates reached a steady state in 3 – 15 ks and constituted ~90% carbon selectivity. Section C.2 shows characteristic data for rate and selectivity during ethane hydrogenolysis reactions as a function of time on stream.

4.3.5 Definitions of Mo-based contact time

We define two distinct measures of Mo-based contact time: (i) $\tau_{Mo,initial}$ [=] $mol_{Mo,initial}$ s mol_C^{-1} which is a time-invariant quantity calculated from the initial number of active Mo atoms – assumed to be equal to the total amount of Mo charged to the catalyst bed – and (ii) τ_{Mo} [=] mol_{Mo} s mol_C^{-1} which changes with time on stream due to deactivation and is calculated from the *instantaneous* number of *active* Mo atoms. Initial and instantaneous Mo-based contact time are given by

$$\tau_{Mo,initial} = \frac{L_{Mo,total}}{\dot{n}_{CH_4,inlet}} \quad \textbf{[4.1]}$$

and

$$\tau_{Mo} = \frac{L_{Mo}(t)}{\dot{n}_{CH_4,inlet}} \quad \textbf{[4.2]}$$

where $\dot{n}_{CH_4,inlet}$ [=] mol_C s^{-1} is the inlet molar flow of methane, $L_{Mo,total}$ [=] $mol_{Mo,initial}$ is the total amount of Mo in the catalyst bed, and $L_{Mo}(t)$ [=] mol_{Mo} is the amount of active Mo at time on stream t.

4.4 Results and Discussion

4.4.1 Relevance of the Mo-to-Al ratio to CH_4 DHA catalysis

We systematically vary Mo loading (Mo/Al = 0.10, 0.25, 0.35) in H-ZSM-5 (Si/Al = 11.5) to control the ratio of Mo sites and framework Al-associated zeolitic Brønsted acid sites (i.e. Mo-to-H^+ ratio) in Mo/H-ZSM-5 catalysts for CH_4 DHA. Concentration of zeolitic protons on Mo/H-ZSM-5 samples and parent H-ZSM-5 with and without high temperature (973 K) thermal treatment is quantified by chemical titration using DME. The density of Brønsted-acid sites on parent H-ZSM-5 zeolite (Si/Al = 11.5) was determined to be $11.2 \pm 0.6 \cdot 10^{-4}$ mol g^{-1}, comparable to the total Al concentration per the Si-to-Al ratio, $13.3 \cdot 10^{-4}$ mol g^{-1}. High temperature thermal treatment to 973 K by an identical thermal treatment protocol applied to MoO_3 + H-ZSM-5 physical mixtures reduces the number of accessible protons in H-ZSM-5 to $7.9 \pm 0.6 \cdot 10^{-4}$ mol g^{-1}, consistent with reported ~50% decrease in Brønsted-acid site concentration, measured by pyridine adsorption and infrared spectroscopy, in H-ZSM-5 treated at 998 K compared to samples deaminated at 623 K (*102*). Increasing concentrations of MoO_3 during $[Mo_2O_5]^{2+}$/H-ZSM-5 thermal synthesis in dry air proportionately decreases the proton density in accordance with the 1:1 Mo-to-Al stoichiometry of the solid-state condensation exchange reaction (Figure 4.1).

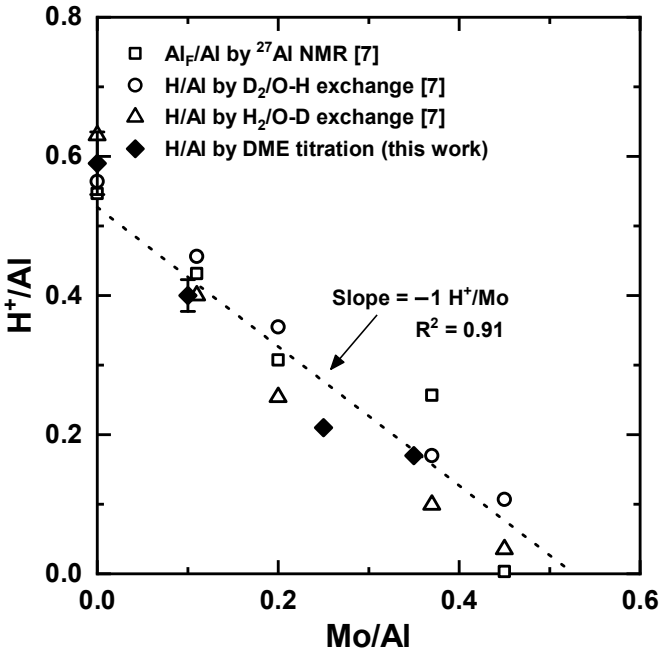

Figure 4.1: The number of Brønsted-acid sites (H^+) or framework Al atoms (Al_F) per total Al in Mo-containing and Mo-free H-ZSM-5 samples treated to 973 K in dry air. Open symbols are from the work of Borry et al. (*42*) Dashed line is the fit to all data in Fig. 4.1.

Observed elimination of Brønsted-acid sites by exchanged Mo cations is in agreement with the work of Borry et al. (Fig. 4.1) wherein the influence of Mo loading to effect decrease in zeolitic Brønsted-acid density is quantified by (i) signal intensity at chemical shift -56ppm assigned to framework Al, Al_F, in ^{27}Al NMR and (ii) HD evolution during $D_{2(g)}$/O-$H_{(s)}$ and subsequent $H_{2(g)}$/O-$D_{(s)}$ exchange on samples with a range of Mo-to-Al ratio (0 – 0.45) and fixed Si/Al = 14.3 (Figure 4.1). Si-to-Al ratio in this work (Si/Al = 11.5) and those of Borry et al. (Si/Al = 14.3) are sufficiently similar for quantitative comparison at Mo-to-Al ratios below the fraction of framework Al pairs within ~5.5 Å, the distance between adjacent Al_F in anchored $(Mo_2O_5)^{2+}$ dimers as identified from radial structure function generated from EXAFS (*38*). Statistical framework Al distribution calculated by Monte Carlo simulation and the Poisson approximation estimate the fraction of Al_F pairs within 5.5 Å on ZSM-5 materials with Si/Al = 11 – 15 to be 0.4 – 0.5 (*103*);

and, ion exchange with two proximate Na^+ cations by Co^{2+} in Na-ZSM-5 enumerates the fraction of "Al_F pairs" to be 0.74 – 0.82 on samples with Si/Al = 12 – 14 (*104*), justifying comparison of DME titration with techniques of Borry et al (*42*). Section C.3 shows separate linear fits to the data of Borry et al. (*42*) and those presented herein are quantitatively similar.

Enumeration of framework Al or Brønsted-acid sites by DME titration, ^{27}Al NMR, and $D_{2(g)}(H_{2(g)})$/O-H(D) isotopic exchange on a suite of oxidic MoO_x/H-ZSM-5 pre-catalysts (Mo/Al = 0 – 0.45) quantitatively demonstrates Mo cations eliminate Brønsted-acid sites in one-to-one correspondence. Systematic variation of the Mo-to-Al ratio therefore engenders change in the number of Mo and H^+, which may plausibly influence rates and product distribution should both sites play catalytic roles. In what follows, we assess the catalytic relevance of both metal and acid sites during DHA reactions by rigorous kinetic analyses which ascertain the influence of Mo and H^+ site count on rates and selectivities both at steady state and during deactivation.

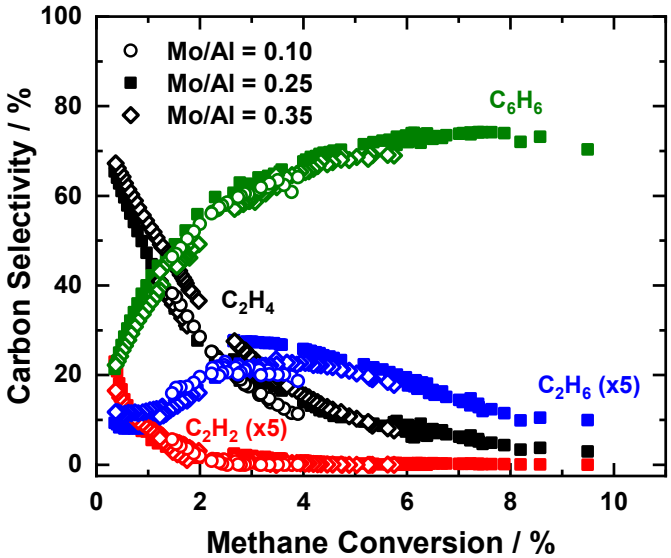

Figure 4.2: Carbon selectivity of C_2 hydrocarbons and benzene as a function of methane conversion over deactivating Mo/H-ZSM-5 catalysts. Reaction conditions: 973 K, ~115 kPa total pressure, total flow of 0.21 – 2.1 $cm^3\ s^{-1}$ with composition 90% CH_4/10% Ar.

Mo/Al = 0.10, g_{cat} = 0.75 – 1.20 (○), Mo/Al = 0.25, g_{cat} = 0.10 – 1.20 (■), Mo/Al = 0.35, g_{cat} = 0.15 – 0.75 (◇).

Figure 4.2 shows the carbon selectivity of C_2 hydrocarbons and benzene as a function of methane conversion during CH_4 DHA reactions on catalyst samples with a range of Mo-to-Al ratio (0.10 – 0.35). Selectivity data is collected as a function of methane conversion on each sample by allowing the catalyst to deactivate with time on stream (TOS). For each Mo-to-Al ratio, conversion-selectivity profiles are measured over two or more catalyst samples with identical feed composition, total pressure, and reactor temperature and different initial methane conversion – changed by varying catalyst mass loading and/or total flow rate. Section C.1 provides time-on-stream profiles for all data in Fig. 4.2.

Scheme 4.1 illustrates putative Mo- and H^+-catalyzed routes for CH_4 DHA based on (i) substantiated equilibration of methane, ethane, and ethylene (*70*, *95*) and (ii) reaction network connectivity per conversion-selectivity profiles in Fig. 4.2 and similar data reported for 0.001 – 0.05% methane conversion (*95*).

Scheme 4.1: Mo/H-ZSM-5-catalyzed CH_4 DHA reaction network

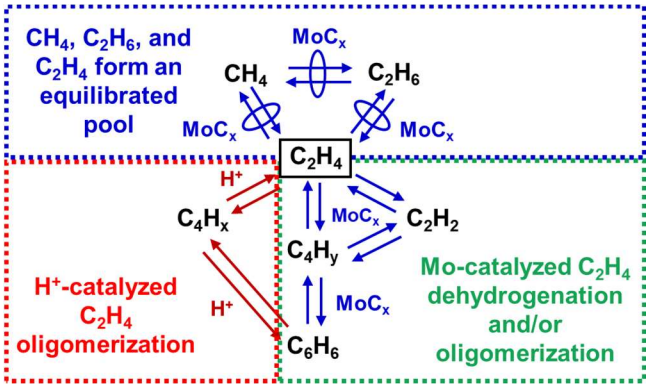

Methane, ethane, and ethylene form an equilibrated pool catalyzed by carbidic Mo sites (⬚) for τ_{Mo} > 7 mol_{Mo} s mol_C^{-1} (*70*, *95*). Ethane is the sole primary product of DHA, confirmed by 100% selectivity to C_2H_6 for <0.001% CH_4 conversion (*95*). Ethylene aromatization has been proposed to proceed via catalytic oligomerization over zeolitic Brønsted-acid sites (⬚) (*19*, *21–24*) or Mo-catalyzed oligomerization and/or C_2H_2-mediated cyclization (⬚) (*25*, *77*).

The congruence of conversion-selectivity profiles from 0.5-8% methane conversion, f, for all hydrocarbon products in Fig. 4.2 demonstrates that deactivation of Mo/H-ZSM-5 is non-selective, or occurs without affecting catalytic properties of residual active sites (*62*, *74*, *95*). We note that it is possible that overlay of conversion versus product selectivity data is resultant from serendipitous, selective change in conversion and product distribution with time such that conversion versus selectivity data remain identical for all examined products across all deactivating samples (*74*). Given the range of (i) concentrations of hydrocarbon products in Fig. 4.2 (0.1 Pa – 1 kPa), (ii) initial catalyst contact time (8 – 40 mol_{Mo} s mol_C^{-1}), (iii) instantaneous methane conversion (0.5 – 8%), (iv) Mo-to-Al ratio (0.10 – 0.35) and (v) Mo-to-H^+ ratio (0.10 – 2.1) during catalysis (*vida infra*), we find it unlikely that Mo/H-ZSM-5 catalysts are deactivating selectively while coincidentally retaining congruence of conversion-selectivity profiles. Non-selective nature of Mo/H-ZSM-5 deactivation in methane dehydroaromatization reactions has been demonstrated previously; however, these investigations only report conversion-selectivity profiles over catalysts with a single Mo loading, or Mo-to-Al ratio (Mo/Al = 0.25 (*95*), Mo/Al = 0.40 (*62*)).

Coincidence of conversion-selectivity profiles across Mo/Al = 0.10 – 0.35 demonstrates that neither the non-selective nature of deactivation nor product distribution is affected by Mo-to-Al ratio – suggesting, plausibly, that only one of Mo or H^+ catalyze all selectivity-controlling steps during DHA in the studied range of Mo-to-H^+ ratio. If methane dehydroaromatization were to proceed through a bifunctional reaction scheme, as proposed (*19*, *21–24*), variation of the Mo-to-Al ratio would engender proportional change

in the rates of metal-catalyzed C-C coupling and acid-catalyzed C_2H_x aromatization, thereby affecting observed product selectivities as a function of methane conversion.

Increasing Mo loading on Mo/H-ZSM-5 materials prepared by both incipient wetness impregnation and solid-state vapor-phase exchange has been shown to enhance steady-state aromatic yields at identical catalyst mass-based contact time (g_{cat} s mol_C^{-1}), suggesting Mo moieties catalyze rate-controlling steps (*9*, *25*, *41*, *42*, *96*, *105*, *106*). We measured steady-state methane conversion on Mo/H-ZSM-5 catalysts with systematic variation of Mo-based contact time by change of Mo content, catalyst mass loading, and total flow rate. Reaction conditions which result in initial catalytic methane conversion $\lesssim$ 2% are characterized by rapid catalyst deactivation which renders elusive measurement of steady-state methane conversion. Figure 4.3 demonstrates that methane conversion is a one-to-one function of Mo-based contact time, τ_{Mo}, regardless of the method of τ_{Mo} variation, indicating that carbidic Mo content uniquely determines the methane conversion rate. We refer to the one-to-one function between methane conversion and contact time as $f(\tau_{Mo})$, or $\tau_{Mo}(f)$. The functions $f(\tau_{Mo})$ and its inverse $\tau_{Mo}(f)$ are composed of piecewise polynomials fit to data shown in Fig. 4.3 and are continuous and differentiable (i.e. the piecewise polynomials and their derivatives are equal at the point of intersection). Section C.1 discusses the uniqueness of $f(\tau_{Mo})$ in the context of the PFR design equation and demonstrates methane conversion shows no quantitative correlation with catalyst mass-based contact time.

Identification of $f(\tau_{Mo})$ is essential to the analyses which follow; the ability to quantify active Mo-based contact time solely from measured effluent methane conversion during deactivation enables transient assessment of net and forward site-time yields which are

normalized by contemporaneous active site count. In essence, contact-time variation experiments can be rigorously performed simply by allowing the catalyst to deactivate non-selectively with time on stream.

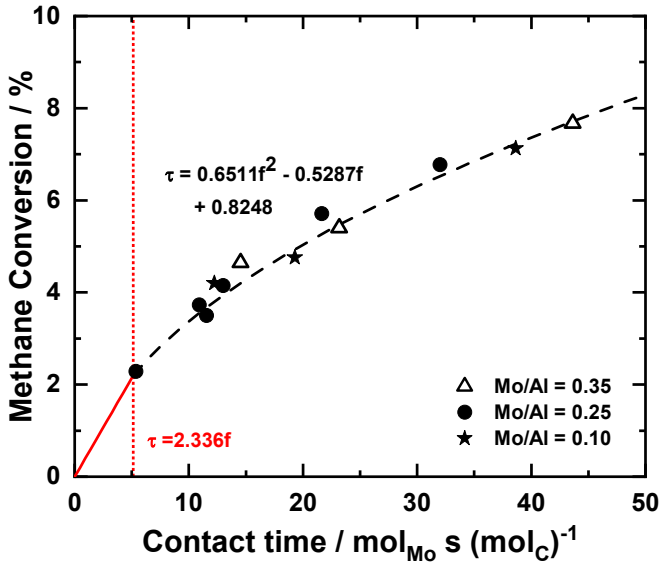

Figure 4.3: Steady-state methane conversion as a function of contact time based on the total Mo content. Reaction conditions: 973 K, ~115 kPa total pressure, total flow of 0.21 – 2.1 cm^3 s^{-1} with composition 90% CH_4/10% Ar, and 0.10 – 1.20 g Mo/H-ZSM-5. The dotted red line indicates the intersection of the piecewise functions used to construct f(τ_{Mo}).

Several reports suggest positive correlation of methane conversion with Mo-based contact time is a manifestation of approach to an optimal balance in the ratio of metal and acid active sites required for bifunctional DHA catalysis (*9*, *24*, *41*, *42*, *59*, *67*, *91*), supported by decrease in maximum instantaneous aromatic yield beyond Mo/Al ~ 0.5. We purport that reduction in aromatization rates with Mo-to-Al ratios exceeding ~0.5 is consequent from poor dispersion of Mo at loadings surpassing the number of framework Al available for cationic exchange and anchoring of Mo in MoO_x/H-ZSM-5 pre-catalysts. Excessive Mo loadings result in (i) coke selectivities surpassing that of hydrocarbon products (Mo/Al = 0.51–2.04) (*91*), (ii) formation of inactive crystalline MoO_3 domains

observed in XRD (Mo/Al = 1.11–1.36) (*105*), and (iii) extraction of Al from the framework to form $Al_2(MoO_4)_3$ identified by -13 ppm chemical shift in ^{27}Al NMR (Mo/Al = 0.68) (*42*). Recently, Khatib and co-workers overcame the ostensible limit to Mo loading by re-dispersing superfluous Mo via *ex situ* reductive pretreatment of oxidic pre-catalysts, improving CO uptake from 58.2 μmol g^{-1} to 211.0 μmol g^{-1} (*107*) and steady-state benzene yields from 4.2% to 8.3%, near the equilibrium limit, on Mo/H-ZSM-5 materials with Mo/Al = 1.11 (*105*, *107*). These reports demonstrate apparent reduction in catalyst activity for Mo/Al $\gtrsim$ 0.5 does not reflect less efficacious coupling of metal and acid catalytic functions; surplus Mo is deleterious to framework integrity and Mo dispersion, and, thusly, catalyst activity. We posit *active* Mo content is the salient descriptor of Mo/H-ZSM-5 catalysts and, in what follows, perform rigorous kinetic analyses to associate active Mo density with forward rate – the fundamental measure of catalytic activity.

4.4.2 DHA net and forward rate normalized by Mo at steady state and during deactivation

Net rates and effluent product concentrations were measured at steady state and during deactivation on Mo/H-ZSM-5 catalysts with varied Mo-to-Al ratio, catalyst loading, and total flow rate. Figure 4.4 shows net rates of benzene formation, taken to be the sum of effluent benzene and naphthalene rate to account for benzene consumption pathways, as a function of Mo-based contact time. We leverage non-selective deactivation to normalize transient rates by the contemporaneous active site count; in other words, net rates measured during deactivation are normalized by τ_{Mo} (Eq. **4.2**) rather than $\tau_{Mo,initial}$ (Eq. **4.1**). Section C.4 details normalization of rates during deactivation by use of $f(\tau_{Mo})$. Steady-state and deactivating net benzene formation rates coincide across a ~20x range in Mo-to-H^+ ratio

and ~50x range in τ_{Mo}, demonstrating Mo aggregates catalyze all kinetically-relevant steps before and during deactivation.

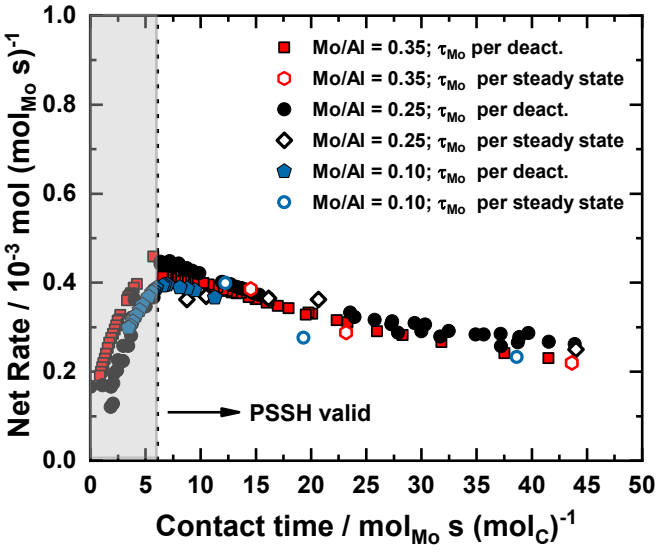

Figure 4.4: Net rate of benzene formation as a function of contact time based on the active Mo content during deactivation (solid symbols) and the total Mo content at steady state (empty symbols). Reaction conditions: 973 K, ~115 kPa total pressure, total flow of 0.21 – 2.1 cm^3 s^{-1} with composition 90% CH_4/10% Ar, and 0.10 – 1.20 g Mo/H-ZSM-5.

The overlay in methane conversion, net DHA rate, and product distribution as a function of Mo-based contact time for Mo/Al = 0.10 – 0.35 catalysts necessitates a coincidence of axial profiles of effective reversibility, and therefore forward rate, as we demonstrate by use of the De Donder equation

$$\vec{R} = \frac{R}{1 - z_{eff}} \qquad [4.3]$$

where R is the overall net rate, $\vec{R}$ is the overall forward rate, and z_{eff} is the effective reversibility defined as

$$z_{eff} \equiv \frac{\overleftarrow{R}}{\vec{R}} = z_{ov}^{1/\bar{\sigma}} \qquad [4.4]$$

The effective reversibility is the overall reversibility (e.g. $z_{ov} = P_{C_6H_6} P_{H_2}^9 \left(P_{CH_4}^6 K_{eq}\right)^{-1}$ for the reaction $6CH_4 \rightleftharpoons C_6H_6 + 9H_2$) corrected by the affinity-averaged stoichiometric number

$$\bar{\sigma} = \sum_{\substack{\text{i=elementary} \\ \text{steps}}} \ln(z_i^{\sigma_i}) \Big/ \sum_{\substack{\text{i=element} \\ \text{steps}}} \ln(z_i) \qquad \textbf{[4.5]}$$

where σ_i and z_i are, respectively, the stoichiometric number and reversibility of elementary step i. In a recent report (*95*), we detail the critical importance of (i) identification of $\bar{\sigma}(\tau_{Mo})$ to correctly calculate z_{eff}, the pertinent thermodynamic resistance in series reactions, and (ii) spatial averaging of $z_{eff}(\tau_{Mo})$ to account for the distinct conveyance of kinetic and thermodynamic information in flow reactors. The forward rate of DHA, calculated from observable effluent quantities, is

$$\vec{R} = \frac{< R >}{< 1 - z_{eff} >} = \frac{F_{C_6H_6} + F_{C_{10}H_8}}{< 1 - z_{ov}^{1/\bar{\sigma}} >} \qquad \textbf{[4.6]}$$

where F_i [=] mol $(mol_{Mo}\ s)^{-1}$ is the active Mo-normalized effluent flow rate of i and the quantity enclosed by angle brackets, < >, is spatially-averaged from reactor inlet to outlet. Section C.5 details use of Eqs. **4.3**-**4.6**.

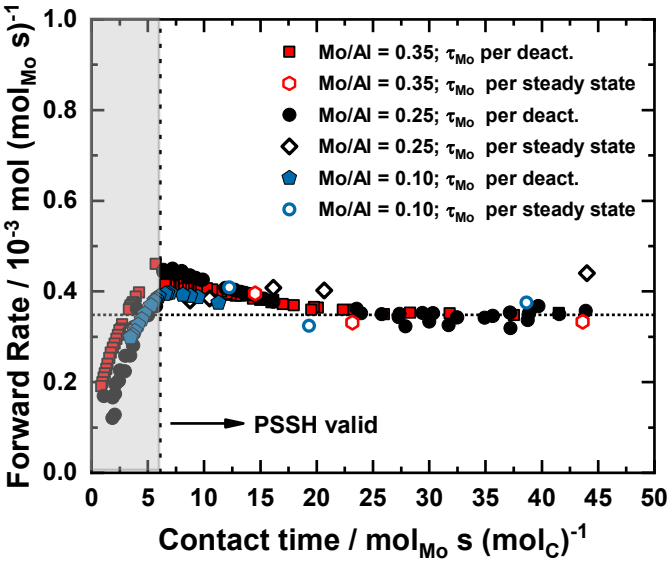

Figure 4.5: Forward rate of benzene formation as a function of contact time based on the active Mo content during deactivation (solid symbols) and the total Mo content at steady state (empty symbols). Reaction conditions: 973 K, ~115 kPa total pressure, total flow of 0.21 – 2.1 $cm^3\ s^{-1}$ with composition 90% CH_4/10% Ar, and 0.10 – 1.20 g Mo/H-ZSM-5.

Figure 4.5 shows Mo-normalized forward benzene formation rate, $\vec{R}$, as a function of τ_{Mo} calculated from data presented in Fig. 4.4 and the formalism described by Eqs. **4.3**-**4.6**. Forward rates initially increase with contact time until $\tau_{Mo} \sim 7\ mol_{Mo}\ s\ mol_C^{-1}$ at which point the DHA reaction network achieves a pseudo-steady state (PSS) coincident with equilibration of methane, ethane, and ethylene (*70*, *95*). Pseudo-steady state forward rates are invariant with τ_{Mo}, suggesting there is no kinetic product inhibition (e.g. competitive adsorption) by H_2 or hydrocarbons. The coincidence of Mo-normalized steady-state and deactivating net rates is reproduced for $\vec{R}$, redoubling conclusions that carbidic Mo catalyzes all steps which exert rate control in the benzene formation reaction pathway.

Methane, ethane, and ethylene form an equilibrated pool (i.e. $z = P_{C_2H_4}P_{H_2}^2\left(P_{CH_4}^2K_{eq}\right)^{-1} = 0.96 – 1.18$ for the overall reaction $2CH_4 \rightleftharpoons C_2H_4 + 2H_2$) for CH_4 conversions $\gtrsim$ 3% during catalytic DHA at 973 – 1073 K on Mo/H-ZSM-5 materials prepared by various syntheses (*39*, *45*, *70*, *95*), indicating all rate-controlling steps to aromatic formation must occur between ethylene and benzene. Ethylene, formed from dehydrogenation of ethane (*95*), is purported to form benzene via (i) dehydrocyclization by formation and cracking of cyclohexane (*19*, *21–24*), (ii) involvement in a hydrocarbon pool composed of radical polyaromatic species (*27*, *108–110*), or (iii) dehydrogenation to and subsequent trimerization of acetylene (*77–79*). Investigations which implicate cyclohexane as an intermediate to aromatic synthesis suggest ethylene undergoes acid-catalyzed chain growth and protolysis on zeolitic Brønsted-acid sites to form benzene and

higher aromatics; and, proposals of a hydrocarbon pool mechanism purport entrained linear polyaromatic species formed in the carburization period serve as organic co-catalysts which mediate formation of light aromatics.

Our prior report details kinetic analyses which indicate (i) DHA proceeds via successive dehydrogenation to ethane, ethylene, and acetylene – which cyclizes to benzene through undetected C_4 intermediates (*69*, *95*) – and (ii) steps between ethylene and benzene are rate- and reversibility-controlling in the pseudo-steady state regime.

Ethylene aromatization rates at 923 K measured by Ha et al. (*78*) confirm C_2H_4 DHA is kinetically-controlled by Mo sites; benzene formation rates over H-ZSM-5 (25 μmol g^{-1} h^{-1}) during C_2H_4 DHA sans methane feed are significantly lower than those on both Mo/H-ZSM-5 (97 μmol g^{-1} h^{-1}) and Mo/SiO_2 (50 μmol g^{-1} h^{-1}), indicating Mo-mediated routes are more facile for aromatic formation, with or without Brønsted-acid sites. These reports (*77–79*, *95*), complemented by observed methane-ethane-ethylene equilibrium (*39*, *70*) and the analyses presented herein, unambiguously demonstrate that all rate-determining steps in methane DHA must occur after ethylene formation and be catalyzed by carbidic Mo sites, thereby falsifying acid-catalyzed olefin oligomerization (–enclosed route in Scheme 4.1) (*19*, *21*, *24*) and radical-mediated hydrocarbon pool catalysis (*27*, *108–110*) as kinetically-relevant routes of benzene formation. We surmise methane DHA is kinetically-controlled by acetylene formation or oligomerization catalyzed by Mo aggregates (C_2H_2-mediated route enclosed by in Scheme 4.1), plausibly in concert with equilibrated H^+-catalyzed cyclization of unsaturated C_{2-4} intermediates; however, we cannot eliminate the possibility that benzene is formed via Mo-catalyzed C-C coupling of ethylene (direct route enclosed by in Scheme 4.1).

Irrespective of the identity of rate-determining elementary steps, identification of Mo-associated species as the kinetically-relevant active site and demonstration of the non-selective nature of deactivation implies loss in catalyst activity must be exclusively attributable to a reduction in the number of residual active Mo, as we confirm hereinafter.

4.4.3 Mo site-counting by ethane hydrogenolysis probe reaction

We assess the relative change in active Mo content over deactivating Mo/H-ZSM-5 catalysts by ethane hydrogenolysis performed after various intervals of DHA catalysis. Our recent investigation (*95*) shows ethane selectivity approaches 100% as $f \rightarrow 0$, evincing ethane as the sole primary gas-phase product of methane DHA. Ethane hydrogenolysis is therefore the reverse of initial C-C coupling in DHA (i.e. $2CH_4 \rightleftharpoons C_2H_6 + H_2$) well-accepted to be catalyzed by Mo moieties rather than Brønsted-acid sites and is an ideal candidate to kinetically probe residual active Mo content.

We measure ethane hydrogenolysis rates on H-ZSM-5 samples (see Section C.6) to confirm ethane hydrogenolysis on Mo/H-ZSM-5 samples is catalyzed by Mo; the measured steady-state H^+-catalyzed ethane hydrogenolysis turnover rate is $1.25 \cdot 10^{-5}$ mol_C $(mol_{H+}\ s)^{-1}$, 0.56% of the Mo-normalized ethane hydrogenolysis turnover rate reported in the following.

Intermittent probe reactions are performed by (i) allowing DHA catalysts to deactivate to a particular extent, (ii) cooling the reactor in inert He to 750 K, (iii) measuring the steady-state rate of ethane hydrogenolysis, and (iv) regenerating the Mo/H-ZSM-5 sample in 1% O_2/He to repeat the protocol with systematically varied durations of DHA. Oxidative regeneration reproducibly restores the initial induction period, steady-state rate, and DHA rates during deactivation, as observed in prior studies (*14*, *62*, *64*, *111*, *112*). Section C.7 provides illustrative data which depicts the temporal overlay of methane conversion and

product distribution on regenerated catalysts. Ethane and hydrogen conversions are kept <2%, ensuring ethane hydrogenolysis is differential and irreversible ($z = P_{C_2H_6}P_{H_2}\left(P_{CH_4}^2 K_{eq}\right)^{-1} < 10^{-6}$).

Figure 4.6 shows ethane hydrogenolysis rates and active Mo content, per τ_{Mo}(f), as a function of time on stream for Mo/Al = 0.10, 0.25, and 0.35. Instantaneous methane conversion in all repeat DHA reactions during cycles of ethane hydrogenolysis and DME titration (*vida infra*) temporally coincide and are averaged between all cycles to calculate Mo content shown in Fig. 4.6. The scales of the left and right ordinate axes in Figs. 4.6(a-c) are chosen to correspond to the line of best fit between ethane hydrogenolysis rate and active Mo content illustrated in Figure 4.7 which quantitatively confirms linear correspondence of ethane hydrogenolysis rates and τ_{Mo}(f). Temporal linear overlay of decay in hydrogenolysis rate and active Mo content explicitly demonstrates that, irrespective of Brønsted-acid site content, the deactivation of Mo/H-ZSM-5 catalysts is attributable to the loss of active, or accessible, catalytic Mo centers.

Heretofore, we speculated that observed rates and selectivities of CH_4 DHA on Mo/H-ZSM-5 catalysts and transients thereof may conceivably be the consequence of an evolving distribution of Mo species diverse in number, speciation, and catalytic activity. The non-selective nature of deactivation, invariance of product distribution with Mo/H^+, and normalization of forward rates by Mo content detailed in this work significantly reduces the possible complexity of Mo disposition. In particular, one of the following must be true: (i) there exists a single (oxy-)carbidic Mo center responsible for catalyzing all rate- and selectivity-controlling steps or (ii) the relative fractions of all MoC_xO_y species which observably contribute to DHA remain unchanged irrespective of extent of deactivation or

Brønsted-acid site content such that all active Mo-associated species appear to behave as a single catalytic site. In either case, active Mo content, as defined and calculated in this work, is a quantitative and seemingly complete descriptor of Mo/H-ZSM-5 activity.

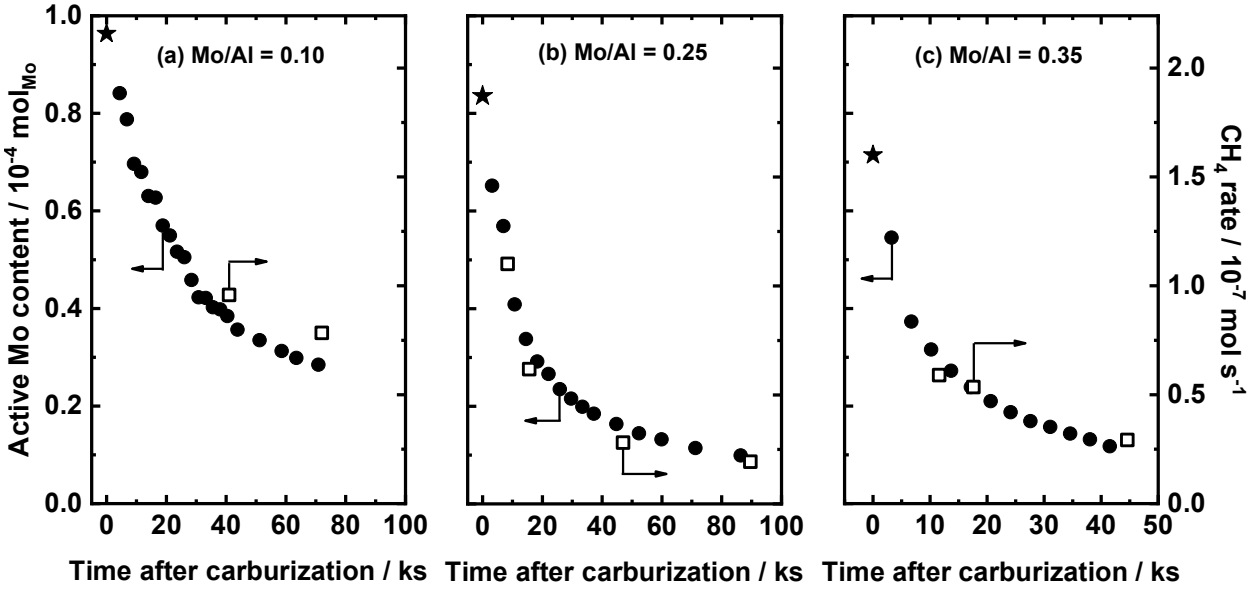

Figure 4.6: Rate of CH_4 formation during ethane hydrogenolysis (□) and active Mo content (●), determined from $\tau_{Mo}(f)$, as a function of duration of DHA catalysis. Total Mo content (i.e. total Mo used during $[Mo_2O_5]^{2+}$/H-ZSM-5 synthesis) (★). DHA reaction conditions: 973 K, ~115 kPa total pressure, total flow of 0.21 $cm^3\ s^{-1}$ with composition 90% CH_4/10% Ar. Ethane hydrogenolysis reaction conditions: 750 K, ~120 kPa total pressure, total flow of 0.49 $cm^3\ s^{-1}$ with composition 46% C_2H_6/49% H_2/balance Ar

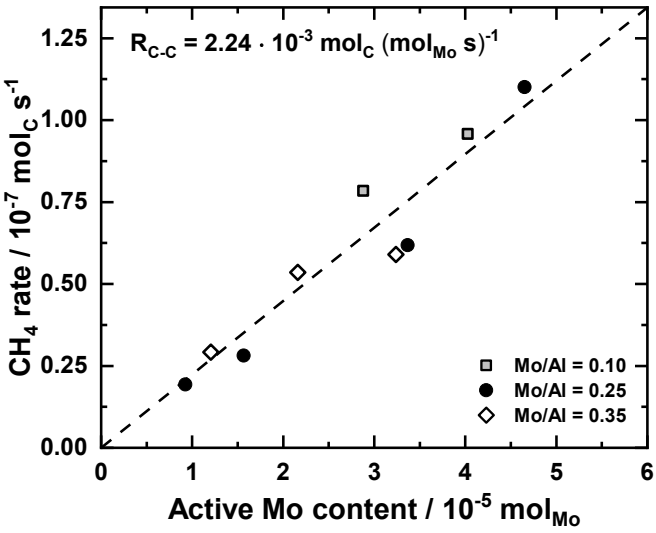

Figure 4.7: Rate of CH_4 formation during ethane hydrogenolysis as a function of active Mo content, determined from $\tau_{Mo}(f)$ at the time of cessation of DHA. All data reproduced from Fig. 4.4.6.

Identification of residual Mo content as the salient descriptor of transient catalytic activity is critical to informing and interpreting efforts to eliminate catalyst deactivation. Deactivated Mo centers are regenerable by either oxidative (*13*, *14*, *62*, *111*, *112*) or reductive (*62*) treatment which restores catalytic activity with and without initial induction period, respectively. Cyclic operation of DHA reactors with intervening O_2 treatment successfully restores initial and transient catalyst activity over six regenerations in ~10 hours and maintains ~50% the activity of a fresh catalyst over one week of cyclic operation (*14*). The virtue of oxidative regeneration protocols such as these has been attributed to removal of deposited carbon and elimination of hard and soft coke formation on Brønsted-acid sites, the external zeolite surface, and/or MoC_x aggregates (*111*). The deposition of carbonaceous species during carburization and catalysis may be relevant to deactivation; however, the efficacy of a deactivation mitigation strategy must be evaluated in terms of the ability to (i) intercept mechanisms which render Mo inactive or (ii) reproducibly return Mo aggregates to their speciation at the onset of the first period of catalysis. The role of Brønsted-acid sites, zeolite topology, or any other catalyst descriptor to accelerate deactivation must be quantitatively assessed by the influence of each on the rate of deactivation, $d\tau_{Mo}/dt$, or the time rate of change of the number of active Mo centers (*74*).

4.4.4 Brønsted-acid site-counting by DME titration

We enumerate Brønsted-acid site density using DME titration over deactivating Mo/H-ZSM-5 catalysts by analogous protocol to Mo-counting by ethane hydrogenolysis rate to show zeolitic protons are immaterial to catalytic rate and product distribution. After varied intervals of DHA catalysis, the reactor is cooled to 423 K in He and treated with regular

doses of dimethyl ether to determine the quantity of Brønsted-acid sites accessible at the time of cessation of catalysis. Mo/H-ZSM-5 materials are subsequently regenerated in 1% O_2/He and used for further catalytic reactions and chemical titrations. Figure 4.8 shows Brønsted-acid site content histories with accompanying histories of active Mo content measured from $\tau_{Mo}(f)$ and ethane hydrogenolysis rates per Figures 4.3, 4.6, and 4.7. Catalytic and titration data presented in Figures 4.6-4.9 are collected over the same catalyst sample for each Mo-to-Al ratio to eliminate possible discrepancy in catalyst synthesis convoluting measurement of rates and site count.

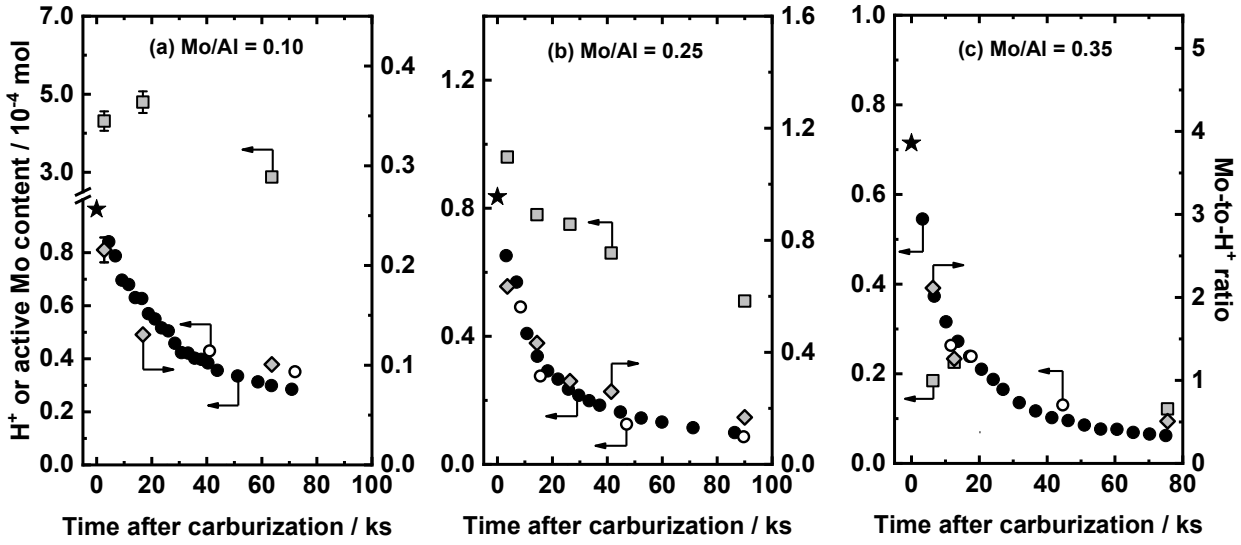

Figure 4.8: Left ordinate axis: Brønsted-acid site density from dimethyl ether titration (■) and active Mo content determined from instantaneous methane conversion (●) and ethane hydrogenolysis rate (○). Total Mo content (i.e. total Mo used during $[Mo_2O_5]^{2+}$/H-ZSM-5 synthesis) (★). Right ordinate axis: Mo-to-H^+ ratio (◆), i.e. the ratio of Mo content per $\tau_{Mo}(f)$ (●) and H^+ content per DME titration (■). Abscissa: duration of DHA catalysis. DHA reaction conditions: 973 K, ~115 kPa total pressure, total flow of 0.21 cm^3 s^{-1} with composition 90% CH_4/10% Ar. Dimethyl ether titration conditions: 423 K, ~120 kPa total pressure, total flow of 0.50 cm^3 s^{-1} with composition 96% He/4% Ar and 0.25–1.00 cm^3 doses of dimethyl ether.

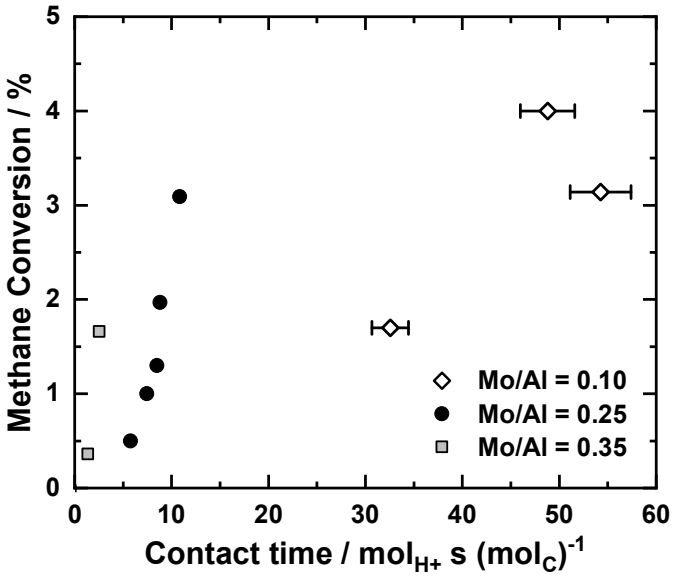

Figure 4.9: Instantaneous methane conversion as a function of contact time based on Brønsted-acid site content determined from dimethyl ether titration. All data reproduced from Fig. 4.4.8.

The quantity of Brønsted-acid sites at early times on stream exceeds that of parent oxidic pre-catalysts (e.g. 2.72 – 16.8 ks in Fig. 4.8(a)) due to a de-anchoring of Mo cations from the zeolite framework during carburization, as observed by Bedard et al. (*19*). Accumulation of coke ostensibly congests zeolite pores, decreasing the number of accessible protons as the catalyst deactivates, as illustrated in Figs. 4.8(a-c). Irrespective of Mo-to-Al ratio, the relative change in acid site count is significantly less than the attendant decrease in Mo density, evinced by Mo-to-H^+ ratio (◆ in Fig. 4.8(a-c)) which linearly overlay with active Mo content (●,○ in Fig. 4.8(a-c)). Disparate decay in Mo and H^+ site count indicates metal and acid sites deactivate by distinct mechanisms and effectuates Mo-to-H^+ ratios decrease with time on stream since Mo sites deactivate more rapidly than zeolitic protons. Mo-to-H^+ ratios which range from 0.25 – 2.1 on pre-catalyst samples result in Mo/H^+ = 0.10 – 2.1 during catalysis – affirming conclusions that Mo sites catalyze all rate- and selectivity-determining steps per the overlay of product distribution (Fig. 4.2),

methane conversion (Fig. 4.3), and DHA net and forward rates (Fig. 4.4 and 5) with Mo content despite concomitant ~40x variation in the number of acid sites.

Comparison of instantaneous acid site densities and methane conversion from data presented in Figure 4.8 permits construction of Figure 4.9 which shows methane conversion as a function of H^+-based contact time, τ_{H+}, analogously to Figure 4.3 used to determine $f(\tau_{Mo})$. Instantaneous methane conversion over non-selectively deactivating Mo/H-ZSM-5 shows no discernable correlation with contemporaneous Brønsted-acid site density over a ~40x range in τ_{H+} = 1.4 – 54 mol_{H+} s mol_C^{-1}, definitively establishing protons as kinetically-irrelevant catalytic centers for methane dehydroaromatization. Proton-based contact time cannot be rigorously compared to methane conversion during steady-state DHA reactions because the concurrent detachment of Mo from exchange sites and deposition of coke during carburization respectively increase and decreases proton density, rendering uncertain the number of accessible Brønsted-acid sites at the onset of catalysis. The irrelevance of Brønsted-acid site count to DHA rate and product distribution does not indicate zeolitic protons are necessarily catalytic inactive; rather, we conclude all acid-catalyzed steps must be equilibrated, tangential to the benzene formation reaction, or masked by faster Mo-catalyzed reactions.

4.5 Conclusion

We scrutinize putative bifunctional dehydroaromatization (DHA) reaction schemes by measurement of rates and product distribution of DHA on a suite of Mo-modified H-ZSM-5 zeolites prepared with Mo/Al = {0.10, 0.25, 0.35}. Gradation of Mo loading stoichiometrically alters the number of Brønsted-acid sites, enumerated by dimethyl ether titration, in a 1:1 correspondence on oxidic pre-catalysts and begets Mo/H^+ = 0.10 – 2.1

during catalysis. Irrespective of Mo-to-H^+ ratio, the distribution of C_2 intermediates and benzene is uniquely determined by methane conversion which, in turn, is a one-to-one function of Mo-based contact time, τ_{Mo}, demonstrating Mo/H-ZSM-5 catalysts (i) contain a single kinetically-relevant active site and (ii) deactivate non-selectively, or without change to catalytic properties of residual active sites.

The one-to-one function, $f(\tau_{Mo})$, between methane conversion, f, and Mo-based contact time, τ_{Mo}, is used to construct axial profiles of net rate, product concentrations, and effective reversibility along the catalyst bed, permitting calculation of DHA forward rate – the intrinsic measure of catalytic activity – at steady state and during deactivation. Mo-based contact time is virtuous in predicting steady state and transient DHA forward rate across a ~20x range in Mo/H^+ and ~50x range in τ_{Mo}, vindicating assignment of Mo as the kinetically-relevant active site.

Ethane hydrogenolysis probe reactions catalyzed by residual active Mo are performed at intervals of catalysis to corroborate non-selective nature of deactivation and identification of Mo as the rate-controlling active site. Steady-state rates of ethane hydrogenolysis linearly correspond with active Mo content, determined from instantaneous methane conversion and $f(\tau_{Mo})$, demonstrating deactivation of Mo/H-ZSM-5 is caused by the loss of active Mo centers which are ostensibly either active or inactive in a binary fashion. Transients in Brønsted-acid site density are analogously measured by intermittent dimethyl ether titration, revealing the number of accessible acid sites is relatively unchanged during catalysis. Brønsted-acid site count has no discernable effect on DHA rate or product distribution; therefore, we surmise all acid-catalyzed steps are either kinetically-irrelevant or tangential to benzene formation. Active carbidic Mo content is

thusly the sole catalyst descriptor required to predict steady state and transient Mo-H-ZSM-5 DHA activity, informing (i) rational design of Mo-modified zeolites for methane valorization and (ii) development of strategies to improve catalyst lifetime by preservation of active Mo.

5 Kinetic description of site ensembles on catalytic surfaces

*Contents herein are reproduced with permission from Razdan, N. K., Bhan, A. Kinetic description of site ensembles on catalytic surfaces. *Proceedings of the National Academy of Sciences*. **2021**, *118*, e2019055118. https://doi.org/10.1073/pnas.2019055118.

5.1 Conspectus

We demonstrate that the Langmuir-Hinshelwood formalism is an incomplete kinetic description and, in particular, that the Hinshelwood assumption (i.e. that adsorbates are randomly-distributed on the surface) is inappropriate even in catalytic reactions as simple as $A + A \rightarrow A_2$. The Hinshelwood assumption results in miscounting of site pairs (e.g. A^*–A^*) and, consequently, in erroneous rates, reaction orders, and identification of rate-determining steps. The clustering and isolation of surface species unnoticed by the Langmuir-Hinshelwood model is rigorously accounted for by derivation of higher-order rate terms containing statistical factors specific to each site ensemble. Ensemble-specific statistical rate terms (i) arise irrespective of and couple with lateral adsorbate interactions, (ii) are distinct for each elementary step including surface diffusion events (e.g. $A^* + * \rightarrow * + A^*$), and (iii) provide physical insight obscured by the non-analytical nature of the kinetic Monte Carlo (kMC) method – with which the higher-order formalism quantitatively agrees. The limitations of the Langmuir-Hinshelwood model are attributed to the incorrect assertion that the rate of an elementary step is the same with respect to each site ensemble. In actuality, each elementary step – including adsorbate diffusion – traverses through each ensemble with unique rate, reversibility, and kinetic-relevance to the overall reaction rate. Explicit kinetic description of ensemble-specific paths (i) is key to the improvements of the higher-order formalism, (ii) enables quantification of ensemble-specific rate, reversibility, and degree of rate control of surface diffusion and (iii) reveals that a single elementary step can, counter-intuitively, be both equilibrated and rate-determining.

5.2 Significance

The kinetic assessment of catalytic reactions is essential to the design and application of thermochemical processes useful in petrochemical synthesis, energy conversion, and environmental remediation. We demonstrate that the ubiquitously-used Langmuir-Hinshelwood formalism is an incomplete kinetic theory which can fail to correctly describe even simple catalytic reactions (e.g. $A + A \rightarrow A_2$). An accurate kinetic description requires explicit rate equations for multi-site configurations (e.g. A^*–A^* pairs) to account for the non-random clustering/isolation of surface species. We rigorously describe clustering/isolation phenomena by derivation of coverage-dependent stoichiometric coefficients which capture the distinct influence each elementary step exerts on each catalytic-site ensemble – thereby overcoming limitations of the mean-field (i.e. Hinshelwood) assumption in describing reactions of mobile Langmuirian adsorbates on catalytic surfaces.

5.3 Introduction

The Langmuir model of adsorption, used ubiquitously in the study of fluid physics (*113–115*), environmental remediation (*116–119*), separations (*120*, *121*), heterogeneous catalysis (*28*, *76*, *122*), and other fields (*123*, *124*), describes the adsorption and desorption of fluid-phase species on solid surfaces under the following conditions:

(I) The absorbent is a perfect, flat 2-D lattice

(II) Each adsorption site can be occupied by at most one occupant

(III) The surface is energetically uniform and adsorbates have no energetic interactions. We refer to this as the system being *thermodynamically-ideal*.

With the above assumptions, the specific rate, r, of reversible adsorption of a gas-phase species $A_{(g)}$ which occupies a single site as surface species a is

$$r = k_{ads}\theta_o - k_{des}\theta_a \quad \textbf{[5.1]}$$

where θ_o and θ_a are respectively the fractional surface coverages of vacant sites and *a*-occupied sites, k_{des} is the rate constant of desorption, and k_{ads} is the product of the rate constant of adsorption and the thermodynamic activity (ideally, partial pressure) of $A_{(g)}$. Catalytic reactions of Langmuirian adsorbates are commonly described by the Langmuir-Hinshelwood theory (*28*), which, in addition to the conditions of Langmuirian adsorption (I)-(III), assumes the following:

> (IV) Adsorbates are randomly distributed on the surface (i.e. there are no spatial correlations between sites). We refer to this as the system being *combinatorially-ideal*.

The Hinshelwood assumption, (IV), permits simple mathematical description of a surface reaction between neighboring adsorbates. Consider, for example, the reaction between two *a* surface species. The general rate expression for such an elementary step is

$$r = k_r\theta_{aa}\left(\frac{z}{2}\right) \quad \textbf{[5.2]}$$

where k_r is the rate constant of the reaction, z is the coordination number of the 2D lattice, and θ_{aa} is the fraction of pairs of sites which contain two *a* species (*125*, *126*). The rate expression in Eq. **5.2** can be simplified in terms of only single-site coverages by use of the Hinshelwood assumption (*28*), giving

$$r = k_r\theta_a^2\left(\frac{z}{2}\right) \quad \textbf{[5.3]}$$

The Hinshelwood assumption reduces coverages of site configurations of any size to a product of coverages of all constituent single-site occupants. In other words, the mean-field metric

$$\mu_{ij} \equiv \frac{\theta_{ij}}{\theta_i\theta_j} \quad \textbf{[5.4]}$$

is taken to be unity for all pairs of site occupants i and j per the Hinshelwood assumption. Similarly, θ_{ijk} is assumed equal to $\theta_i\theta_j\theta_k$ and so on.

The veracity of the Hinshelwood assumption is contingent on a sufficiently-randomizing process – namely, arbitrarily-fast surface diffusion – to achieve a uniform adsorbate distribution. Kinetic Monte Carlo studies of CO oxidation (*126*), CO_2 hydrogenation (*127*), CO methanation (*128*), and NO oxidation and NO_2 reduction (*129*) have recognized the shortcomings of the Hinshelwood assumption and demonstrated surface diffusion in catalytic systems is often insufficiently-fast to validate the Langmuir-Hinshelwood formalism even in the absence of lateral interactions – evinced by mean-field metrics which deviate from unity by factors $\gtrsim$100× (*126*, *128*) and significantly miscalculated rates and reaction orders (*126–129*). These deficiencies arise because multi-site requirements of elementary steps induce clustering ($\mu_{ij} > 1$) and isolation ($\mu_{ij} < 1$) of surface species to which the Langmuir-Hinshelwood assumption is ignorant; each site ensemble uniquely combinatorially-couples to the -sorptive/reactive/diffusive configuration of each elementary step and thusly requires unique rate terms to capture the propensity of each step to engender islanding or partitioning of surface species which constitute the considered ensemble.

In this work, we develop an analytical formalism which derives higher-order rate terms necessary to describe dynamics of ensembles of any size and shape. The Langmuir-Hinshelwood formalism is the 0^{th}-order variant of the presented mathematical framework (i.e. retains only terms of the 0^{th}-order) and consequently can only reliably describe catalytic sequences consisting of exclusively single-site elementary steps – thereby prohibiting quantitative description of surface diffusion events which inherently require

two sites (e.g. *ao* ⇌ *oa*). The 1st-order treatment retains terms of the 0th- and 1st-order, enabling quantitative description of *combinatorial non-idealities* that (i) are neglected by the Hinshelwood assumption and (ii) are necessary to generally describe catalytic reactions of mobile Langmuirian adsorbates. Closed-form 1st-order rate expressions permit calculation of ensemble-specific degrees of rate control and reaction orders inaccessible to kMC simulation; the kMC method does accurately predict adsorbate clustering/isolation and the kinetic consequences thereof, however, in doing so stochastically, is unable to identify compendious rate terms responsible for these phenomena.

5.4 Combinatorial non-idealities in Langmuirian adsorption

We introduce the general mathematical framework used to describe catalysis of Langmuirian adsorbates through the simplest example of a combinatorially non-ideal rate process – irreversible adsorption of unreactive, immobile dimers, *dd*, on a 2D square lattice (*130–133*). Consider the filling of the lattice starting from an empty state, depicted in Scheme 5.1. As dimers randomly adsorb on the surface, some fraction of vacant sites, *o*, will become irreversibly isolated (e.g. grey site in *half-filled lattice* in Scheme 5.1). Therefore, at saturation, the population of vacant pairs will be zero, but the coverage of isolated vacant sites will be finite (i.e. $\mu_{oo} = 0$). The unfilled, saturated lattice is said to be in a "jammed" state, and the saturation coverage is referred to as the dimer jamming limit for a 2D square lattice (*130–133*). The Langmuir-Hinshelwood formalism is unable to reproduce jamming phenomena such as these because the fraction of site pairs available for adsorption is always taken to be θ_o^2 which cannot be zero when θ_o is non-zero (i.e. μ_{oo} is assumed to be unity, which is inaccurate). The inability to capture jamming behavior

exemplifies the limitations of the Langmuir-Hinshelwood model to describe combinatorially non-ideal dynamics of thermodynamically-ideal adsorbates.

Scheme 5.1: Jamming of adsorbing dimers on a 2D square lattice

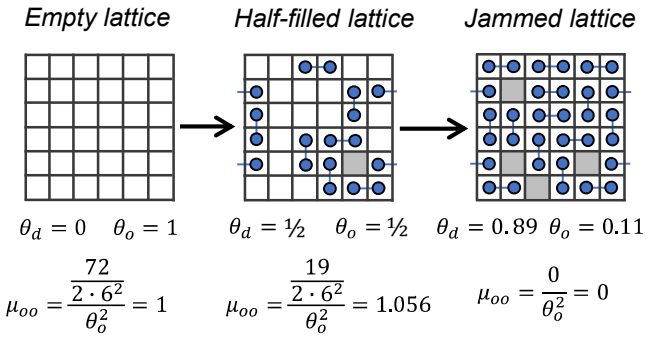

Snapshots of irreversible adsorption of unreactive dimers (●–●) on a 6 × 6 square lattice with periodic boundary conditions. Bonds (–) extending outside the lattice indicate dimers adsorbed on either side of the periodic boundary. Grey lattice sites (□) indicate isolated vacant sites.

5.4.1 Hierarchical rate equations

The complete analytical description of catalysis of Langmuirian adsorbates generalizes formalisms for jamming coverages (*130–134*) to include desorption, surface reaction, and surface diffusion processes by construction of an infinite set of hierarchical rate equations which describe time-evolution of coverages of all possible site configurations of any size (*131*, *132*). By hierarchical we mean to say that the rate equations for populations of configurations containing n sites is dependent on populations of configurations of containing $n + 1$ sites, thereby generating an un-ending list of rate equations considering ever-larger configurations of sites. The hierarchical nature of the rate equations confers a complete description of combinatorially non-ideal catalysis which we regard as the analytical-analog to the kinetic Monte Carlo method; however, completeness must be sacrificed to make the analytical pen-and-paper model tractable. The infinite hierarchy of rate equations demands a consistent truncation scheme to yield a finite, solvable set of coupled rate equations. In the following, we first explicate the hierarchical nature of

catalytic rate equations and then introduce and provide an example of the 1st-order truncation procedure – which we regard as having the optimum balance of completeness and simplicity (*135*).

Scheme 5.2: Elimination of *oo* pairs by $D_{2(g)}$ adsorption ($D_{2(g)} + oo \rightarrow dd$).

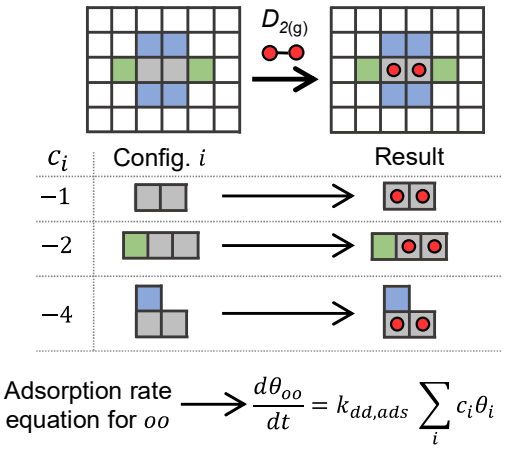

d monomers are shown by filled red circles (●). Greyed lattice sites (□) are those which host adsorption. Blue (□) and green (□) sites are nearest neighbors to the adsorption center.

We continue the example of irreversible dimer adsorption on a square lattice to demonstrate the hierarchical nature of rate equations. We derive the rate equation describing the time-evolution of vacant site pairs, *oo*, during dimer adsorption with the aid of Scheme 5.2 which illustrates all configurations which annihilate *oo* site pairs. Color-coded in accordance with Scheme 5.2, the adsorption rate equation for *oo* is

$$\frac{d\theta_{oo}}{dt} = -k_{dd,ads}\left(\theta_{oo} + \mathbf{2\theta_{ooo}} + \mathbf{4\theta^{o}_{oo}}\right) \qquad \textbf{[5.5]}$$

where $k_{dd,ads}$ is the product of the rate constant of adsorption and the thermodynamic activity of the fluid-phase species adsorbing as *dd*. The first term enclosed in parenthesis in Eq. **5.5** accounts for the annihilation of *oo* for every adsorption event – as shown in the first row of Scheme 5.2. The last two terms in Eq. **5.5** account for annihilation of an additional *oo* pair if the adsorption center is neighbored by another vacant site at any of the

six nearest neighbor positions per the second and third rows of Scheme 5.2. From inspection of Eq. **5.5**, we see that the population, or probability, of the two-site configuration *oo* is dependent on populations of three-site configurations. Further, rate equations for three-site configurations, for example *ooo*, are functions of populations of four-site configurations, e.g.

$$\frac{d\theta_{ooo}}{dt} = -k_{dd,ads}\left(2\theta_{ooo} + 2\theta_{oooo} + 2\theta_{\substack{o\\ooo}} + 4\theta_{\substack{o\\ooo}}\right) \qquad \textbf{[5.6]}$$

and the rate equations for four-site configurations are functions of populations of five-site configurations and so on *ad infinitum*. Therefore, the complete analytical description of irreversible dimer adsorption, or any rate process involving Langmuirian adsorbates, requires an *infinite hierarchy* of rate equations – capable of capturing combinatorial non-idealities involving site ensembles of arbitrary size and shape. The complete, infinite set of equations is made finite and solvable by introduction of a mathematically-consistent *truncation* procedure – formally detailed in the work of Nord and Evans (*131*, *132*, *136*). The truncation procedure operates directly on *conditional* probabilities and is described in the following.

5.4.2 Conditional probabilities and truncation of hierarchical rate equations

Consider the conditional probability, χ, that a particular *conditioned* site is vacant, *o*, provided the neighboring *conditioning* site, ϕ, is known to be vacant. We distinguish ϕ from *o* since the site indicated by ϕ is vacant with 100% probability. The described conditional probability is written as $\chi_{o\phi}$ and is given by

$$\chi_{o\phi} = \frac{\theta_{oo}}{\theta_o} \qquad \textbf{[5.7]}$$

Similarly, conditional probabilities of three-site configurations, such as $\chi_{o\phi\phi}$, are given by

$$\chi_{o\phi\phi} = \frac{\theta_{ooo}}{\theta_{oo}} \quad \textbf{[5.8]}$$

The order of the truncation procedure is the number of lattice vectors from the conditioned site (e.g. o) within which conditioning sites (e.g. ϕ) are retained (*131–134*). Therefore, the 0^{th}-order truncation scheme only explicitly considers configurations of one site and is simply that of the Langmuir-Hinshelwood treatment. For example,

$$\theta_{oo} = \chi_{o\phi}\theta_o = \chi_o\theta_o = \theta_o^2 \quad \textbf{[5.9]}$$

The 1^{st}-order procedure truncates all conditioning sites except nearest neighbors to the conditioned site. For example, in a 1^{st}-order truncation scheme, $\chi_{o\phi\phi\phi\phi}$ truncates to $\chi_{o\phi}$. Therefore, the first-order scheme only explicitly considers probabilities of configurations with two sites or fewer; probabilities of configurations with three or more sites are reduced to products and quotients of probabilities of one- and two-site configurations. The first-order scheme is consequently an incomplete improvement of the Langmuir-Hinshelwood model and is ignorant to spatial correlations between next-nearest neighbors and beyond – which requires retention of $>1^{st}$-order terms. Truncation schemes of order greater than one, however, introduce significant mathematical complexity which we regard insufficiently remunerative for processes occurring on one or two sites (*134*, *135*). For example, 1^{st}-order calculations for jamming limits of dimers (θ_d = 0.8889) on square lattices are in nearly quantitative agreement with 3^{rd}- (θ_d = 0.9064) and 4^{th}-order predictions (θ_d = 0.9068) despite only considering configurations of two sites or fewer and using >100 fewer equations (*131*). To our knowledge, a scheme of order greater than one has not been used for cases other than reactions on 1D lattices and the calculation of jamming coverages (*133–135*, *137–139*).

5.5 1^{st}-order model of catalysis of mobile Langmuirian surface species

This work hereinafter is dedicated to the construction and evaluation of 1st-order rate equations which may be generally applied to any catalytic reaction of mobile Langmuirian surface species. To explicate the execution of the 1st-order truncation scheme, we return to the dimer jamming example. We simplify Eq. **5.5** by first re-writing in terms of conditional probabilities, retaining color-coding from Scheme 5.2

$$\frac{d\theta_{oo}}{dt} = -k_{dd,ads}\theta_{oo}\left(1 + \mathbf{2}\boldsymbol{\chi_{o\phi\phi}} + \mathbf{4}\boldsymbol{\chi}^{o}_{\phi\phi}\right) \qquad \textbf{[5.10]}$$

and then truncating conditioning sites to within one lattice vector of the conditioned site

$$\frac{d\theta_{oo}}{dt} = -k_{dd,ads}\theta_{oo}\left(1 + \mathbf{2}\boldsymbol{\chi_{o\phi}} + \mathbf{4}\boldsymbol{\chi_{o\phi}}\right) \qquad \textbf{[5.11]}$$

which, collecting terms, gives

$$\frac{d\theta_{oo}}{dt} = -k_{dd,ads}\theta_{oo}\left(1 + \frac{6\theta_{oo}}{\theta_o}\right) \qquad \textbf{[5.12]}$$

The construction of Eq. **5.12** explicates the provenance of coverage-dependent stoichiometric coefficients which characterize the 1st-order and are absent in the Langmuir-Hinshelwood formalism. Rate equations for all multi-site ensembles require consideration of populations of configurations larger than that on which the rate event occurs, resulting in new coverage-dependent rate terms derived from truncation of conditional probabilities specific to each site configuration. For example, the stoichiometric coefficient $1 + 6\theta_{oo}/\theta_o$ in Eq. **5.12** is derived from truncation of three-site conditional probabilities (Eq. **5.10-5.11**) and accounts for adsorbate proximity effects unique to θ_{oo}; in the Langmuir-Hinshelwood model, θ_{oo} is simply taken to be θ_o^2 and the rate equation for vacant sites, $d\theta_o/dt = -4k_{dd,ads}\theta_o^2$ features no consideration of the proximity effects which engender isolation of *o*-sites characteristic of jamming phenomena.

The 1st-order model of irreversible dimer adsorption is completed by use of site balances, detailed in Eqs. **5.14** and **5.15** to follow, and by coupling Eq. **5.12** with the rate equation for θ_o

$$\frac{d\theta_o}{dt} = -4k_{dd,ads}\theta_{oo} \qquad \textbf{[5.13]}$$

where the factor of '4' accounts for the coordination number of the square lattice. By comparison, the 2nd-order treatment requires independent rate equations for populations of seven configurations, $\theta_o, \theta_{oo}, \theta_{oo}^{o}, \theta_{ooo}, \theta_{oo}^{oo}, \theta_{ooo}^{o}$, and θ_{ooo}^{o} – each in terms of truncated conditional probabilities of configurations with as many as six sites (*130*).

Through a procedure analogous to derivation of Eq. **5.12**, 1st-order rate equations may be constructed for any rate process involving mobile Langmuirian adsorbates. Tables D.1-D.2 and D.3-D.4 respectively provide the general 1st-order rate equations for (i) monomer and homogeneous dimer -sorption and (ii) heterogeneous two-site events (e.g. surface reactions such as $NH_2^* + H^* \rightarrow NH_{3(g)} + **$ and $N^* + H^* \rightarrow NH^* + *$). Table D.5 reports the 1st-order rate equations for adsorbate surface diffusion (e.g. $N^* + * \rightarrow * + N^*$) which is a two-site process that does not affect single-site coverages; and, consequently, cannot be described by the Langmuir-Hinshelwood formalism. The 1st-order formalism explicitly describes surface diffusion of each adsorbate by incorporation of unique rate terms for each multi-site ensemble – thereby accounting for the propensity of each diffusion event to ally isolated (disperse clustered) surface species.

From Tables D.1-D.5, the reader may construct a 1st-order model for any catalytic system of mobile Langmuirian adsorbates in which all elementary steps involve at most two sites. Case studies to follow will tabulate full 1st-order microkinetic models for particular reaction systems.

The rate equations in the 1st-order model are constrained by overall and component site balances, respectively

$$1 = \sum_{\substack{j=sit \\ occupants}} \theta_j \qquad \textbf{[5.14]}$$

and

$$\theta_i = \sum_{\substack{j=sit \\ occupants}} \theta_{ij} \qquad \textbf{[5.15]}$$

where indices *i* and *j* for site occupants include vacant sites, *o*. We refer to time derivatives of Eqs. **5.14**-**5.15** as rate balances

$$0 = \sum_{\substack{j=site \\ occupants}} \frac{d\theta_j}{dt} \qquad \textbf{[5.16]}$$

and

$$\frac{d\theta_i}{dt} = \sum_{\substack{j=sit \\ occupants}} \frac{d\theta_{ij}}{dt} \qquad \textbf{[5.17]}$$

The 1st-order rate equations, in conjunction with site (Eqs. **5.14**-**5.15**) and rate (Eqs. **5.16**-**5.17**) balances, constitute a kinetic description distinct to, yet in agreement with, kMC simulations; the ensemble-specificity of 1st-order rate terms is absent in kMC algorithms. The two methods nonetheless predict quantitatively similar results because of their respective analytical and computational capacity to explicitly count site-pair populations.

5.6 Degree of rate control, reaction order, and reversibility

We assess the kinetic descriptions of the Langmuir-Hinshelwood, 1st-order, and kMC methods by comparison of degrees of rate control, reaction orders, and reversibilities. We

note here that rate constants in definitions of kinetic descriptors in this section are intrinsic rate constants and do not include activities of fluid-phase species.

The kinetic degree of rate control, $X_{RC,i}$, of the transition state shared by steps *i* and *–i* , *TS,i*, is given by

$$X_{RC,i} = \left(\frac{\partial ln\, r}{\partial(-G^0_{TS,i}/k_B T)}\right)_{G^0_{TS,j\neq TS,i}} = \left(\frac{\partial ln\, r}{\partial\, ln\, k_i}\right)_{K_i, k_{j\neq i}} \quad \textbf{[5.18]}$$

where k_i is the forward rate constant of step *i*, K_i is the equilibrium constant of step *i* and $-G^0_{TS,i}$ is the standard free energy of the transition state in step *i* (*72*, *83–85*, *140–142*). The degree of rate control for a kinetically-irrelevant step is zero and the sum of all $X_{RC,i}$ is unity. Therefore, if there exists a single rate-determining step (rds), $X_{RC,rds} = 1$ and $X_{RC,i\neq rds} = 0$.

The reaction order of species *j*, given by

$$\Psi_j = \left(\frac{\partial ln\, r}{\partial ln\, a_j}\right)_{a_{k\neq j}} \quad \textbf{[5.19]}$$

is the fractional change in turnover rate per fractional change in the thermodynamic activity (ideally, partial pressure) of species *j*, a_j.

The reversibility of elementary step *i* in a fluid-phase reaction or in the Langmuir-Hinshelwood model is

$$z_i = \frac{r_{-i}}{r_i} \quad \textbf{[5.20]}$$

In a model of order greater than zero, however, the stoichiometric coefficient in the rate equation of step *i* for each species *j* is coverage-dependent and distinct (e.g. $d\theta_{oo}/dt = -k_{dd,ads}\theta_{oo} \times (1 + 6\theta_{oo}/\theta_o)$ for dimer adsorption). Therefore, there is not a single rate

expression assignable to step i or $-i$. We thusly define a reversibility of step i for each site configuration j retained by the truncation scheme

$$z_{i,[j]} = \frac{r_{-i,[j]}}{r_{i,[j]}} \quad \textbf{[5.21]}$$

Distinct $z_{i,[j]}$ calculable in higher-order truncation schemes provide physical insight obscured by the Langmuir-Hinshelwood formalism which only considers single-site configurations. Indeed, single-site configurations in schemes of any truncation order always have numeric, coverage-independent stoichiometric coefficients which confer identical reversibilities for all single-site configurations j^1 since $r_{-i,[j^1]}$ and $r_{i,[j^1]}$ are proportional to rates of the fundamental rate process (e.g. for dimer adsorption, $d\theta_o/dt = -4k_{dd,ads}\theta_{oo}$). We therefore equivalently refer to all $z_{i,[j^1]}$ as z_i since the definition of z_i in Eq. **5.20** is equal to $z_{i,[j^1]}$ for all j^1.

Ensemble-specific coverage-dependent stoichiometric coefficients also demand definition of ensemble-specific rate constants $k_{i,[j]}$, sensitivities $s_{i,[j]}$, and degrees of rate control $X_{RC,i,[j]}$ for each step i and ensemble j. We define reaction sensitivities, s_i, derive $s_{i,[j]}$ and $X_{RC,i,[j]}$, and discuss the relationship between $s_{i,[j]}$ and $z_{i,[j]}$ in Section D.1.

5.7 Results and Discussion

In the following, we present three case studies of catalytic reaction systems which exemplify the limitations of the Langmuir-Hinshelwood formalism and demonstrate the insight provided by the 1st-order model. Case Studies I-III respectively illustrate that (I) Langmuir-Hinshelwood description of simple catalytic reactions (i.e. $A + A \rightarrow A_2$) of immobile, thermodynamically-ideal adsorbates is inappropriate even if adsorption is equilibrated and the surface is essentially-bare, (II) the inaccuracies of the Hinshelwood assumption persist with moderate rates of kinetically-relevant surface diffusion and, as

expected, are rectified if diffusion is equilibrated with respect to all site ensembles and (III) the Langmuir-Hinshelwood formalism miscalculates degrees of rate control in the industrially-relevant ammonia synthesis reaction on Ru(0001) step sites because of an ignorance to islanding of N^* species which must be scavenged by kinetically-relevant N^* surface hydrogenation and diffusion.

5.7.1 Case Study I: Bimolecular catalytic reaction A + A → A_2 with immobile adsorbates

Let us return to the catalytic system presented in the introduction and summarized in Table 5.1.

Table 5.1: Bimolecular catalytic reaction

#	Step	Rate constants
1	$A_{(g)} + o \rightarrow a$	$k_{ads}{}^*$
–1	$a \rightarrow A_{(g)} + o$	k_{des}
2	$aa \rightarrow oo + A_{2(g)}$	k_r

k_{ads} is the product of the rate constant of adsorption and the thermodynamic activity (ideally, partial pressure) of $A_{(g)}$

Table 5.2 compares 0th-order and 1st-order rate equations which describe the $A + A \rightarrow A_2$ reaction summarized in Table 5.1. The rate equation for each elementary step with respect to each site configuration is the product of (i) the corresponding entry in the row labeled "Rate" and (ii) the corresponding entry in the ensemble-labeled row. For example, $(d\theta_{aa}/dt)_{des} = -2\theta_{aa}/\theta_a \times k_{des}\theta_a$ in the 1st-order formalism. In the Langmuir-Hinshelwood formalism, coverages of site pairs are set by the condition $\mu_{ij} = 1$ and therefore do not have unique rate equations or stoichiometric coefficients. The results to follow demonstrate that the inability of the Langmuir-Hinshelwood formalism to identify rate terms unique to each

multi-site ensemble results in miscalculated rates and reaction orders and misinterpretation of (quasi-)equilibrated $A_{(g)}$ adsorption.

Table 5.2: Rate equations in the 0th- and 1st-order

	Langmuir-Hinshelwood			**1st-order**		
Step	*ads.*	*des.*	*rxn.*	*adsorption*	*desorption*	*reaction*
Rate	$k_{ads}\theta_o$	$k_{des}\theta_a$	$k_r\theta_a^2$	$k_{ads}\theta_o$	$k_{des}\theta_a$	$k_r\theta_{aa}$
Ensemble-Specific Stoichiometric Coefficients						
$\boldsymbol{d\theta_a/dt}$	1	– 1	– 4	1	– 1	– 4
$\boldsymbol{d\theta_o/dt}$	– 1	1	4	– 1	1	4
$\boldsymbol{d\theta_{aa}/dt}$	No explicit rate equations. $\theta_{ij} = \theta_i\theta_j$			$2\theta_{ao}/\theta_o$	$-2\theta_{aa}/\theta_a$	$-(1 + 6\theta_{aa}/\theta_a)$
$\boldsymbol{d\theta_{ao}/dt}$				$(\theta_{oo} - \theta_{ao})/\theta_o$	$(\theta_{aa} - \theta_{ao})/\theta_a$	$3(\theta_{aa} - \theta_{ao})/\theta_a$
$\boldsymbol{d\theta_{oo}/dt}$				$-2\theta_{oo}/\theta_o$	$2\theta_{ao}/\theta_a$	$(1 + 6\theta_{ao}/\theta_a)$

Rate equations for each ensemble and each elementary step are constructed by product of the fundamental rate of the step (e.g. $k_{ads}\theta_o$ for $A_{(g)}$ adsorption) and the corresponding ensemble-specific stoichiometric coefficient (e.g. $2\theta_{ao}/\theta_o$ for *aa* for $A_{(g)}$ adsorption in the 1st-order). The Langmuir-Hinshelwood model is unable to describe dynamics of multi-site ensembles and therefore entries for *aa*, *ao*, and *oo* are absent.

In the Langmuir-Hinshelwood model, description of the $A + A \rightarrow A_2$ reaction requires summation and solution of -sorption and surface reaction rate equations for one of θ_o and θ_a – the other is algebraically fixed by overall site balance $\theta_o + \theta_a = 1$. We choose θ_a; using Table 5.2

$$\frac{d\theta_a}{dt} = k_{ads}\theta_o - k_{des}\theta_a - 4k_r\theta_a^2 \qquad \textbf{[5.22]}$$

The 1st-order formulation explicitly describes rate equations for five site configurations {*a*, *o*, *aa*, *ao*, *oo*} and is constrained by one overall site balance ($\theta_o + \theta_a = 1$) and two component site balances ($\theta_{oo} + \theta_{ao} = \theta_o$ and $\theta_{aa} + \theta_{ao} = \theta_a$). Therefore, we require summation and solution of -sorption and surface reaction rate equations for the 5 – 3 = 2 independent ensembles; we choose *aa* and *ao*. Using Table 5.2, the rate equations for *aa* and *ao* are

$$\frac{d\theta_{aa}}{dt} = k_{ads}\theta_o\left(\frac{2\theta_{ao}}{\theta_o}\right) - k_{des}\theta_a\left(\frac{2\theta_{aa}}{\theta_a}\right) - k_r\theta_{aa}\left(1 + \frac{6\theta_{aa}}{\theta_a}\right) \qquad \textbf{[5.23]}$$

$$\frac{d\theta_{ao}}{dt} = k_{ads}\theta_o\left(\frac{\theta_{oo}}{\theta_o} - \frac{\theta_{ao}}{\theta_o}\right) - k_{des}\theta_a\left(\frac{\theta_{ao}}{\theta_a} - \frac{\theta_{aa}}{\theta_a}\right) - k_r\theta_{aa}\left(\frac{3\theta_{ao}}{\theta_a} - \frac{3\theta_{aa}}{\theta_a}\right) \quad \textbf{[5.24]}$$

Eqs. **5.22** and **5.23-5.24** explicate the distinct rate terms which characterize the 0th- and 1st-order, namely, the coverage-dependent ensemble-specific stoichiometric coefficients required for Eqs. **5.23-5.24** which explicitly treat dynamics of multi-site ensembles.

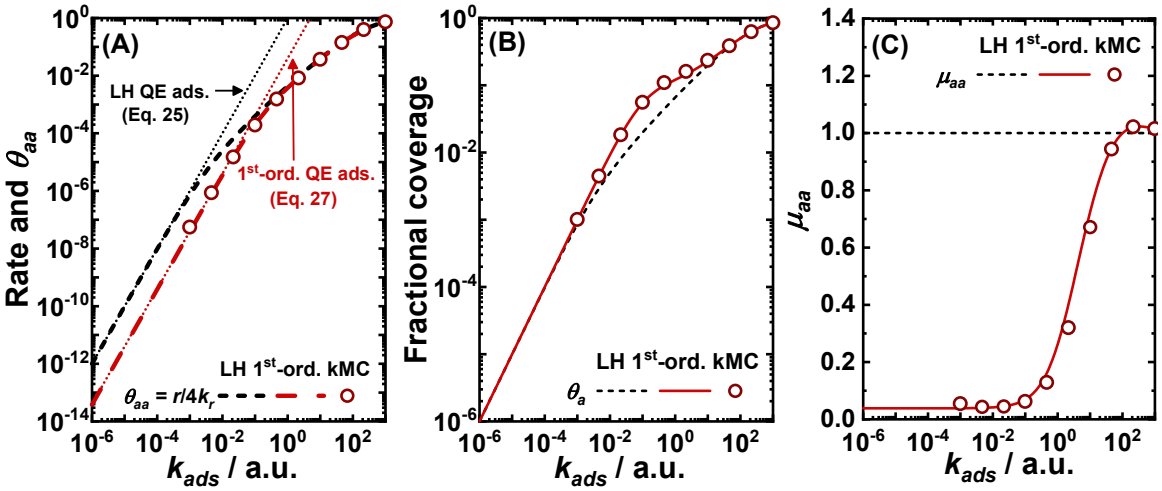

Figure 5.1: (A) Rate of $A_{2(g)}$ formation and fractional coverage of *aa* pairs ($\theta_{aa} = r/4k_r$) calculated by the Langmuir-Hinshelwood (- - -), 1st-order (— —), and kMC (o) methods and by closed-form, QE rate expressions per the Langmuir-Hinshelwood (Eq. **5.25**) (···) and 1st-order (Eq. **5.27**) (···) formalisms. (B) Fractional coverage of *a* species, θ_a, calculated by the Langmuir-Hinshelwood (- - -), 1st-order (—), and kMC (o) methods. (C) Mean-field metric μ_{aa} calculated by the Langmuir-Hinshelwood (- - -), 1st-order (—), and kMC (o) methods. Calculations are of the reaction network in Table 5.1 with rate constants $k_{des} = 1$, $k_r = 50$. Standard mean error bars for kMC simulation are smaller than corresponding symbols and are therefore not shown.

The steady-state rates and coverages for the 0th- and 1st-order models are solved in Matlab starting from a clean surface and forward integrating until all coverages are time-invariant. Results from the analytical models are compared to those of kinetic Monte Carlo simulations averaged over at least twenty simulations.

Figure 5.1 shows rates, coverages, and mean-field metrics calculated by the Langmuir-Hinshelwood (LH), 1st-order, and kMC methods for $k_{des} = 1$ and $k_r = 50$. All three models predict near-identical rates and coverages for $k_{ads} \geq 10$ since $\mu_{aa} \sim 1$ consistent with the

Hinshelwood assumption. Mean-field metrics calculated by the 1st-order model and kMC simulation agree for all k_{ads} and slightly exceed unity for k_{ads} = 50 – 100 due to (i) a small clustering of *aa* pairs resultant from irreversibility of $A_{(g)}$ adsorption and (ii) a balance in rate-control of adsorption and reaction – the combination of which limits the desorption process $aa \rightarrow ao$. For $k_{ads} \leq 10$, μ_{aa} deviates significantly from unity and asymptotically approaches ~0.038 as $k_{ads} \rightarrow 0$ and $\theta_a \rightarrow 0$.

In the 0th-order scheme, the inappropriate assumption that $\theta_{aa} = \theta_a^2$ both (i) increasingly overestimates the coverage of rapidly-scavenged *aa* pairs as $k_r/k_{ads} \rightarrow \infty$ and (ii) underestimates θ_a in the regime of large $|d\mu_{aa}/dk_{ads}|$ which engenders accumulation of *a* due to the scarcity of *a* neighbors with which to react. The coverage of *a* calculated by the three models converges for $k_{ads} \leq 10^{-4}$ due to equilibration of $A_{(g)}$ adsorption (Fig. 5.2(A)) which algebraically fixes $\theta_a = K_{ads}(1+K_{ads})^{-1}$ where $K_{ads} = k_{ads}/k_{des}$.

The Langmuir-Hinshelwood overestimation of $r = 4k_r\theta_{aa}$ by ~25× in the low *a* coverage regime ($\theta_a \sim K_{ads} < 10^{-3}$) and agreement with the 1st-order in the moderate-to-high *a* coverage regime ($\theta_a \gtrsim 0.1$) differentiates the catalytic consequences of (i) ensemble site effects (i.e. combinatorial non-idealities) and (ii) lateral adsorbate interactions (i.e. thermodynamic non-idealities). Adsorbate interactions are most consequential on high-coverage surfaces in which preponderant adsorbate-adsorbate pairs induce significant changes to elementary step activation energy barriers – as we show in Section D.2 (*33*, *35*). Contrarily, combinatorial non-idealities manifest profoundly on essentially-bare surfaces because disparate elementary steps rates and ensemble-site requirements tend to engender non-random distribution in low-coverage species which have greater configurational flexibility than high-coverage species (e.g. $\mu_{oo} = \theta_{oo}\theta_o^{-2} \approx 1 \times 1^{-2} = 1$ for $\theta_a < 10^{-3}$ and μ_{aa}

$= \theta_{aa}\theta_a^{-2} \approx 1 \times 1^{-2} = 1$ for $\theta_a \sim 1$ in this case study). Lateral interactions, of course, may be incorporated as an additional consideration in 1st-order descriptions of catalytic reactions proceeding through site ensembles; however, these thermodynamic non-idealities are a distinct, superimposed phenomena which only exacerbate existing combinatorial non-idealities inherent to ensemble-site catalysis (see Section D.2).

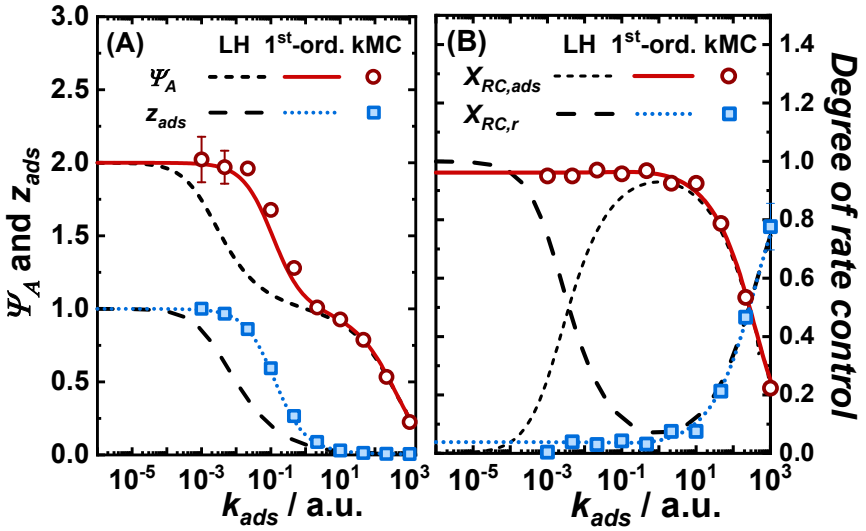

Figure 5.2: (A) $A_{(g)}$ reaction order and reversibility of $A_{(g)}$ adsorption (Ψ_A, z_{ads}) calculated by the Langmuir-Hinshelwood (- - -, – –), 1st-order (—, ···), and kMC (○, □) methods. (B) Degrees of rate control of adsorption and surface reaction ($X_{RC,ads}$, $X_{RC,r}$) calculated by the Langmuir-Hinshelwood (- - -, – –), 1st-order (—, ···), and kMC (○, □) methods. Calculations are of the reaction network in Table 5.1 with rate constants $k_{des} = 1$, $k_r = 50$. kMC error bars are the standard error of the mean (SEM) and are only shown if larger than the corresponding symbol.

Figure 5.2 shows reaction orders, degrees of rate control, and reversibilities calculated by analytical and kMC treatments. Reaction orders and degrees of rate control of the three methods are in agreement for $k_{ads} \geq 10$, the same conditions for which rates and coverages agree. The Langmuir-Hinshelwood model underestimates the reaction order in $A_{(g)}$, Ψ_A, by as much as 0.68 in the same regime wherein θ_a is underestimated because the Hinshelwood assumption is ignorant to the extent of $A_{(g)}$ adsorption required to replenish *aa* pairs for reaction. The consequences of neglecting site partitioning effects are manifest in the

degrees of rate control calculated by the 0th-order model compared to the 1st-order and kMC methods. As $k_{ads} \rightarrow 0$ and $\mu_{aa} \rightarrow 0.038$, the isolation of a species, undetected in the 0th-order, results in rate-determining adsorption of $A_{(g)}$, or $X_{RC,r} \sim 0$ and $X_{RC,ads} \sim 1$ (Fig. 5.2(B)).

The adsorption of $A_{(g)}$ equilibrates (i.e. $z_{ads} \rightarrow 1$ in Fig. 5.2(A)) for $k_{ads} \lesssim 10^{-3}$ in all three models, enabling accurate application of the quasi-equilibrium (QE) approximation. Conjunction of (quasi-)equilibrated adsorption and $\theta_a << 1$ (Fig. 5.1(B)) enables derivation of a simple closed-form Langmuir-Hinshelwood rate expression

$$r_{LH} = 4k_r K_{ads}^2 \qquad \textbf{[5.25]}$$

which agrees with the full Langmuir-Hinshelwood microkinetic model for $k_{ads} < 10^{-3}$ (see Fig. 5.1(A)). In the 1st-order model, however, application of the QE approximation for $A_{(g)}$ adsorption and recognition of $\theta_a << 1$ yields a distinct closed-form rate expression

$$r_{1st} = \frac{4k_r K_{ads}^2}{1 + \frac{k_r}{2k_{des}}} \qquad \textbf{[5.26]}$$

which we derive in detail in Section D.3. Eqs. **5.25** and **5.26** are identical if $k_r/2k_{des} << 1$; however, since $k_r/2k_{des} = 25 >> 1$ in this case study, Eq. **5.26** simplifies to

$$r_{1st} = 8k_{des} K_{ads}^2 = 8k_{ads} K_{ads} \qquad \textbf{[5.27]}$$

which agrees with the full 1st-order microkinetic model for $k_{ads} < 10^{-1}$ (see Fig. 5.1(A)), and, remarkably, does not contain the rate constant of surface reaction. Inspection of Eqs. **5.25** and **5.27** makes clear the disparate rate-determining steps identified by the Langmuir-Hinshelwood and 1st-order models, respectively. In Eq. **5.25** (Eq. **5.27**), k_r (k_{ads}) is the sole intrinsic rate constant and is linearly proportional to rate. Thusly, the Langmuir-Hinshelwood and 1st-order models respectively identify surface reaction and $A_{(g)}$ adsorption as rate-determining steps for $k_{ads} < 10^{-3}$ (Fig. 5.2(B)). We regard this result to

be highly counter-intuitive; prevailing kinetic understanding of chemical reactions suggests (quasi-)equilibrated steps cannot be rate-determining and, conversely, are kinetically-irrelevant. The ostensible paradox of a rate-determining, equilibrated step is resolved by inspection of ensemble-specific adsorption reversibilities identifiable in the 1st-order model, but impossible to calculate in the Langmuir-Hinshelwood model.

The ensemble-specific adsorption reversibilities of *aa*, *ao*, and *oo* are the ratios of respective desorption and adsorption rates in Table 5.2

$$z_{ads,[aa]} = \frac{r_{des,[aa]}}{r_{ads,[aa]}} = \frac{k_{des}\theta_{aa}}{k_{ads}\theta_{ao}} \quad \textbf{[5.28]}$$

$$z_{ads,[ao]} = \frac{r_{des,[ao]}}{r_{ads,[ao]}} = \frac{k_{des}(\theta_{ao} - \theta_{aa})}{k_{ads}(\theta_{oo} - \theta_{ao})} \quad \textbf{[5.29]}$$

$$z_{ads,[oo]} = \frac{r_{des,[oo]}}{r_{ads,[oo]}} = \frac{k_{des}\theta_{ao}}{k_{ads}\theta_{oo}} \quad \textbf{[5.30]}$$

and are shown in Fig. 5.3.

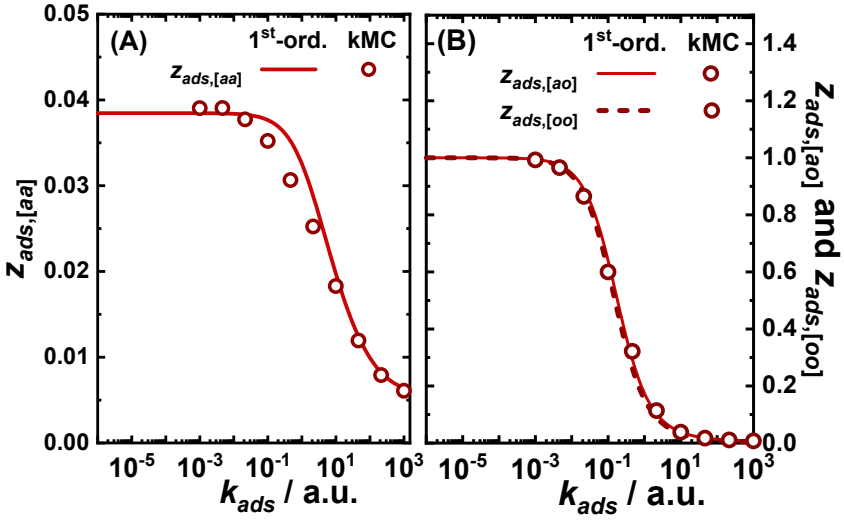

Figure 5.3: 1st-order- and kMC-calculated $A_{(g)}$ adsorption reversibility (—, o) for *aa* (A), *ao* and *oo* (B) site ensembles. kMC-calculated $z_{ads,[ao]}$ and $z_{ads,[oo]}$ are within error and are therefore shown with a single symbol (o). Calculations are of the reaction network in Table 5.1 with rate constants $k_{des} = 1$, $k_r = 50$. Standard mean error bars for kMC simulation are smaller than corresponding symbols and are therefore not shown.

Fig. 5.3 demonstrates that, although $A_{(g)}$ adsorption for *a*, *o*, *ao*, and *oo* is equilibrated for $k_{ads} \leq 10^{-3}$ in the 1st-order model, the adsorption process for *aa* is nearly irreversible (i.e. $z_{ads,[aa]} = 0.038$ as shown in (Fig. 5.3(A)). The irreversibility of adsorption for *aa* pairs is resultant from isolation of *a* species for $k_{ads} = 10^{-6}$–10^{-1}. In fact, we find that as $k_{ads} \rightarrow 0$, $z_{ads,[aa]} \rightarrow \mu_{aa}$. This equality becomes apparent from evaluation of Eq. **5.28** taking note that $z_{ads} = \mu_{ao} = 1$ for $k_{ads} \leq 10^{-4}$. Substituting coverages of site-pairs with mean-field metrics in Eq. **5.28** gives

$$z_{ads,[aa]} = \frac{k_{des}\theta_{aa}}{k_{ads}\theta_{ao}} = \frac{k_{des}\theta_a}{k_{ads}\theta_o} \cdot \frac{\theta_a}{\theta_a} \cdot \frac{\mu_{aa}}{\mu_{ao}} = z_{ads} \cdot \frac{\mu_{aa}}{\mu_{ao}} = \mu_{aa} = 0.038 \qquad \textbf{[5.31]}$$

as $k_{ads} \rightarrow 0$. The irreversibility of adsorption for the *aa* ensemble is thusly a direct consequence of the scarcity of *aa* pairs imperceptible in the Langmuir-Hinshelwood model and resolves the conundrum of a rate-determining, equilibrated step. The Langmuir-Hinshelwood model incorrectly asserts that the (quasi-)equilibrium of an elementary step with respect to single-site configurations (i.e. $z_{ads,[j^1]} = z_{ads} = 1$) guarantees the step is *entirely* equilibrated with respect to *all* site ensembles (*143*). In actuality, as the 1st-order model and kMC method correctly identify, each ensemble is described by a unique reversibility and only in the case that the reversibility with respect to each ensemble is unity can a step be identified as *entirely* (quasi-)equilibrated and, thusly, kinetically-irrelevant. In this example, $A_{(g)}$ adsorption is equilibrated with respect to all site ensembles except the reactive configuration *aa*, thereby allowing $A_{(g)}$ adsorption to be both equilibrated, in the sense that $z_{ads} = 1$, and rate-determining.

From this case study, we conclude that (quasi-)equilibrated adsorption is insufficient to guarantee validity of the Hinshelwood assumption. Mean-field metrics which deviate from unity by ~25× even for $z_{ads} = 1$ demonstrate that the QE condition cannot ensure use

of the Langmuir-Hinshelwood formalism is appropriate; the Hinshelwood assumption is accurate only if all adsorption steps are *entirely* equilibrated (i.e. $z_{ads,[j]} = 1$ for all site ensembles *j*) – as is guaranteed in the case of arbitrarily-fast surface diffusion (*143*). In the following, we introduce surface diffusion of *a* surface species to the $A + A \rightarrow A_2$ reaction to demonstrate that the Langmuir-Hinshelwood model (i) remains inaccurate for moderate diffusion rates and (ii) agrees exactly with the 1st-order and kMC methods if characteristic diffusion rates far exceed those of -sorption and reaction steps, as expected.

5.7.2 Case Study II: Bimolecular catalytic reaction A + A → A₂ with adsorbate surface diffusion

Adsorbate surface diffusion rates in catalytic surface reactions has been proposed as a kinetically-relevant consideration in CO oxidation (*126*, *142*, *144*) and methanation (*128*), ammonia decomposition (*145*), and NO reduction (*146*). Analytical description of surface diffusion steps require >0th-order formalisms which contain explicit rate equations for multi-site ensembles. To assess the importance of surface diffusion rates in determining rates, reaction orders, and degrees of rate control, we introduce diffusion of *a* species to the $2A_{(g)} \rightarrow A_{2(g)}$ reaction (Table 5.3).

Table 5.3: Bimolecular catalytic reaction with surface diffusion

#	Step	Rate constants
1	$A_{(g)} + o \rightarrow a$	k_{ads}^{*}
–1	$a \rightarrow A_{(g)} + o$	k_{des}
2	$aa \rightarrow oo + A_{2(g)}$	k_r
3	$ao \rightarrow oa$	k_{diff}

k_{ads} is the product of the rate constant of adsorption and the thermodynamic activity of $A_{(g)}$.

Table 5.4: Diffusion rate equations in the 0th- and 1st-order

	Langmuir-Hinshelwood	1st-order

Step	*diffusion* ($ao \rightarrow oa$)	
Rate	$k_{diff}\theta_a\theta_o$	$k_{diff}\theta_{ao}$
Ensemble-Specific Stoichiometric Coefficients		
$d\theta_a/dt$	0	0
$d\theta_o/dt$	0	0
$d\theta_{aa}/dt$	No explicit rate equations. $\theta_{ij} = \theta_i\theta_j$	$6(\theta_{ao}/\theta_o - \theta_{aa}/\theta_a)$
$d\theta_{ao}/dt$		$3(\theta_{aa} - \theta_{ao})/\theta_a + 3(\theta_{oo} - \theta_{ao})/\theta_o$
$d\theta_{oo}/dt$		$6(\theta_{ao}/\theta_a - \theta_{oo}/\theta_o)$

The rate equation for surface diffusion with respect to each site configuration is the product of (i) the corresponding entry in the row labeled "Rate" and (ii) the corresponding entry in the ensemble-labeled row. For example, $(d\theta_{aa}/dt)_{diff} = 6(\theta_{ao}/\theta_o - \theta_{aa}/\theta_a) \times k_{diff}\theta_{ao}$ in the 1st-order. The Langmuir-Hinshelwood model is unable to describe dynamics of multi-site ensembles and therefore entries for *aa*, *ao*, and *oo* are absent.

Table 5.4 compares 0th- and 1st-order rate equations for *a* diffusion. Since surface diffusion does not change the total coverage of any site-occupants, the Langmuir-Hinshelwood model contains no explicit description of surface reaction; rather, the Hinshelwood assumption implicitly assumes surface diffusion of all species is arbitrarily-fast, ensuring $\theta_{ij} = \theta_i\theta_j$. The 1st-order formalism is completed by addition of diffusion rate equations listed in Table 5.4 to those for -sorption and reaction listed in Table 5.2.

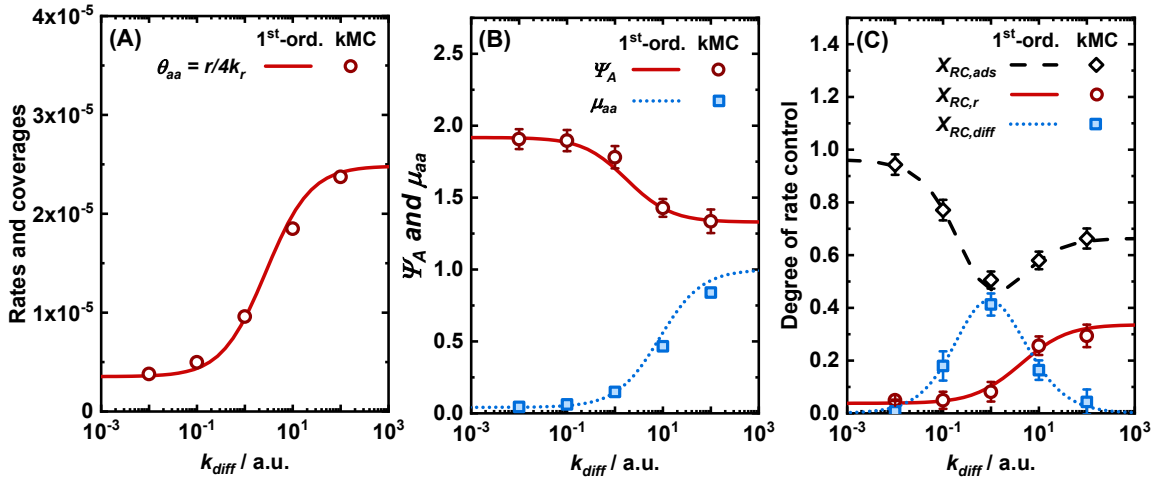

Figure 5.4: (A) Rate of $A_{2(g)}$ formation and fractional coverage of *aa* pairs ($\theta_{aa} = r/4k_r$) calculated by the 1st-order (—) and kMC (○) methods. (B) $A_{(g)}$ reaction order and mean-field metric of *aa* pairs (Ψ_A, μ_{aa}) calculated by the 1st-order (—, ···) and kMC (○, □) methods. (C) Degrees of rate control of adsorption, surface reaction, and surface diffusion calculated by the 1st-order (– –, —, ···) and kMC (◇, ○, □) methods. Calculations are of the

reaction network in Table 5.3 with rate constants $k_{ads} = 10^{-2}$, $k_{des} = 1$, $k_r = 50$. kMC error bars are the standard error of the mean (SEM) and are only shown if larger than the corresponding symbol.

Figure 5.4 shows rates, coverages, reaction orders, mean-field metrics, and degrees of rate control calculated by the 1st-order and kMC methods as a function of k_{diff} with $k_{des} = 1$ and $k_r = 50$, identically to Case Study I, and with $k_{ads} = 10^{-2}$ – at which condition the 1st-order and Langmuir-Hinshelwood models disagree significantly in the absence of surface diffusion (see Figs. 5.1 – 5.3). All kinetic descriptors calculated for $k_{diff} = 0$ ($k_{diff} \geq 10^3$) agree with 1st-order and kMC (Langmuir-Hinshelwood) results in the previous case study.

Figure 5.4(A) demonstrates that $r = 4k_r\theta_{aa}$ is a strong function of k_{diff}; larger diffusion rates ally previously-isolated *a* species, thereby increasing the coverage of *aa* pairs and the rate of their self-annihilation. $A_{2(g)}$ formation rates asymptotically approach the Langmuir-Hinshelwood limit as $k_{diff} \rightarrow \infty$ randomizes the surfaces to effect $\mu_{aa} \rightarrow 1$ (Fig. 5.4(B)). The sigmoidal increase of θ_{aa} and μ_{aa} as a function of k_{diff} demonstrates that surface diffusion only exerts significant rate control when k_{diff} is similar in magnitude to rate constants for -sorption and reaction (Fig. 5.4(C)). Indeed, the degree of rate control of surface reaction reaches a maximum value of ~0.4 for $k_{diff} \sim k_{des}$ because $A_{(g)}$ desorption is the only other mode of surface relaxation capable of randomizing the surface and increasing μ_{aa} – evinced by agreement of Eqs. **5.25** and **5.26** for $k_{des} >> k_r$ even if adsorbates are immobile.

In the same regime that surface diffusion is kinetically-relevant, the reaction order in $A_{(g)}$, Ψ_A, and the rate-control of $A_{(g)}$ adsorption, $X_{RC,ads}$, decrease since $A_{(g)}$ adsorption is no longer the only process actively generating *aa* pairs. Similarly to all other kinetic descriptors, Ψ_A and $X_{RC,ads}$ plateau as $X_{RC,diff} \rightarrow 0$ for sufficiently large k_{diff}. The waning influence of surface diffusion for $k_{diff} \gtrsim k_r$ is qualitatively attributed to diffusion rates being 'infinitely-fast' (*126*, *142*) – a condition which we contend requires quantitative evaluation.

To this end, we derive ensemble-specific reversibilities for surface diffusion which, just as for any other elementary step, must all equal unity to affirm the infinitely-fast nature of diffusion relative to all other steps.

The two-site diffusion rate equations listed in Table 5.4 proffer a means to define ensemble-specific reversibilities of surface diffusion based on the microscopically-reversible elementary diffusion steps which create and consume multi-site ensembles. For example the diffusion events which consume/produce *aa* pairs are all of the form

$$aoa \rightleftharpoons aao \qquad \textbf{[5.32]}$$

save for configurational variance. The elementary steps which produce and consume *aa* pairs are therefore the microscopic reverse of one another and occur with reversibility

$$z_{diff,[aa]} = \frac{\overleftarrow{r}_{diff,[aa]}}{\vec{r}_{diff,[aa]}} = \frac{k_{diff}\theta_{ao}\frac{\theta_{aa}}{\theta_a}}{k_{diff}\theta_{ao}\frac{\theta_{ao}}{\theta_o}} = \frac{\mu_{aa}}{\mu_{ao}} \qquad \textbf{[5.33]}$$

which explicitly demonstrates that all *a*-relevant mean-field metrics must be unity for surface diffusion to be equilibrated with respect to *aa* pairs. We note that μ_{aa} and μ_{ao} cannot be equal unless both are unity because component site balance constrains $\mu_{aa}\theta_a + \mu_{ao}\theta_o = 1$.

Eq. **5.33** provides a rigorous metric by which to evaluate the fidelity of surface diffusion to randomize the distribution of *aa* pairs. Indeed, diffusion is only considered arbitrarily-fast, or "entirely" equilibrated, in the case that $z_{diff,[j]} = 1$ for all site ensembles *j* (*143*). The diffusion reversibilities for the remaining ensembles *oo* and *ao* are the respective ratios of ensemble-specific elementary step consumption and production rates and are functions of mean-field metrics

$$z_{diff,[oo]} = \frac{\mu_{oo}}{\mu_{ao}} \quad \textbf{[5.34]}$$

$$z_{diff,[ao]} = \frac{\mu_{oo}\theta_o + \mu_{aa}\theta_a}{\mu_{ao}} \quad \textbf{[5.35]}$$

Eqs. **5.33**-**5.35** effectively quantify the rapidity of surface diffusion and tend to unity as the adsorbate distribution randomizes with increasing k_{diff}, as shown in Figure 5.5.

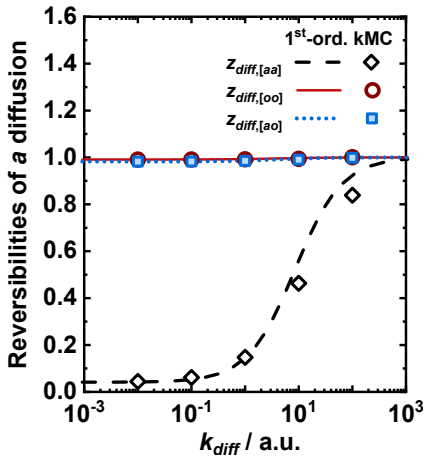

Figure 5.5: Surface diffusion reversibilities for *aa*, *oo*, and *ao* ensembles calculated by the 1st-order (– –, —, ···) and kMC (◇, ○, □) methods. Calculations are of the reaction network in Table 5.3 with rate constants $k_{ads} = 10^{-2}$, $k_{des} = 1$, $k_r = 50$. kMC error bars are the standard error of the mean (SEM) and are only shown if larger than the corresponding symbol.

The scarcity of *aa* pairs for $k_{diff} \lesssim 1$ is manifest in $z_{diff,[aa]}$ which is the only diffusion reversibility not equal to unity and quantifies the increase in diffusion rate necessary to achieve a random surface. The reversibility of diffusion with respect to *aa* pairs, $z_{diff,[aa]}$, thusly provides a compendious metric to evaluate the kinetic significance of surface diffusion; other kinetic descriptors such as the degree of rate control fail to recognize potential of increase in k_{diff} to unite isolated *a* species and enhance $A_{2(g)}$ formation rate (i.e. $X_{RC,diff} \sim 0$ for $k_{diff} < 10^{-2}$). The ensemble-specificity conferred by the 1st-order model is key to identifying synoptic kinetic descriptors such as $z_{diff,[aa]}$ and is necessary to capture combinatorial non-idealities conferred by elementary step ensemble site requirements.

The kinetic influence of thermodynamic non-idealities (e.g. adsorbate lateral interactions) may also be readily described by the 1st-order formalism and is profoundly affected by surface diffusion rates and reversibilities – as we intend to detail in a subsequent study; until such time, Section D.2 discusses and contains a simple demonstration of incorporating lateral interactions and surface diffusion in the 1st-order formalism. Briefly, explicit rate equations for multi-site ensembles prove critical for describing lateral interactions and provide an alternative to the heuristic use of linear coverage-dependent activation energy relations in microkinetic models. We stress that adsorbate interactions (i) are an additional non-ideal phenomenon distinct to combinatorial non-idealities, (ii) are most relevant in high coverage regimes, antithetically to clustering/isolation phenomena on bare surfaces described herein, and (iii) only exacerbate the inadequacies of the Langmuir-Hinshelwood model we redress by explicit counting of site-pair populations in the 1st-order formalism.

5.7.3 Case Study III: Ammonia synthesis on Ru (0001) step sites

The two case studies examined heretofore, although simple, typify the inadequacies of the Langmuir-Hinshelwood model and demonstrate the capacity of 1st-order terms to accurately describe kinetic consequences of site ensembles – as evidenced by quantitative agreement with kMC-calculated rates, selectivities, reaction orders, and degrees of rate control. We further demonstrate the critical significance of combinatorial non-idealities in catalysis of mobile Langmuirian adsorbates by examination of the industrially-relevant ammonia synthesis reaction (Table 5.5) using (i) DFT-calculated pre-exponential factors and activation energies reported by Logadóttir and Nørskov for reaction and -sorption steps (*147*) and (ii) DFT-calculated (*145*, *148*, *149*) and experimentally-measured (*32*, *149*, *150*) activation energies for surface diffusion of all adsorbed species. Pre-exponential factors for

diffusion are calculated to be similar to those for -sorption and reaction and are within an order of magnitude of experimentally-determined (*32*, *149*, *150*) and previously-calculated (*145*, *148*, *149*) values. All kinetic parameters are tabulated in Section D.5.

Table 5.5: Ammonia synthesis on Ru (0001) step sites

#	Step	Rate constants*
1	$N_{2(g)} + ** \rightleftharpoons 2N^*$	k_1, k_{-1}
2	$N^* + H^* \rightleftharpoons NH^* + *$	k_2, k_{-2}
3	$NH^* + H^* \rightleftharpoons NH_2^* + *$	k_3, k_{-3}
4	$NH_2^* + H^* \rightleftharpoons NH_3^* + *$	k_4, k_{-4}
5	$NH_3^* \rightleftharpoons NH_{3(g)} + *$	k_5, k_{-5}
6	$H_{2(g)} + ** \rightleftharpoons 2H^*$	k_6, k_{-6}

*Rate constants for ammonia synthesis are intrinsic rate constants and do not include activities of fluid-phase species. Diffusion steps are not shown and can be found in Table D.10.

Figure 5.6 shows select mean-field metrics, elementary step rates, and degrees of rate control calculated by the 0th- and 1st-order description at industrially-practiced NH_3 synthesis conditions: 200 bar, 20% N_2/60% H_2/20% NH_3, 623 K – 823 K. The well-known difficulty of activating N≡N triple bonds results in very low coverages of N^* ($\theta_{N*} = 10^{-6} – 10^{-5}$) and surface saturation by H adatoms ($\theta_{H*} = 0.93 – 0.99$), as shown in Fig. D.7(A). Similar to $\theta_a << 1$ enabling $\mu_{aa} << 1$ in Case Studies I and II, the very low coverages of N^* permit significant non-randomness in the distribution of N^*–N^* and N^*–NH^* pairs; Fig. 5.6(A) shows $\theta_{N*–N*}$ ($\theta_{N*–NH*}$) is 10^5 (10^2) times greater than θ_{N*}^2 ($\theta_{N*}\theta_{NH*}$) – demonstrating that surface diffusion can be kinetically-relevant even on covered surfaces ($\theta_* = 0.006 – 0.08$). Mean-field metrics $\mu_{N*–j*}$ for $j^* \neq \{N^*, NH^*\}$ are near-unity and identical, however, because N^* and NH^* are the only two sites which experience significant isolation or clustering; surface diffusion rates are sufficient to randomize the distribution of all other adsorbed species.

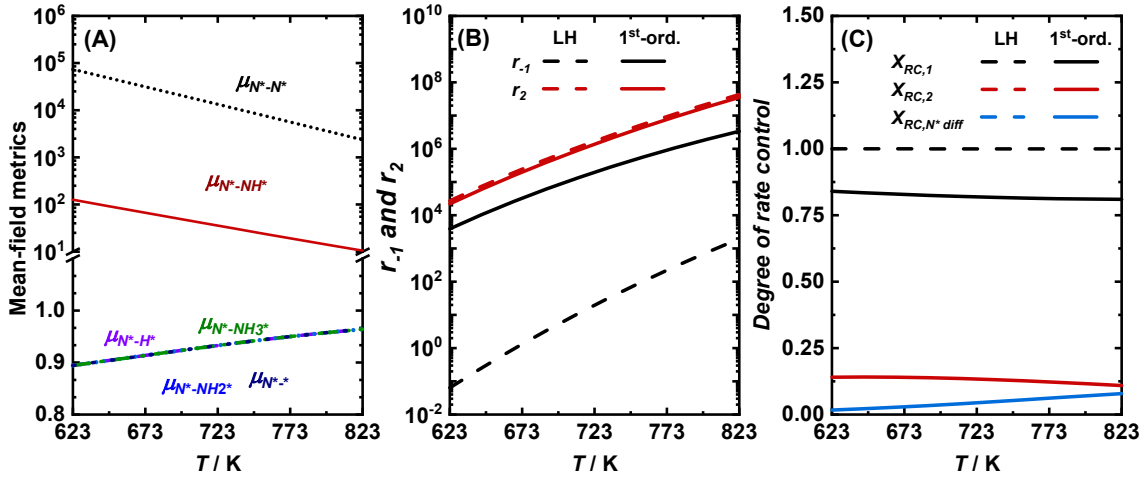

Figure 5.6: (A) Mean-field metrics $\mu_{N^*-j^*}$ calculated by the 1st-order model. All $\mu_{N^*-j^*} = 1$ by definition in the Langmuir-Hinshelwood model. (B) Directional elementary step rates r_{-1} and r_2 calculated by the Langmuir-Hinshelwood (– –) and 1st-order (—) models. (C) Degrees of rate control calculated by the Langmuir-Hinshelwood (– –) and 1st-order (—) models. X_{RC} only shown are if $|X_{RC}| > 10^{-2}$. $X_{RC,1} = 1$ in the Langmuir-Hinshelwood model and therefore no other X_{RC} are shown. Calculations are of the reaction network in Table 5.5 at 200 bar total pressure with composition 20% N_2/60% H_2/20% NH_3.

The significant clustering of N^*–N^* pairs results from the disparate combinatorially-ideal rates of recombinative $N_{2(g)}$ desorption and N^* hydrogenation – the only two steps besides N^* surface diffusion that can annihilate N^*–N^* pairs (Fig. 5.6(B)). On a random, uniform surface (i.e. in the Langmuir-Hinshelwood model), the rate of N^* hydrogenation, r_2, is 10^4-10^6 times faster than $N_{2(g)}$ desorption, r_{-1}, due to the high coverage of H^* ($\theta_{H^*}/\theta_{N^*} \sim 10^5$) and $k_2 \sim k_{-1}$. Quantitatively accounting for surface diffusion, however, the relative rapidity of N^* hydrogenation results in an accumulation of N^*–N^* pairs because annihilation by recombinative desorption or diffusion is prohibitively slow – thereby enhancing the $N_{2(g)}$ desorption rate relative to that on a uniform surface (Fig. 5.6(B)).

In essence, if surface diffusion is not arbitrarily-fast, the surface must counter-balance disparate production and consumption rates by clustering slowly consumed species (e.g. $\mu_{N^*-N^*} = 10^{3.5}$-10^5) and isolating rapidly consumed species (e.g. $\mu_{aa} = 0.038$ in Case Study I). The enhancement to r_{-1} due to N^*–N^* clustering effects orders of magnitude increase to

the reversibility of $N_{2(g)}$ adsorption (see SI Appendix, Fig. D.7(B)) and, consequently, decreases the kinetic degree of rate control $X_{RC,1}$ which is equal to unity in the Langmuir-Hinshelwood model (Fig. 5.6(C)) which incorrectly assumes N^* and NH^* diffusion to be infinitely-fast. In the 1st-order model, rate control shifts to N^* hydrogenation and surface diffusion which bear a kinetic burden to scavenge congregated N^* and initiate the rapid hydrogenation cascade from NH^* to $NH_3{}^*$.

5.8 Conclusion

The analytical kinetic description of mobile Langmuirian adsorbates by use of the Hinshelwood assumption is generally inappropriate and, as we demonstrate heretofore, results in erroneous (i) interpretation of (quasi-)equilibrium, (ii) calculation of rates and reaction orders, and (iii) identification of rate-determining steps. We present a higher-order kinetic theory which, by derivation of multi-site ensemble-specific rate terms, faithfully describes any catalytic surface reaction of mobile, thermodynamically-ideal adsorbates proceeding through two sites or fewer. The concepts we establish in derivation of 1st-order rate equations are robust to the inclusion of lateral adsorbate interactions and to retention of ≥2nd-order terms to describe catalytic reactions proceeding through three or more sites.

Consequences of ensemble site-requirements analytically described in this work are purported to be significant in reactions including alkane dehydrogenation and hydrogenolysis (*151–153*), alkene hydrogenation (*154*, *155*) and epoxidation (*156*, *157*), and NO decomposition (*158*, *159*) – all of which have been largely analyzed in the context of the Langmuir-Hinshelwood formalism. We contend accurate kinetic interpretation and microkinetic modeling of catalytic surface reactions such as these must quantitatively account for, or rationalize neglect of, combinatorial non-idealities – especially if surface

diffusion is not known to be facile and/or constituent elementary steps require large site ensembles.

5.9 Materials and Methods

All calculations were performed using Matlab code found at the link https://github.com/neilrazdan/RazdanBhan-SiteEnsembles or by communication with the authors. Briefly, kinetic Monte Carlo (kMC) simulations were performed on periodic 2D square lattices with time incremented in accordance with Poisson statistics for calculation of steady-state coverages and ensemble-specific rates. Steady-state kinetic descriptors of Langmuir-Hinshelwood and 1st-order formalisms were calculated using stiff ordinary differential equation solvers ode23s or ode15s in Matlab.

6 Catalytic site ensembles: A context to reexamine the Langmuir-Hinshelwood kinetic description

*Contents herein are reproduced with permission from Razdan, N. K., Bhan, A. Catalytic site ensembles: A context to reexamine the Langmuir-Hinshelwood kinetic description. *Journal of Catalysis*. **2021**, *404*, 726–744. https://doi.org/10.1016/j.jcat.2021.09.016.

6.1 Conspectus

The Langmuir-Hinshelwood formalism describes catalytic reactions of Langmuirian surface species under the assumption that all adsorbates are randomly-distributed – enabling adjacency of surface-bound intermediates to be determined solely by coverages of single-site occupants. We demonstrate herein that this approximation is inappropriate even for simple catalytic reactions (e.g. $A + A \rightarrow A_2$) and manifestly neglects islanding of slowly-consumed species and partitioning of highly-reactive species inherently engendered by ≥two-site elementary steps (e.g. $A^*–A^* \rightarrow A_{2(g)} + *–*$). Rigorous description of kinetically-consequential islanding/partitioning phenomena requires explicit description of the coverage and chemical dynamics of all multi-site ensembles. Higher-order, ensemble-specific rate terms identify the particular microscopic events relevant to each ensemble, and, in doing so, reveal that each elementary step (e.g. $A_{(g)}$ adsorption) describes not one event (e.g. $A_{(g)} + * \rightarrow A^*$) , but a sum over all ensemble-specific paths (e.g. $A_{(g)} + *–* \rightarrow A^*–*$ and $A_{(g)} + A^*–* \rightarrow A^*–A^*$). De-convoluting each elementary step into its constituent multi-site paths proffers kinetic detail otherwise inaccessible – enabling (i) identification of rate- and selectivity-determining site ensembles, (ii) calculation of rates and degrees of rate control of ensemble-specific elementary steps, (iii) incorporation of adsorbate surface diffusion, (iv) incorporation of lateral adsorbate interactions, and (v) quantitative description of catalysis of multi-site-occupying intermediates (e.g. $^*C_nH_m^*$ species in hydrocarbon (de-)hydrogenation and *C*-*C* bond coupling/cleavage reactions) which we

demonstrate is inaccessible to the Langmuir-Hinshelwood formalism even if adsorbate surface diffusion is infinitely-fast.

6.2 Introduction

Catalytic sequences on surfaces with elementary steps that require multiple sites (e.g. H_2 + *–* ⇌ H^*–H^*) are sensitive to the concentration and distribution of multi-site ensembles (e.g. *–* and H^*–H^*). Non-random adsorbate distribution, characterized by clustering or isolation of surface species, profoundly affects reaction kinetics and controls relative propagation of competing reaction paths proceeding through ensembles of disparate size and/or composition. Distinct ensemble site requirements of competing pathways has been leveraged to control selectivity in alkene epoxidation/oxidation (*157*, *160*), alkane (de-)hydrogenation/hydrogenolysis (*153*, *161*), and oxygenate dehydrogenation/dehydration (*162*) by judicious introduction of poisons or promoters which regulate the assembly of selectivity-determining ensembles. Pre-eminent mean-field kinetic models such as the Langmuir-Hinshelwood formalism have experimentally (*163*–*165*) and computationally (*29*, *126*, *128*) been demonstrated to be incapable of accurately describing such ensemble (i.e. geometric) effects due to an inability to explicitly enumerate populations of multi-site ensembles on which elementary steps occur. Miscounting of ensemble coverages consequents miscalculation of reaction rates, reaction orders, and degrees of rate control – resulting in a kinetic description unreliable for mechanistic interpretation (e.g. rationalization of observed reaction kinetics) or comparison with *ab initio* calculation of kinetic parameters (e.g. by DFT, density functional theory) (*126*, *128*, *166*).

This work is dedicated to description and explication of a mathematical framework which explicitly enumerates ensembles of any size, shape, and composition and, in doing

so, redresses the principal shortcoming of the Langmuir-Hinshelwood formalism. As a means of introduction to the mathematical treatment to follow, we first define the Langmuir-Hinshelwood kinetic description and detail the manner by which the method miscounts multi-site ensembles.

The Langmuir-Hinshelwood method describes catalytic surface reactions of adsorbed species obeying the conditions of the Langmuir theory of adsorption:

(I) The adsorbent/catalytic surface is a defect-free, flat 2D lattice

(II) Each site is either vacant or occupied by at most one adspecies

(III) Each site is energetically identical and adsorbates have no energetic interactions. We refer to this as the system being *thermodynamically-ideal*.

Provided all elementary steps require only a single catalytic site, no further conditions are required to construct an analytical kinetic description of sorption/reaction of Langmuirian surface species. Many catalytic reaction sequences, however, involve ≥two-site elementary steps such as dissociative adsorption ($H_2 + {*}–{*} \rightleftharpoons H^*–H^*$), the rate of which is determined by coverages of the requisite multi-site ensembles. The Langmuir-Hinshelwood formalism addresses this complication by application of the Hinshelwood approximation:

(IV) The spatial distribution of adsorbates is random (i.e. there are no spatial correlations between sites). We refer to this as the system being *combinatorially-ideal* or *configurationally-ideal*.

The utility of the Hinshelwood approximation is in reducing coverages of multi-site ensembles to a product of coverages of the constituent single-site occupants (*28*, *126*, *167*). That is to say, for example, that the fractional coverage of $H^*–H^*$ pairs, $\theta_{H*–H*}$, is assumed equal to θ_{H*}^2. This simplifying approximation is ubiquitous and foundational to catalytic

kinetic formalisms of Boudart and Djéga-Mariadassou (*168*), Hill (*169*), and Hougen and Watson (*170*) – all of which are modified variants or particular representations of the Langmuir-Hinshelwood kinetic description. The Hinshelwood approximation, however, evidently neglects the possibility of configurational biasing manifest as H^* islanding ($\theta_{H^*-H^*} > \theta_{H^*}^2$) or partitioning ($\theta_{H^*-H^*} < \theta_{H^*}^2$) which inherently accompanies any reaction sequence comprised of elementary steps requiring two or more sites, even in the absence of thermodynamic non-idealities (e.g. lateral adsorbate interactions) (*29*, *126*, *166*). The principal development of this work is to provide an analytical framework which improves upon the spatial myopia of the Hinshelwood approximation, enabling explicit retention of multi-site coverages such as $\theta_{H^*-H^*}$ as independent variables with unique, coverage-dependent elementary step rates.

The Langmuir-Hinshelwood kinetic formalism, and variants thereof (e.g. Langmuir-Hinshelwood-Hougen-Watson models (*170*)), do not retain terms such as $\theta_{H^*-H^*}$ and, consequently, are only reliable for description of catalytic reactions of Langmuirian adsorbates if adspecies surface diffusion is rapid compared to catalysis and thusly randomizes the adsorbate distribution – a condition which is not ensured by (quasi-)equilibration of sorption steps (*166*) and which is prohibited by the presence of multi-site occupying species (e.g. two-site occupying $^*C_2H_4^*$ in catalytic (de-)hydrogenation) as detailed in Case Study III herein. Accurate kinetic description of configurational non-idealities imperceptible to the Langmuir-Hinshelwood formalism requires relaxation of the Hinshelwood mean-field approximation (IV) to quantify the effect of adspecies islanding/partitioning phenomena on rates, selectivities, and elementary step activation energies.

We recently developed a formalism which explicitly describes dynamics of multi-site ensembles by inclusion of higher-order rate terms specific to each ensemble and each elementary step (*166*). Coverage-dependent, ensemble-specific rate terms reveal that each elementary step cannot be wholly described by a single rate expression, rate constant, and reversibility; instead, each multi-site ensemble is associated with a unique rate for each elementary step – the collection of which describes a distinct, ensemble-specific path from reactants to products. Remarkably, even single-site elementary steps require a unique kinetic description for each ensemble.

Consider, for example, the adsorption of gas-phase $A_{(g)}$ onto a vacant site

$$A_{(g)} + * \rightleftharpoons A^* \qquad \textbf{[6.1]}$$

The rate with respect to single-site ensembles follows directly from the law of mass action

$$r_{ads,[A^*]} = -r_{ads,[*]} = k_{ads} a_A \theta_* - k_{des} \theta_{A^*} \qquad \textbf{[6.2]}$$

where $r_{ads,[i]}$ is the rate of adsorption with respect to site occupant i, a_A is the thermodynamic activity of $A_{(g)}$, k_{ads} and k_{des} are the rate constants of adsorption and desorption, respectively, and θ_i is the fractional coverage of site occupant i. The rate with respect to site pairs, however, depends on the occupation of sites neighboring each adsorption center; A^*–A^* pairs, for example, are only generated by adsorption events such as $A_{(g)} + A^*$–$* \rightarrow A^*$–A^*, the rate of which is determined by the two-site fractional coverage θ_{A^*-*}. Quantitative definition of such two-site coverages, neglected in the Langmuir-Hinshelwood formalism, requires account of statistical factors pertaining to lattice coordination, c, and inherent two-site occupancy of site pairs

$$\theta_{ij} \equiv \frac{N_{ij}}{N_{pairs}} = \frac{N_{ij}}{N_{sites}\left(\frac{c}{2}\right)} \qquad \textbf{[6.3]}$$

where N_{ij} is the number of *ij* pairs, N_{pairs} is the total number of pairs, N_{sites} is the total number of sites, and $c = 4$ for a 2D square lattice. In comparison, definition of single-site coverages requires no consideration of lattice coordination (i.e. $\theta_i \equiv N_i/N_{sites}$).

We note that Eq. **6.3** follows the convention that heterogeneous ensembles are distinguishable and of equal population (*131–133*). That is to say *ij* and *ji* pairs are distinct, $\theta_{ij} = \theta_{ji}$, and $(\theta_{ij})_{max} = (\theta_{ji})_{max} = ½$. This convention is distinct from that of Boudart and Djéga-Mariadassou (*168*) and is chosen so that (i) $\theta_{ij} = \theta_{ji} = \theta_i\theta_j$ for a random adsorbate distribution and (ii) the *i* species balance is $\theta_i = \Sigma_j\, \theta_{ij}$. Boudart and Djéga-Mariadassou (*168*), Hougen and Watson (*170*), and Zhdanov (*34*) consider *ij* and *ji* pairs indistinguishable, giving (i) $\theta_{ij} = (2 - \delta_{ij}) \times \theta_i\theta_j$ for a random adsorbate distribution and (ii) species balance $\theta_i = \Sigma_j\, \theta_{ij} \times (2 - \delta_{ij})^{-1}$ where δ_{ij} is the Kronecker delta. As the mathematical treatment to follow will demonstrate, the convention distinguishing *ij* and *ji* pairs which we adopt – absent δ_{ij} terms – is particularly conducive for physical interpretation of the concentration, distribution, and kinetic relevance of homogeneous and heterogeneous ensembles alike.

Scheme 6.1 provides visualization of the definition of θ_{ij} in Eq. **6.3** by enumeration of all one- and two-site ensembles on a 3 × 3 square lattice with periodic boundaries. The visual aid identifies all $½c \times (3 \times 3) = 18$ site pairs and, in doing so, calculates $\theta_{A^*–A^*}$, $\theta_{*–*}$, and $\theta_{A^*–*} = \theta_{*–A^*}$ which do not conform to the generally unreliable Hinshelwood approximation. We encourage the reader to follow and/or reproduce enumeration of site ensembles in Scheme 6.1 to ensure the theory and results hereinafter are interpreted in the appropriate context.

Scheme 6.1: Illustrative enumeration of two-site ensembles

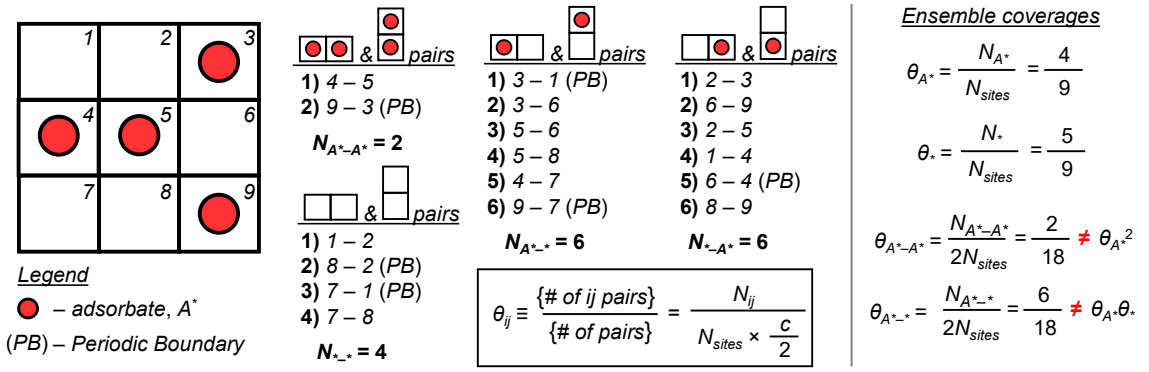

Lattice sites are either vacant, *, or occupied by adsorbate A^* (●). Each lattice site is numbered for identification of all 18 site pairs as A^*–A^*, A^*–*, *–A^* or *–*. The coordination number, c, is equal to 4 on a square lattice. Edge sites are subject to periodic boundaries such that sites *6* and *4*, for example, are considered nearest neighbors.

Definition of two-site ensemble coverages in hand, we derive ensemble-specific $A_{(g)}$ sorption rate equations with aid of Scheme 6.2 which illustrates enumeration of the sorptive configurations relevant to the population of each site pair. Consider, for example, the rate of adsorption with respect to the A^*–A^* ensemble, $r_{ads,[A^*-A^*]}$, shown in the second row of Scheme 6.2. Enumeration of the relevant sorptive configurations reveals that all sorption events which generate/eliminate A^*–A^* pairs are elementary steps of the form

$$A_{(g)} + A^* - * \rightleftharpoons A^* - A^* \qquad \textbf{[6.4]}$$

which, per the law of mass action, gives

$$r_{ads,[A^*-A^*]} = 2k_{ads}a_A\theta_{A^*-*} - 2k_{des}\theta_{A^*-A^*} \qquad \textbf{[6.5]}$$

where the statistical factor of '2' accounts for the two distinct adsorptive configurations, *–A^* and A^*–*, which can generate A^*–A^* pairs. Similarly, *–* pairs are generated by desorption from both *–A^* and A^*–* pairs, giving analogous statistical factors of '2'

$$r_{ads,[*-*]} = -2k_{ads}a_A\theta_{*-*} + 2k_{des}\theta_{A^*-*} \qquad \textbf{[6.6]}$$

because of the two mirror-image microscopically-reversible sorption events which generate/eliminate *–* pairs (see bottom row of Scheme 6.2). Sorption rate equations for the heterogeneous ensemble A^*–* are absent the statistical factor '2'

$$r_{ads,[A^*-*]} = k_{ads}a_A(\theta_{*-*} - \theta_{A^*-*}) - k_{des}(\theta_{A^*-*} - \theta_{A^*-A^*}) \qquad \textbf{[6.7]}$$

because creation/annihilation of the *–A^* pair is irrelevant with the convention of distinguishing *ij* and *ji* pairs. Explicit derivation of sorption rate equations for *–A^* pairs is unremunerative because *–A^* pairs are necessarily always equal in population to A^*–* pairs; therefore, throughout this text, we do not replicate rate equations for *ij* and *ji* pairs.

Scheme 6.2: Enumeration of two-site adsorption rate equations

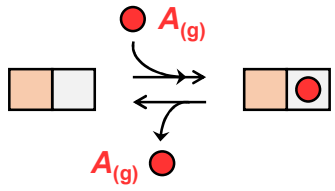

$$r_{ads} = k_{ads}a_A[\square] - k_{des}[\square]$$

$$r_{ads,[A^*-A^*]} = k_{ads}a_A[\square\square + \square\square] - k_{des}[\square\square + \square\square]$$

$$r_{ads,[A^*-*]} = k_{ads}a_A[\square\square - \square\square] - k_{des}[\square\square - \square\square]$$

$$r_{ads,[*-*]} = -k_{ads}a_A[\square\square + \square\square] + k_{des}[\square\square + \square\square]$$

Adsorption of $A_{(g)}$ (●) onto the vacant white lattice site (□) generates adsorbed A^* and creates/eliminates site pairs A^*–A^*, A^*–*, and *–* depending on the occupation of the neighboring lattice site (■).

Eqs. **6.5** – **6.7** explicate the provenance of multi-site ensemble-specific rates which enable description of non-idealities in adsorbate distribution inaccessible to the Langmuir-Hinshelwood formalism. We quantify configurational biasing effected by ensemble site requirements by calculation of the mean-field metric

$$\mu_{ij} \equiv \frac{\theta_{ij}}{\theta_i\theta_j} \qquad \textbf{[6.8]}$$

which is assumed unity in the Langmuir-Hinshelwood method. Deviations from $\mu_{ij} = 1$ quantify the inaccuracy of the Hinshelwood approximation and provide physical insight regarding the clustering and partitioning of each site pair. Similarly, $\mu_{ijk} \equiv \theta_{ijk}(\theta_i\theta_j\theta_k)^{-1}$ quantifies the aggregation and dispersion of three-site ensembles, and so on.

Intuitively, the clustering of one site pair must be counter-balanced by the partitioning of another. This constraint is quantitatively described by combination of overall and component site balances

$$1 = \sum_{\substack{j=site \\ occupants}} \theta_j \qquad \textbf{[6.9]}$$

and

$$\theta_i = \sum_{\substack{j=site \\ occupants}} \theta_{ij} \qquad \textbf{[6.10]}$$

where indices *i* and *j* for site occupants include vacant sites, *. Division of Eq. **6.10** by θ_i gives the mean-field metric balance

$$1 = \sum_{\substack{j=sit \\ occupant}} \mu_{ij}\theta_j \;\; \forall \;\; i \qquad \textbf{[6.11]}$$

which accounts for the necessary concomitance of adsorbate clustering and isolation (i.e. if $\mu_{ij} < 1$ then at least one $\mu_{ik} > 1$). We note that the particular form of the component and mean-field metric balances is predicated on the convention that heterogeneous pairs *ij* and *ji* are distinguishable and of equal population – as is discussed in Eq. **6.3** and Scheme 6.1. If heterogeneous pairs *ij* and *ji* are considered indistinguishable, then $(\theta_{ij})_{max} = 1$ and each term in the sum of Eq. **6.10** must adjoin the multiplicative term $(2 - \delta_{ij})^{-1}$. The chosen convention ensures $\mu_{ij} = 1$ implies combinatorial ideality regardless of homogeneity or heterogeneity of the considered ensemble.

In the absence of thermodynamic non-idealities, adsorbate clustering and isolation is caused by disparate elementary step rates and site-size requirements engendering (i) aggregation ($\mu_{ij} >> 1$) of slowly-consumed ensembles and (ii) partitioning ($\mu_{ij} << 1$) of

rapidly-consumed ensembles – resulting in a 'poorly-mixed' or 'transport-limited' surface. Adsorbate surface diffusion resolves rate-controlling 'transport limitations' by dispersing clustered species and allying highly-reactive, isolated species. In the limit of infinitely-fast surface diffusion (i.e. a reaction-limited, rather than transport-limited surface), adsorbate distribution randomizes and the Hinshelwood approximation becomes valid – save for catalytic surfaces populated by multi-site occupying adsorbates (e.g. $^{*}C_2H_4^{*}$) as discussed in Case Study III (*vide infra*).

Our recently developed formalism quantitatively accounts for the effect of surface diffusion to redress poor 'surface mixing' and identifies compendious kinetic descriptors inaccessible to the Langmuir-Hinshelwood formalism or lattice-based kinetic Monte Carlo (kMC) simulation. Retention of higher-order rate terms, analogous to those derived in Scheme 6.2, reveal each ensemble experiences a unique microscopically-reversible elementary diffusion event, analogous to the ensemble-specific elementary adsorption event in Eq. **6.4**. The ensemble-specificity with which each elementary step is described is key to the improvements of higher-order formalisms and enables quantitative identification of hitherto incognizable rate- and selectivity-determining ensembles, as in Case Study I (*vide infra*). The improved descriptive scope proffered by the higher-order formalism is robust to inclusion of lateral adsorbate interactions (see Section 6.5.2) and non-uniform site distributions (see Section 6.5.1) in both the rationalization of experimental rate data and the interpretation of *ab initio* calculation of kinetic parameters. In fact, we posit that DFT-generated reaction mechanisms are most appropriately studied either by lattice-based kMC simulation or by higher-order microkinetic models – both of which redress inability

of the Langmuir-Hinshelwood method to capture thermodynamic or combinatorial non-idealities.

In what follows, we (i) explicate higher-order descriptions of multi-site elementary steps, (ii) introduce established and novel kinetic descriptors useful for interpretation of catalytic reaction sequences, and (iii) present three case studies which highlight limitations of the Langmuir-Hinshelwood (i.e. zeroth order) formalism and the improved descriptive scope and depth of higher-order formalisms.

The ensemble-specific description of multi-site elementary steps is complicated by the inherent spatial coupling conferred by the reacting/sorbing/diffusing ensemble. Consider, for example, the reaction of two neighboring A^* species to form $A_{2(g)}$

$$A^* - A^* \rightarrow A_{2(g)} + * - * \qquad \textbf{[6.12]}$$

which occurs with rate

$$-r_{sr,[A^*]} = r_{sr,[*]} = c \cdot k_{sr}\theta_{A^*-A^*} = 4k_{sr}\theta_{A^*-A^*} \qquad \textbf{[6.13]}$$

where c is the coordination number and $c = 4$ on a square lattice. As Eq. **6.13** explicates, the involvement of multiple sites in the surface reaction step consequents a rate with respect to single-site ensembles which necessarily depends on coverages – and therefore rates – of larger ensembles (i.e. $\theta_{A^*-A^*}$). This complexity – absent in kinetic description of single-site elementary steps (see Eqs. **6.2**, **6.5** – **6.7**) – extends to rate equations for two-site ensembles; for example, the rate of surface reaction with respect to A^*-A^* pairs on a 2D square lattice is

$$-r_{sr,[A^*-A^*]} = k_{sr}\left[\theta_{A^*-A^*} + 2\theta_{A^*-A^*-A^*} + 4\theta_{\substack{A^*-A^* \\ | \\ A^*}}\right] \qquad \textbf{[6.14]}$$

which is in terms of three-site coverages, as illustrated in Scheme 6.3. The first term in Eq. **6.14** accounts for the annihilation of an A^*-A^* pair for each reaction event, and the second and third terms account for additional loss of A^*-A^* pairs if A^* species neighbor the reacting ensemble (e.g. orange (▢) and green (▢) A^*-occupied sites in Scheme 6.3). Evidently, the coupling of the reacting ensemble with neighboring sites results in coverage terms for ensembles larger than A^*-A^*. The rate equation for $\theta_{A*-A*-A*}$ similarly couples with ensembles of size four (e.g. $\theta_{A*-A*-A*-A*}$) and so on. The complete kinetic description of multi-site elementary steps is therefore an *infinite* set of hierarchical rate equations describing dynamics of ever-larger ensembles.

Scheme 6.3: Schematic derivation of ensemble-specific surface reaction rate for A^*-A^* pairs

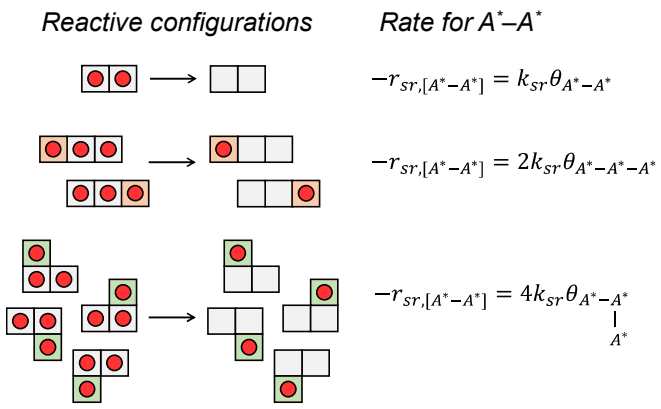

Surface reaction of two A^* species (●) occupying neighboring white lattice sites (□) eliminates site pairs A^*-A^* with ensemble-specific rate $r_{sr,[A^*-A^*]}$ enhanced by A^*-occupation of neighboring sites forming linear (▢) or bent (▢) three-site configurations.

The unbounded set of hierarchical rate equations is made finite and solvable by a mathematically-rigorous truncation procedure which retains only terms up to a specified order – analogously to the truncation of Taylor series expansions. The complete Taylor series expansion of e^x, for example, is an infinite series $e^x = \Sigma_n x^n/n!$ and is only exact in the limit $n \to \infty$. Retention of terms up to order one, however, (i.e. $e^x = 1 + x$) is, for $x << 1$,

sufficiently accurate and deemed the optimum balance of completeness and simplicity. In much the same way, the infinite hierarchy of rate equations is truncated to retain coverage terms up to a specified order – the appropriateness of which is determined by the shape and size of ensembles through which elementary steps proceed.

The truncation of hierarchical, ensemble-specific rate equations operates directly on ensemble site coverages and is detailed in our recent work (*166*). Briefly, truncation procedures of order *n* wholly retain coverages of ensembles wherein each constituent site is separated from every other constituent site by at most *n* lattice vectors. For example, Scheme 6.4 illustrates the A^*-covered ensembles wholly retained by the zeroth-, first-, and second-order formalisms. The zeroth-order formalism only explicitly describes ensembles in which all constituent sites are separated by zero lattice vectors – trivially, only single-site configurations – and, therefore, is exactly the Langmuir-Hinshelwood formalism. Coverages of multi-site ensembles cannot be completely described by the zeroth-order method and are thus reduced to a product of single-site coverages, as shown in Scheme 6.4(b). Similarly, the first-order formalism can only explicitly describe coverages of one- and two-site ensembles. Larger ensemble coverages – which are retained in the second order – must be reduced to a product/quotient of one- and two-site ensembles coverages, as shown in Scheme 6.4(b) and explicated in the following section.

Scheme 6.4: Comparison of zeroth, first, and second order formalisms

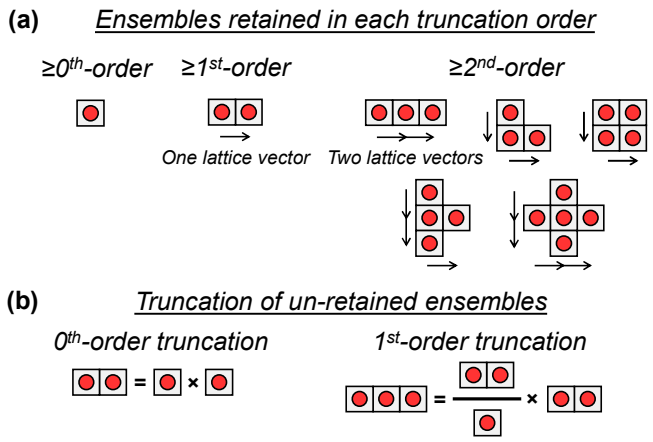

(a) A^*-covered ensembles on a 2D square lattice retained in each truncation order. For example, all truncation orders ≥1 retain ensembles of size two. Ensembles wholly retained by truncation orders ≥2 are composed of sites separated by at most two lattice vectors. (b) Ensembles not explicitly retained in a given order must be reduced to a product/quotient of retained ensembles. For example, in the zeroth-order, $\theta_{A^*\text{–}A^*} = \theta_{A^*} \times \theta_{A^*}$ and, in the first-order, $\theta_{A^*\text{–}A^*\text{–}A^*} = (\theta_{A^*\text{–}A^*}/\theta_{A^*}) \times \theta_{A^*\text{–}A^*}$.

In general, propriety of truncation order is determined by the number of lattice vectors needed to wholly retain all ensembles on which elementary steps occur. The first-order formalism is therefore sufficient to accurately describe all catalytic sequences occurring through at most two sites. The Langmuir-Hinshelwood, or zeroth-order, formalism, however, can only reliably describe catalytic sequences involving at most one site and is consequently inappropriate for description of two-site steps such as bimolecular surface reactions (e.g. $N^* + H^* \rightleftharpoons NH^* + *$) (*147*, *171*). Case Studies hereinafter compare zeroth-order, first-order, second-order, and kMC kinetic description of catalytic sequences proceeding through two or more sites to affirm invalidity of the Langmuir-Hinshelwood formalism and demonstrate quantitative accuracy and profound physical insight conferred by the ensemble-specificity of higher-order analytical descriptions.

6.3 Methods

6.3.1 Truncation of hierarchical rate equations

Coverages of ensembles too large to be retained in a specified order must be systematically truncated to a product/quotient of wholly retained ensembles. The

truncation procedure, formally detailed in the work of Nord and Evans (*131*, *132*, *137*), operates on conditional probabilities – which we regard best defined by example. Consider the conditional probability, $\chi_{A^*-\alpha^*}$, that a *conditioned* site is A^*-occupied given the neighboring *conditioning* site α^* is A^*-occupied with 100% probability

$$\chi_{A^*-\alpha^*} = \frac{\theta_{A^*-A^*}}{\theta_{A^*}} \qquad \textbf{[6.15]}$$

As Eq. **6.15** exemplifies, the conditional probability provides a rigorous relation between ensembles of disparate size and is therefore useful for the truncation of ensembles unwieldy in a particular order (e.g. A^*-A^* ensembles in the zeroth order). Conditional probabilities are truncated to order *n* by only retaining *conditioning* sites (e.g. α^*) within *n* lattice vectors of the *conditioned* site (e.g. A^*). Therefore, the zeroth-order truncation in Scheme 6.4(b) is rigorously derived as

$$\theta_{A^*-A^*} = \chi_{A^*-\alpha^*} \times \theta_{A^*} \xrightarrow{\substack{0^{th}\ order \\ truncation}} \chi_{A^*} \times \theta_{A^*} = \theta_{A^*} \times \theta_{A^*} \qquad \textbf{[6.16]}$$

where the zeroth order truncates $\chi_{A^*-\alpha^*}$ to $\chi_{A^*} = \theta_{A^*}$ because A^* and α^* are separated by more than zero lattice vectors. Similarly, the first order truncation in Scheme 6.4(b) is

$$\theta_{A^*-A^*-A^*} = \chi_{A^*-\alpha^*-\alpha^*} \times \theta_{A^*-A^*} \xrightarrow{\substack{1^{st}\ order \\ truncation}} \chi_{A^*-\alpha^*} \times \theta_{A^*-A^*} = \frac{\theta_{A^*-A^*}}{\theta_{A^*}} \times \theta_{A^*-A^*} \qquad \textbf{[6.17]}$$

where the first order truncates $\chi_{A^*-\alpha^*-\alpha^*}$ to $\chi_{A^*-\alpha^*} = \theta_{A^*-A^*}/\theta_{A^*}$ because A^* and the rightmost α^* are separated by more than one lattice vector. Ensemble-specific rate equations used in the Case Studies to follow are derived by (i) enumerating relevant ensembles as in Scheme 6.3 and Eq. **6.14** and (ii) truncating unwieldy ensembles by the procedure exemplified in Eqs. **6.16** and **6.17**. For example, Eq. **6.14** is truncated to the first order by re-writing in terms of conditional probabilities

$$r_{sr[A^*-A^*]} = -k_{sr}\theta_{A^*-A^*}\left[1 + 2\chi_{A^*-\alpha^*-\alpha^*} + 4\chi_{A^*-\substack{\alpha^* \\ | \\ \alpha^*}}\right] \quad \textbf{[6.18]}$$

and truncating as in Eq. **6.17** to give

$$\begin{aligned} r_{sr[A^*-A^*]} &= -k_{sr}\theta_{A^*-A^*}[1 + 2\chi_{A^*-\alpha^*} + 4\chi_{A^*-\alpha^*}] \\ &= k_{sr}\theta_{A^*-A^*} \times \left[-1 - 6\frac{\theta_{A^*-A^*}}{\theta_{A^*}}\right] \end{aligned} \quad \textbf{[6.19]}$$

The bracketed term is the ensemble-specific stoichiometric coefficient $\nu_{sr,[A^*-A^*]}$ and is reported in Table 6.2 and visualized in Scheme 6.5. Ensemble-specific elementary step rates are, in general, a product of the fundamental rate of the step (e.g. $k_{sr}\theta_{A^*-A^*}$) and the ensemble-specific stoichiometric coefficient (e.g. $\nu_{sr,[A^*-A^*]} = -[1 + 6\theta_{A^*-A^*}/\theta_{A^*}]$). Our recent work (*166*) derives and tabulates ensemble-specific first-order rate equations for all one- and two-site elementary steps including surface diffusion (e.g. $A^* + * \rightleftharpoons * + A^*$). Rigorous incorporation of lateral adsorbate interactions into ensemble-specific elementary step rates is detailed in Section 6.5.2 and, more thoroughly, in our recent work (*166*).

6.3.2 Definition of kinetic descriptors

We assess the kinetic descriptions of the Langmuir-Hinshelwood, first order, second order, and kMC methods by comparison of reactions orders, degrees of rate control, and degrees of selectivity control – all of which we calculate from reaction sensitivities, the salient descriptor of composite reactions (*72*, *84*, *140–142*, *172–174*).

The sensitivity of step *i* is the fractional change in turnover rate, *r*, per fractional change in rate constant k_i

$$s_i = \left(\frac{\partial \ln r}{\partial \ln k_i}\right)_{k_{j\neq i}} \quad \textbf{[6.20]}$$

The reaction order of a fluid phase species j, Ψ_j, quantifies the increment ($\Psi_j > 0$) or decrement ($\Psi_j < 0$) in rate achieved by increase of thermodynamic activity of species j, a_j, and is related to reaction sensitivities by

$$\Psi_j \equiv \left(\frac{\partial \ln r}{\partial \ln a_j}\right)_{a_{k\neq j}} = -\sum_{i=steps} s_i \nu_{ij} [\nu_{ij} < 0] \qquad \textbf{[6.21]}$$

where brackets in Eq. **6.21** are per Iverson Bracket notation, ν_{ij} is the stoichiometric coefficient of fluid phase species j in step i, and $[\nu_{ij} < 0]$ is unity if the enclosed inequality is true and zero if false (*140*, *172*).

The sum of the forward and reverse sensitivity of step i is the kinetic degree of rate control, $X_{RC,i}$, of the shared transition state, TS,i, given by

$$s_i + s_{-i} = X_{RC,i} = \left(\frac{\partial \ln r}{\partial(-G^0_{TS,i}/k_B T)}\right)_{G^0_{j\neq TS,i}} = \left(\frac{\partial \ln r}{\partial \ln k_i}\right)_{k_{j\neq i}, K_i} \qquad \textbf{[6.22]}$$

where $-G^0_{TS,i}$ is the standard free energy of the transition state in step i. Degrees of rate control are constrained by the condition

$$\sum_{i=steps} X_{RC,i} = 1 \qquad \textbf{[6.23]}$$

for each overall reaction. If there exists a single rate-determining step (rds), $X_{RC,rds} = 1$ and $X_{RC,i\neq rds} = 0$. In branched reaction networks, the degree of selectivity control is defined in terms of the selectivity, S, of a specified product

$$X_{SC,i} = \left(\frac{\partial \ln S}{\partial \ln k_i}\right)_{k_{j\neq i}, K_i} \qquad \textbf{[6.24]}$$

which is subject to the constraint $\Sigma_i X_{SC,i} = 0$ and, analogously to $X_{RC,i}$, is a sum of reaction *selectivity* sensitivities

$$X_{SC,i} = s_{Sel,i} + s_{Sel,-i} = \left(\frac{\partial \ln S}{\partial \ln k_i}\right)_{k_{j\neq i}} + \left(\frac{\partial \ln S}{\partial \ln k_{-i}}\right)_{k_{j\neq -i}} \quad \textbf{[6.25]}$$

Reaction/selectivity sensitivities and degrees of rate/selectivity control defined in Eqs. **6.20**, **6.21** – **6.25** are calculated from partial derivative of the rate or selectivity function with respect to elementary step rate constants at a given temperature and concentration(s); however, as Scheme 6.2 demonstrates, there is not a single rate – or, by extension, rate constant – assignable to each elementary step. Rather, each elementary step is described by a set of ensemble-specific rates which, for truncation orders greater than zero, are functionally distinct (i.e. depend on distinct ensemble coverages). Distinct ensemble-specific rates for each step i and ensemble j, $r_{i,[j]}$, are attended by distinct rate constants, $k_{i,[j]}$, and, therefore, distinct reaction sensitivity, $s_{i,[j]}$. Zeroth-order, or Langmuir-Hinshelwood, formalisms are ignorant to distinct ensemble-specific elementary step descriptors because consideration solely of single-site coverages effects ensemble-specific rates which are all functionally-equivalent and vary only by numeric stoichiometric coefficients. In higher-order formalisms, $s_{i,[j]}$ carry profound information regarding the kinetic influence of each ensemble; and, as we reported (*166*), sum to yield conventional reaction sensitivity defined in Eq. **6.20**

$$s_i = \sum_{\substack{j=independent \\ site\ ensembles}} s_{i,[j]} = \sum_j \left(\frac{\partial \ln r}{\partial \ln k_{i,[j]}}\right)_{k_{m,[n]\neq i,[j]}} \quad \textbf{[6.26]}$$

where j is an index over all independent site ensembles (i.e. those ensembles not relatable by site balances). Ensemble-specificity of reaction sensitivities confers ensemble-specificity of degrees of rate control

$$X_{RC,i} = \sum_j X_{RC,i,[j]} = \sum_j \left(\frac{\partial \ln r}{\partial \ln k_{i,[j]}} \right)_{k_{m,[n]\neq i,[j]}, K_{i,[j]}} \quad \textbf{[6.27]}$$

and degrees of selectivity control

$$X_{SC,i} = \sum_j X_{SC,i,[j]} = \sum_j \left(\frac{\partial \ln S}{\partial \ln k_{i,[j]}} \right)_{k_{m,[n]\neq i,[j]}, K_{i,[j]}} \quad \textbf{[6.28]}$$

If, for a given step, there exists a rate-determining ensemble (rde), then $X_{RC,i,[rde]} = X_{RC,i}$ and $X_{RC,i,[j\neq rde]} = 0$. Similarly, an ensemble, *sde*, is considered entirely responsible for the selectivity-control of a step if $X_{SC,i,[sde]} = X_{SC,i}$ and $X_{SC,i,[j\neq sde]} = 0$. In Case Study I to follow, ensemble-specific degrees of selectivity control, $X_{SC,i,[j]}$, will prove virtuous in explicating the inaccuracies of the Langmuir-Hinshelwood formalism and identifying the ensembles which prescribe selectivity between catalytic paths proceeding through ensembles of disparate size.

6.3.3 Kinetic Monte Carlo Simulation

Lattice-based kinetic Monte Carlo (kMC) simulation provides an exact stochastic-computational description of catalytic surface reactions under any specified conditions (e.g. Conditions (I)-(III)) and, therefore, serves as a useful reference by which to evaluate accuracy of the higher-order kinetic formalism detailed herein. As results to follow demonstrate, the higher-order formalism agrees quantitatively with all kMC-calculated kinetic descriptors at far less computational expense. We posit that, so long as the truncation order is sufficiently large (≈ size of largest reactive ensemble – 1), higher-order formalisms will concur with kMC simulation and provide physical information inaccessible to the non-analytical technique (e.g. ensemble-specific degrees of rate and selectivity control). We note that both kMC and higher-order methods are robust to inclusion of energetic adsorbate interactions and suggest kMC simulation may be preferred

if required truncation orders are prohibitively large (e.g. ≳4) and consequent unwieldy microkinetic models. The difficulties presented by magnitude of ≳4-order microkinetic models may be overcome by efficient computational-algorithmic generation of rate equations – a challenge we encourage readers to investigate.

We perform kMC simulation on square lattices of size $>128^2$ with periodic boundary conditions. In each iteration, the kMC algorithm selects, at random, an elementary step i to execute with probability p_i correspondent to elementary step rates determined by the law of mass action (e.g. $p_{sr} = k_{sr}\theta_{A*-A*}[\Sigma_j r_j]^{-1}$). The selected step is performed on an appropriate ensemble chosen at random, the lattice is updated, and the algorithm iterates. In this manner, the lattice-based kMC method is able to simulate catalytic reaction sequences with complete retention of spatial information. Provided the lattice is sufficiently large, populations of ensembles of arbitrary size, shape, and composition are exactly calculable by the square-lattice kMC algorithm.

After each Monte Carlo event, Poisson time is incremented by

$$\delta t = \frac{-\ln(\rho)}{\sum_j r_j} \qquad \textbf{[6.29]}$$

where the denominator is a sum over the rates of all elementary step processes and ρ is a uniformly-distributed random number between zero and unity. Poisson time is used to calculate steady-state overall and ensemble-specific elementary step rates for quantitative comparison to analytical kinetic descriptions.

Matlab code used to perform kinetic Monte Carlo simulations in this work may be found at the link https://github.com/neilrazdan/RazdanBhan-SiteEnsembles or by communication with the authors.

6.4 Results

We explicate the limitations and inaccuracies of the Langmuir-Hinshelwood formalism by comparison with first-order, second-order, and lattice-based kMC descriptions in the context of three conceptually-distinct case studies. Case Studies I-III respectively demonstrate that the Langmuir-Hinshelwood formalism (I) is unable to account for the propensity of multi-site ensembles to dictate selectivity, (II) cannot reliably calculate elementary step activation entropies and enthalpies, and (III) is incorrect even in the limit of infinitely-fast surface diffusion if adsorbates occupy more than one site (e.g. ${}^{*}C_nH_m{}^{*}$ in catalytic alkane hydrogenolysis).

6.4.1 Case Study I: A + A → A_2 with competitive Eley-Rideal pathway A + B → AB

The catalytic consequences of distinct ensemble site requirements on selectivity has been proposed as an important consideration in competitive alkane (de-)hydrogenation and hydrogenolysis (*153*, *175*, *176*), olefin epoxidation and combustion (*156*, *157*, *160*), and hydrodeoxygenation and hydrogenolysis (*177*, *178*). We examine the profundity of ensemble clustering/isolation in determining selectivity by comparing zeroth-order, first-order, and kMC description of competitive scavenging of immobile, thermodynamically-ideal adsorbed A^* species via (i) two-site surface reaction $A^*\text{–}A^* \rightarrow A_{2(g)} + *\text{–}*$ and (ii) one-site Eley-Rideal reaction $A^* + B_{(g)} \rightarrow AB_{(g)} + *$ (Table 6.1).

Table 6.1: Bimolecular catalytic reaction with competitive Eley-Rideal pathway

#	Step	Rate constants
1	$A_{(g)} + * \rightarrow A^*$	k_{ads} = 1 (bar · s)$^{-1}$
–1	$A^* \rightarrow A_{(g)} + *$	k_{des} = 1 s^{-1}
2	$A^* - A^* \rightarrow A_{2(g)} + * - *$	k_{sr} = 50 s^{-1}
3	$B_{(g)} + A^* \rightarrow AB_{(g)} + *$	k_{ER} = 1 (bar · s)$^{-1}$

We note Case Study I is an extension of an example presented in our recent work (*166*) which studies the $2A_{(g)} \rightarrow A_{2(g)}$ reaction described by steps 1, –1, and 2 in Table 6.1 to explicate the capacity of the first-order and kMC descriptions to correctly account for A^*–A^* partitioning (i.e. $\theta_{A^*-A^*} << \theta_{A^*}^2$) and identify $A_{(g)}$ sorption is *both equilibrated and rate-determining* – an apparent impossibility per the Langmuir-Hinshelwood formalism. The ostensible paradox of an equilibrated, rate-determining step is resolved by examination of ensemble-specific elementary step rates which reveal $A_{(g)}$ sorption is equilibrated in the sense $r_{des}/r_{ads} = 1$, but is irreversible with respect to scarce A^*–A^* pairs unperturbed by desorption of stranded A^* (i.e. $r_{des,[A^*-A^*]}/r_{ads,[A^*-A^*]} = 0$). We therefore surmise that $A_{(g)}$ sorption is not *entirely* equilibrated, permitting the step to be rate-determining and equilibrated in the canonical sense (i.e. $r_{des}/r_{ads} = 1$) (*166*).

The reaction sequence in Table 6.1 is described by the zeroth-order and first-order formalisms by respective one-site and ≤two-site ensemble-specific elementary-step rates reported in Table 6.2. The ensemble-specific rate of each elementary step is the product of (i) the fundamental rate of the step (e.g. $r_{des} = k_{des}\theta_{A^*}$ for $A_{(g)}$ desorption) and (ii) the appropriate ensemble-specific stoichiometric coefficient (e.g. $\nu_{des,[A^*-A^*]} = -2\theta_{A^*-A^*}/\theta_{A^*}$ in the first order) – as is illustrated in Scheme 6.5. The Hinshelwood approximation prohibits identification of two-site ensemble-specific stoichiometric coefficients; and, therefore, the Langmuir-Hinshelwood formalism contains no such entries in Table 6.2. Instead, the full zeroth-order microkinetic model only explicitly describes dynamics of single-site ensembles A^* and * by (i) use of overall site balance $\theta_* = 1 - \theta_{A^*}$ and (ii) forward integration of rate equation for A^* species

$$\frac{d\theta_{A^*}}{dt} = k_{ads}P_A\theta_* - k_{des}\theta_{A^*} - 4k_{sr}\theta_{A^*}^2 - k_{ER}P_B\theta_{A^*} \qquad \textbf{[6.30]}$$

determined by use of ’-labeled entries in Table 6.2.

Table 6.2: Elementary step rates in the Langmuir-Hinshelwood and first-order formalisms

	Langmuir-Hinshelwood				**First-order**			
Step, *i*	*ads.*	*des.*	*rxn.*	*E-.R.*	*adsorption*	*desorption*	*reaction*	*Eley-Rideal*
Rate, r_i	$k_{ads}P_A\theta_*$	$k_{des}\theta_{A^*}$	$k_{sr}\theta_{A^*}^2$	$k_{ER}P_B\theta_{A^*}$	$k_{ads}P_A\theta_*$	$k_{des}\theta_{A^*}$	$k_{sr}\theta_{A^*-A^*}$	$k_{ER}P_B\theta_{A^*}$
***Ensemble-Specific Stoichiometric Coefficients*, $\nu_{i,[j]}$**								
$\nu_{i,[A^*]}$	1’	– 1’	– 4’	– 1’	1	– 1	– 4	– 1
$\nu_{i,[*]}$	– 1	1	4	1	– 1	1	4	1
$\nu_{i,[A^*-A^*]}$	No explicit rate equations. $\theta_{ij} = \theta_i\theta_j$				$\frac{2\theta_{A^*-*}}{\theta_*}''$	$-\frac{2\theta_{A^*-A^*}}{\theta_{A^*}}''$	-1 $-\frac{6\theta_{A^*-A^*}}{\theta_{A^*}}''$	$-\frac{2\theta_{A^*-A^*}}{\theta_{A^*}}''$
$\nu_{i,[A^*-*]}$					$\frac{\theta_{*-*} - \theta_{A^*-*}}{\theta_*}''$	$\frac{\theta_{A^*-A^*} - \theta_{A^*-*}}{\theta_{A^*}}''$	$\frac{3(\theta_{aa} - \theta_{ao})}{\theta_a}$	$\frac{\theta_{aa} - \theta_{ao}}{\theta_a}'''$
$\nu_{i,[*-*]}$					$-\frac{2\theta_{*-*}}{\theta_*}$	$\frac{2\theta_{A^*-*}}{\theta_{A^*}}$	$1 + \frac{6\theta_{A^*-*}}{\theta_{A^*}}$	$\frac{2\theta_{A^*-*}}{\theta_{A^*}}$
***Ensemble-Specific Elementary Step Rates*, $r_{i,[j]}$**								
$r_{i,[j]} = r_i \times \nu_{i,[j]}$								

The rate equation for an elementary step with respect to a particular site ensemble is the product of (i) the fundamental rate of the step in the row labeled ‘Rate, r_i’ and (ii) the ensemble-specific stoichiometric coefficient of the concerned ensemble. For example, in the first order, $r_{ER,[aa]} = r_{ER} \times \nu_{ER,[aa]} = k_{ER}P_B\theta_a \times (-2\theta_{aa}/\theta_a)$. ’-labeled, ’’-labeled, and ’’’-labeled entries respectively are used for derivation of Eqs. **6.30**, **6.31**, and **6.32**. The ’’-labeled entries are also visually derived in Scheme 6.5. First-order ensemble-specific stoichiometric coefficients for adsorption and desorption were derived in Eqs. **6.5 – 6.7** and illustrated in Scheme 6.2.

Scheme 6.5: Visualization of **Eq. 6.31** and ’’-labeled entries of **Table 6.2**

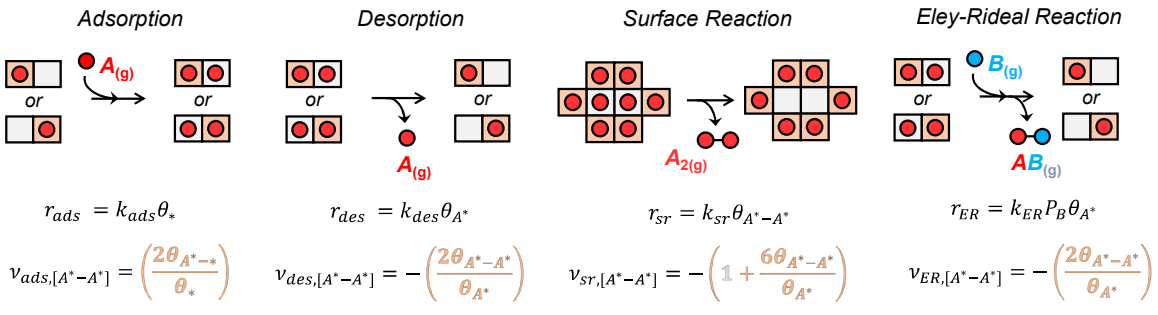

Visualization of $[A^*–A^*]$-specific rates reported in ’’-labeled entries of Table 6.2 and in Eq. **6.31**. The rate of each elementary step with respect to $A^*–A^*$ pairs is illustrated with white-colored sites (□) hosting the elementary step and orange-colored sites (□) spatially coupling to generate/consume $A^*–A^*$ pairs. The number of □-sites in illustration of each step corresponds to the numeric factor adjoining each ensemble-specific stoichiometric coefficient. For example, there are six □-sites neighboring the □□ pair hosting surface reaction

and, correspondingly, the stoichiometric coefficient $\nu_{r,[A^*–A^*]}$ contains a factor of '6'. The additional additive factor of unity accounts for the necessary reactive $A^*–A^*$ pair and is thusly shaded white rather than orange.

The first-order formalism wholly describes the dynamics of five ensembles {*, A^*, *–*, A^*–*, A^*–A^*}, coverages of which are constrained by one overall ($1 = \theta_* + \theta_{A^*}$) and two component ($\theta_j = \theta_{j–*} + \theta_{j–A^*}$ for j = *, A^*) site balances. The full first-order microkinetic model therefore requires 5 – 3 = 2 rate equations

$$\frac{d\theta_{A^*-A^*}}{dt} = 2k_{ads}P_A\theta_{A^*-*} - 2k_{des}\theta_{A^*-A^*} - k_{sr}\theta_{A^*-A^*}\left(1 + 6\frac{\theta_{A^*-A^*}}{\theta_{A^*}}\right) - 2k_{ER}P_B\theta_{A^*-A^*} \quad \textbf{[6.31]}$$

and

$$\frac{d\theta_{A^*-*}}{dt} = k_{ads}P_A(\theta_{*-*} - \theta_{A^*-*}) + k_{des}(\theta_{A^*-A^*} - \theta_{A^*-*}) + k_{sr}\theta_{A^*-A^*}\frac{3(\theta_{A^*-A^*} - \theta_{A^*-*})}{\theta_{A^*}} + k_{ER}P_B(\theta_{A^*-A^*} - \theta_{A^*-*}) \quad \textbf{[6.32]}$$

respectively determined by use of ''-labeled and '''-labeled entries in Table 6.2. Eqs. **6.31** and **6.32** exemplify the ensemble-specificity of the first-order formalism and kinetically describe the unique reaction paths experienced by each ensemble. For example, Scheme 6.5 illustrates the [A^*–A^*]-specific path described by Eq. **6.31** to aid visualization of the ensemble-specific spatial coupling responsible for each coverage-dependent stoichiometric coefficient $\nu_{i,[A^*–A^*]}$ for steps i = {*ads*, *des*, *sr*, *ER*}. As Scheme 6.5 depicts, surface reaction is capable of eliminating as many as seven A^*–A^* pairs per elementary step event (i.e. $[1 + 6\theta_{A^*–A^*}/\theta_{A^*}]_{max} = 7$) and, thusly, strands self-annihilating A^* species if $k_{sr} >> k_{i\neq sr}$ – as is the case per Table 6.1. Results to follow demonstrate that seclusion of A^* species unidentifiable in the Langmuir-Hinshelwood formalism is quantitatively accounted for by the first-order and kMC methods and manifests in preponderance of A^*–* pairs which selectively promote one-site Eley-Rideal reaction indifferent to the scarcity of A^*–A^*.

Preparatory to examination of Figs. 6.1 – 6.3, we encourage readers to replicate the ensemble-specific stoichiometric coefficients in Table 6.2 by construction and inspection of visual aids akin to Schemes 2, 3, and 5. Interpretation of results hereinafter is predicated on physical meaning and mathematical provenance of first-order rate terms derived hereinbefore.

Figure 6.1 shows coverages, selectivities, and mean-field metrics of the reaction system in Table 6.1 calculated by the Langmuir-Hinshelwood (LH), first-order, and kMC methods. First-order- and kMC-calculated descriptors quantitatively agree for $P_A = 10^{-3}$–10^{3} bar and all three models are in agreement for $P_A > 10$ bar; high $A_{(g)}$ pressures beget an A^*-covered surface (Fig. 6.1(A)), giving $\theta_{A^*-A^*} = \theta_{A^*} = \mu_{A^*-A^*} = 1$ (Fig. 6.1(C)) and 100% selectivity to $A_{2(g)}$ formation which benefits from high A^* coverages more profoundly than $AB_{(g)}$ formation (Fig. 6.1(B)).

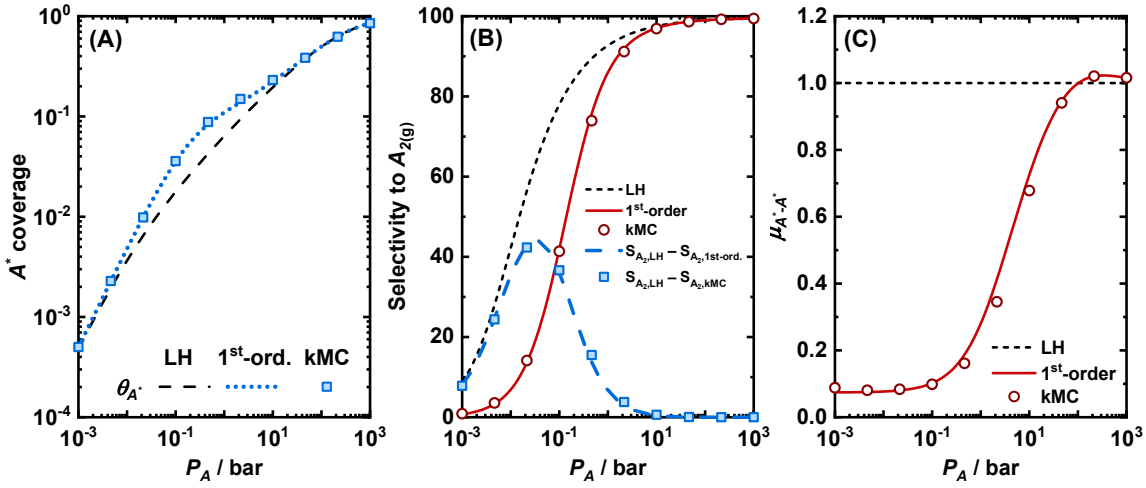

Figure 6.1: (A) Fractional coverage $\theta_{A^*} = R_{AB}(P_B k_{ER})^{-1}$ calculated by the Langmuir-Hinshelwood (– –), first-order (···), and kMC (□) methods. (B) Selectivity to $A_{2(g)}$ calculated by model j, $S_{A_2,j}$, calculated by the Langmuir-Hinshelwood (- - -), first-order (—), and kMC (○) methods. Differences in calculated selectivities $S_{A_2,LH} - S_{A_2,1^{st}\text{-}ord.}$ (– –) and $S_{A_2,LH} - S_{A_2,kMC}$ (□). (C) Mean-field metric $\mu_{A^*-A^*}$ calculated by the Langmuir-Hinshelwood (- - -), first-order (—), and kMC (○) methods. Calculations are of the reaction network in Table

6.1 with P_B = 1 bar. Standard mean error bars for kMC simulation are smaller than corresponding symbols and are therefore not shown.

Pressures of $A_{(g)}$ below 10 bar effect significant isolation of A^* species quantified by $\mu_{A^*-A^*} << 1$ with asymptotic approach of $\mu_{A^*-A^*} \rightarrow 0.1$ for $P_A \rightarrow 0$ (Fig. 6.1(C)). In the same regime for which the Langmuir-Hinshelwood model overestimates $\theta_{A^*-A^*}$ by ≤10×, A^* coverage is underestimated by as much as ~5× (Fig. 6.1(A); $P_A = 10^{-2}$–10^{1} bar). Although ostensibly antithetical, respective over- and under-prediction of $\theta_{A^*-A^*}$ and θ_{A^*} by the zeroth-order formalism both result from $k_{sr} >> k_{i\neq sr}$ which effects rapid annihilation of A^*–A^* pairs, thereby engendering isolation (i.e. $\mu_{A^*-A^*} << 1$) and accumulation (i.e. increment in θ_{A^*}) of A^* species due to the scarcity of A^* neighbors with which to react. As discussed heretofore and quantified by the mean-field metric balance in Eq. **6.11**, the segregation of A^*–A^* is necessarily attended by an accumulation of A^*–* pairs selective for the one-site Eley-Rideal reaction. Consequently, $A_{2(g)}$ selectivities are decremented relative to a uniform surface and are overestimated by the Langmuir-Hinshelwood model by as much as 45% (Fig. 6.1(B)). The inability of the zeroth-order formalism to capture isolation of A^* species prohibits quantitative description of selectivity-control exercised by the A^*–A^* and A^*–* ensembles which (i) necessarily aggregate and segregate in concert (Eq. **6.11**) and (ii) promote distinct reaction paths.

Figure 6.2 compares degrees of selectivity control calculated by the zeroth-order, first-order, and kMC methods to guide interpretation of pertinent kinetic information overlooked by the Hinshelwood approximation. $X_{SC,i}$ calculated by all three models converge to zero for large P_A because A^*-saturation of the surface attenuates selectivity control of all steps. Low $A_{(g)}$ pressures bare the surface (Fig. 6.1(A)), effecting asymptotic approach of all $X_{SC,i}$ as $P_A \rightarrow 0$. On bare surfaces, one-site $A_{(g)}$ sorption and Eley-Rideal

steps respectively promote and suppress $A_{2(g)}$ selectivity in both the zeroth and first order because of respective propensities of each step to generate and scavenge A^*–A^* pairs. The Langmuir-Hinshelwood formalism incorrectly identifies surface reaction as selectivity-determining ($X_{SC,sr}$ = 1) because of the miscalculated abundance of reactive A^*–A^* ensembles; in actuality, increase to k_{sr} exacerbates 'transport-limitations' which strand A^* and render surface reaction ineffective in improving selectivity ($X_{SC,sr} \sim 0$).

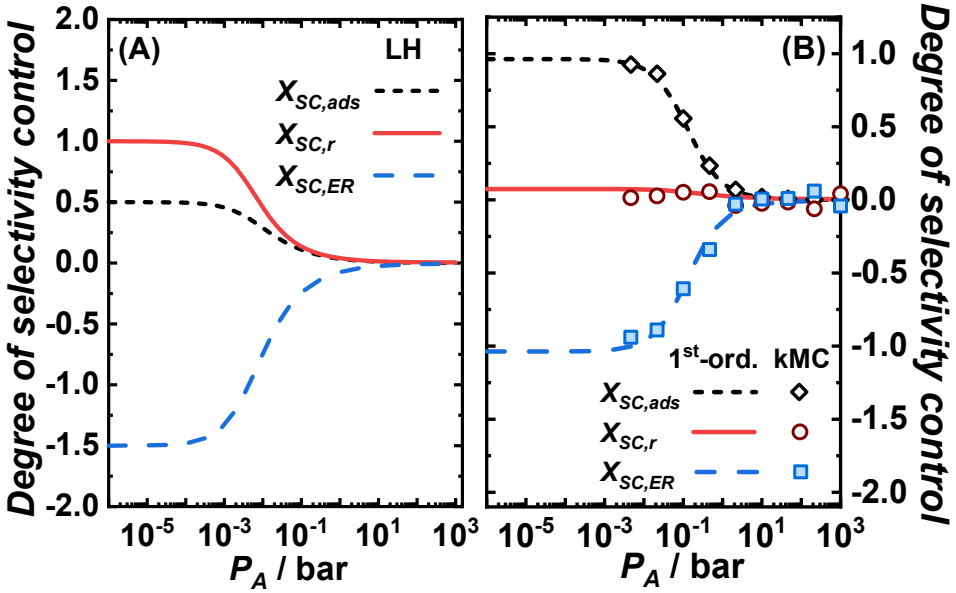

Figure 6.2: Degrees of selectivity control calculated by (A) the Langmuir-Hinshelwood formalism and (B) the first-order formalism and kMC method. Calculations are of the reaction network in Table 6.1 with P_B = 1 bar. Standard mean error bars for kMC simulation are smaller than corresponding symbols and are therefore not shown. X_{SC} are not calculated by the kMC method for $P_A \leq 10^{-3}$ because A^* coverages are prohibitively small for numerical differentiation.

The decrement in $X_{SC,sr}$ relative to a uniform surface is re-apportioned to increase in $X_{SC,ads}$ and $X_{SC,ER}$. The dearth of A^*–A^* pairs reinforces the kinetic burden on $A_{(g)}$ adsorption to generate reactive pairs and consequents $X_{SC,ads} = -X_{SC,ER} = 1$ from which we surmise the selectivity to $A_{2(g)}$ is entirely controlled by the competition between (i) adsorption which adjoins A^*–* ensembles with $A_{(g)}$ to create A^*–A^* pairs and (ii) Eley-Rideal reaction which scavenges A^*–* ensembles with $B_{(g)}$ to create $AB_{(g)}$. We quantitatively assess this

interpretation and the contribution of A^*–* and A^*–A^* ensembles to the selectivity control of each step by calculation of ensemble-specific $X_{SC,i,[j]}$ only identifiable in higher-order, analytical formalisms.

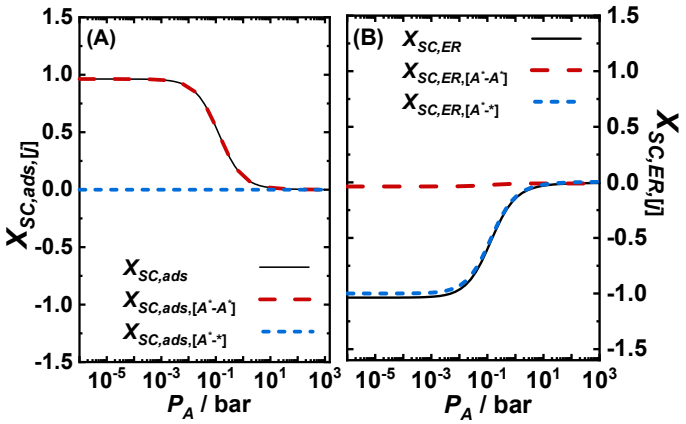

Figure 6.3: Ensemble-specific degrees of selectivity control for (A) adsorption of $A_{(g)}$ and (B) Eley-Rideal reaction. Calculations are of the reaction network in Table 6.1 with P_B = 1 bar. Ensemble-specific $k_{i,[j]}$ are not definable in the kMC method and, therefore, $X_{SC,i,[j]}$ cannot be calculated.

Figures 3(A) and 3(B) respectively show $X_{SC,ads,[j]}$ and $X_{SC,ER,[j]}$ for j = {A^*–*, A^*–A^*} calculated from application of Eq. **6.28** to the first-order microkinetic model, Eqs. **6.31-6.32**. Selectivity control of $A_{(g)}$ sorption and Eley-Rideal reaction are respectively entirely attributable to the creation of A^*–A^* ensembles and scavenging of A^*–* ensembles – evincing interpretation of $X_{SC,i}$ in Fig. 6.**2**. The elementary adsorption step ($A_{(g)}$ + A^*–* ⇌ A^*–A^*) occurs with rate $r_{ads,[A^*-A^*]} = 2k_{ads}P_A\theta_{A^*-*} - 2k_{des}\theta_{A^*-A^*} \approx 2k_{ads}P_A\theta_{A^*-*}$, as illustrated in Scheme 6.2, and is the only process capable of generating the requisite, rapidly self-annihilating A^*–A^* pairs. This kinetic burden on $A_{(g)}$ sorption to create exiguous A^*–A^* pairs is manifest in $X_{SC,ads} = X_{SC,ads,[A^*-A^*]} = 1$. The [$A^*$–*]-specific selectivity control of sorption is negligible because A^*–* constitute ≥97% of A^*–j pairs and are already produced by the majority of adsorption events since $\theta_{*-*} >> \theta_{A^*-*}$.

The preponderance of A^*–* is, however, largely responsible for the selectivity control of Eley-Rideal reaction. $AB_{(g)}$ formation occurs with rate $r_{ER} = k_{ER}P_B(\theta_{A^*-*} + \theta_{A^*-A^*}) \approx k_{ER}P_B\theta_{A^*-*}$ and is therefore most accelerated by A^*–* ensembles which outnumber A^*–A^* by ~10^4×. Accordingly, $|X_{SC,ER,[A^*-*]}| >> |X_{SC,ER,[A^*-A^*]}|$ and $X_{SC,ER,[A^*-*]} \approx X_{SC,ER}$. The ensemble-specificity of compendious kinetic descriptors such as $X_{SC,ER,[A^*-*]}$ are incalculable in the zeroth-order formalism or kMC method and quantitatively inform interpretation of ensemble site effects observed to dictate selectivity in catalytic reactions of industrial interest (*156*, *157*, *160*, *176*). We postulate that the limitations of the Hinshelwood approximation, bared herein, grow in significance with the size of elementary step ensembles and, therefore, particularly caution against the use of the Langmuir-Hinshelwood formalism for reactions proceeding through large catalytic site ensembles.

In the following example, we further explicate the unreliability of the Langmuir-Hinshelwood formalism for description of multi-site catalytic sequences by comparing intrinsic elementary step activation barriers calculated using zeroth- and first-order closed-form rate expressions.

6.4.2 Case Study II: Activation parameters of rate-determining steps in A + ½B_2 → AB

Chemical interpretation of rate-determining steps/transition states in catalytic reaction sequences is predicated on the determination of elementary step activation enthalpies, $\Delta H_{rds}^{0,\ddagger}$, and entropies, $\Delta S_{rds}^{0,\ddagger}$, to discern quantitative, molecular-level insight concerning the interactions which dictate reactivity. Calculation of $\Delta H_{rds}^{0,\ddagger}$ and $\Delta S_{rds}^{0,\ddagger}$ relies on fitting experimentally-measured kinetic data with mechanistically-based rate expressions which, to-date, have almost exclusively been derived using the Langmuir-Hinshelwood formalism. Examples include kinetic studies of catalytic alkane hydrogenolysis and

dehydrogenation (*153*, *163–165*, *175*), aldol condensation (*179*), methanol oxidative dehydrogenation (*180*), water gas shift (*140*, *173*), formic acid dehydrogenation (*162*), and methane reforming and oxidation (*181*, *182*) – all of which proceed through rate-determining steps occurring on two sites (e.g. rate-determining $CH_{4(g)} + *–O^* \rightarrow CH_3{}^*–OH^*$ in methane reforming). As we demonstrated previously (*166*) and explicate again herein, the Langmuir-Hinshelwood formalism cannot explicitly enumerate populations of two-site reactive ensembles (e.g. $*–O^*$ required to activate methane) and is therefore unreliable for identification of rate-determining steps and/or elementary step activation parameters – even if Langmuir-Hinshelwood rate expressions describe measured rate data quantitatively.

Table 6.3: Elementary steps and activation parameters of bimolecular catalytic surface reaction

#	Step	k_i(300 K)	$\Delta H_i^{0,\ddagger}$ kJ mol^{-1}	$\Delta S_i^{0,\ddagger}$ J mol^{-1} K^{-1}
1	$A_{(g)} + * \rightarrow A^*$	$k_{A,ads}$ = 1 (bar · s)$^{-1}$	36.1	–124.6
–1	$A^* \rightarrow A_{(g)} + *$	$k_{A,des}$ = 10^3 s^{-1}	65.0	29.3
2	$B_{2(g)} + * - * \rightarrow B^* - B^*$	$k_{B_2,ads}$= 1 (bar · s)$^{-1}$	36.1	–124.6
–2	$B^* - B^* \rightarrow B_{2(□)} + * - *$	$k_{B_2,des}$ = ½ · 10^4 s^{-1}	55.4	10.5
3	$A^* - B^* \rightarrow AB_{(g)} + * - *$	k_{sr} = ¼ · 10^5 s^{-1}	45.7	–8.3

Consider the bimolecular catalytic reaction $A + ½B_2 \rightarrow AB$ transpiring through the series of elementary steps in Table 6.3 wherein all adsorbed species are immobile. Two-site requirements for $B_{2(g)}$ sorption and $A^*–B^*$ surface reaction steps prohibit virtuous use of the Hinshelwood approximation and demand a first-order kinetic description to explicitly enumerate kinetically-relevant site pairs (e.g. *–* pairs required for and

eliminated by $B_{2(g)}$ adsorption). Tables 4(A) and 4(B) compare elementary steps rates for select ensembles in the zeroth-order and first-order formalisms, respectively.

Table 6.4: Select rate equations in the (A) Langmuir-Hinshelwood (zeroth-order) formalism and (B) first-order formalism

(A)

	Langmuir-Hinshelwood				
Step, *i*	$A_{(g)}$ *ads.*	$A_{(g)}$ *des.*	$B_{2(g)}$ *ads.*	$B_{2(g)}$ *des.*	*reaction*
Rate, r_i	$k_{A,ads}P_A\theta_*$	$k_{A,des}\theta_{A^*}$	$k_{B_2,ads}P_{B_2}\theta_*^2$	$k_{B_2,des}\theta_{B^*}^2$	$k_{sr}\theta_{A^*}\theta_{B^*}$
Ensemble-Specific Stoichiometric Coefficients					
$\boldsymbol{\nu_{i,[A^*]}}$	1	– 1	0	0	– 4
$\boldsymbol{\nu_{i,[*]}}$	– 1	1	– 4	4	8
$\boldsymbol{\nu_{i,[A^*-A^*]}}$	No explicit rate equations. $\theta_{ij} = \theta_i\theta_j$				
$\boldsymbol{\nu_{i,[A^*-*]}}$					
$\boldsymbol{\nu_{i,[A^*-B^*]}}$					

The rate equation for an elementary step with respect to a particular site ensemble is the product of (i) the fundamental rate of the step in the row labeled 'Rate, r_i' and (ii) the ensemble-specific stoichiometric coefficient of the concerned ensemble. For example, $r_{A,ads,[A^*]} = r_{A,ads} \times \nu_{A,ads,[A^*]} = k_{A,ads}P_A\theta_* \times 1$.

(B)

	First-order				
Step, *i*	$A_{(g)}$ *ads.*	$A_{(g)}$ *des.*	$B_{2(g)}$ *ads.*	$B_{2(g)}$ *des.*	*reaction*
Rate, r_i	$k_{A,ads}P_A\theta_*$	$k_{A,des}\theta_{A^*}$	$k_{B_2,ads}P_{B_2}\theta_{*-*}$	$k_{B_2,des}\theta_{B^*-B^*}$	$k_{sr}\theta_{A^*-B^*}$
Ensemble-Specific Stoichiometric Coefficients					
$\boldsymbol{\nu_{i,[A^*]}}$	1	– 1	0	0	– 4
$\boldsymbol{\nu_{i,[*]}}$	– 1	1	– 4	4	8
$\boldsymbol{\nu_{i,[A^*-A^*]}}$	$\frac{2\theta_{A^*-*}}{\theta_*}$	$-\frac{2\theta_{A^*-A^*}}{\theta_{A^*}}$	0	0	$-\frac{6\theta_{A^*-A^*}}{\theta_{A^*}}$
$\boldsymbol{\nu_{i,[A^*-*]}}$	$\frac{\theta_{*-*}-\theta_{A^*-*}}{\theta_*}$	$\frac{\theta_{A^*-A^*}-\theta_{A^*-*}}{\theta_{A^*}}$	$-\frac{3\theta_{A^*-*}}{\theta_*}$	$\frac{3\theta_{A^*-B^*}}{\theta_{B^*}}$	$3\left(\frac{\theta_{A^*-A^*}-\theta_{A^*-*}}{\theta_{A^*}}+\frac{\theta_{A^*-B^*}}{\theta_{B^*}}\right)$
$\boldsymbol{\nu_{i,[A^*-B^*]}}$	$\frac{\theta_{B^*-*}}{\theta_*}$	$-\frac{\theta_{A^*-B^*}}{\theta_{A^*}}$	$\frac{3\theta_{A^*-*}}{\theta_*}$	$-\frac{3\theta_{A^*-B^*}}{\theta_{B^*}}$	$-1-3\left(\frac{\theta_{A^*-B^*}}{\theta_{A^*}}+\frac{\theta_{A^*-B^*}}{\theta_{B^*}}\right)$

The rate equation for an elementary step with respect to a particular site ensemble is the product of (i) the fundamental rate of the step in the row labeled 'Rate, r_i' and (ii) the ensemble-specific stoichiometric coefficient of the concerned ensemble. For example, $r_{A,ads,[A^*-B^*]} = r_{A,ads} \times \nu_{A,ads,[A^*-B^*]} = k_{A,ads}P_A\theta_* \times (\theta_{B^*-*}/\theta_*)$. Grey-shaded entries are used for derivation of Eq. **6.33**.

From Table 6.4, we derive zeroth- and first-order closed-form rate expressions for $AB_{(g)}$ formation under conditions

(I) $A_{(g)}$ and $B_{2(g)}$ sorption are equilibrated in the sense $r_{i,des}/r_{i,ads} = 1$

(II) The surface is bare in the sense $\theta_* = 1$, $\theta_{A*} << 1$, and $\theta_{B*} << 1$

to explicate zeroth- and first-order calculation of $\Delta H_{rds}^{0,\ddagger}$ and $\Delta S_{rds}^{0,\ddagger}$ from experimental rate data.

Per Condition (I), coverages of A^* and B^* are algebraically-determined by equilibrium constants $K_A \equiv k_{A,ads}/k_{A,des}$ and $K_{B_2} \equiv k_{B_2,ads}/k_{B_2,des}$. Condition (II) further simplifies calculation of A^* and B^* coverages by ensuring adsorption is non-competitive, giving $\theta_{A*} = K_A P_A$ and $\theta_{B*} = (K_{B_2} P_{B_2})^{1/2}$. The rate of $AB_{(g)}$ formation per the Langmuir-Hinshelwood formalism is therefore

$$R_{AB_{(g)},LH} = 4k_{sr}\theta_{A*}\theta_{B*} = 4k_{sr}K_A P_A \sqrt{K_{B_2} P_{B_2}} \qquad \textbf{[6.33]}$$

which, with knowledge of K_A and K_{B_2}, is used to determine k_{sr} by fit to experimental rate data which conform with reaction orders $\Psi_A = 1$ and $\Psi_{B_2} = 1/2$ – as shown in Figure 6.4.

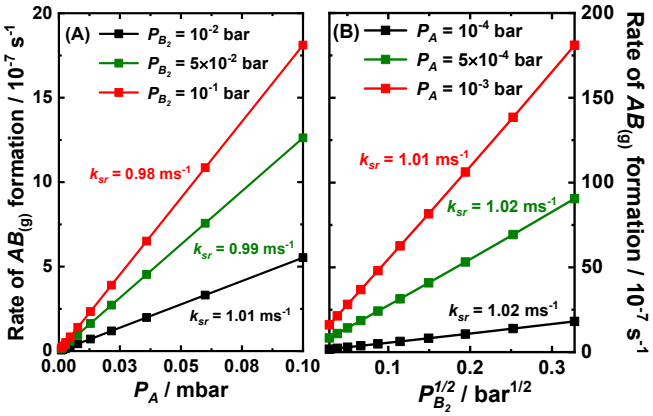

Figure 6.4: Rates of $AB_{(g)}$ formation calculated by the full first-order microkinetic model (■) as a function of (A) P_A and (B) $P_{B_2}^{1/2}$ at 300 K using kinetic parameters in Table 6.3. 'Rate data' determined by simulation of the full first-order microkinetic model are fit to the closed-form Langmuir-Hinshelwood rate expression in Eq. 6.33 to calculate $k_{rds} = k_{sr}$

$= 10^3\ s^{-1}$. In actuality, *rds* = *A*,*des*, giving $k_{rds} = k_{A,des} = 10^3\ s^{-1}$ per Eq. 6.43 and in agreement with Table 6.3.

Ex situ measurement of sorption equilibrium constants (e.g. by microcalorimetry (*183–185*) or temperature-programmed desorption (*186*)), leaves a single unknown kinetic parameter, k_{sr}, determined by linear fit of $R = [4K_A(K_{B_2}P_{B_2})^{½}] \times k_{sr}P_A$ and $R = [4K_AP_AK_{B_2}^{½}] \times k_{sr}P_{B_2}^{½}$ in Figs. 6.4(A) and 6.4(B), respectively. Quantitative fits in Fig. 6.4 calculate $k_{sr} = 10^3\ s^{-1}$, underestimating the rate constant of apparently rate-determining surface reaction by 25× (Table 6.3). Profound miscalculation of k_{sr} is entirely attributed to the erroneous Hinshelwood approximation $\theta_{A^*-B^*} = \theta_{A^*}\theta_{B^*}$ which obfuscates kinetic consequences of A^*–B^* isolation effected by rapid surface reaction. We redress ignorance to A^*–B^* partitioning by derivation of a closed-form, first-order correction to Eq. **6.33** which clarifies kinetic provenance of the particular combinatorial non-idealities which render the Langmuir-Hinshelwood formalism inappropriate.

The first-order correction to the Langmuir-Hinshelwood rate expression is simply the mean-field metric

$$\mu_{A^*-B^*} \equiv \frac{\theta_{A^*-B^*}}{\theta_{A^*}\theta_{B^*}} = \frac{4k_{sr}\theta_{A^*-B^*}}{4k_{sr}\theta_{A^*}\theta_{B^*}} = \frac{r_{1st}}{r_{LH}} \qquad \textbf{[6.34]}$$

which we derive in closed form by examination of the steady-state rate equation for A^*–B^* pairs

$$\begin{aligned}\frac{d\theta_{A^*-B^*}}{dt} = 0 = {} & k_{A,ads}P_A\theta_{B^*-*} - k_{A,des}\theta_{A^*-B^*} + 3k_{B_2,ads}P_{B_2}\theta_{*-*}\frac{\theta_{A^*-*}}{\theta_*} \\ & - 3k_{B_2,des}\theta_{B^*-B^*}\frac{\theta_{A^*-B^*}}{\theta_{B^*}} \\ & - k_{sr}\theta_{A^*-B^*}\left(1 + 3\frac{\theta_{A^*-B^*}}{\theta_{A^*}} + 3\frac{\theta_{\square^*-B^*}}{\theta_{B^*}}\right)\end{aligned} \qquad \textbf{[6.35]}$$

determined by the sum of elementary step rates with respect to A^*–B^* listed in the grey-shaded entries in Table 6.4(B). Conditions (I) and (II) permit simplification of Eq. **6.35** by ensuring mean-field metrics for pairs $ij \neq A^*$–B^* are very near unity.

Briefly, the preponderance of vacant sites and equilibration of sorption ensures all ensembles not dictating rates of disproportionally slow or fast steps are *essentially* randomly-distributed (i.e. $\mu_{ij\neq A^*-B^*}$ deviate negligibly from unity). We emphasize that no mean-field metric is exactly unity; partitioning of A^*–B^* pairs, to be demonstrated in the following, necessarily effects at least one $\mu_{ij\neq A^*-B^*} > 1$ which requires at least one $\mu_{ik\neq A^*-B^*} < 1$ and so on. The near-saturation coverage of vacant sites, however, minimizes requisite deviation from $\mu_{ij\neq A^*-B^*} = 1$ by ensuring weighting factors (θ_*, θ_{A^*}, θ_{B^*}) in the mean-field metric balance (Eq. **6.11**) are all either unity or very small. Consequently, rapidity of surface reaction effects $\mu_{A^*-B^*} << 1$ without appreciably disturbing combinatorially-ideal distribution of all other ensembles.

Application of Conditions (I) and (II) is therefore useful in re-expressing Eq. **6.35**

$$\begin{aligned}\frac{d\theta_{A^*-B^*}}{dt} = 0 = {} & k_{A,ads}P_A\theta_{B^*}\theta_* - k_{A,des}\theta_{A^*-B^*} + 3k_{B_2,ads}P_{B_2}\theta_*^2\theta_{A^*} \\ & - 3k_{B_2,des}\theta_{B^*}\theta_{A^*-B^*} \\ & - k_{sr}\theta_{A^*-B^*}(1 + 3\mu_{A^*-B^*}\theta_{B^*} + 3\mu_{A^*-B^*}\theta_{A^*})\end{aligned} \quad \textbf{[6.36]}$$

making use of unity mean-field metrics (i.e. $\mu_{B^*-B^*} = \mu_{B^*-*} = \mu_{*-*} = \mu_{A^*-*} = 1$) to yield quantitatively justifiable zeroth-order coverage terms. We emphasize $\mu_{A^*-B^*}$ cannot reliably be assumed unity because A^*–B^* pairs are the only ensemble dictating the rate of a non-equilibrated elementary step and self-annihilate ≤ 7× per irreversible surface reaction event (i.e. $\nu_{sr,[A^*-B^*]} = [1 + 3\theta_{A^*-B^*}/\theta_{A^*} + 3\theta_{A^*-B^*}/\theta_{B^*}] \leq 7$).

Eq. **6.36** is simplified by evoking Condition (II) to permit efface of redundant multiplicative and additive identities (i.e. $\theta_* = 1$, $\theta_{A^*} << 1$, and $\theta_{B^*} << 1$) to yield

$$\frac{d\theta_{A^*-B^*}}{dt} = 0 = k_{A,ads}P_A\theta_{B^*} - k_{A,des}\theta_{A^*-B^*} + 3k_{B_2,ads}P_{B_2}\theta_{A^*} - 3k_{B_2,des}\theta_{B^*}\theta_{A^*-B^*} - k_{sr}\theta_{A^*-B^*} \quad \textbf{[6.37]}$$

We now rearrange and solve for $\theta_{A^*-B^*}$

$$\theta_{A^*-B^*} = \frac{k_{A,ads}P_A\theta_{B^*} + 3k_{B_2,ads}P_{B_2}\theta_{A^*}}{k_{A,des} + 3k_{B_2,des}\theta_{B^*} + k_{sr}} \quad \textbf{[6.38]}$$

which, dividing numerator and denominator by $k_{B_2,des}$, is

$$\theta_{A^*-B^*} = \frac{\frac{k_{A,ads}P_A\theta_{B^*}}{k_{B_2,des}} + \frac{3k_{B_2,ads}P_{B_2}}{k_{B_2,des}}\theta_{A^*}}{\frac{k_{A,des}}{k_{B_2,des}} + 3\theta_{B^*} + \frac{k_{sr}}{k_{B_2,des}}} \quad \textbf{[6.39]}$$

Again evoking Conditions (I) and (II) and collecting terms gives

$$\theta_{A^*-B^*} = \frac{\theta_{A^*}\theta_{B^*}\left(\frac{k_{A,des}}{k_{B_2,des}} + 3\theta_{B^*}\right)}{\left(\frac{k_{A,des}}{k_{B_2,des}} + 3\theta_{B^*}\right) + \frac{k_{sr}}{k_{B_2,des}}} \quad \textbf{[6.40]}$$

Eq. **6.38** is the most general closed-form solution for $\theta_{A^*-B^*}$ under Conditions (I) and (II) and is only further simplified by recognizing that $3\theta_{B^*} << k_{A,des}/k_{B_2,des} \sim 1$ per Table 6.3, permitting accurate redaction to

$$\theta_{A^*-B^*} = \frac{\theta_{A^*}\theta_{B^*}}{1 + \frac{k_{sr}}{k_{A,des}}} \quad \textbf{[6.41]}$$

From re-arrangement of Eq. **6.41**, we see

$$\mu_{A^*-B^*} \equiv \frac{\theta_{A^*-B^*}}{\theta_{A^*}\theta_{B^*}} = \frac{1}{1 + \frac{k_{sr}}{k_{A,des}}} \quad \textbf{[6.42]}$$

indicating $k_{sr}/k_{A,des}$ is the salient parameter in determining the profundity of ensemble site-size effects under Conditions (I) and (II).

If $k_{sr} >> k_{A,des}$, A^*–B^* reaction out-competes sorption-mediated conveyance of A^* and effects a 'transport limited' surface. If $k_{sr} << k_{A,des}$, A^* desorption and re-adsorption provides a rapid means of A^*–B^* generation, precipitating a 'surface-reaction limited' catalytic rate and random adsorbate distribution. Table 6.3 confirms $k_{sr} >> k_{A,des}$ in this case study, from which we derive the remarkable result

$$R_{AB_{(g)},1st} = 4k_{A,des}K_A P_A \sqrt{K_{B_2} P_{B_2}} \qquad \textbf{[6.43]}$$

in which the rate constant of surface reaction does not appear and is replaced by $k_{A,des}$. Consequently, we surmise (i) $A_{(g)}$ adsorption is *both equilibrated and rate-determining* and (ii) the Langmuir-Hinshelwood formalism erroneously calculates elementary step activation parameters in accordance with the erroneous identification of surface reaction as the rate-determining step.

We explicate miscalculation of activation enthalpies and entropies in the following by fit of 'rate data' calculated by the full first-order microkinetic model with transition-state theory (TST) forms of closed-form expressions for rate

$$R_{AB_{(g)}} = \frac{4k_B T}{h} P_A \sqrt{P_{B_2}} e^{\frac{\Delta S^{0,\ddagger}_{app}}{k_B N_{Av}} - \frac{\Delta H^{0,\ddagger}_{app}}{k_B N_{Av}}\left(\frac{1}{T}\right)} \qquad \textbf{[6.44]}$$

where k_B and h are the Boltzmann and Planck constants respectively. Apparent activation parameters $\Delta S^{0,\ddagger}_{app}$ and $\Delta H^{0,\ddagger}_{app}$ are respectively

$$\Delta S^{0,\ddagger}_{app} = \Delta S^{0,\ddagger}_{rds} + \Delta S^{0}_{A,ads} + \frac{1}{2}\Delta S^{0}_{B_2,ads} \qquad \textbf{[6.45]}$$

and

$$\Delta H_{app}^{0,\ddagger} = \Delta H_{rds}^{0,\ddagger} + \Delta H_{A,ads}^{0} + \frac{1}{2}\Delta H_{B_2,ads}^{0} \quad \textbf{[6.46]}$$

and describe the thermodynamic driving forces dictating equilibrium between the most populous stable initial states (i.e. $A_{(g)}$ and $B_{2(g)}$) and the rate-controlling transition state. We note that the statistical factor '4' in Eq. **6.44**, correspondent to coordination of a square lattice, is easily forgotten in TST-formulation of reaction rates and is required to accurately quantify entropic changes from the initial to transition state.

From transition-state theory, the apparent equilibrium between the transition state and reactants can be quantified as

$$ln(K^{\ddagger}) = ln\left(\frac{a_{app}^{\ddagger}}{P_A\sqrt{P_{B_2}}}\right) \equiv \frac{\Delta S_{app}^{0,\ddagger}}{k_B N_{Av}} - \frac{\Delta H_{app}^{0,\ddagger}}{k_B N_{Av}}\left(\frac{1}{T}\right) = ln\left(\frac{R_{AB_{(g)}}}{\frac{4k_BT}{h}P_A\sqrt{P_{B_2}}}\right) \quad \textbf{[6.47]}$$

where $a^{\ddagger}$ is the thermodynamic activity of the apparent (i.e. rate-determining) transition state, activities of ideal gas-phase species $A_{(g)}$ and $B_{2(g)}$ are equal to partial pressures normalized by 1 bar, and N_{Av} is the Avogadro constant. Fit of zeroth-order (Eq. **6.33**) and first-order rate (Eq. **6.43**) expressions in the form of Eq. **6.47** determines $\Delta S_{rds}^{0,\ddagger}$ and $\Delta H_{rds}^{0,\ddagger}$ – provided standard state sorption enthalpies and entropies are measured *ex situ* (e.g. by microcalorimetry (*183–185*)) or are reliably calculated (e.g. by density functional theory (*185*)).

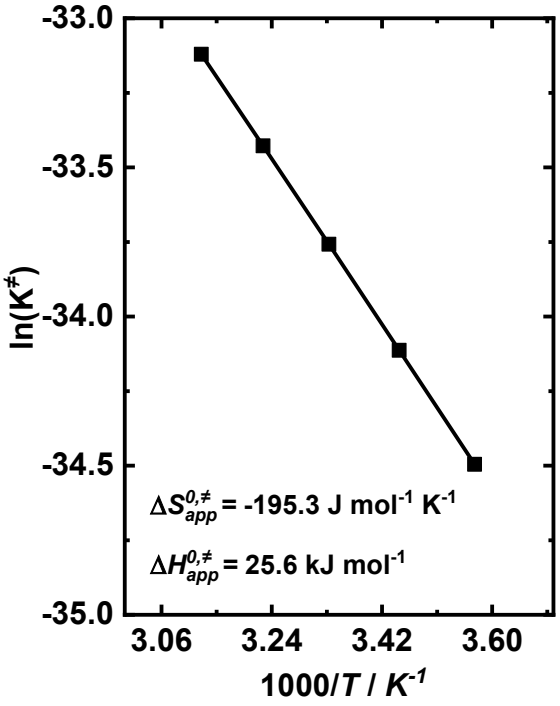

Figure 6.5: Apparent transition-state equilibrium constant, $K^{\ddagger}$, calculated by the full first-order microkinetic model method (■) as a function of T^{-1} for $P_A = 10^{-6}$ bar and $P_{B_2} = ½ \times 10^{-3}$ bar. 'Rate data' (■) are fit to Eq. 6.47 (—) to calculate apparent activation parameters $\Delta S_{app}^{0,\ddagger}$ and $\Delta H_{app}^{0,\ddagger}$.

Figure 6.5 shows $ln(K^{\ddagger})$ calculated by the full first-order microkinetic model and fit by Eq. **6.47** for T = 280 K – 320 K. Closed-form rate expressions in the zeroth order (Eq. **6.33**) and first order (Eq. **6.43**) are identical, save for respective linearity with respect to k_{sr} and $k_{A,des}$, and, therefore, both formalisms calculate, per Eqs. **6.45-6.46**, $\Delta S_{rds}^{0,\ddagger}$ = 26.2 J mol^{-1} K^{-1} and $\Delta H_{rds}^{0,\ddagger}$ = 64.2 kJ mol^{-1} which deviate negligibly from $A_{(g)}$ desorption activation parameters because $A_{(g)}$ sorption is nearly-entirely rate-determining (i.e. $X_{RC,A,ads} \sim 0.95$). The Langmuir-Hinshelwood formalism, however, misidentifies *rds* = *sr*, and consequently mistakenly attributes the entropic gain of 26.2 J mol^{-1} K^{-1} to the associative formation of the $(A^*–B^*)^{\ddagger}$ transition state which, in actuality, is formed with an entropic loss of –8.3 J mol^{-1} K^{-1}. The identical quantitative fits but disparate physical interpretation of zeroth- and

first-order rate expressions highlight the unreliability of goodness-of-fit to assess the veracity of a kinetic model. Accurate predictions of $A_{(g)}$ and $B_{2(g)}$ reaction orders and quantitative fit to temperature-dependent rate data do not guarantee appropriateness of Langmuir-Hinshelwood or any other kinetic formalism. Instead, the veracity and reliability of a kinetic description is predicated on (i) the fidelity with which the mathematical formulation of the theory describes its foundational physical precepts and (ii) the extent to which the physical precepts of a theory agree with the considered natural phenomenon. In the case of the Langmuir-Hinshelwood formalism, the approximation $\mu_{ij} = 1$ fundamentally conflicts with (i + ii) the established ability of Langmuirian adsorbates to diffuse with non-infinite rate and proscribes reliable application of the formalism to describe any catalytic system without known infinitely-fast diffusion of all surface species.

The immobility of adsorbates in the $A + \frac{1}{2}B_2 \rightarrow AB$ reaction is incognizable to the Langmuir-Hinshelwood formalism and is responsible for the ascription of $\Delta S_{rds}^{0,\ddagger} = 26.2$ J mol^{-1} K^{-1} to the surface reaction step which instead forms the $(A^*–B^*)^\ddagger$ transition state with an entropic loss. Misattribution of intrinsic entropic activation barriers to surface reaction therefore fundamentally misrepresents entropic drivers for the formation of the ostensibly rate-controlling $(A^*–B^*)^\ddagger$ transition state. Similarly, enthalpic barriers to $(A^*–B^*)^\ddagger$ formation are overestimated by 18.5 kJ mol^{-1} – a profound miscalculation given the apparent simplicity of the reaction network and quantitative zeroth-order fit. In actuality, as the first-order formalism correctly describes, the calculated rate-controlling entropic and enthalpic barriers reflect activation energetics of A^* desorption responsible for liberating immobile, isolated A^* only allied to B^* by $A_{(g)}$ re-adsorption with rate $r_{A,ads,[A^*–B^*]} = k_{A,ads}P_A\theta_{B^*} = k_{A,des}P_AK_A(K_{B_2}P_{B_2})^{\frac{1}{2}} = \frac{1}{4}R$. In this sense, the rate-determining step is, most specifically, the

irreversible, two-site adsorption event $A_{(g)} + B^*–* \rightarrow A^*–B^*$ which exemplifies the critical importance of first-order description of ostensibly single-site elementary steps (e.g. $A_{(g)}$ adsorption) which may control rates via an ensemble-specific two-site path.

The limitations of the Langmuir-Hinshelwood model responsible for unfaithful description of the $A + ½B_2 \rightarrow AB$ reaction are entirely resolved by arbitrarily-fast surface diffusion which rids $A_{(g)}$ sorption of the kinetic burden to generate $A^*–B^*$ pairs. However, as we describe in the following, infinitely-fast surface diffusion is insufficient to guarantee accuracy of the Hinshelwood approximation if adsorbed species occupy more than one site.

6.4.3 Case Study III: Kinetic consequences of two-site associative B_2 adsorption in $A + B_2 \rightarrow AB_2$

Catalytic chemistries which (de-)hydrogenate, fragment, and/or grow hydrocarbon chains commonly involve multi-site-occupying intermediates which arbitrate rates of kinetically-relevant and selectivity-determining steps (*153*, *161*, *164*, *187–189*). Multi-site occupation of reactive intermediates confers an inherent clustering of constituent fragments (e.g. CH_2^* in $^*CH_2CH_2^*$) indescribable by zeroth- or first-order truncation procedures. Challenges in analytically describing catalysis of multi-site occupants arise from difficulty in distinguishing between (i) unbound, neighboring fragments that are facilely unpaired (e.g. $CH_2^*CH_2^*$) and (ii) bonded fragments that constitute a single adspecies which cannot be disassembled (e.g. $^*CH_2CH_2^*$). Inseparability of bound methylene moieties in adsorbed ethylene is formulated analytically by prohibition of ensembles and ensemble-specific elementary steps which wrongly isolate CH_2^*. Specification of precluded ensembles requires a second-order kinetic description to wholly retain and bar configurations such as $*–CH_2^*–*$ on linear lattices and analogous five-site ensembles which strand CH_2^* on square lattices.

Scheme 6.6: Ensembles forbidden in catalytic ethylene hydrogenation

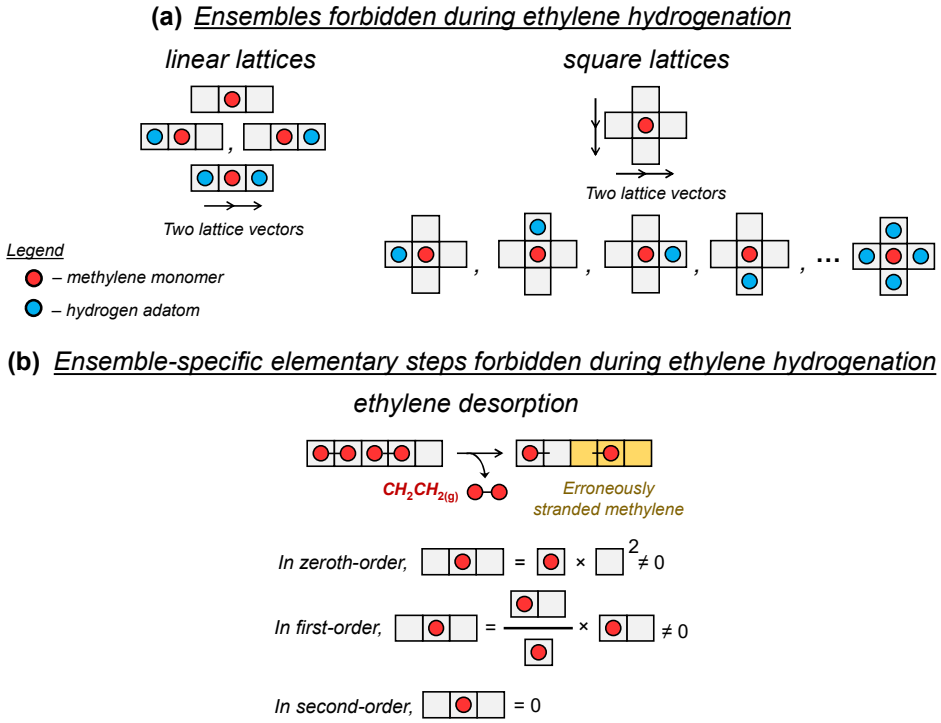

(a) Ensembles on linear and square lattices which isolate monomeric methylene fragments (●) and are erroneously permitted in zeroth- and first-order truncations. Two lattice vectors are needed to wholly retain each ensemble and, therefore, a ≥second-order truncation procedure is required. (b) Elementary step events which wrongly strand monomeric methylene fragments. Zeroth- and first-order ensembles are unable to specify $\theta_{*\text{–}CH2\text{*}\text{–}*} = d\theta_{*\text{–}CH2\text{*}\text{–}*}/dt = 0$ and, therefore, permit the illustrated ethylene desorption event.

Scheme 6.6 illustrates such forbidden ensembles in the context of catalytic ethylene hydrogenation and explicates the necessity of the second-order truncation procedure. Zeroth- and first-order methods erroneously permit elementary steps such as ethylene desorption to segregate bonded $^{*}CH_2CH_2^{*}$ pairs, as shown in Scheme 6.6, and, consequently, predict non-physical isolation of methylene fragments in hydrogenation reactions. Explicit retention of three-site configurations in the second order is a pre-requisite for disallowing methylene isolation (e.g. via ethylene desorption) and is critical to quantitatively distinguishing between coverages of compositionally-identical but chemically-distinct $CH_2{}^{*}CH_2^{*}$ and $^{*}CH_2CH_2^{*}$ ensembles.

Table 6.5: Horiuti-Polanyi-type reaction of a two-site-occupying adsorbate

#	Step	Rate constants
1	$A_{2(g)} + * - * \rightarrow {}^{*}AA^{*}$	$k_{A_2,ads}$= 1 (bar · s)$^{-1}$
–1	${}^{*}AA^{*} \rightarrow A_{2(g)} + * - *$	$k_{A_2,des}$ = 1 s^{-1}
2	$B_{2(g)} + * - * \rightarrow B^{*} - B^{*}$	$k_{B_2,ads}$= 1 (bar · s)$^{-1}$
–2	$B^{*} - B^{*} \rightarrow B_{2(g)} + * - *$	$k_{B_2,des}$ = 1 s^{-1}
3	${}^{*}AA^{*} - B^{*} \rightarrow A_2B_{(g)} + * - * - *$	k_{sr} = 1 s^{-1}
n/a	${}^{*}AA^{*} - * \leftrightarrow * - {}^{*}AA^{*}$	$k_{A,diff} \geq 10^5$ s^{-1}
n/a	$B^{*} - * \leftrightarrow * - B^{*}$	$k_{B,diff} \geq 10^5$ s^{-1}

We explicate second-order distinction between bonded and unbound surface fragments in the context of a simple, generic Horiuti Polanyi mechanism analogous to catalytic ethylene hydrogenation (*155*, *190–192*). The hydrogenation-type mechanism $A_2 + B_2 \rightarrow A_2B$ occurs on a linear lattice via the sequence of elementary steps in Table 6.5 wherein (i) the adsorbed analog of $A_{2(g)}$, ${}^{*}AA^{*}$, occupies two sites analogously to ${}^{*}CH_2CH_2{}^{*}$, (ii) $B_{2(g)}$ adsorbs dissociatively analogously to molecular hydrogen, and (iii) diffusion of all adsorbates is arbitrarily-fast compared to catalysis. The intrinsic non-randomness conferred by inseparable ${}^{*}AA^{*}$ pairs is not facilely overcome by surface diffusion and requires $k_{diff}/k_{i\neq diff} \geq 10^5$ to be regarded infinitely-fast – a condition we quantitatively confirm by calculation of ensemble-specific diffusion reversibilities. Bonded ${}^{*}AA^{*}$ pairs and unbound $A^{*}A^{*}$ ensembles are of identical occupancy and, therefore, are not naturally distinguished by the second order truncation procedure; instead, the distinction between these ensembles must be enforced by explicit prohibition of three-site ensembles which isolate A^{*}

$$\theta_{*-A^{*}-*} = \theta_{B^{*}-A^{*}-*} = \theta_{B^{*}-A^{*}-B^{*}} = 0 \qquad \textbf{[6.48]}$$

Non-random ensemble constraints described by Eq. **6.48** effect configurational non-idealities in the distribution of all other ensembles, as captured by second-order site balances akin to first-order balances in Eq. **6.10**

$$\theta_{ij} = \sum_{\substack{k=site \\ occupants}} \theta_{ijk} = \sum_{\substack{m=site \\ occupants}} \theta_{mij} \qquad \textbf{[6.49]}$$

where *k* and *m* are indices over all single-site occupants. Diametric placement of *k* and *m* on either side of the *ij* pair gives distinct ensemble balances without analogy in zeroth- and first-order methods. For example, Eq. **6.49** gives two distinct balances on A^*–B^* pairs

$$\theta_{A^*-B^*} = \sum_{\substack{m=site \\ occupants}} \theta_{m-A^*-B^*} = \theta_{A^*-\square^*-B^*} + \theta_{B^*-A^*-B^*} + \theta_{*-A^*-B^*} \qquad \textbf{[6.50]}$$

$$= \theta_{A^*-A^*-B^*}$$

which reduces to a single term per Eq. **6.48**, and

$$\theta_{A^*-B^*} = \sum_{\substack{k=sit \\ occupants}} \theta_{A^*-B^*-k} = \theta_{A^*-B^*-A^*} + \theta_{A^*-B^*-B^*} + \theta_{A^*-B^*-*} \qquad \textbf{[6.51]}$$

which retains three coverage terms – none of which appear in Eq. **6.50**. In this way, the second-order formalism describes two-site ensembles with spatial detail which (i) is lost in ≤first-order truncation procedures and (ii) provides information critical to describing non-random distribution and chemical dynamics of kinetically-relevant ensembles such as the reactive A^*–A^*–B^* configuration derived to be equal in population to the two-site A^*–B^* pair (Eq. **6.50**). Analogous second-order balance on A^*–* pairs gives $\theta_{A^*-*} = \theta_{A^*-A^*-*}$ from which we derive a simplified balance on $\theta_{A^*-A^*}$, the total coverage of as-yet undistinguished bonded and unbound A^* pairs

$$\theta_{A^*-A^*} = \sum_{\substack{m=sit \\ occupants}} \theta_{m-A^*-A^*} = \theta_{A^*-B^*} + \theta_{A^*-*} + \theta_{A^*-A^*-A^*} \quad \textbf{[6.52]}$$

Eq. **6.52** provides a constraint on populations of all two-site A^*-containing ensembles, motivating combination with the first-order balance

$$\theta_{A^*} = \sum_{\substack{k=sit \\ occupants}} \theta_{A^*-k} = \theta_{A^*-B^*} + \theta_{A^*-*} + \theta_{A^*-A^*} \quad \textbf{[6.53]}$$

Eqs. **6.52** and **6.53** communicate distinct, complementary spatial information, the concert of which reveals that the coverage of all A^*–A^* ensembles is the sum of two terms

$$\theta_{A^*-A^*} = \frac{\theta_{A^*}}{2} + \frac{\theta_{A^*-A^*-A^*}}{2} \quad \textbf{[6.54]}$$

each accounting for a chemically-distinct A^*–A^* pair. Eq. **6.54** is only derivable because of the spatial detail captured by the second-order balance (Eq. **6.52**) and makes clear that (i) $\theta_{*AA*} = ½\theta_{A*}$ consistent with the stoichiometry of $^*AA^*$ species and (ii) $\theta_{A*A*} = ½\theta_{A*-A*-A*}$ because neighboring, unbound A^* must be members of distinct $^*AA^*$ adsorbates. From Eq. **6.54**, the absolute lower bound on the coverage of all A^*–A^* ensembles is evidently $(\theta_{A*-A*})_{min} = \theta_{*AA*} = ½\theta_{A*}$ corresponding to surfaces wherein no adsorbed analogs of $A_{2(g)}$ neighbor one another. The two-site occupancy of $^*AA^*$ species therefore prescribes an absolute lower bound on the mean-field metric of A^*–A^* pairs

$$(\mu_{A^*-A^*})_{min} \equiv \frac{(\theta_{A^*-A^*})_{min}}{\theta_{A^*}^2} = \frac{1}{2 \cdot \theta_{A^*}} \quad \textbf{[6.55]}$$

which demands $\mu_{A*-A*} > 1$ for $\theta_{A*} < ½$ – excluding accuracy of the Hinshelwood approximation (i.e. $\mu_{ij} = 1$) even if surface diffusion of all adspecies is arbitrarily-fast. We therefore surmise that there is no condition which permits reliable use of the zeroth-order formalism to describe catalytic sequences involving ≥two-site-occupying surface

intermediate(s) – as we demonstrate by comparison of zeroth-order (Table 6.6) and second-order (Table 6.7) microkinetic models in what follows.

We report elementary step rates for select ensembles in Tables 7(A) and 7(B) which provide a representative sample of the complexity and variety of rate terms retained in the second order formalism.

Table 6.6: Langmuir-Hinshelwood rate equations for Horiuti-Polanyi reaction $A_2 + B_2 \rightarrow A_2B$

Langmuir-Hinshelwood							
Step, *i*	$A_{2(g)}$ *ads.*	$A_{2(g)}$ *des.*	$B_{2(g)}$ *ads.*	$B_{2(g)}$ *des.*	*reaction*	A^* *diffusion*	B^*-B^* *diffusion*
Rate, r_i	$k_{A_2,ads}P_{A_2}\theta_*$	$k_{A_2,des}\theta_{A^*}^2$	$k_{B_2,ads}P_{B_2}\theta_*^2$	$k_{\square_2,des}\theta_{B^*}^2$	$k_{sr}\theta_{A^*}^2\theta_{B^*}$	$k_{A,diff}\theta_{A^*}^2\theta_*$	$k_{B,diff}\theta_{B^*}\theta_*$
Ensemble-Specific Stoichiometric Coefficients							
$\boldsymbol{\nu_{i,[A^*]}}$	2	– 2	0	0	– 4	0	0
$\boldsymbol{\nu_{i,[A^*-B^*]}}$	No explicit rate equations. $\theta_{ij} = \theta_i\theta_j$						
$\boldsymbol{\nu_{i,[*-*-*]}}$	No explicit rate equations. $\theta_{ijk} = \theta_i\theta_j\theta_k$						

Rate equations for each ensemble and each elementary step are constructed by product of the fundamental rate of the step (e.g. $k_{B_2,ads}P_{B_2}\theta_*^2$ for $B_{2(g)}$ adsorption) and the corresponding ensemble-specific stoichiometric coefficient (e.g. 2 for B^* for $B_{2(g)}$ adsorption).

Table 6.7: Second-order rate equations for Horiuti-Polanyi reaction $A_2 + B_2 \rightarrow A_2B$

(A)

Second-order				
Step, *i*	$A_{2(g)}$ *ads.*	$A_{2(g)}$ *des.*	$B_{2(g)}$ *ads.*	$B_{2(g)}$ *des.*
Rate, r_i	$k_{A_2,ads}P_{A_2}\theta_{*-*}$	$k_{B_2,des}\theta_{A^*-A^*}$	$k_{B_2,ads}P_{B_2}\theta_{*-*}$	$k_{B_2,des}\theta_{B^*-B^*}$
Ensemble-Specific Stoichiometric Coefficients				
$\boldsymbol{\nu_{i,[A^*]}}$	2	– 2	0	0
$\boldsymbol{\nu_{i,[A^*-B^*]}}$	$\frac{\theta_{B^*-*-*}}{\theta_{*-*}}$	$-\frac{\theta_{B^*-A^*-A^*}}{\theta_{A^*-A^*}}$	$\frac{\theta_{A^*-*-*}}{\theta_{*-*}}$	$-\frac{\theta_{A^*-B^*-B^*}}{\theta_{B^*-B^*}}$
$\boldsymbol{\nu_{i,[*-*-*]}}$	$-2\frac{\theta_{*-*-*}}{\theta_{*-*}} - 2\frac{\theta_{*-*-*}^2}{\theta_{*-*}^2}$	$2\frac{\theta_{A^*-A^*-*}}{\theta_{A^*-A^*}} + 2\frac{\theta_{A^*-A^*-*}\theta_{A^*-*-*}}{\theta_{A^*-A^*}\theta_{A^*-*}}$	$-2\frac{\theta_{*-*-*}}{\theta_{*-*}} - 2\frac{\theta_{*-*-*}^2}{\theta_{*-*}^2}$	$2\frac{\theta_{B^*-B^*-*}}{\theta_{B^*-B^*}} + 2\frac{\theta_{B^*-B^*-*}\theta_{B^*-*-*}}{\theta_{B^*-B^*}\theta_{B^*-*}}$

Rate equations for each ensemble and each elementary step are constructed by product of the fundamental rate of the step (e.g. $k_{B_2,ads}P_{B_2}\theta_{*\_*}$ for $B_{2(g)}$ adsorption) and the corresponding ensemble-specific stoichiometric coefficient (e.g. $\theta_{A^*\_*\_*}/\theta_{*\_*}$ for A^*–B^* for $B_{2(g)}$ adsorption).

(B)

Second-order			
Step, i	*reaction*	A^* *diffusion*	B^*– B^* *diffusion*
Rate, r_i	$k_{sr}\theta_{A^*-A^*-B^*}$	$k_{A,\square iff}\theta_{A^*-A^*-*}$	$k_{B,diff}\theta_{B^*-*}$
Ensemble-Specific Stoichiometric Coefficients			
$\boldsymbol{\nu_{i,[A^*]}}$	– 4	0	0
$\boldsymbol{\nu_{i,[A^*-B^*]}}$	$-1-\frac{\theta_{A^*-B^*-A^*}}{\theta_{A^*-B^*}}-\frac{\theta_{B^*-A^*-A^*}}{\theta_{A^*-A^*}}$	$\frac{\theta_{A^*-*-B^*}}{\theta_{A^*-*}}-\frac{\theta_{B^*-A^*-A^*}}{\theta_{A^*-A^*}}$	$\frac{\theta_{A^*-*-B^*}-\theta_{A^*-B^*-*}}{\theta_{B^*-*}}$
$\boldsymbol{\nu_{i,[*-*-*]}}$	$2\left(1+\frac{\theta_{A^*-B^*-*}}{\theta_{A^*-B^*}}+\frac{\theta_{A^*-A^*-*}}{\theta_{A^*-A^*}}+\frac{\theta_{A^*-B^*-*}\theta_{B^*-*-*}}{\theta_{A^*-B^*}\theta_{B^*-*}}+\frac{\theta_{A^*-A^*-*}\theta_{A^*-*-*}}{\theta_{A^*-A^*}\theta_{A^*-*}}\right)$	$2\frac{\theta_{A^*-A^*-*}\theta_{A^*-*-*}}{\theta_{A^*-A^*}\theta_{A^*-*}}-2\frac{\theta_{A^*-*-*}\theta_{*-*-*}}{\theta_{A^*-*}\theta_{*-*}}$	$2\frac{\theta_{B^*-*-*}\theta_{*-B^*-*}}{\theta_{B^*-*}^2}-2\frac{\theta_{*-*-*}\theta_{B^*-*-*}}{\theta_{*-*}\theta_{B^*-*}}$

Rate equations for each ensemble and each elementary step are constructed by product of the fundamental rate of the step (e.g. $k_{B,diff}\theta_{B^*-*}$ for B^* diffusion) and the corresponding ensemble-specific stoichiometric coefficient (e.g. $[\theta_{A^*-*-B^*}-\theta_{A^*-B^*-*}]/\theta_{B^*-*}$ for A^*–B^* for B^* diffusion).

Figure 6.6 compares mean-field metrics, coverages, reaction orders, and degrees of rate control calculated by the zeroth- and second-order microkinetic models as a function of P_{A_2} using rate constants listed in Table 6.5. Surface diffusion of ${}^*AA^*$ and B^* is confirmed to be infinitely-fast by calculation of ensemble-specific diffusion reversibilities – all of which are unity – and by invariance of all kinetic parameters with increase to $k_{A,diff}$ or $k_{B,diff}$. Fig. 6.6(A) demonstrates infinitely-fast adsorbate diffusion is incapable of guaranteeing $\mu_{A^*-A^*} = 1$ for $A_{2(g)}$ pressures sufficiently low to effect $\theta_{A^*} < ½$ (Fig. 6.6(B)). The second-order formalism correctly captures the precipitous increase of $\mu_{A^*-A^*}$ as A^* coverage is decremented and intrinsic clustering of ${}^*AA^*$ compels supra-random A^* aggregation. Second-order calculations of $\mu_{A^*-A^*}$ slightly exceed $(\mu_{A^*-A^*})_{min} = ½\theta_{A^*}{}^{-1}$ because of the small contribution of unbound A^*A^* pairs.

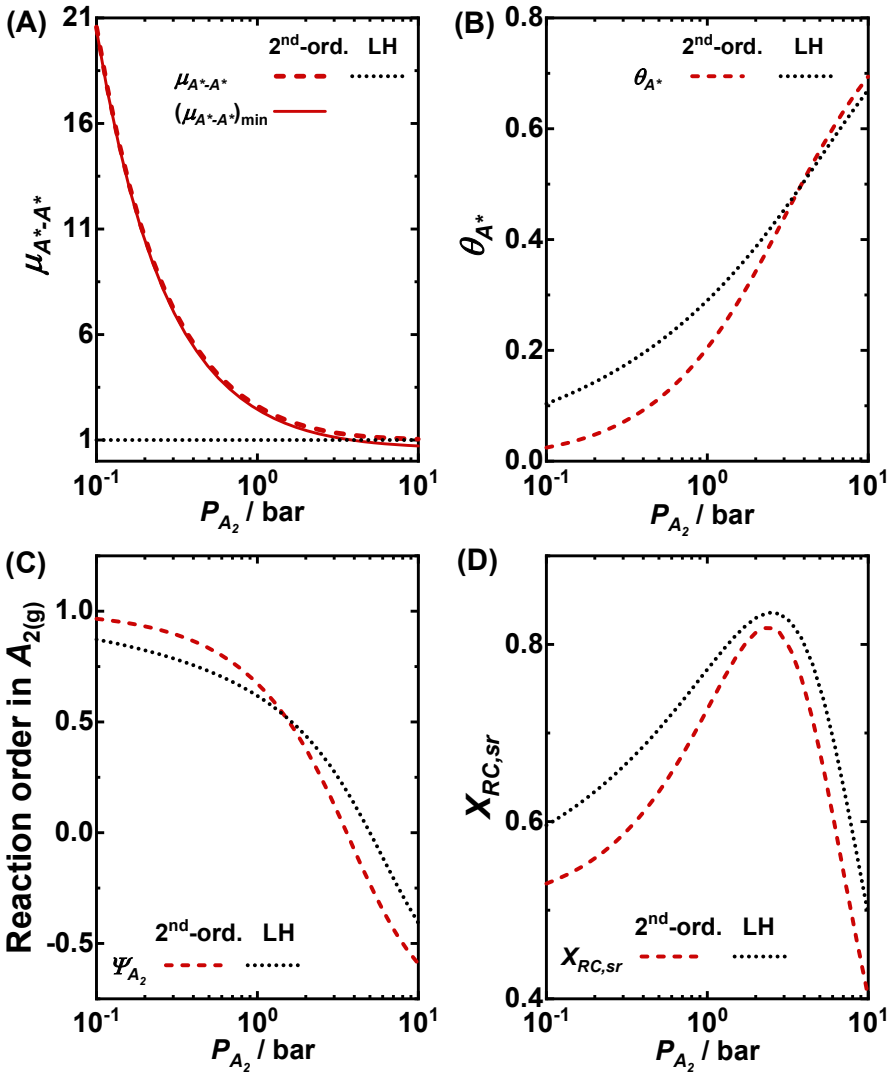

Figure 6.6: (A) Mean-field metric of A^* pairs, $\mu_{A^*\text{–}A^*}$, calculated by Langmuir-Hinshelwood (···) and second-order (---) formalisms and compared to the absolute lower bound $(\mu_{A^*\text{–}A^*})_{min} = (2\theta_{A^*})^{-1}$ (—) per Eq. **6.53**. (B) Fractional coverage of A^*-occupied sites, (C) reaction order in $A_{2(g)}$, and (D) degree of rate control of surface reaction calculated by Langmuir-Hinshelwood (···) and second-order (---) formalisms. Calculations are of the reaction network in Table 6.5 with $P_{B_2} = 1$ bar.

Total coverages of A^* fragments are profoundly overestimated by the Langmuir-Hinshelwood model for $P_{A_2} < 1$ bar. The Hinshelwood approximation $\mu_{A^*\text{–}A^*} = 1$ becomes increasingly poor as $\theta_{A^*} \rightarrow 0$ and, as a result, the rate of A^* consumption $r = k_{sr}\theta_{A^*}{}^2\theta_{B^*}$ is underestimated – effecting an erroneous accumulation of A^* species which, in actuality, react rapidly because of the ensured proximity of a bonded A^* species (i.e. ${}^*AA^*$ adspecies

prescribe $\theta_{A^*-A^*-B^*}/\theta_{A^*-B^*} = 1 \neq \theta_{A^*}$). Invalidity of the $\theta_{A^*-A^*-B^*}/\theta_{A^*-B^*} = \theta_{A^*}$ approximation is unresolved by surface diffusion at all coverages and, consequently, reaction orders in $A_{2(g)}$ and degrees of rate control of surface reaction are generally miscalculated by the Langmuir-Hinshelwood method (Figs. 6.6(C) and 6.6(D)). In this way, the inability of ≤first-order formalisms to inventory $^*A$-A^* bonds begets uncertainty in all kinetic descriptors – despite the ostensible capacity of surface diffusion to randomize adsorbate distribution. Intrinsic non-randomness conferred by $^*AA^*$ two-site occupancy cannot be overcome by any set of rate parameters and is only reliably neglected on $^*AA^*$-saturated surfaces which warrant $\theta_{A^*-A^*-B^*}/\theta_{A^*-B^*} = \theta_{A^*} = 1$. We therefore caution against use of the Langmuir-Hinshelwood formalism to describe any catalytic sequence mediated by multi-site occupants and advocate efforts to develop and computationally implement higher-order formalisms for general use in the description of catalytic surface reactions.

6.5 Discussion

In an effort to preempt misconception of the higher-order kinetic formalism described in this work, we discuss and reiterate below a selection of key concepts related to the definition of site ensembles and the scope and application of the presented kinetic framework.

6.5.1 Definition of catalytic site ensembles

We define a site ensemble to be a collection of sites which (i) are contiguous and (ii) each have a specified occupancy. A site ensemble is therefore identified by its connectivity (i.e. size and shape) and composition (i.e. occupation of each site). For example, distinct site ensembles A^*–A^* and *–* are identical in connectivity and are distinguished by

composition. Conversely, distinct site ensembles $A^*–A^*–A^*$ and $\begin{matrix} A^* - A^* \\ \quad\quad\ | \\ \quad\quad A^* \end{matrix}$ are identical in composition and are distinguished by connectivity.

We stress that ensembles of disparate size and identical composition (i.e. * and *–*) do not refer to distinct sites of different nuclearity or spatial extent. That is to say, * and *–* do not refer, as an example, to atop and hollow sites, respectively. Ensembles of multiple *types* of sites (e.g. $*_{atop}–*_{hollow}$) are not addressed in this work; however, we hope to illustrate in future studies that the combined chemical and spatial specificity proffered by the higher-order kinetic formalism we present herein is uniquely suited to describe the dynamics of ensembles of multiple types of sites (e.g. on metal alloy catalysts (*193*, *194*)).

6.5.2 Thermodynamic non-idealities: lateral adsorbate interactions

The primary development of this work is provision of a reliable method by which to enumerate ≥two-site ensemble populations on any catalytic surface. Although we present the mathematical framework in the context of Langmuirian surfaces and species, Conditions (I)-(III) are not a pre-requisite of the described method. Hierarchical rate equations constructed by enumeration and truncation of conditional probabilities may be derived even if (i) the absorbent/catalytic surface contains an arbitrary distribution of an arbitrary number of sites, (ii) each site can accommodate more than one occupant, or (iii) adsorbed species energetically interact.

The incorporation of each of these non-idealities into higher-order descriptions requires an increment in the amount of retained information and, therefore, an increment in the number of independent variables. To explicate the capacity of the higher-order method to account for such non-idealities – and the attendant increase in complexity – we detail

inclusion of lateral adsorbate interactions into a first-order description of $A_{(g)}$ desorption on a 2D square lattice.

We introduce thermodynamic non-idealities by considering adjacent A^* species to interact with energy $\varepsilon_{A^*-A^*}$. For simplicity, we regard vacant sites and transition states as non-interacting – a condition which is relaxed in a more general treatment of adsorbate interactions in our recent work (*166*). The kinetic consequences of A^*–A^* energetic interactions are determined by (i) the polarity and strength of interaction, quantified by $\varepsilon_{A^*-A^*}$, and (ii) the frequency of interaction, quantified by $\theta_{A^*-A^*}$. An analytical treatment of nearest-neighbor adsorbate interactions therefore requires reliable enumeration of A^*–A^* pairs – as is achieved by the first-order method.

Previous attempts to analytically describe thermodynamic non-idealities rely on approximations which, similarly to the Hinshelwood approximation, enable site-pair populations to be expressed in terms of single-site coverages. The quasi-chemical approximation (QCA) (*33–35*), for example, assumes the surface is energetically-equilibrated and correspondingly applies the thermodynamic constraint

$$\frac{\theta_{A^*-*}^2}{\theta_{A^*-A^*}\theta_{*-*}} = e^{\epsilon_{A^*-A^*}/k_BT} \qquad \textbf{[6.58]}$$

which, coupled to site and component balances, is sufficient to reduce the number of independent ensembles to 5 – 4 = 1, meaning a microkinetic model only requires rate equations for A^* or *. The equilibrium condition in Eq. **6.58**, however, is only applicable if surface diffusion is infinitely-fast compared to catalysis and ensures the adsorbate distribution energetically equilibrates. In this sense, QCA is a generalization of the Hinshelwood approximation to thermodynamically non-ideal surfaces. A general description of lateral adsorbate interactions requires $\theta_{A^*-A^*}$ be retained as an independent

variable and be described by ensemble-specific thermodynamically non-ideal rate equations.

Consider, for example, desorption of A^* from a square lattice. The desorbing A^* species has m = 0, 1, 2, 3, or 4 nearest-neighboring A^* species. The number of A^*–A^* pairs eliminated by desorption affects the energy of the desorbing initial state relative to the transition state and, therefore, alters the effective activation energy of desorption. The rate of desorption with m neighboring A^* species is therefore

$$r_{des,\{m\}} = \omega_{des,\{m\}} \times k_{des} e^{\frac{m\epsilon_{A^*-A^*}}{k_B T}} \theta_{des,m} \qquad \textbf{[6.59]}$$

where k_{des} is the thermodynamically-ideal desorption rate constant, $\theta_{des,m}$ is the coverage of five-site desorptive configurations with exactly m neighboring A^* species, and $\omega_{des,\{m\}}$ is the multiplicity of five-site desorptive configurations with exactly m neighboring A^* species. For example, for m = 3,

$$r_{des,\{3\}} = 4k_{des} e^{\frac{3\epsilon_{A^*-A^*}}{k_B T}} \theta_{\substack{A^* \\ | \\ A^*-A^*-* \\ | \\ A^*}} \qquad \textbf{[6.60]}$$

where $\omega_{des,\{3\}}$ = 4 because the neighboring * site may be at any of the four positions neighboring the central, desorbing A^* species. The rate of desorption is a sum of terms analogous to Eq. **6.60** for m = 0 to m = 4 which, after execution of the first-order truncation procedure, gives

$$r_{des} = k_{des}\theta_{A^*}\left[\frac{\theta_{A^*-A^*} e^{\frac{\epsilon_{A^*-A^*}}{k_B T}} + \theta_{A^*-*}}{\theta_{A^*}}\right]^4 \qquad \textbf{[6.61]}$$

The bracketed term compendiously captures the propensity of lateral adsorbate interactions to affect the activation energy of desorption and is referred to in the following as Γ_{des}. The

interaction term Γ_{des} is a function of $\theta_{A^*-A^*}$ and θ_{A^*-*} and therefore couples to rate equations for two-site ensembles derived analogously to Eq. **6.61**

$$r_{des,[A^*-A^*]} = k_{des}\theta_{A^*}\left[-\frac{2\theta_{A^*-A^*}}{\theta_{A^*}}e^{\frac{\epsilon_{A^*-A^*}}{k_BT}}\Gamma_{des}^3\right] \quad \textbf{[6.62]}$$

$$r_{des,[A^*-*]} = k_{des}\theta_{A^*}\left[\frac{\theta_{A^*-A^*}}{\theta_{A^*}}e^{\frac{\epsilon_{A^*-A^*}}{k_BT}}\Gamma_{des}^3 - \frac{\theta_{A^*-*}}{\theta_{A^*}}\Gamma_{des}^3\right] \quad \textbf{[6.63]}$$

$$r_{des,[A^*-A^*]} = k_{des}\theta_{A^*}\left[\frac{2\theta_{A^*-*}}{\theta_{A^*}}\Gamma_{des}^3\right] \quad \textbf{[6.64]}$$

where the bracketed terms in Eqs. **6.62** – **6.64** entirely describe the non-ideal energetic and spatial contributions pertinent to desorption with respect to each ensemble. Eqs. **6.62** – **6.64** provide a rigorous description of the kinetic influence of A^*–A^* nearest neighbor interactions on $A_{(g)}$ desorption and include only one independent variable, $\varepsilon_{A^*-A^*}$, not found in the thermodynamically-ideal case. Analogous first-order rate equations are readily derived for any thermodynamically non-ideal one- or two-site elementary step – as is detailed in our prior work (*166*) – and provide an analytical method by which to reliably account for both combinatorial and thermodynamic non-idealities.

6.5.3 Incorrect representation of multi-site elementary steps

We address a common misrepresentation of multi-site elementary step events to prevent erroneous application of the first-order truncation procedure. Consider the surface reaction of A^*–A^* pairs adjacent to a vacant site

$$A^* - A^* - * \rightarrow A_{2(g)} + * - * - * \quad \textbf{[6.65]}$$

occurring with rate $k_{sr}\theta_{A^*-A^*-*}$ which, in the first order, is truncated in terms of one- and two-site ensemble coverages. To ensure appropriate application of the truncation method, we discourage writing this elementary step event as

$$A^* - A^* + * \rightarrow A_{2(g)} + * - * + *$$ **[6.66]**

because this representation erroneously suggests the rate of the concerned event may be written as $k_{sr}\theta_{A^*-A^*}\theta_*$ per the law of mass action. This rate expression is incorrect because (i) the event may equivalently be written as

$$A^* + A^* - * \rightarrow A_{2(g)} + * + * - *$$ **[6.67]**

giving rate $k_{sr}\theta_{A^*-*}\theta_{A^*} \neq k_{sr}\theta_{A^*-A^*}\theta_*$, and (ii) the coverage of the reacting three-site ensemble is, in actuality, $\theta_{A^*-A^*-*} = \theta_{A^*-A^*}\theta_{A^*-*}/\theta_{A^*}$ following the first order truncation procedure detailed in Section 6.3.1.

The incorrect rate expressions which follow naturally from Eqs. **6.66** and **6.67** highlight the importance of writing multi-site elementary step events in terms of the *entire contiguous ensemble* on which the event occurs – as in Eq. **6.65**.

6.5.4 Relation of the described method to density functional theory (DFT) calculations

We stress that this work does not provide an alternative to DFT methods for calculation of elementary step kinetic parameters. Rather, the described methodology is complementary to DFT and serves to improve upon mean-field microkinetic models heretofore employed for the calculation of rates of composite reactions based on DFT-determined initial-state and transition-state energies. DFT calculations provide identical inputs for both higher-order and mean-field (e.g. Langmuir-Hinshelwood) microkinetic models; however, compared to mean-field methods, the higher-order framework more faithfully describes all relevant catalytic phenomena including, but not limited to, ensemble site requirements of elementary steps and surface species, lateral adsorbate interactions, and adsorbate surface diffusion. In this manner, the described formalism provides an alternative to lattice-based kMC simulation – previously the only method capable of

simultaneously capturing thermodynamic and combinatorial non-idealities in catalytic surface reactions.

6.6 Conclusion

Multi-site requirements of elementary steps and/or surface species generally exclude reliability of the Langmuir-Hinshelwood kinetic description which is predicated on a random, uniform distribution of adspecies. Disparate site-size requirements and rates of elementary steps fundamentally engender islanding/partitioning of adsorbates which affects a 'poorly mixed' surface and profoundly influences all kinetic descriptors (e.g. rates, selectivities, and activation energies). Poor 'surface mixing' is only rectified by infinitely-fast surface diffusion if all adspecies occupy a single site; there is no physical condition which generally guarantees validity of the Langmuir-Hinshelwood method to describe catalysis of multi-site occupants (e.g. $^{*}C_nH_m^{*}$ in catalytic hydrogenolysis).

The catalytic consequences of (i) finitely-fast adsorbate diffusion, (ii) multi-site elementary step requirements, (iii) multi-site occupation of surface intermediates, and (iv) lateral adsorbate interactions (i.e. thermodynamic non-idealities) are all incognizable to the Langmuir-Hinshelwood formalism and are rigorously describable by higher-order kinetic theories presented herein. Description of each of these non-ideal phenomena, (i)-(iv), requires ensemble-specific rate terms which quantitatively capture the unique influence each site ensemble exerts on each elementary step – and *vice versa*. Faithful kinetic description of ensemble-specific, microscopically-reversible elementary step events achieved by higher-order analytical methods proffers greater quantitative accuracy and descriptive scope compared to zeroth-order, Langmuir-Hinshelwood methods. In particular, first- and second-order descriptions examined herein reveal (i) relative propagation of competing catalytic reaction paths is dictated by the coverage and biased

distribution of prevalent site ensembles, (ii) a single elementary step can, counter-intuitively, be both equilibrated and rate-determining, (iii) adsorbate islanding/partitioning phenomena profoundly influence the physical interpretation of activation enthalpies and entropies, and (iv) multi-site occupation of surface intermediates confers stringent constraints on adsorbate coverage/distribution which is responsible for the Langmuir-Hinshelwood formalism erroneously calculating non-physical quantities. These observations affirm the need for higher-order analytical methods to generally describe catalytic phenomena and provide an informative, quantitative framework for the kinetic (re-)interpretation of all catalytic reactions proceeding via ≥two-site elementary steps and/or surface species.

7 A generalized Butler-Volmer equation and an equation for Tafel slope applicable at all overpotential

7.1 Conspectus

We re-interpret prevalent kinetic descriptors (e.g. Tafel slope) and descriptions (e.g. Butler-Volmer equation) of composite electrochemical reactions in the context of transition state theory (TST) and the concept of elementary-step degree of rate control to formulate a mathematical framework which (i) extends the scope of the Butler-Volmer equation beyond the requirement of a single rate-determining step, (ii) explains the preponderance of Tafel slopes of 120 mV/dec at large overpotential, (iii) quantitatively de-convolutes anodic and cathodic contributions to Tafel slope at low overpotential, and (iv) prescribes new methods to identify the kinetic-relevance of each elementary step directly from measurement of reaction orders, surface coverages, and Tafel slope. The foundation of the developed formalism is the construction of a TST rate function for the overall reaction, r_{TST}, which, in a single equation, compendiously captures the kinetic and thermodynamic relevance of each intervening half-step in a form entirely analogous to the TST description of an elementary step. By applying the principle of microscopic reversibility to r_{TST}, we derive exactly the conditions which justify employ of the Butler-Volmer equation and, in doing so, establish a simple method by which to simultaneously determine anodic and cathodic transfer coefficients from a single measurement of net Tafel slope.

7.2 Significance

Kinetic and mechanistic assessment of electrochemical reactions is largely founded on (i) the Butler-Volmer equation and (ii) interpretation of the dependency of rate, or current density, on the applied potential — i.e. the Tafel slope. We demonstrate that the Butler-

Volmer framework and commonly-employed relationships between the Tafel slope and the identity of the rate-determining step are of prohibitively narrow scope. This work establishes a transition-state-theory-based mathematical framework, general to homogeneous and heterogeneous thermochemical and electrochemical reactions, which (i) extends the descriptive scope of the Butler-Volmer equation, (ii) establishes a general equation for Tafel slope applicable at all conditions, and (iii) prescribes new, quantitative tools for kinetic study in low and high overpotential regimes.

7.3 Introduction

The net electrical current, J, generated by a reversible electrocatalytic reaction is a sum of unidirectional anodic and cathodic contributions

$$J = J_a + J_c \qquad \textbf{[7.1]}$$

where, by convention, the anodic current, J_a, is positive and the cathodic current, J_c, is negative. Kinetic and mechanistic assessment of electrocatalytic composite reactions is often founded on measurement of Tafel slopes

$$b_a \equiv \frac{\partial E}{\partial\, log_{10}(J_a)} \qquad \textbf{[7.2]}$$

and

$$b_c \equiv -\frac{\partial E}{\partial\, log_{10}(-J_c)} \qquad \textbf{[7.3]}$$

which quantify the influence of the applied potential, E, on directional currents and are commonly measured sufficiently far from the equilibrium potential, E_{eqm}, to ensure the anodic or cathodic route dominates and, correspondingly, the net Tafel slope

$$b \equiv \frac{\partial E}{\partial\, log_{10}(J)} \qquad \textbf{[7.4]}$$

is equal to b_a or b_c (*195*, *196*). Tafel slopes measured as a function of overpotential, $\eta \equiv E - E_{eqm}$, are interpreted in the context of postulated reaction mechanisms to infer kinetic relevance of constituent elementary steps and rationalize proposed rate expressions commonly of the Butler-Volmer form

$$J = J_{eqm}\left(\chi_a e^{\frac{\alpha_a e_0 \eta}{k_B T}} - \chi_c e^{\frac{-\alpha_c e_0 \eta}{k_B T}}\right) \quad \textbf{[7.5]}$$

where k_B is the Boltzmann constant, T is thermodynamic temperature, J_{eqm} is the anodic and cathodic current at equilibrium, α_a (α_c) is the anodic (cathodic) transfer coefficient, and χ_a (χ_c) captures the functional dependence of the anodic (cathodic) current on thermodynamic activities of reactants and products (*195–199*). Electrochemical transfer coefficients in Eq. **7.5** are essentially the inverse of unidirectional Tafel slopes

$$\alpha_a \equiv \frac{k_B T}{e_0}\left(\frac{\partial\, ln(J_a)}{\partial E}\right) = \frac{k_B T}{e_0}\left(\frac{ln(10)}{b_a}\right) \quad \textbf{[7.6]}$$

and

$$\alpha_c \equiv -\frac{k_B T}{e_0}\left(\frac{\partial\, ln(-J_c)}{\partial E}\right) = \frac{k_B T}{e_0}\left(\frac{ln(10)}{b_c}\right) \quad \textbf{[7.7]}$$

only directly measurable under irreversible conditions such that either α_a or α_c is equal to the net transfer coefficient

$$\alpha \equiv \frac{k_B T}{e_0}\left(\frac{\partial\, ln(J)}{\partial E}\right) = \frac{k_B T}{e_0}\left(\frac{ln(10)}{b}\right) \quad \textbf{[7.8]}$$

Electrochemical transfer coefficients (α, α_a, α_c) are often preferred to Tafel slopes (b, b_a, b_c) in the assessment and construction of microkinetic models because of their non-dimensionality and ostensible connections to elementary step symmetry factors, reaction stoichiometry, and the identity of the rate-determining step. In particular, many mechanistic investigations expound and employ the relation

$$\alpha_a = \beta_{rds} n_{rds} + {}^{\gamma}/_{\sigma_{rds}} \quad \textbf{[7.9]}$$

where γ is the number of electrons transferred before the rate-determining step (rds) and β_{rds}, n_{rds}, and σ_{rds} are, respectively, the symmetry factor, number of transferred electrons, and the stoichiometric number of the rds (*200–206*). The cathodic transfer coefficient is then determined by the stoichiometric constraint

$$\alpha_c + \alpha_a = {}^{n}/_{\sigma_{rds}} \quad \textbf{[7.10]}$$

where n is the number of electrons transferred in the overall composite reaction. Eqs. **7.9-7.10** have been derived heuristically by assignment of a single non-equilibrated step and under the assumption of a bare surface, but the general veracity of both equations is, as-yet, unconfirmed (*203*, *204*). Indeed, the use of Eq. **7.9** for interpretation of Tafel slopes measured at high overpotential appears to misidentify rate-determining steps and is unable to explain the ubiquitous observation of $b \approx 120\ \mathrm{mV/dec}$, correspondent to $\alpha \approx ½$ at ambient temperature, for sufficiently large η. Furthermore, as numerous studies have discussed (*204*, *207–209*), the felicity of the ubiquitous Butler-Volmer equation has only been demonstrated for elementary steps — not for composite reaction sequences. The uncertain descriptive scope of the Butler-Volmer framework (Eq. **7.5**), Tafel slopes (Eqs. **7.2-7.4**), and transfer coefficients (Eqs. **7.6-7.10**) compels derivation of (i) the criteria for their applicability and (ii) a generalized mathematical formulation that codifies the functional form of each in description of elementary (half-)steps and composite reaction sequences alike.

This work establishes a novel framework for the description of electrochemical reactions by re-interpreting the aforementioned canonical kinetic descriptors in terms of transition state theory (TST) and the concept of degree of rate control (*140*, *172*, *197*, *210*).

The unification of these kinetic formalisms rigorously connects observable macrokinetic descriptors (e.g. α) to the analogous elementary step descriptor (e.g. β) and consequently reduces the complexity of composite reaction sequences to the simplicity of elementary steps. Foundational to the mathematical framework we describe is the formulation of transition-state-theory rate functions for the overall net, anodic, and cathodic reactions — each of which takes a form respectively analogous to elementary step, anodic half-step, and cathodic half-step rates (*172*). These TST rate functions serve as a mathematical link through which we extend fundamental theories of elementary step kinetics (e.g. the law of mass action) and thermodynamics (e.g. the principle of microscopic reversibility) beyond their strict domain of relevance (*143*, *172*, *211*, *212*). Justifiably applying these principles to composite reaction rate expressions, appropriately formulated as a function of all constituent elementary steps, is critically enabling in (i) constructing a generalized TST-form Butler-Volmer rate equation, (ii) proving Eqs. **7.9** and **7.10** and the requisite conditions for their validity, (iii) reconciling the ubiquity of $b \approx 120\ \mathrm{mV/dec}$ at large overpotential, for which Eq. **7.9** is proven invalid, and (iv) deriving mathematical relationships which enable simultaneous determination of α_a and α_c at low overpotential.

Transition-state-theory rate functions, presented here in the context of the net rate (r), are formally interpreted as a first-order Taylor series expansion of the composite reaction rate in terms of rates of each elementary half-step, $\pm i$ (Scheme 7.1). The derivative terms of the Taylor series expansion are therefore

$$s_{\pm i} \equiv \left(\frac{\partial\, ln\, r}{\partial\, ln\, r_{\pm i}}\right)_{r_{\mp i}, r_{\pm j}} = \left(\frac{\partial\, ln\, r}{\partial\, ln\, k_{\pm i}}\right)_{k_{\mp i}, k_{\pm j}} \qquad \textbf{[7.11]}$$

referred to as the reaction sensitivity of the net rate with respect to half-step $\pm i$, for which $r_{\pm i}$ and $k_{\pm i}$ are, respectively, the rate and rate constant (*84*, *140*). In quantifying the kinetic relevance of each half-step, reaction sensitivities are constrained by the elementary step reversibility, Z_i, per the principle of microscopic reversibility

$$Z_i \equiv \frac{r_{-i}}{r_{+i}} = \frac{-s_{-i}}{s_{+i}} \qquad \textbf{[7.12]}$$

While the quotient of half-step sensitivities is constrained by the salient *thermodynamic* descriptor of an elementary step, Z_i, the sum determines the salient *kinetic* descriptor of an elementary step: Campbell's kinetic degree of rate control

$$X_{RC,i} \equiv \left(\frac{\partial \, ln \, r}{\partial(-G^0_{TS,i}/k_B T)}\right)_{G^0_{TS,j\neq i}} = s_{+i} + s_{-i} \qquad \textbf{[7.13]}$$

where $G^0_{TS,i} = H^0_{TS,i} - TS^0_{TS,i}$ is the standard chemical free energy of the transition state (TS) of step i and is the sum of enthalpic ($H^0_{TS,i}$) and entropic ($-TS^0_{TS,i}$) terms (*84*, *140*); we define *chemical* free energies in this work to be absent electrochemical terms that are accounted for separately (i.e. by overpotential and symmetry factors). The kinetic degree of rate control ($X_{RC,i}$) quantifies exactly the kinetic relevance (i.e. rate control) of each elementary step i, or, equivalently, each transition state TS, i, and, in doing so, formalizes the concept of a rate-determining step, for which $X_{RC,rds} = 1$ and $X_{RC,i\neq rds} = 0$. The kinetic relevance of each species j is similarly quantified by the thermodynamic degree of rate control

$$X_{TRC,j} \equiv \left(\frac{\partial \, ln \, r}{\partial(-G^0_j/k_B T)}\right)_{G^0_{k\neq j}} = \sum_{\pm i} s_{\pm i}\nu_{\pm ij} \qquad \textbf{[7.14]}$$

where we define $\nu_{\pm ij}$ to be negative for reactants and zero for products of half-step $\pm i$ such that the stoichiometric number of species j in step i is $\nu_{ij} \equiv \nu_{+ij} - \nu_{-i}$. Thermodynamic

degrees of rate control are identical in magnitude to the macroscopic reaction order of species *j*

$$\Psi_j \equiv \left(\frac{\partial \ln r}{\partial \ln a_j}\right)_{a_{k\neq j}} = -X_{TRC,j} \qquad \textbf{[7.15]}$$

and thusly serve to (i) generalize the concept of reaction order to intermediates and surface species and (ii) codify the connection of reaction order to elementary half-step stoichiometry ($\nu_{\pm ij}$) and kinetic relevance ($s_{\pm i}$) (*84*, *140*).

In what follows, we leverage the microkinetic descriptors in Eqs. **7.11-7.15** to derive a generalized, TST-based description of rates of electrochemical reactions that (i) explains the prevalence of cardinal Tafel slopes, (ii) generalizes the Butler-Volmer formalism, (iii) provides new mathematical tools for the measurement and interpretation of electrochemical kinetics, and (iv) formalizes the connection between macrokinetic observables (e.g. Tafel slopes and reaction orders) and microkinetic descriptors. The thermodynamic consistency of these connections is interrogated by the De Donder formalism and the principle of microscopic reversibility to derive exactly the criteria that permit (i) formulation of a Butler-Volmer form rate equation and (ii) employ of Eq. **7.9** and analogous relations for kinetic interpretation of electrochemical reactions.

7.4 Results and Discussion

7.4.1 Transition-state-theory formulation of composite electrochemical reactions

The transition-state-theory rate functions for elementary forward/anodic and reverse/cathodic half-steps are

$$r_{+i} = \frac{k_B T}{h} e^{-\left(G^0_{TS,i} + \sum_j \nu_{+ij} G^0_j\right)/k_B T} \prod_j a_j^{-\nu_{+ij}} e^{\frac{\beta_i n_i e_0 \left(E - E_{ref}\right)}{k_B T}} \qquad \textbf{[7.16]}$$

and

$$r_{-i} = \frac{k_B T}{h} e^{-\left(G^0_{TS,i} + \sum_j \nu_{-ij} G^0_j\right)/k_B T} \prod_j a_j^{-\nu_{-ij}} e^{\frac{(\beta_i - 1) n_i e_0 \left(E - E_{ref}\right)}{k_B T}} \quad \textbf{[7.17]}$$

where G_j^0 and a_j are the standard state chemical free energy and thermodynamic activity of species j, $\nu_{\pm ij}$ is the stoichiometric coefficient of species j in half-step $\pm i$, n_i is the number of electrons transferred in step i, and β_i is the symmetry factor of step i. The symmetry factor, $0 < \beta_i < 1$, captures the influence of the electric potential, E, on the electrochemical potential of transition state i and may be physically interpreted as the fraction of charge transferred to (from) the electrode to form the transition state in the anodic (cathodic) half-step (*198*, *204*). The difference of half-step TST rates in Eqs. **7.16**-**7.17** yields the elementary step rate function

$$r_i = \frac{k_B T}{h} \left(e^{-\frac{\Delta G^0_{TS,+i}}{k_B T}} \prod_j a_j^{-\nu_{+ij}} e^{\frac{\beta_i n_i e_0 \left(E - E_{ref}\right)}{k_B T}} - e^{-\frac{\Delta G^0_{TS,-i}}{k_B T}} \prod_j a_j^{-\nu_{-ij}} e^{\frac{(\beta_i - 1) n_i e_0 \left(E - E_{ref}\right)}{k_B T}} \right) \quad \textbf{[7.18]}$$

where $\Delta G^0_{TS,\pm i} \equiv G^0_{TS,i} + \sum_j \nu_{\pm ij} G^0_j$. Choosing the reference condition (ref) to be an equilibrium state with defined electric potential, temperature, and species activities allows Eq. **7.18** to be recast in the form of the Butler-Volmer equation (Eq. **7.5**)

$$r_i = r_{i,eqm} \left(\prod_j \left(\frac{a_j}{a_{j,eqm}} \right)^{-\nu_{+ij}} e^{\frac{\beta_i n_i e_0 \eta}{k_B T}} - \prod_j \left(\frac{a_j}{a_{j,eqm}} \right)^{-\nu_{-ij}} e^{\frac{(\beta_i - 1) n_i e_0 \eta}{k_B T}} \right) \quad \textbf{[7.19]}$$

where $r_{i,eqm}$ is the unidirectional rate at equilibrium (i.e. the exchange rate). The analogous presence of transfer coefficients in Eq. **7.5** and symmetry factors in Eq. **7.19** motivates definition of elementary half-step transfer coefficients to codify the apparent consonance of α_a (α_c) and β_i ($1 - \beta_i$). By analogy to Eqs. **7.6**-**7.7**, we define

$$\alpha_{\pm i} \equiv \frac{k_B T}{e_0}\left(\frac{\partial \ ln\, r_{\pm i}}{\partial E}\right)_{G_j^0, a_j} = \begin{Bmatrix} \beta_i n_i & for\ +i \\ (\beta_i - 1)n_i & for\ -i \end{Bmatrix} \quad \textbf{[7.20]}$$

Eq. **7.20** in hand, we write generally elementary half-step rate constant functions

$$k_{\pm i} = \frac{k_B T}{h} e^{-\frac{\left(G_{TS,i}^0 + \sum_j \nu_{\pm ij} G_j^0 - \alpha_{\pm i} e_0 (E - E_{ref})\right)}{k_B T}} \quad \textbf{[7.21]}$$

and rate functions

$$r_{\pm i} = k_{\pm i} \prod_j a_j^{-\nu_{\pm ij}} \quad \textbf{[7.22]}$$

which act, interchangeably, as the canonical independent variables in TST-based Taylor expansion of net, forward, and reverse rates of composite reactions (i.e. reaction sensitivity in Eq. **7.11** is equivalently defined as a derivative with respect to $r_{\pm i}$ or $k_{\pm i}$) (*140*). Hereinafter, we employ the definitions of $k_{\pm i}$ in Eq. **7.21** and $r_{\pm i}$ in Eq. **7.22** to (i) detail, step-by-step, the construction of r_{TST}, the net TST rate function (remainder of Section 7.4.1), (ii) derive and utilize a new, general formulation of α in exclusive terms of β_i, n_i, $X_{RC,i}$, and Z_i (Sections 7.4.2-7.4.3), and (iii) demonstrate the necessity of *unidirectional* TST rate functions ($\vec{r}_{TST}, \overleftarrow{r}_{TST}$) and correspondent *unidirectional* degrees of rate control ($\vec{X}_{RC,i}, \overleftarrow{X}_{RC,i}$) to competently describe reversible electrochemical reactions — for which net descriptors (e.g. α) are insufficient for mechanistic study (Section 7.4.4).

The TST-based Taylor series approximation of the net rate is formulated by expanding $\ln r$ about a steady-state reaction condition $\boldsymbol{X}$, which contains the steady-state species activities, overpotential, reaction temperature, *etc*. Neglecting ≥second-order terms, $\ln r$ in the vicinity of $\boldsymbol{X}$ is

$$ln\, r \approx ln\, r_{TST} \equiv ln\, r|_{\boldsymbol{X}} + \sum_{\pm i} \left(\frac{\partial\, ln\, r}{\partial\, ln\, r_{\pm i}} \right)_{r_{\mp i}, r_{\pm j}} \left(ln\, r_{\pm i} - ln\, r_{\pm i}\big|_{\boldsymbol{X}} \right) \qquad \textbf{[7.23]}$$

where r_{TST} is defined to be the first-order Taylor series approximation to the exact, complete rate function r and, by virtue of its method of construction, r_{TST} is equal to r and all first derivatives of r at condition $\boldsymbol{X}$ — as is illustrated in Scheme 7.1.

Substituting the definition of reaction sensitivity (Eq. **7.11**) and separating vector ($\ln r_{\pm i}$) and scalar ($\ln r_{\pm i}\big|_{\boldsymbol{X}}$) terms, we have

$$ln\, r_{TST} = ln\, r|_{\boldsymbol{X}} + \sum_{\pm i} s_{\pm i}\, ln\, r_{\pm i} - \sum_{\pm i} s_{\pm i}\, ln\, r_{\pm i}\big|_{\boldsymbol{X}} \qquad \textbf{[7.24]}$$

which, via exponentiation, we convert from a sum to product

$$r_{TST} = r|_{\boldsymbol{X}} \times \prod_{\pm i} r_{\pm i}^{s_{\pm i}} \times \left(\prod_{\pm i} r_{\pm i}^{s_{\pm i}}\big|_{\boldsymbol{X}} \right)^{-1} \qquad \textbf{[7.25]}$$

Collecting the scalar terms, we find that the rate of a composite reaction is, in essence, a sensitivity-weighted geometric average of the rates of all constituent half-steps

$$r_{TST} = \kappa_{app} \prod_{\pm i} r_{\pm i}^{s_{\pm i}} \qquad \textbf{[7.26]}$$

where $\kappa_{app} = r|_{\boldsymbol{X}} \left(\prod_{\pm i} r_{\pm i}^{s_{\pm i}}\big|_{\boldsymbol{X}} \right)^{-1}$ is a scalar quantity between zero and unity formally interpreted as the apparent TST transmission coefficient of the composite reaction — as detailed by Foley and Bhan (*140*).

Scheme 7.1: Depiction of the relationship between $\boldsymbol{r}$ and the first-order Taylor approximation $\boldsymbol{r_{TST}}$

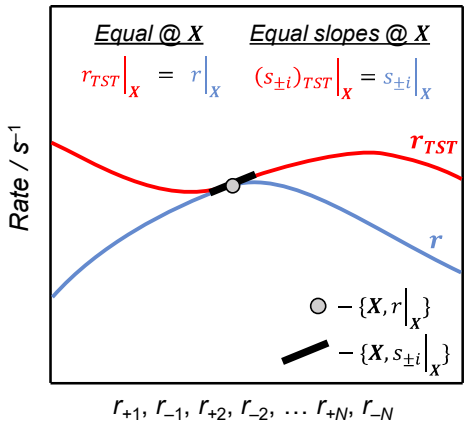

Taylor expansion of r about the condition $\boldsymbol{X}$ gives the first-order Taylor series TST rate function r_{TST} which is identical to r in the vicinity of $\boldsymbol{X}$ such that all first derivatives of r and r_{TST} are equal at condition $\boldsymbol{X}$. First derivatives, $s_{\pm i}$, are defined in Eq. **7.11**.

The general expression of reaction rate in explicit terms of $r_{\pm i}$ enables formulation of r_{TST} in a form identical to that of an elementary step. Substituting elementary half-step TST rates per Eqs. **7.21** and **7.22** into Eq. **7.26** gives

$$r_{TST} = \kappa_{app}\left(\frac{k_B T}{h}\right)^{\sum s_{\pm i}} e^{-\sum s_{\pm i}\left(G^0_{TS,i}+\sum_j \nu_{\pm ij} G^0_j - \alpha_{\pm i} e_0 (E-E_{ref})\right)/k_B T} \prod_j a_j^{-\sum s_{\pm i}\nu_{\pm ij}} \qquad \textbf{[7.27]}$$

which is simplified by recognizing reaction sensitivities sum to unity, as proven by Foley and Bhan (*140*), and by substituting kinetic (Eq. **7.13**) and thermodynamic (Eq. **7.14**) degrees of rate control

$$r_{TST} = \kappa_{app}\frac{k_B T}{h} e^{-\frac{\left(\sum X_{RC,i} G^0_{TS,i} + \sum X_{TRC,j} G^0_j\right)}{k_B T}} e^{\frac{\sum s_{\pm i}\alpha_{\pm i} e_0 (E-E_{ref})}{k_B T}} \prod_j a_j^{-X_{TRC,j}} \qquad \textbf{[7.28]}$$

where $G^0_{TS,app} = \sum X_{RC,i}\, G^0_{TS,i}$ and $G^0_{IS,app} = -\sum X_{TRC,j}\, G^0_j$ define the apparent rate-controlling transition state and initial state such that the overall reaction sequence behaves as if it were a single elementary step with initial state energy $-\sum X_{TRC,j}\, G^0_j$ and transition state energy $\sum X_{RC,i}\, G^0_{TS,i}$. In this sense, Eq. **7.27** codifies the kinetic interpretation of the overall reaction as a single apparent elementary step which is a weighted-average of all

constituent steps — the contribution of each quantified by elementary half-step reaction sensitivities. This interpretation, established for thermochemical systems (*140*), is yet to be realized for electrochemical reactions, which are distinguished by the electronic driving force, η, moderated by $\sum s_{\pm i}\,\alpha_{\pm i}$.

7.4.2 Electrochemical transfer coefficient: Relationship to elementary step kinetics and thermodynamics

We rigorously interpret α as the sensitivity-weighted average of elementary half-step transfer coefficients by applying the general definition of the transfer coefficient (Eq. **7.8**) to Eq. **7.28**

$$\alpha \equiv \frac{k_B T}{e_0}\left(\frac{\partial\, ln(J)}{\partial E}\right) = \frac{k_B T}{e_0}\left(\frac{\partial\, ln(r_{TST})}{\partial E}\right) = \sum s_{\pm i}\,\alpha_{\pm i} \qquad \textbf{[7.29]}$$

and, in doing so, facilitate the construction of a general expression for α that compendiously synthesizes the kinetic and thermodynamic/stoichiometric contributions of each elementary (half-)step to the observed Tafel slope (Scheme 7.2). The general formulation of α, in a form more intuitive and explicative than Eq. **7.29**, is derived by substitution of elementary step symmetry factors for $\alpha_{\pm i}$ via Eq. **7..20**

$$\alpha = \sum_{+i} s_{+i}\beta_i n_i + \sum_{-i} s_{-i}(\beta_i - 1)n_i \qquad \textbf{[7.30]}$$

and simplifying to a single sum by re-expressing s_{-i} as $-s_{+i}Z_i$ via Eq. **7.12**

$$\alpha = \sum_{+i} s_{+i} n_i (\beta_i(1 - Z_i) + Z_i) \qquad \textbf{[7.31]}$$

Now, to write α in terms of steps rather than half-steps, we combine Eqs. **7.12** and **7.13** to substitute $X_{RC,i} = s_{+i}(1 - Z_i)$ and find

$$\alpha = \sum_{i} X_{RC,i} n_i \left(\beta_i + \frac{Z_i}{1 - Z_i}\right) \qquad \textbf{[7.32]}$$

which quantifies α in explicit terms of stoichiometry (n_i), symmetry factors (β_i), and the salient kinetic ($X_{RC,i}$) and thermodynamic (Z_i) descriptors of elementary steps.

We regard Eq. **7.32** as a mathematically- and physically-edifying construal of α competent for generic application to any reaction network or overpotential regime — as we illustrate hereinafter and summarize in Scheme 7.2. The formulation of α as a function of Z_i in Eq. **7.32**, for example, is unprecedented and essential to (i) proof of Eq. **7.9** on a bare surface and with a single non-equilibrated elementary step (Section E.1.1), (ii) disproof of Eq. **7.9** if kinetically-irrelevant steps are not equilibrated (Section E.1.2) and (iii) demonstration that the consistent observation of $b \approx 120\ \mathrm{mV/dec}$ at large overpotential is independent of the identity of the rate-determining step and is fundamentally caused by elementary step irreversibility — not by coverage effects, as is often suggested (*203*, *208*, *213–216*).

Scheme 7.2: General and case-specific expressions for $\boldsymbol{\alpha}$

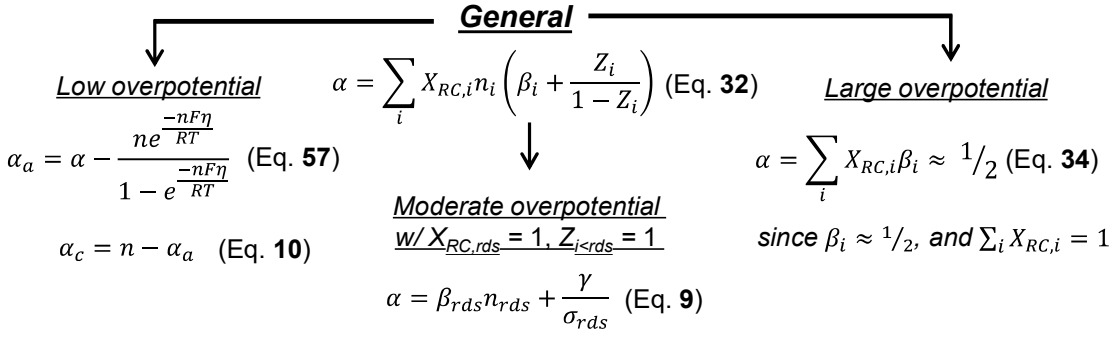

Eqs. **7.32**, **7.34**, **7.57** are derived herein for the first time. Eqs. **7.9** and **7.10** are established results, proven herein from the general expression for α, Eq. **7.32**. "Low overpotential" results are subject to the condition that $\sigma_i = 1$ for all steps i.

7.4.3 Electrochemical transfer coefficient: Universal convergence to ½ at large overpotential

Decades of experimental study of electrochemical kinetics has established, but not unambiguously explained, the preponderance of Tafel slopes near $120\ \mathrm{mV/dec}$ at large

overpotential (*216–221*). Thorough theoretical investigation of electrocatalytic reactions such as oxygen reduction/evolution (ORR/OER) (*203*, *208*, *215*), chlorine evolution (CER) (*205*), and hydrogen evolution/oxidation (HER/HOR) (*208*, *216*) have all affirmed these experimental observations and demonstrated, through use of detailed (micro-)kinetic models, that α appears to converge to ½ at large anodic and cathodic overpotential, irrespective of the identity of the rate-determining step. Indeed, seminal work from Takanabe and co-workers (*208*) demonstrates that, regardless of the kinetic-relevance of electrochemical elementary steps, the Tafel slopes of HER/HOR and ORR/OER consistently converge to $120\,\mathrm{mV/dec}$ for sufficiently large overpotential, provided chemical steps (e.g. $2H^* \rightleftharpoons H_2 + 2*$) are kinetically-irrelevant. In other words, the distribution of rate control between electrochemical steps *has no effect* on the Tafel slope. This result is in evident disagreement with Eq. **7.9** — a discrepancy commonly attributed to changes in surface coverage (*203*, *208*, *213–216*).

We contend that, while coverages appreciably change at large overpotential, the fundamental reason for the (i) breakdown of Eq. **7.9** and (ii) preponderance of $b \approx 120\,\mathrm{mV/dec}$ is that large η compels irreversibility of all electrochemical elementary steps. The application of overpotential drives the thermodynamic affinity, or equilibrium constant ($K_i = k_{+i}/k_{-i}$), of each step by $(60\,\mathrm{mV/dec})^{-1} = 17\,\mathrm{dec/V}$ — meaning $\eta = 1\,\mathrm{V}$ biases, in unison, all electrochemical steps to such an extent that the (quasi-)equilibrium approximation is physically unreasonable. Consider, for example, two kinetically-facile steps in series, $R^- + I_1^* \leftrightarrow I_2^* + e^-$ and $R^- + I_2^* \leftrightarrow I_3^* + e^-$, that precede the rate-determining step at $\eta = 1\,\mathrm{V}$ and, as is convention, are assumed equilibrated. Since both steps are, by definition, equilibrated at $\eta = 0\,\mathrm{V}$, the ratio $\theta_{I_3^*}/\theta_{I_1^*}$ at $\eta = 1\,\mathrm{V}$ must

increase relative to that at $\eta = 0\,\mathrm{V}$ by a factor of $(17\,\mathrm{dec/V}) \cdot 1\,\mathrm{V} \cdot 2 = 10^{34}$ — a variation correspondent to one molecule of I_1^* for every ten billion moles of I_3^*. We regard such a condition as infeasible and indicative of the necessary irreversibility of electrochemical elementary steps.

We explicate the compulsory convergence of $\alpha \approx$ ½ for sufficiently large η by leveraging the general formulation of α in terms of degrees of rate control and reversibilities (Eq. **7.32**) under the condition that $Z_i \ll 1$ for all i

$$\alpha = \sum_i X_{RC,i} n_i \beta_i \qquad \textbf{[7.33]}$$

We highlight that the simplification of α solely in terms of $X_{RC,i}$, n_i, and β_i is only possible because of the rigorous connection of kinetic and thermodynamic information provided by reaction sensitivities (i.e. $Z_i = -s_{-i}/s_{+i}$ per Eq. **7.12**) which enables unambiguous deconvolution of the distinct additive contributions of β_i and $Z_i(1 - Z_i)^{-1}$. Eq. **7.33** is further simplified by assuming all kinetically-relevant steps are electrochemical (i.e. $X_{RC,i} = 0$ for all i such that $n_i = 0$) and all electrochemical steps involve transfer of a single electron (i.e. $n_i = 1$ for all $n_i \neq 0$) since concerted multi-electron transfer is improbable (*198*). Now, we have

$$\alpha = \sum_i X_{RC,i} \beta_i \qquad \textbf{[7.34]}$$

and, since symmetry factors are typically ~½ and $\Sigma_i X_{RC,i} = 1$,

$$\alpha \approx {}^1\!/_2 \sum_i X_{RC,i} = {}^1\!/_2 \qquad \textbf{[7.35]}$$

demonstrating that large overpotential invariably compels Tafel slopes near $120\,\mathrm{mV/dec}$ regardless of the identity of rate-controlling step(s) simply because $\beta_i \approx$ ½ and $Z_i \ll 1$.

We reinforce our contention that irreversibility is the fundamental cause of $\alpha \approx ½$ at large overpotential by deriving, simply from $Z_i \ll 1$, the appreciation in intermediate surface coverages often attributed as the reason for invalidity of Eq. **7.9**. To do so, we again leverage $s_{\pm i}$-based connections between macrokinetic observables and microkinetic descriptors. In particular, if all elementary steps involve at most one surface intermediate, then $-X_{TRC,j^*}$ is equal to the coverage of surface species j^*

$$\theta_{j^*} = -X_{TRC,j^*} = -\sum_{\pm i} s_{\pm i}\nu_{\pm ij} \qquad \textbf{[7.36]}$$

as proven by Foley and Bhan (*140*). Under the condition that $Z_i \ll 1$, we have $s_{-i} = -Z_i s_{+i} = 0$ per Eq. **7.12** and $X_{RC,i} = s_{+i} + s_{-i} = s_{+i}$ per Eq. **7.13**. Therefore, Eq. **7.36** simplifies to

$$\theta_{j^*} = -\sum_{i} X_{RC,i}\nu_{+ij} \qquad \textbf{[7.37]}$$

where $\nu_{+ij} = 0$ or -1 per the aforementioned condition that all elementary steps involve at most one adspecies. Eq. **7.37** reveals that the condition of irreversibility throughout a reaction sequence necessitates a surface wherein coverages of all adspecies are simply equal to the sum of the degrees of rate control of steps which consume them. Thus, if all steps are irreversible and there is a single rds, then the surface species reacting in the rds will be the most abundant surface intermediate ($MASI$) — rationalizing consistent observation of the precipitous increase in kinetically-relevant surface intermediate coverage at large overpotential (*203*, *208*, *216*, *220*, *222*, *223*). Derivation of these surface dynamics simply from the condition $Z_i \ll 1$ demonstrates that 'coverage effects' are not the fundamental reason for inappropriateness of Eq. **7.9** at large overpotential; rather, both

$\alpha \approx$ ½ per Eq. **7.35** and $\theta_{MASI} = X_{RC,rds} = 1$ per Eq. **7.37** are direct consequences of $Z_i \ll 1$ induced by increasing η.

In the following, we explicate the felicity of Eqs. **7.35** and **7.37** to describe and predict trends in Tafel slope, surface coverage, and X_{RC} with overpotential by examination of a simple, familiar mechanism for the hydrogen oxidation reaction (HOR).

7.4.4 Case Study I: Hydrogen oxidation reaction (HOR) in alkaline media

Consider the two-step Heyrovsky-Volmer mechanism in Table 7.1 wherein (i) H_2 dissociatively adsorbs on a vacant site, $*$, with assistance from OH^- anions (Heyrovsky step) and, subsequently, (ii) the adsorbed H^* is recovered by OH^- to form product H_2O and complete the catalytic cycle (Volmer step) (*208*). The exact, closed-form steady-state rate expression for the two-step HOR is

$$r = \frac{k_{+1}k_{+2}a_{OH^-}^2 a_{H_2} - k_{-1}k_{-2}a_{H_2O}^2}{k_{+1}a_{OH^-}a_{H_2} + k_{-1}a_{H_2O} + k_{+2}a_{OH^-} + k_{-2}a_{H_2O}} \qquad \textbf{[7.38]}$$

with η-dependent rate constants referenced to $\eta = 0$ V such that

$$k_{\pm i} = k_{\pm i}^0 e^{\frac{\alpha_{\pm i} e_0 \eta}{k_B T}} \qquad \textbf{[7.39]}$$

with $k_{\pm i}^0$ and symmetry factors listed in Table 7.1. Closed-form expressions for surface coverages and elementary step reversibilities are also readily derivable and are provided in Section E.2.

Rate constants are chosen such that HOR is equilibrated at zero overpotential and the Heyrovsky step is expected to be equilibrated since $k_{-1} \gg k_{+2}$. Conventional interpretation of this mechanism therefore posits that the Volmer step is rate-determining and that the transfer coefficient is, per Eq. **7.9**, $\alpha = \beta_2 + n_1 = \frac{3}{2}$, correspondent to $b = \left(60\frac{\text{mV}}{\text{dec}}\right) \cdot \left(\frac{3}{2}\right)^{-1} = 40\frac{\text{mV}}{\text{dec}}$. This analysis is indeed correct at moderate overpotential;

however, as we detail in the following, $\eta \gtrsim 0.4\ \mathrm{V}$ promotes anodic half-steps to such an extent that (i) the quasi-equilibrium (QE) approximation for step 1 is inappropriate, (ii) $\alpha = ½$ irrespective of the distribution of rate control, and (iii) $\theta_* = X_{RC,1}$ and $\theta_{H^*} = X_{RC,2}$ per Eq. **7.37**.

Table 7.1: Heyrovsky-Volmer hydrogen oxidation reaction (HOR) mechanism

#	Step	Rate constants @ $\eta = 0\ V$	Symmetry factor
1	$H_2 + OH^- + * \rightleftharpoons H^* + H_2O + e^-$	$k_{+1}^0 = 1,\ k_{-1}^0 = 10^5$	$\beta_1 = ½$
2	$H^* + OH^- \rightleftharpoons H_2O + * + e^-$	$k_{+2}^0 = 3,\ k_{-2}^0 = 3 \cdot 10^{-5}$	$\beta_2 = ½$

$k_{\pm i}^0$ is half-step rate constant $k_{\pm i}$ at $\eta = 0\ \mathrm{V}$. Thermodynamic activities of fluid-phase species are $a_{OH^-} = a_{H_2} = a_{H_2O} = 1$ for simplicity.

Figure 7.1 shows rates (r), reversibilities (Z_1 and Z_2), coverages (θ_* and θ_{H^*}), and degrees of rate control ($X_{RC,1}$ and $X_{RC,2}$) of the HOR mechanism summarized in Table 1. At $\eta = 0\ \mathrm{V}$, the surface is bare and the reaction is at equilibrium, evidenced by $r \to 0$ and $Z_1 = Z_2 = 1$. With modest increase to overpotential, step 2 becomes irreversible ($Z_2 = 0$) and is rate-determining ($X_{RC,2} = 1$) while step 1 remains equilibrated ($Z_1 = 1$) and vacant sites remain the $MASI$ ($\theta_* = 1$). Indeed, throughout the moderate overpotential range $0.05\ \mathrm{V} < \eta < 0.25\ \mathrm{V}$, reversibilities, coverages, and degrees of rate control entirely conform with the aforementioned conventional kinetic interpretation, and Eq. **7.9** correctly predicts the observed Tafel slope $40\ \mathrm{mV/dec}$. Beyond $\eta = 0.25\ \mathrm{V}$, however, step 1 de-equilibrates and, for $\eta > 0.45\ \mathrm{V}$, is impelled to irreversibility by the profound thermodynamic bias manifest in anodic/forward rate constants incremented by $17\ \mathrm{dec/V} \cdot 0.45\ \mathrm{V} = 10^{7.6}$ relative to reverse/cathodic rate constants. In this irreversible regime, the rate control of each step is determined solely by forward rate constants and, therefore,

$$X_{RC,1} = \frac{k_{+2}}{k_{+1} + k_{+2}} \qquad \textbf{[7.40]}$$

and

$$X_{RC,2} = \frac{k_{+1}}{k_{+1} + k_{+2}} \qquad \textbf{[7.41]}$$

which are respectively (i) $\frac{3}{4}$ and $\frac{1}{4}$ per k_{+i}^{0} in Table 1 and (ii) equal to θ_* and θ_{H^*} per Eq. **7.37** — as is evident in Fig. 7.1B (see Section E.2 for derivation of Eqs. **7.40**-**7.41**).

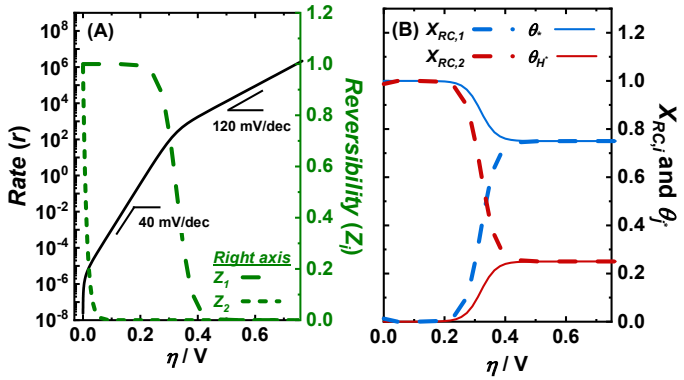

Figure 7.1: (A) *Left*: Rate (r) as a function of overpotential. Tafel slopes indicated in moderate and high overpotential regimes are respectively described by Eq. **7.9** and Eq. **7.35**. *Right*: Elementary step reversibilities (Z_i) as a function of overpotential. (B) Elementary step degrees of rate control ($X_{RC,i}$) and surface coverages (θ_{j^*}) as a function of overpotential. Congruence between blue- and red-colored lines in the high overpotential regime is predicted by Eq. **7.37**.

The equality of $X_{RC,1}$ and $X_{RC,2}$ with θ_* and θ_{H^*} evinces Eq. **7.37** and thusly verifies that changes in adsorbate coverage at large overpotential are a *consequence* of elementary step irreversibility and not the fundamental *cause* of error in Eq. **7.9**. The change in Tafel slope from 40 mV/dec to 120 mV/dec illustrated in Fig. 7.1A plainly coincides with de-equilibration of step 1 in full accord with Eq. **7.35**, which, for the HOR reaction, takes the particular form

$$\alpha = \sum X_{RC,i}\beta_i n_i = \frac{k_{+1}\beta_1 + k_{+2}\beta_2}{k_{+1} + k_{+2}} \qquad \textbf{[7.42]}$$

per $X_{RC,i}$ from Eqs. **7.40**-**7.41**. Since $\beta_1 = \beta_2 = ½$ in this example, α will equal always ½ for any $X_{RC,1}$ and $X_{RC,2}$ — exemplifying the constancy of cardinal Tafel slope $b \approx 120\ \mathrm{mV/dec}$ at large overpotential, which *cannot* be used to infer $X_{RC,i}$ unless symmetry factors of candidate rate-determining steps are distinct and known *a priori*. This result decidedly explains the consistent observation of transition in Tafel slope at sufficient overpotential from $b < 60\ \mathrm{mV/dec}$ — indicating one or more QE steps preceding the rds — to $b \approx 120\ \mathrm{mV/dec}$ (*205*, *208*, *213*, *215–221*). In this kinetic regime, $\alpha = (m-1) + ½$ no longer indicates that the m^{th} electron transfer is rate-determining per Eq. **7.9** and, therefore, new mathematical tools must be relied upon for mechanistic analysis.

We purport that Eq. **7.37**, established herein for the first time, motivates an alternative method to interrogate candidate rate-determining steps at high overpotential simply by measurement of intermediate surface coverages, which rigorously reflect the kinetic control of constituent steps (e.g. $\theta_{H^*} = X_{RC,2}$). This formalized connection between θ_{j^*} and $X_{RC,i}$ epitomizes the mathematical clarity and kinetic insight proffered by interpretation of electrochemical reactions in terms of r_{TST} and reaction sensitivities, and, we contend, corroborates the mechanistic utility of our approach.

In what follows, we extend our mathematical framework to low overpotential regimes wherein all steps exhibit finite reversibility (e.g. $\eta < 0.05\ \mathrm{V}$ in Fig. 7.1) and, therefore, observed Tafel slopes conflate anodic and cathodic reaction paths — necessitating simultaneous quantification of α_a and α_c for virtuous kinetic and mechanistic assessment. To this end, we detail new mathematical tools that unify the Butler-Volmer equation with transition state theory and *unidirectional* degrees of rate control (i.e. degrees of rate control of J_a or J_c). In doing so, we prescribe new methods to quantitatively de-convolute anodic

and cathodic contributions to all macrokinetic observables —including rate, reaction order, and Tafel slope — solely from kinetic measurements of the net current, J, at low overpotential.

7.4.5 Electrochemical transfer coefficient: Relationship to the Butler-Volmer equation at low overpotential

We detail the construction of a generalized Butler-Volmer TST-form rate equation (r_{BV-TST}) by scrutinizing $\vec{r}_{TST}$ and $\overleftarrow{r}_{TST}$, derivations of which are detailed in Section E.3 and follow an identical procedure to that for r_{TST}, yielding

$$\vec{r}_{TST} = \vec{\kappa}_{app} \frac{k_B T}{h} e^{-\frac{\left(\sum \vec{X}_{RC,i} G^0_{TS,i} + \sum \vec{X}_{TRC,j} G^0_j\right)}{k_B T}} e^{\frac{\vec{\alpha} e_0 (E - E_{ref})}{k_B T}} \prod_j a_j^{-\vec{X}_{TRC,j}} \qquad \textbf{[7.43]}$$

which mirrors $\overleftarrow{r}_{TST}$, omitted for brevity. The unidirectional degrees of rate control ($\vec{X}_{RC,i}$, $\vec{X}_{TRC,j}$) and transfer coefficients ($\vec{\alpha}$) which parameterize Eq. **7.43** are defined in terms of unidirectional reaction sensitivities

$$\vec{s}_{\pm i} \equiv \left(\frac{\partial \ln \vec{r}}{\partial \ln r_{\pm i}}\right)_{r_{\mp i}, r_{\pm j}} = \left(\frac{\partial \ln \vec{r}}{\partial \ln k_{\pm i}}\right)_{k_{\mp i}, k_{\pm j}} \qquad \textbf{[7.44]}$$

which, per the principle of microscopic reversibility, are constrained, not by Eq. **7.12**, but

$$s_{\pm i} = \frac{\vec{s}_{\pm i} - Z_{eff} \overleftarrow{s}_{\pm i}}{1 - Z_{eff}} \qquad \textbf{[7.45]}$$

where $Z_{eff} \equiv \overleftarrow{r}/\vec{r}$ is the thermodynamic descriptor of the composite reaction akin to $Z_i = r_{-i}/r_{+i}$ for elementary steps (*95*, *172*). Eq. **7.45** establishes a quantitative relationship between unidirectional, elementary half-step kinetic descriptors ($\vec{s}_{\pm i}$, $\overleftarrow{s}_{\pm i}$) and the salient thermodynamic measure of the overall reaction sequence (Z_{eff}) which has, heretofore, been unrecognized in the context of electrochemical reactions and is crucial to re-expressing α in terms of

$$\vec{\alpha} \equiv \sum \vec{s}_{\pm i}\, \alpha_{\pm i} = \alpha_a \qquad \textbf{[7.46]}$$

and

$$\overleftarrow{\alpha} \equiv \sum \overleftarrow{s}_{\pm i}\, \alpha_{\pm i} = -\alpha_c \qquad \textbf{[7.47]}$$

where the negative sign in Eq. **7.47** derives from the convention of defining both anodic (α_a) and cathodic (α_c) transfer coefficients to be positive. The definition of α_a and α_c in terms of unidirectional reaction sensitivities $\vec{s}_{\pm i}$ and $\overleftarrow{s}_{\pm i}$ is essential; α_a and α_c are fundamentally unidirectional descriptors and, therefore, cannot be faithfully described by net descriptors (i.e. $s_{\pm i}$ and $X_{(T)RC,i}$) alone unless the reaction is irreversible and α equals α_a or α_c — as is the case for $\eta > 50$ mV in Case Study I and in recent applications of degree of rate control to electrochemical reactions (*197*, *210*).

By leveraging connections between kinetics and thermodynamics, however, we can recast α_a and α_c in terms of α through the process of constructing r_{BV-T} and validating Eq. **7.10** (i.e. $\alpha_a + \alpha_c = n/\sigma_{rds}$). To do so, we evoke the De Donder equation for a composite reaction sequence in the context of the unidirectional TST rate functions

$$\frac{\overleftarrow{r}_{TST}}{\vec{r}_{TST}} = Z_{eff} = \prod_i Z_i \qquad \textbf{[7.48]}$$

Z_{eff} is, in general, a complex function of reactant, product, intermediate, and transition state activities (*95*, *172*) and is only a purely thermodynamic, path-independent entity if (i) there exists a single non-equilibrated, rate-determining step such that all path-dependence is captured by σ_{rds} or (ii) the stoichiometric number of each step in the reaction is unity such that $\sigma_{rds} = 1$ unequivocally. We discuss construction of r_{BV-T} from the first condition in Section E.4 and consider hereinafter only the case of *stoichiometric regularity* (i.e. $\sigma_i = 1$ for all i) — which is more decidable than the case of a sole non-equilibrated

step and is applicable for many reactions of interest (e.g. ORR/OER (*200*, *203*, *208*), CER (*206*, *222*), HER/HOR (*208*, *216*, *217*, *219*, *224*), CO oxidation (*225*, *226*) and reduction (*227*, *228*), and CO_2 reduction (*229*, *230*)).

If the stoichiometric number of all steps is unity, Z_{eff} can be written exclusively in terms of measurable quantities: the applied overpotential (η), thermodynamic activity of reactants and products (a_j), reaction stoichiometry (ν_j, n), and standard state free energy change of the overall reaction (ΔG^0)

$$\frac{\overleftarrow{r}_{TST}}{\vec{r}_{TST}} = \left(\frac{\prod_j a_j^{\nu_j}}{exp\left(-\frac{\Delta G^0 - ne_0\eta}{k_B T}\right)} \right) \quad \textbf{[7.49]}$$

The right-hand side of Eq. **7.49** is a path-independent, thermodynamic entity and, crucially, has no dependence on intermediates and transition states. Therefore, the left-hand side, which is an identical function (*172*), must not have any dependence on intermediate or transition state energies and must have a dependence on a_j and η which is identical to that of the right-hand side. Substituting the full functional form of $\vec{r}_{TST}$ and $\overleftarrow{r}_{TST}$ (Eq. **7.43**), we find that requisite functional equivalence of the left- and right-hand sides of Eq. **7.49** implies

$$\vec{X}_{RC,i} = \overleftarrow{X}_{RC,i} = X_{RC,i} \quad \textbf{[7.50]}$$

$$\vec{X}_{TRC,m} = \overleftarrow{X}_{TRC,m} = X_{TRC,m} \quad for\ intermediates\ m \quad \textbf{[7.51]}$$

since the functional dependence of $\vec{r}_{TST}$ and $\overleftarrow{r}_{TST}$ on intermediates and transition states must be identical, and

$$\vec{X}_{TRC,k} - \overleftarrow{X}_{TRC,k} = \nu_k \quad for\ reactants\ and\ products\ k \quad \textbf{[7.52]}$$

$$\vec{\alpha} - \overleftarrow{\alpha} = n \quad \textbf{[7.53]}$$

the latter being equivalent to Eq. **7.10** with σ_{rds} trivially equal to unity since $\sigma_i = 1$ for each step. The substitution of $\vec{r}_{TST}$ and $\overleftarrow{r}_{TST}$ (Eq. **7.43**) into Eq. **7.49** and the observations therefrom are detailed in Section E.4.

We interpret Eqs. **7.50-53** as the mathematical manifestations of the principles of microscopic reversibility and mass action extended to reversible composite reaction sequences which behave, kinetically and thermodynamically, akin to elementary steps. That is to say (i) that $\vec{X}_{RC,i} = \overleftarrow{X}_{RC,i}$ (Eq. **7.50**) codifies the requirement that the forward and reverse routes are the microscopic reverse of one another, and (ii) that $\vec{X}_{TRC,m} = \overleftarrow{X}_{TRC,m}$ (Eq. **7.51**) and $\vec{X}_{TRC,k} - \overleftarrow{X}_{TRC,k} = \nu_k$ (Eq. **7.52**) codify the equivalence of stoichiometric coefficients and unidirectional reaction orders prescribed by the law of mass action. We emphasize that the extension of these elementary step principles to composite reactions is not generally appropriate; without the condition of stoichiometric regularity, $\vec{X}_{RC,i} \neq \overleftarrow{X}_{RC,i}$ and the overall forward and reverse reactions are *not* microscopically reversible, but, rather, proceed via kinetically-distinct paths with distinct apparent transition states (i.e.$\sum \vec{X}_{RC,i}\, G^0_{TS,i} \neq \sum \overleftarrow{X}_{RC,i}\, G^0_{TS,i}$) (*172*). Only with the simplifications proffered by elementary step behavior (Eqs. **7.50-7.53**) can the difference between $\vec{r}_{TST}$ and $\overleftarrow{r}_{TST}$ be written in the Butler-Volmer form

$$r_{BV-TST} = k_{BV-TST}\left[e^{\frac{\vec{\alpha} e_0 \eta}{k_B T}} e^{-\frac{\sum_k \vec{X}_{TRC,k} G_k}{k_B T}} - e^{\frac{\overleftarrow{\alpha} e_0 \eta}{k_B T}} e^{-\frac{\sum_j \overleftarrow{X}_{TRC,k} G_k}{k_B T}}\right] \qquad \textbf{[7.54]}$$

where $G_k = G^0_k + k_B T \ln(a_k)$ and the Butler-Volmer rate constant is

$$k_{BV-TST} = \vec{\kappa}_{app} \frac{k_B T}{h} e^{-\frac{\sum_i X_{RC,i} G^0_{TS,i}}{k_B T}} e^{-\frac{\sum_m X_{TRC,m} G_m}{k_B T}} \qquad \textbf{[7.55]}$$

which is condition-dependent, unlike the elementary step analogue r_{eqm} (Eq. **7.19**). Indeed, the functional forms of Eqs. **7.54** and **7.55** illustrate that, despite the simplifications conferred by Eqs. **7.50**-**7.53**, Butler-Volmer rate constants, reaction orders, and transfer coefficients of composite reactions are all complex functions of the net ($s_{\pm i}$), anodic ($\vec{s}_{\pm i}$), and/or cathodic ($\overleftarrow{s}_{\pm i}$) kinetic control of each elementary half-step and, therefore, cannot be considered constant parameters in the fitting or interpretation of experimental data. The combination of Eqs. **7.52** and **7.53** with the thermodynamic constraint on $\vec{s}_{\pm i}$ and $\overleftarrow{s}_{\pm i}$ in Eq. **7.45** does, however, submit a quantitative method by which to extract kinetic information by the identification of α_a and α_c ($\vec{\Psi}_j$ and $\overleftarrow{\Psi}_j$) simply from measurement of α (Ψ_j) and η

$$\vec{\Psi}_j = \Psi_j - \frac{\nu_j Z_{eff}}{1 - Z_{eff}} \; ; \quad \overleftarrow{\Psi}_j = \Psi_j - \frac{\nu_j}{1 - Z_{eff}} \qquad \textbf{[7.56]}$$

$$\vec{\alpha} = \alpha - \frac{n Z_{eff}}{1 - Z_{eff}} \; ; \quad \overleftarrow{\alpha} = \alpha - \frac{n}{1 - Z_{eff}} \qquad \textbf{[7.57]}$$

where $Z_{eff} = \mathrm{e}^{\frac{-ne_0\eta}{k_B T}}$ with judicious choice of equilibrium reference state. We contend that the clarification of the interrelation of reaction kinetics and thermodynamics evident in Eqs. **7.56**-**7.57** exemplifies the descriptive potence of formulating reversible electrochemical reactions in terms of $\vec{s}_{\pm i}$ and $\overleftarrow{s}_{\pm i}$ and is eminently useful in mechanistic study — as we illustrate by re-examination of the hydrogen oxidation reaction at low overpotential.

7.4.6 Case Study II: Hydrogen oxidation reaction (HOR) in alkaline media revisited

Consider again the two-step Heyrovsky-Volmer HOR mechanism (Table 7.1). In the overpotential regime $|\eta| \leq 30$ mV, both anodic and cathodic currents appreciably

contribute to J and, consequently, the net transfer coefficient (α) conflates α_a and α_c — proscribing mechanistic interpretation of α detailed in Case Study I, in which the overall hydrogen oxidation reaction is irreversible (i.e. $Z_{eff} = Z_1 Z_2 \ll 1$ for $\eta > 50$ mV). Competent mechanistic study of HOR at low overpotential therefore requires a robust method by which to quantify and interpret α_a and α_c to facilitate the identification of rate-controlling step(s). The quantification of unidirectional transfer coefficients and reaction orders pertinent to HOR follows directly from Eqs. **7.56-7.57** which, at a known overpotential, quantifies α_a directly from α and quantifies $\overrightarrow{\Psi}_{H_2}$ directly from Ψ_j. To extract the rate-controlling character of the Heyrovsky and Volmer steps from these unidirectional descriptors, we derive, from the framework detailed in Section 7.4.4, simple mathematical expressions that specify the relationship between α_a, X_{RC}, and macroscopically-observable reaction orders and surface coverages.

We derive a case-specific expression for α_a in terms of X_{RC} by first recalling the definition of α_a as a forward sensitivity weighted average of half-step transfer coefficients (Eq. **7.46**) which, in terms of symmetry factors, is

$$\alpha_a = \sum (\vec{s}_i + \vec{s}_{-i})\beta_i n_i - \sum \vec{s}_{-i} n_i \qquad \textbf{[7.58]}$$

Since the stoichiometric number of each step in the HOR mechanism is unity, $\vec{s}_i + \vec{s}_{-i} = X_{RC,i}$ per Eq. **7.50**, and

$$\begin{aligned} \alpha_a &= \sum X_{RC,i}\beta_i n_i - \sum \vec{s}_{-i} n_i \\ &= ½ - (\vec{s}_{-1} + \vec{s}_{-2}) \end{aligned} \qquad \textbf{[7.59]}$$

where $\beta_1 = \beta_2 = ½$ and $n_1 = n_2 = 1$.

Without a thermodynamic constraint on $\vec{s}_{-i}$ akin to Eq. **7.12**, we must simplify Eq. **7.59** by relating $\vec{s}_{-i}$ to observable kinetic descriptors — namely the reaction order of H_2 and surface coverage of H^*. From the definition of the forward reaction order, analogous to Eqs. **7.14-7.15**, we have

$$\overrightarrow{\Psi}_{H_2} \equiv -\sum \vec{s}_{\pm i}\nu_{\pm iH_2} = \vec{s}_{+1} \qquad \textbf{[7.60]}$$

which, upon rearrangement, gives

$$\vec{s}_{-1} = X_{RC,1} - \overrightarrow{\Psi}_{H_2} \qquad \textbf{[7.61]}$$

quantifying $\vec{s}_{-1}$ in terms of macrokinetic observables ($\overrightarrow{\Psi}_{H_2}$) and the desired microkinetic information ($X_{RC,1}$). We derive an analogous expression for $\vec{s}_{-2}$ by writing θ_{H^*} in terms of forward reaction sensitivities via the definition of $-\vec{X}_{TRC,H^*}$

$$\theta_{H^*} = -\vec{X}_{TRC,H^*} \equiv -\sum \vec{s}_{\pm i}\nu_{\pm iH^*}$$

$$= \vec{s}_{-1} + \vec{s}_{+2} \qquad \textbf{[7.62]}$$

Substituting a combination of Eq. **7.61**, $\vec{s}_{-2} = X_{RC,2} - \vec{s}_{+2}$, and $X_{RC,2} = 1 - X_{RC,1}$ into Eq. **7.62** with judicious rearrangement gives

$$\vec{s}_{-2} = 1 - \overrightarrow{\Psi}_{H_2} - \theta_{H^*} \qquad \textbf{[7.63]}$$

which, in conjunction with $\vec{s}_{-1}$ per Eq. **7.61** and α per Eq. **7.59** enables quantification of the degree of rate control of step 1

$$X_{RC,1} = 2\overrightarrow{\Psi}_{H_2} + \theta_{H^*} - \alpha_a - ½ \qquad \textbf{[7.64]}$$

thereby prescribing a method to identify the rate-determining character of the Heyrovsky step ($X_{RC,1}$) and Volmer step ($X_{RC,2} = 1 - X_{RC,1}$) directly from measurement of Tafel slope, reaction order, and surface coverage.

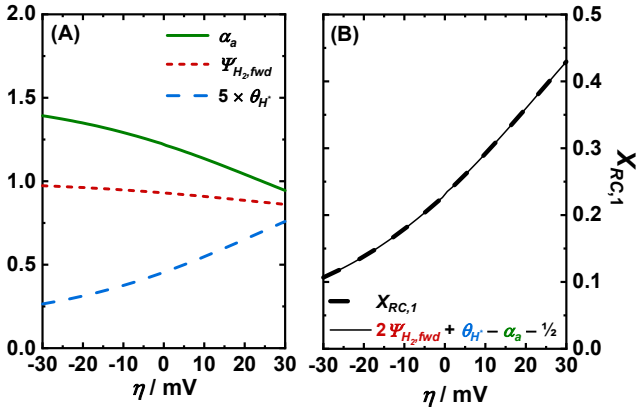

Figure 7.2: (A) Forward/anodic transfer coefficient ($\boldsymbol{\alpha_a}$), forward/anodic reaction order in $\boldsymbol{H_2}$ ($\boldsymbol{\Psi_{H_2,fwd} = \vec{\Psi}_{H_2}}$), and surface coverage of $\boldsymbol{H^*}$ ($\boldsymbol{\theta_{H^*}}$) as a function of overpotential. (B) Degree of rate control of step 1 ($\boldsymbol{X_{RC,1}}$) calculated directly (Eq. 7.13) and predicted by Eq. 7.64 ($\boldsymbol{X_{RC,1} = 2\vec{\Psi}_{H_2} + \theta_{H^*} - \alpha_a - ½}$) color-coded in the legend of (B) to indicate correspondence to (A).

Figure 7.2 shows the anodic/forward transfer coefficient (α_a), anodic/forward reaction order in H_2 ($\vec{\Psi}_{H_2}$), surface coverage of H^* (θ_{H^*}), and degree of rate control of step 1 for the HOR mechanism with Table 1 with cathodic half-step rate constants $k_{-1}^0 = 10^1$ and $k_{-2}^0 = 3 \cdot 10^{-1}$ respectively decremented and incremented by a factor of 10^4 relative to Case Study I. We adjust rate constants in Case Study II to demonstrate the utility of Eq. **7.64** to elucidate $X_{RC,1}$ and $X_{RC,2}$ which are both non-zero and which vary within the low overpotential regime $|\eta| \leq 30$ mV. As Figure 7.2A illustrates, the unidirectional descriptors α_a and $\vec{\Psi}_{H_2}$ are well-behaved (i.e. are finite and continuous) and take values which are familiar and suitable for intuitive interpretation (e.g. $\vec{\Psi}_{H_2} \approx 1$ accurately suggests $\theta_* \gg \theta_{H^*}$). Net descriptors α and Ψ_{H_2}, on the other hand, diverge to infinite values in the range $|\eta| \leq 30$ mV and, therefore, are difficult to interpret physically (see Section E.5). The disparate behavior of net and unidirectional descriptors for reactants/products (e.g. H_2 and e^-) is absent for intermediates and transition states which, per the principle of microscopic reversibility, must exert identical kinetic and thermodynamic control on the

anodic and cathodic reaction routes. Consequently, $-\vec{X}_{TRC,H^*} = -X_{TRC,H^*} = \theta_{H^*}$ and $\vec{X}_{RC,1} = X_{RC,1}$ — both of which are critically enabling in prediction of degrees of rate control directly from α_a, $\overrightarrow{\Psi}_{H_2}$, and θ_{H^*} (Fig. 7.2B); without the condition $-\vec{X}_{TRC,H^*} = \theta_{H^*}$, for example, surface coverages cannot be related to α_a and $\overrightarrow{\Psi}_{H_2}$ in any manner both rigorous and practical.

7.5 Conclusion

We develop a mathematical framework for the kinetic description of electrochemical reactions by leveraging transition state theory (TST) to formulate rigorous connections between macrokinetic observables (e.g. transfer coefficient, α) and elementary step parameters (e.g. symmetry factor, β_i) in terms of (unidirectional) reaction sensitivities. Reaction sensitivities of the net ($s_{\pm i}$), forward/anodic ($\vec{s}_{\pm i}$), and reverse/cathodic ($\overleftarrow{s}_{\pm i}$) reactions quantify the kinetic control of each elementary half-step, $\pm i$, on each reaction path and thereby enable re-interpretation of anodic ($\alpha_a = \vec{\alpha}$) and cathodic ($\alpha_c = -\overleftarrow{\alpha}$) transfer coefficients, for example, as respectively $\vec{s}_{\pm i}$- and $\overleftarrow{s}_{\pm i}$-weighted averages of elementary step symmetry factors. Mathematical connections of each observable kinetic descriptor to microkinetic, elementary-step analogues are synthesized into a single TST-form rate equation, r_{TST}, which takes a form entirely analogous to the TST formulation of an elementary step and serves as the foundation for the development of new mathematical tools and mechanistic insights. In particular, from r_{TST}, we derive (i) a generalized Butler-Volmer equation valid for composite electrochemical reactions under rigorously-specified conditions, (ii) mathematical connections between the transfer coefficient and elementary step reversibility that explain the universal convergence of Tafel slope to ~120 mV/dec at large overpotential, and (iii) new, general formulations of α, α_a, and α_c which facilitate

mechanistic interpretation of Tafel slope at all overpotential and which serve as a mathematical link between surface coverages, reaction orders, and the kinetic relevance of elementary steps. The mechanistic clarity provided by these mathematical developments is exemplified in examination of the Heyrovsky-Volmer HOR/HER mechanism for which we systematically and quantitatively explain observed trends in Tafel slope, surface coverage, reaction orders, and the identity of rate-determining steps in all overpotential regimes.

7.6 Materials and Methods

All calculations were performed using Matlab code found at the link https://github.com/neilrazdan/ButlerVolmerKinetics or by communication with the authors. Steady-state kinetic descriptors were calculated using stiff ordinary differential equation solver ode23s in Matlab.

Bibliography

1. J. H. Lunsford, Catalytic conversion of methane to more useful chemicals and fuels: a challenge for the 21st century. *Catal. Today*. **63**, 165–174 (2000).
2. J. A. Labinger, J. E. Bercaw, Understanding and exploiting C–H bond activation. *Nature*. **417**, 507–514 (2002).
3. D. Wang, J. H. Lunsford, M. P. Rosynek, Characterization of a Mo/ZSM-5 Catalyst for the Conversion of Methane to Benzene. *J. Catal.* **169**, 347–358 (1997).
4. Y. Song, Q. Zhang, Y. Xu, Y. Zhang, K. Matsuoka, Z.-G. Zhang, Coke accumulation and deactivation behavior of microzeolite-based Mo/HZSM-5 in the non-oxidative methane aromatization under cyclic CH_4 - H_2 feed switch mode. *Appl. Catal. A Gen.* **530**, 12–20 (2017).
5. Z. Liu, M. A. Nutt, E. Iglesia, The Effects of CO_2, CO and H_2 co-reactants on methane reactions catalyzed by Mo/H-ZSM-5. *Catal. Letters*. **81**, 271–279 (2002).
6. C. H. L. Tempelman, E. J. M. Hensen, On the deactivation of Mo/HZSM-5 in the methane dehydroaromatization reaction. *Appl. Catal. B Environ.* **176**–**177**, 731–739 (2015).
7. F. Solymosi, J. Cserényi, A. Szöke, T. Bánsági, A. Oszkó, Aromatization of methane over supported and unsupported Mo-based catalysts. *J. Catal.* **165**, 150–161 (1997).
8. P. Schwach, X. Pan, X. Bao, Direct Conversion of Methane to Value-Added Chemicals over Heterogeneous Catalysts: Challenges and Prospects. *Chem. Rev.* **117**, 8497–8520 (2017).
9. L. Wang, L. Tao, M. Xie, G. Xu, Dehydrogenation and aromatization of methane under non-oxidizing conditions. *Catal. Letters*. **21**, 35–41 (1993).
10. K. Velebná, M. Horňáček, V. Jorík, P. Hudec, M. Čaplovičová, L. Čaplovič, The

influence of molybdenum loading on activity of ZSM-5 zeolite in dehydroaromatization of methane. *Microporous Mesoporous Mater.* **212**, 146–155 (2015).

11. H. Liu, W. Shen, X. Bao, Y. Xu, Methane dehydroaromatization over Mo/HZSM-5 catalysts: The reactivity of MoCx species formed from MoOx associated and non-associated with Brønsted acid sites. *Appl. Catal. A Gen.* **295**, 79–88 (2005).
12. I. Vollmer, B. Van Der Linden, S. Ould-Chikh, A. Aguilar-Tapia, I. Yarulina, E. Abou-Hamad, Y. G. Sneider, A. I. Olivos Suarez, J.-L. Hazemann, F. Kapteijn, J. Gascon, On the dynamic nature of Mo sites for methane dehydroaromatization. *Chem. Sci.* **9**, 4801–4807 (2018).
13. N. Kosinov, F. J. A. G. Coumans, E. Uslamin, F. Kapteijn, E. J. M. Hensen, Selective Coke Combustion by Oxygen Pulsing During Mo/ZSM-5-Catalyzed Methane Dehydroaromatization. *Angew. Chemie Int. Ed.* **55**, 15086–15090 (2016).
14. N. Kosinov, F. J. A. G. Coumans, G. Li, E. Uslamin, B. Mezari, A. S. G. Wijpkema, E. A. Pidko, E. J. M. Hensen, Stable Mo/HZSM-5 methane dehydroaromatization catalysts optimized for high-temperature calcination-regeneration. *J. Catal.* **346**, 125–133 (2017).
15. N. Kosinov, A. S. G. Wijpkema, E. Uslamin, R. Rohling, F. J. A. G. Coumans, B. Mezari, A. Parastaev, A. S. Poryvaev, M. V. Fedin, E. A. Pidko, E. J. M. Hensen, Confined Carbon Mediating Dehydroaromatization of Methane over Mo/ZSM-5. *Angew. Chemie Int. Ed.* **57**, 1016–1020 (2018).
16. B. Li, S. Li, N. Li, H. Chen, W. Zhang, X. Bao, B. Lin, Structure and acidity of Mo/ZSM-5 synthesized by solid state reaction for methane dehydrogenation and

aromatization. *Microporous Mesoporous Mater.* **88**, 244–253 (2006).

17. I. Vollmer, G. Li, I. Yarulina, A. Nikolay Kosinov, E. J. Hensen, K. Houben, D. Mance, M. Baldus, J. Gascon, F. Kapteijn, Relevance of the Mo-precursor state in H-ZSM-5 for methane dehydroaromatization. *Catal. Sci. Technol*. **8**, 916 (2018).
18. A. Kumar, K. Song, L. Liu, Y. Han, A. Bhan, Absorptive hydrogen scavenging for enhanced aromatics yield during non-oxidative methane dehydroaromatization on Mo/H-ZSM-5 catalysts. *Angew. Chemie Int. Ed.* **130**, 15803–15808 (2018).
19. J. Bedard, D.-Y. Hong, A. Bhan, CH_4 dehydroaromatization on Mo/H-ZSM-5: 1. Effects of co-processing H_2 and CH_3COOH. *J. Catal.* **306**, 58–67 (2013).
20. N. K. Razdan, A. Bhan, Carbidic Mo is the sole kinetically-relevant active site for catalytic methane dehydroaromatization on Mo/H-ZSM-5. *J. Catal.* **389**, 667–676 (2020).
21. D. Wang, J. H. Lunsford, M. P. Rosynek, Catalytic conversion of methane to benzene over Mo/ZSM-5. *Top. Catal.* **3**, 289–297 (1996).
22. Y.-H. Kim, R. W. Borry III, E. Iglesia, Surface Structure of Mo/H-ZSM5 Catalyst for CH_4 Activation. *Appl. Chem.* **3**, 368–371 (1999).
23. J.-P. Tessonnier, B. Louis, S. Walspurger, J. Sommer, M.-J. Ledoux, C. Pham-Huu, Quantitative Measurement of the Bronsted Acid Sites in Solid Acids: Toward a Single-Site Design of Mo-Modified ZSM-5 Zeolite. *J. Phys. Chem. B*. **110**, 10390–10395 (2006).
24. B. M. Weckhuysen, D. Wang, M. P. Rosynek, J. H. Lunsford, Conversion of Methane to Benzene over Transition Metal Ion ZSM-5 Zeolites I. Catalytic Characterization. *J. Catal.* **175**, 338–346 (1998).

25. N. Kosinov, F. J. A. G. Coumans, E. A. Uslamin, A. S. G. Wijpkema, B. Mezari, E. J. M. Hensen, Methane Dehydroaromatization by Mo/HZSM-5: Mono-or Bifunctional Catalysis? *ACS Catal.* **7**, 520–529 (2016).

26. U. Menon, M. Rahman, S. J. Khatib, A critical literature review of the advances in methane dehydroaromatization over multifunctional metal-promoted zeolite catalysts. *Appl. Catal. A Gen.* **608**, 117870 (2020).

27. I. Vollmer, N. Kosinov, Á. Szécsényi, G. Li, I. Yarulina, E. Abou-Hamad, A. Gurinov, S. Ould-Chikh, A. Aguilar-Tapia, J.-L. Hazemann, E. Pidko, E. Hensen, F. Kapteijn, J. Gascon, A site-sensitive quasi-in situ strategy to characterize Mo/HZSM-5 during activation. *J. Catal.* **370**, 321–331 (2019).

28. C. N. Hinshelwood, *Kinetics of chemical change in gaseous systems* (Oxford University Press, Oxford, 1926).

29. H. C. Kang, W. H. Weinberg, M. W. Deem, Reactant segregation in a Langmuir-Hinshelwood surface reaction. *J. Chem. Phys.* **93**, 6841–6850 (1990).

30. A. H. Motagamwala, J. A. Dumesic, Chemical kinetics for generalized two-step reaction schemes. *J. Catal.* **404**, 850–863 (2021).

31. B. Demir, T. Kropp, K. R. Rivera-Dones, E. B. Gilcher, G. W. Huber, M. Mavrikakis, J. A. Dumesic, A. contributions, J. designed research, E. performed research, J. analyzed data, A self-adjusting platinum surface for acetone hydrogenation. *Proc. Natl. Acad. Sci.* **117**, 3446–3450 (2020).

32. I. Farbman, Z. Rosenzweig, M. Asscher, Diffusion of Ammonia on Re(001). *Faraday Discuss*. **96**, 307–316 (1993).

33. V. P. Zhdanov, Effect of the lateral interaction of adsorbed molecules on

preexponential factor of the desorption rate constant. *Surf. Sci. Lett.* **111**, L662–L666 (1981).

34. V. P. Zhdanov, Lattice-gas model of bimolecular reaction on surface. *Surf. Sci. Lett.* **102**, L35–L40 (1981).

35. V. P. Zhdanov, Lattice-gas model for description of the adsorbed molecules of two kinds. *Surf. Sci.* **111**, 63–79 (1981).

36. M. Bowker, D. A. King, Adsorbate diffusion on single crystal surfaces. I.The influence of lateral interactions. *Surf. Sci.* **71**, 583–598 (1978).

37. B. M. Weckhuysen, D. Wang, M. P. Rosynek, J. H. Lunsford, Conversion of Methane to Benzene over Transition Metal Ion ZSM-5 Zeolites II. Catalyst Characterization by X-Ray Photoelectron Spectroscopy. *J. Catal.* **175**, 347–351 (1998).

38. W. Li, G. D. Meitzner, R. W. B. III, E. Iglesia, Raman and X-Ray Absorption Studies of Mo Species in Mo/H-ZSM5 Catalysts for Non-Oxidative CH_4 Reactions. *J. Catal.* **191**, 373–383 (2000).

39. H. S. Lacheen, E. Iglesia, Stability, structure, and oxidation state of Mo/H-ZSM-5 catalysts during reactions of CH_4 and CH_4-CO_2 mixtures. *J. Catal.* **230**, 173–185 (2005).

40. H. S. Lacheen, E. Iglesia, Isothermal activation of $Mo_2O_5^{2+}$-ZSM-5 precursors during methane reactions: effect of reaction products on structural evolution and catalytic properties. *Phys. Chem. Chem. Phys.* **7**, 538–547 (2005).

41. L. Y. Chen, L. Lin, Z. Xu, X. Li, T. Zhang, Dehydro-oligomerization of methane to ethylene and aromatics over molybdenum/HZSM-5 catalyst. *J. Catal.* **157**, 190–200

(1995).

42. R. W. Borry III, A. Huffsmith, Y. H. Kim, J. A. Reimer, E. Iglesia, Structure and Density of Mo and Acid Sites in Mo-Exchanged H-ZSM5 Catalysts for Nonoxidative Methane Conversion. *J. Phys. Chem. B*. **103**, 5787–5796 (1999).

43. B. M. Weckhuysen, M. P. Rosynek, J. H. Lunsford, Characterization of surface carbon formed during the conversion of methane to benzene over Mo/H-ZSM-5 catalysts. *Catal. Letters*. **52**, 31–36 (1998).

44. Z. Liu, L. Li, E. Iglesia, Catalytic pyrolysis of methane on Mo/H-ZSM5 with continuous hydrogen removal by permeation through dense oxide films. *Catal. Letters*. **82**, 175–180 (2002).

45. L. Li, R. W. Borry, E. Iglesia, Reaction-transport simulations of non-oxidative methane conversion with continuous hydrogen removal: homogeneous-heterogeneous reaction pathways. *Chem. Eng. Sci.* **56**, 1869–1881 (2001).

46. R. W. Borry, E. C. Lu, Y.-H. Kim, E. Iglesia, Non-oxidative catalytic conversion of methane with continuous hydrogen removal. *Nat. Gas Convers. V*. **119**, 403–410 (1998).

47. N. K. Razdan, A. Kumar, A. Bhan, Controlling kinetic and diffusive length-scales during absorptive hydrogen removal in methane dehydroaromatization on MoC_x/H-ZSM-5 catalysts. *J. Catal.* **372**, 370–381 (2019).

48. O. Levenspiel, *Chemical Reaction Engineering* (John Wiley & Sons, NY, ed. 3, 1999).

49. T. J. Marshall, A Relation Between Permeability and Size Distribution of Pores. *J. Soil Sci.* **9**, 1–8 (1958).

50. T. J. Marshall, The Diffusion of Gases Through Porous Media. *J. Soil Sclence*. **10**, 79–82 (1959).

51. N. Matsunaga, M. Hori, A. Nagashima, Measurement of Mutual Diffusion Coefficients of Gases by the Taylor Method: Measurements on H_2–Air, H_2–N_2, and H_2–O_2 Systems. *Heat Trans Asian Res*. **31**, 182–193 (2002).

52. G. I. Taylor, Diffusion by Continuous Movements. *Proc. London Math. Soc.* **2**, 196–212 (1922).

53. H. Grad, in *Thermodynamics of Gases* (Springer, Berlin, Heidelberg, 1958), pp. 205–294.

54. V. M. H. Govindarao, G. F. Froment, Voidage Profiles in Packed Beds of Spheres. *Chem. Eng. Sci.* **41**, 533–539 (1986).

55. K. A. Terrani, M. Balooch, D. Wongsawaeng, S. Jaiyen, D. R. Olander, The kinetics of hydrogen desorption from and adsorption on zirconium hydride. *J. Nucl. Mater.* **397**, 61–68 (2010).

56. P. V. Danckwerts, Continuous flow systems: distribution of residence times. *Chem. Eng. Sci.* **2**, 1–13 (1953).

57. J. Bedard, D.-Y. Hong, A. Bhan, Co-processing CH_4 and oxygenates on Mo/HZSM5: 2. CH_4-CO_2 and CH_4-HCOOH mixtures. *Phys. Chem. Chem. Phys*. **15**, 12173 (2013).

58. K. S. Wong, J. W. Thybaut, E. Tangstad, M. W. Stöcker, G. B. Marin, Methane aromatisation based upon elementary steps: Kinetic and catalyst descriptors. *Microporous Mesoporous Mater.* **164**, 302–312 (2012).

59. W. Ding, G. D. Meitzner, E. Iglesia, The Effects of Silanation of External Acid Sites

on the Structure and Catalytic Behavior of Mo/H-ZSM5. *J. Catal.* **206**, 14–22 (2002).

60. A. I. Olivos-Suarez, Á. Szécsényi, E. J. M. Hensen, J. Ruiz-Martinez, E. A. Pidko, J. Gascon, Strategies for the Direct Catalytic Valorization of Methane Using Heterogeneous Catalysis: Challenges and Opportunities. *ACS Catal.* **6**, 2965–2981 (2016).

61. Y.-H. Kim, R. W. Borry III, E. Iglesia, Catalytic Properties of Mo/HZSM-5 for CH_4 Aromatization. *J. Ind. Eng. Chem.* **6**, 72–78 (2000).

62. Y.-H. Kim, R. W. Borry III, E. Iglesia, Genesis of methane activation sites in Mo-exchanged H–ZSM-5 catalysts. *Microporous Mesoporous Mater.* **35**–**36**, 495–509 (2000).

63. I. Lezcano-González, R. Oord, M. Rovezzi, P. Glatzel, S. W. Botchway, B. M. Weckhuysen, A. M. Beale, Molybdenum Speciation and its Impact on Catalytic Activity during Methane Dehydroaromatization in Zeolite ZSM-5 as Revealed by Operando X-Ray Methods. *Angew. Chemie Int. Ed.* **55**, 5215–5219 (2016).

64. J. Gao, Y. Zheng, J. M. Jehng, Y. Tang, I. E. Wachs, S. G. Podkolzin, Identification of molybdenum oxide nanostructures on zeolites for natural gas conversion. *Science*. **348**, 686–690 (2015).

65. L. Li, R. W. Borry, E. Iglesia, Design and optimization of catalysts and membrane reactors for the non-oxidative conversion of methane. *Chem. Eng. Sci.* **57**, 4595–4604 (2002).

66. M. C. Iliuta, I. Illiuta, B. P. A. Grandjean, F. Larachi, Kinetics of Methane Nonoxidative Aromatization over Ru-Mo/HZSM-5 Catalyst. *Ind. Eng. Chem. Res*.

42, 3203–3209 (2003).

67. C. Karakaya, S. H. Morejudo, H. Zhu, R. J. Kee, Catalytic Chemistry for Methane Dehydroaromatization (MDA) on a Bifunctional Mo/HZSM-5 Catalyst in a Packed Bed. *Ind. Eng. Chem. Res.* **55**, 9895–9906 (2016).

68. B. Kee, C. Karakaya, H. Zhu, S. DeCaluwe, R. J. Kee, The Influence of Hydrogen-Permeable Membranes and Pressure on Methane Dehydroaromatization in Packed-Bed Catalytic Reactors. *Ind. Eng. Chem. Res.* **56**, 3551–3559 (2017).

69. C. Karakaya, H. Zhu, R. J. Kee, Kinetic modeling of methane dehydroaromatization chemistry on Mo/Zeolite catalysts in packed-bed reactors. *Chem. Eng. Sci.* **123**, 474–486 (2015).

70. Y. Song, Y. Xu, Y. Suzuki, H. Nakagome, X. Ma, Z.-G. Zhang, The distribution of coke formed over a multilayer Mo/HZSM-5 fixed bed in H_2 co-fed methane aromatization at 1073 K: Exploration of the coking pathway. *J. Catal.* **330**, 261–272 (2015).

71. R. Gounder, E. Iglesia, Catalytic hydrogenation of alkenes on acidic zeolites: Mechanistic connections to monomolecular alkane dehydrogenation reactions. *J. Catal.* **277**, 36–45 (2011).

72. J. A. Dumesic, Analyses of Reaction Schemes Using De Donder Relations. *J. Catal.* **185**, 496–505 (1999).

73. J. Bedard, D.-Y. Hong, A. Bhan, C to H effective ratio as a descriptor for coprocessing light oxygenates and CH_4 on Mo/HZSM-5. *RSC Adv.* **4**, 49446 (2014).

74. B. L. Foley, B. A. Johnson, A. Bhan, A Method for Assessing Catalyst Deactivation: A Case Study on Methanol-to-Hydrocarbons Conversion. *ACS Catal.* **9**, 7065–7072

(2019).

75. V. Ramasubramanian, H. Ramsurn, G. L. Price, Methane dehydroaromatization – A study on hydrogen use for catalyst reduction, role of molybdenum, the nature of catalyst support and significance of Bronsted acid sites. *J. Energy Chem.* **34**, 20–32 (2019).

76. M. Boudart, G. Djéga-Mariadassou, in *Kinetics of Heterogenous Catalytic Reactions*, J. M. Prausnitz, L. Brewer, Eds. (Princeton University Press, Princeton, ed. 1, 1984), pp. 78–90.

77. P. Meriaudeau, L. V Tiep, V. T. T. Ha, C. Naccache, G. Szabo, Aromatization of methane over Mo/H-ZSM-5 catalyst: on the possible reaction intermediates. *J. Mol. Catal. A Chem.* **144**, 469–471 (1999).

78. V. T. T. Ha, L. V. Tiep, P. Meriaudeau, C. Naccache, Aromatization of methane over zeolite supported molybdenum: active sites and reaction mechanism. *J. Mol. Catal. A Chem.* **181**, 283–290 (2002).

79. P. Mériaudeau, V. T. T. Ha, L. Van Tiep, Methane aromatization over Mo/H-ZSM-5: on the reaction pathway. *Catal. Letters*. **64**, 49–51 (2000).

80. P. Tsai, J. R. Anderson, Reaction of Acetylene over ZSM-5-Type Catalysts. *J. Catal.* **80**, 207–214 (1983).

81. A. M. Dean, Detailed Kinetic Modeling of Autocatalysis in Methane Pyrolysis. *J. Phys. Chem.* **94**, 1432–1439 (1990).

82. M. Boudart, Some Applications of the Generalized De Donder Equation to Industrial Reactions. *Ind. Eng. Chem. Fundam.* **25**, 70–75 (1986).

83. C. T. Campbell, Finding the Rate-Determining Step in a Mechanism Comparing

DeDonder Relations with the “Degree of Rate Control.” *J. Catal.* **204**, 520–524 (2001).

84. C. Stegelmann, A. Andreasen, C. T. Campbell, Degree of Rate Control: How Much the Energies of Intermediates and Transition States Control Rates. *J. Am. Chem. Soc.* **131**, 8077–8082 (2009).

85. R. D. Cortright, J. A. Dumesic, Kinetics of Heterogeneous Catalytic Reactions: Analysis of Reaction Schemes. *Adv. Catal.* **46**, 161–264 (2001).

86. C. F. Cullis, N. H. Franklin, The pyrolysis of acetylene at temperatures from 500 to 1000 °C. *Proc. R. Soc. London. Ser. A. Math. Phys. Sci.* **280**, 139–152 (1964).

87. S. W. Benson, Radical processes in the pyrolysis of acetylene. *Int. J. Chem. Kinet.* **24**, 217–237 (1992).

88. B. L. Foley, A. Bhan, Personal Communication (2019).

89. H. M. Spencer, Empirical Heat Capacity Equations of Gases and Graphite. *Ind. Eng. Chem.* **40**, 2152–2154 (1948).

90. C. L. Yaws, in *The Yaws Handbook of Physical Properties for Hydrocarbons and Chemicals* (Elsevier Inc., Waltham, MA, ed. 2, 2015), pp. 1–683.

91. S. Liu, L. Wang, R. Ohnishi, M. Ichikawa, Bifunctional Catalysis of Mo/HZSM-5 in the Dehydroaromatization of Methane to Benzene and Naphthalene XAFS/TG/DTA/ MASS/FTIR Characterization and Supporting Effects. *J. Catal.* **181**, 175–188 (1999).

92. O. Anomohanran, Determination of greenhouse gas emission resulting from gas flaring activities in Nigeria. *Energy Policy*. **45**, 666–670 (2012).

93. C. D. Elvidge, M. D. Bazilian, M. Zhizhin, T. Ghosh, K. Baugh, F. C. Hsu, The

potential role of natural gas flaring in meeting greenhouse gas mitigation targets. *Energy Strateg. Rev.* **20**, 156–162 (2018).

94. C. Ménard, A. Avalos Ramirez, J. Nikiema, M. Heitz, Biofiltration of methane and trace gases from landfills: A review. *Environ. Rev.* **20**, 40–53 (2012).

95. N. K. Razdan, A. Kumar, B. L. Foley, A. Bhan, Influence of ethylene and acetylene on the rate and reversibility of methane dehydroaromatization on Mo/H-ZSM-5 catalysts. *J. Catal.* **381**, 261–270 (2020).

96. Y. Xu, W. Liu, S.-T. Wong, L. Wang, X. Guo, Dehydrogenation and aromatization of methane in the absence of oxygen on Mo/HZSM-5 catalysts before and after NH_4OH extraction. *Catal. Letters*. **40**, 207–214 (1996).

97. R. G. Brown, S. D. Ross, The vibrational spectra of some condensed tetrahedral anions $[X_2O_7]^{n-}$. *Spectrochim. Acta*. **28A**, 1263–1274 (1972).

98. J. H. Denning, R. F. Hudson, D. R. Laughlin, S. D. Ross, A. M. Sparasci, The vibrational spectra of some rare-earth pyrosilicates. *Spectrochim. Acta*. **28A**, 1787–1791 (1972).

99. J. P. Tessonnier, B. Louis, S. Rigolet, M. J. Ledoux, C. Pham-Huu, Methane dehydro-aromatization on Mo/ZSM-5: About the hidden role of Brønsted acid sites. *Appl. Catal. A Gen.* **336**, 79–88 (2008).

100. H. S. Lacheen, P. J. Cordeiro, E. Iglesia, Structure and Catalytic Function of Re-Oxo Species Grafted onto H-MFI Zeolite by Sublimation of Re_2O_7. *J. Am. Chem. Soc.* **128**, 15082–15083 (2006).

101. P. Cheung, A. Bhan, G. J. Sunley, D. J. Law, E. Iglesia, Site requirements and elementary steps in dimethyl ether carbonylation catalyzed by acidic zeolites. *J.*

Catal. **245**, 110–123 (2007).

102. S. M. Campbell, D. M. Bibby, J. M. Coddington, R. F. Howe, R. H. Meinhold, Dealumination of HZSM-5 zeolites: I. Calcination and hydrothermal treatment. *J. Catal.* **161**, 338–349 (1996).

103. B. R. Goodman, K. C. Hass, W. F. Schneider, J. B. Adams, Statistical analysis of Al distributions and metal ion pairing probabilities in zeolites. *Catal. Letters*. **68**, 85–93 (2000).

104. J. Dědeček, D. Kaucký, B. Wichterlová, O. Gonsiorová, Co^{2+} ions as probes of Al distribution in the framework of zeolites. ZSM-5 study. *Phys. Chem. Chem. Phys.* **4**, 5406–5413 (2002).

105. M. Rahman, A. Sridhar, S. J. Khatib, Impact of the presence of Mo carbide species prepared ex situ in Mo/HZSM-5 on the catalytic properties in methane aromatization. *Appl. Catal. A Gen.* **558**, 67–80 (2018).

106. J. Lu, Y. Xu, Y. Suzuki, Z. G. Zhang, A rapid and effective method for evaluating the initial activity of Mo/HZSM-5 catalyst in the methane dehydroaromatization reaction at severe conditions. *Catal. Commun.* **12**, 127–131 (2010).

107. M. Rahman, A. Infantes-Molina, A. Boubnov, S. R. Bare, E. Stavitski, A. Sridhar, J. Khatib, Sheima, Increasing the catalytic stability by optimizing the formation of zeolite-supported Mo carbide species ex situ for methane dehydroaromatization. *J. Catal.* **375**, 314–328 (2019).

108. N. Kosinov, E. A. Uslamin, F. J. A. G. Coumans, A. S. G. Wijpkema, R. Y. Rohling, E. J. M. Hensen, Structure and Evolution of Confined Carbon Species during Methane Dehydroaromatization over Mo/ZSM-5. *ACS Catal.* **8**, 8459–8467 (2018).

109. E. A. Uslamin, H. Saito, N. Kosinov, E. Pidko, Y. Sekine, E. J. M. Hensen, Aromatization of ethylene over zeolite-based catalysts. *Catal. Sci. Technol.* **10**, 2774–2785 (2020).

110. G. Li, I. Vollmer, C. Liu, J. Gascon, E. A. Pidko, Structure and Reactivity of the Mo/ZSM-5 Dehydroaromatization Catalyst: An Operando Computational Study. *ACS Catal.* **9**, 8731–8737 (2019).

111. M. T. Portilla, F. J. Llopis, C. Martínez, Non-oxidative dehydroaromatization of methane: An effective reaction-regeneration cyclic operation for catalyst life extension. *Catal. Sci. Technol.* **5**, 3806–3821 (2015).

112. S. J. Han, S. K. Kim, A. Hwang, S. Kim, D.-Y. Hong, G. Kwak, K.-W. Jun, Y. T. Kim, Non-oxidative dehydroaromatization of methane over Mo/H-ZSM-5 catalysts: A detailed analysis of the reaction-regeneration cycle. *Appl. Catal. B, Environ.* **241**, 305–318 (2019).

113. N. T. P. Le, C. White, J. M. Reese, R. S. Myong, Langmuir-Maxwell and Langmuir-Smoluchowski boundary conditions for thermal gas flow simulations in hypersonic aerodynamics. *Int. J. Heat Mass Transf.* **55**, 5032–5043 (2012).

114. R. S. Myong, Gaseous slip models based on the Langmuir adsorption isotherm. *Phys. Fluids*. **16**, 104 (2004).

115. H. Singh, F. Javadpour, Langmuir slip-Langmuir sorption permeability model of shale. *Fuel*. **164**, 28–37 (2016).

116. D. M. Manohar, K. A. Krishnan, T. S. Anirudhan, Removal of mercury(II) from aqueous solutions and chlor-alkali industry wastewater using 2-mercaptobenzimidazole-clay. *Water Res.* **36**, 1609–1619 (2002).

117. Y. Wu, S. Zhang, X. Guo, H. Huang, Adsorption of chromium(III) on lignin. *Bioresour. Technol.* **99**, 7709–7715 (2008).

118. J. K. Syers, M. G. Browman, G. W. Smillie, R. B. Corey, Phosphate Sorption by Soils Evaluated by the Langmuir Adsorption Equation. *Soil Sci. Soc. Am. J.* **37**, 358–363 (1973).

119. A. Mittal, L. Kurup, J. Mittal, Freundlich and Langmuir adsorption isotherms and kinetics for the removal of Tartrazine from aqueous solutions using hen feathers. *J. Hazard. Mater.* **146**, 243–248 (2007).

120. P. Zhang, L. Wang, Extended Langmuir equation for correlating multilayer adsorption equilibrium data. *Sep. Purif. Technol.* **70**, 367–371 (2010).

121. P. Forssén, J. Samuelsson, T. Fornstedt, Relative importance of column and adsorption parameters on the productivity in preparative liquid chromatography II: Investigation of separation systems with competitive Langmuir adsorption isotherms. *J. Chromatogr. A*. **1347**, 72–79 (2014).

122. H. S. Taylor, A theory of the catalytic surface. *Proc. R. Soc. London*. **108**, 105–111 (1925).

123. J. J. Park, S. H. De, P. Lacerda, S. K. Stanley, B. M. Vogel, S. Kim, J. F. Douglas, D. Raghavan, A. Karim, Langmuir Adsorption Study of the Interaction of CdSe/ZnS Quantum Dots with Model Substrates: Influence of Substrate Surface Chemistry and pH. *Langmuir*. **25**, 443–450 (2009).

124. G. R. Belton, Langmuir Adsorption, the Gibbs Isotherm, and Interfacial Kinetics in Metal Liquid Systems. *Metall. Trans. B*. **7B**, 35–42 (1976).

125. J. R. Anderson, M. Boudart, in *Fundamentals of chemical reaction engineering*

(Springer-Verlag, 2003), pp. 133–183.

126. B. Temel, H. Meskine, K. Reuter, M. Scheffler, H. Metiu, Does phenomenological kinetics provide an adequate description of heterogeneous catalytic reactions? *J. Chem. Phys.* **126**, 204711 (2007).

127. Q.-J. Hong, Z.-P. Liu, Mechanism of CO_2 hydrogenation over Cu/ZrO_2 (212) interface from first-principles kinetics Monte Carlo simulations. *Surf. Sci.* **604**, 1869–1876 (2010).

128. M. Andersen, C. P. Plaisance, K. Reuter, Assessment of mean-field microkinetic models for CO methanation on stepped metal surfaces using accelerated kinetic Monte Carlo. *J. Chem. Phys.* **147**, 152705 (2017).

129. M. Pineda, M. Stamatakis, Beyond mean-field approximations for accurate and computationally efficient models of on-lattice chemical kinetics. *J. Chem. Phys.* **147**, 024105 (2017).

130. K. J. Vette, T. W. Orent, D. K. Hoffman, R. S. Hansen, Kinetic model for dissociative adsorption of a diatomic gas. *J. Chem. Phys.* **60**, 4854–4861 (1974).

131. R. S. Nord, J. W. Evans, Irreversible immobile random adsorption of dimers, trimers, ... on 2D lattices. *J. Chem. Phys.* **82**, 2795–2810 (1985).

132. J. W. Evans, R. S. Nord, Competitive irreversible random one-, two-, three-, . . . point adsorption on two-dimensional lattices. *Phys. Rev. B*. **31**, 1759–1769 (1985).

133. J. W. Evans, D. R. Burgess, D. K. Hoffman, Irreversible random and cooperative processes on lattices: Exact and approximate hierarchy truncation and solution. *J. Chem. Phys*. **79**, 5011–5022 (1983).

134. J. W. Evans, Random and cooperative sequential adsorption. *Rev. Mod. Phys.* **65**,

1281–1329 (1993).

135. B. Weng, W. H. Weinberg, J. W. Evans, Transitions in the kinetics and steady states of irreversible A+BC surface-reaction models. *Phys. Rev. E*. **48**, 3577–3588 (1993).

136. J. W. Evans, R. S. Nord, Random Dimer Filling of Lattices: Three-Dimensional Application to Free Radical Recombination Kinetics. *J. Stat. Phys.* **38**, 681–705 (1985).

137. J. W. Evans, D. K. Hoffman, D. R. Burgess, Competing irreversible cooperative adsorption on polymer chains. *J. Chem. Phys.* **80**, 936–943 (1984).

138. D. Zhong, D. Ben-Avraham, M. A. Muñoz, Mean-field solution of the parity-conserving kinetic phase transition in one dimension. *Eur. Phys. J. B*. **35**, 505–511 (2003).

139. H. Hinrichsen, Non-equilibrium critical phenomena and phase transitions into absorbing states. *Adv. Phys.* **49**, 815–958 (2000).

140. B. L. Foley, A. Bhan, Degree of rate control and De Donder relations-An interpretation based on transition state theory. *J. Catal.* **384**, 231–251 (2020).

141. Z. Mao, C. T. Campbell, The degree of rate control of catalyst-bound intermediates in catalytic reaction mechanisms: Relationship to site coverage. *J. Catal.* **381**, 53–62 (2020).

142. H. Meskine, S. Matera, M. Scheffler, K. Reuter, H. Metiu, Examination of the concept of degree of rate control by first-principles kinetic Monte Carlo simulations. *Surf. Sci.* **603**, 1724–1730 (2009).

143. G. N. Lewis, A new principle of equilibrium. *Proc. Natl. Acad. Sci.* **11**, 179–183 (1925).

144. S. Matera, H. Meskine, K. Reuter, Adlayer inhomogeneity without lateral interactions: Rationalizing correlation effects in CO oxidation at RuO_2 (110) with first principles kinetic Monte Carlo. *J. Chem. Phys.* **134**, 64713 (2011).

145. H. Mortensen, L. Diekhöner, A. Baurichter, E. Jensen, A. C. Luntz, Dynamics of ammonia decomposition on Ru(0001). *J. Chem. Phys*. **113**, 6882 (2000).

146. L. A. Avalos, V. Bustos, R. Uñac, F. Zaera, G. Zgrablich, Dynamic Monte Carlo Simulation of the NO + CO Reaction on Rh(111). *J. Phys. Chem. B*. **110**, 24964–24971 (2006).

147. Á. Logadóttir, J. K. Nørskov, Ammonia synthesis over a Ru(0001) surface studied by density functional calculations. *J. Catal.* **220**, 273–279 (2003).

148. B. Hammer, Adsorption, diffusion, and dissociation of NO, N and O on flat and stepped Ru(0001). *Surf. Sci.* **459**, 323–348 (2000).

149. T. N. Truong, D. G. Truhlar, J. R. Chelikowsky, M. Y. Chou, A new ab initio potential energy surface for H on Ru(0001) and its use for variational transition state theory and semiclassical tunneling calculations of the surface diffusion of H and D. *J. Phys. Chem.* **94**, 1973–1981 (1990).

150. T. Zambelli, J. Trost, J. Wintterlin, G. Ertl, Diffusion and Atomic Hopping of N Atoms on Ru(0001) Studied by Scanning Tunneling Microscopy. *Phys. Rev. Lett.* **76**, 795–798 (1996).

151. A. Frennet, Adsorption Site of Alkanes and Associated Hydrogen Pressure Effects. *Catal. Today*. **12**, 131–137 (1992).

152. G. C. Bond, R. H. Cunningham, Alkane Transformations on Supported Platinum Catalysts 4. Kinetics of Hydrogenolysis of Ethane, Propane, and n-Butane on

Pt/Al_2O_3 (EUROPT-3) and $PtRe/Al_2O_3$ (EUROPT-4). *J. Catal.* **166**, 172–185 (1997).

153. M. M. Sullivan, A. Bhan, Effects of oxygen coverage on rates and selectivity of propane-CO_2 reactions on molybdenum carbide. *J. Catal.* **357**, 195–205 (2018).

154. R. D. Cortright, S. A. Goddard, J. E. Rekoske, J. A. Dumesic, Kinetic Study of Ethylene Hydrogenation. *J. Catal.* **127**, 342–353 (1991).

155. A. S. McLeod, L. F. Gladden, Monte Carlo simulation of kinetic discontinuities in hydrocarbon hydrogenation reactions. *Catal. Letters*. **43**, 189–194 (1997).

156. C. Stegelmann, N. C. Schiødt, C. T. Campbell, P. Stoltze, Microkinetic modeling of ethylene oxidation over silver. *J. Catal.* **221**, 630–649 (2004).

157. C. T. Campbell, B. E. Koel, Chlorine Promotion of Selective Ethylene Oxidation over Ag(110): Kinetics and Mechanism. *J. Catal.* **92**, 272–283 (1985).

158. S. J. Alas, L. Vicente, TPD study of NO decomposition on Rh(111) by dynamic Monte Carlo simulation. *Surf. Sci.* **604**, 957–964 (2010).

159. A. G. Makeev, M. M. Slinko, Mathematic modelling of the peculiarities of NO decomposition on Rh(111). *Surf. Sci.* **359**, L467–L472 (1996).

160. C.-J. Chen, J. W. Harris, A. Bhan, Kinetics of Ethylene Epoxidation on a Promoted Ag/α-Al2O3 Catalyst-The Effects of Product and Chloride Co-Feeds on Rates and Selectivity. *Chem. Eur. J.* **24**, 1–12 (2018).

161. T. C. Wong, L. F. Brown, G. L. Haller, Hydrogenolysis and Hydrogenation of Hydrocarbons on Supported Rh-Ir Bimetallic Catalysts. *J. Chem. Soc. Faraday Transcations*. **71**, 519–533 (1981).

162. E. Iglesia, M. Boudart, Structure-Sensitivity and Ensemble Effects In Reactions of

Strongly Adsorbed Intermediates. Catalytic Dehydrogenation and Dehydration of Formic Acid on Nickel. *J. Phys. Chem.* **95**, 7011–7016 (1991).

163. C. T. Campbell, M. T. Paffett, A. F. Voter, Testing site size requirements in chemisorption: Experiment and theory. *J. Vac. Sci. Technol. A*. **4**, 1342–1346 (1986).

164. R. G. Windham, B. E. Koel, T. Paffett, Studies of the Ensemble Size Requirements for Ethylene Adsorption and Decomposition on Pt(lll): Ethylene and Bismuth Coadsorption. *Langmuir*. **4**, 1113–1118 (1988).

165. G. A. Martin, R. Dutartre, S. Yuan, C. Marquez-Alvarez, C. Mirodatos, Applicability and Limits of the Ensemble Model in Catalysis by Metals: The Kinetics of Ethane Hydrogenolysis over Pt/SiO_2. *J. Catal.* **177**, 105–112 (1998).

166. N. K. Razdan, A. Bhan, Kinetic description of site ensembles on catalytic surfaces. *Proc. Natl. Acad. Sci.* **118**, 1–11 (2021).

167. J. W. Evans, Kinetic Phase Transitions in Catalytic Reaction Models. *Langmuir*. **7**, 2514–2519 (1991).

168. M. Boudart, G. Djéga-Mariadassou, in *Kinetics of Heterogenous Catalytic Reactions*, J. M. Prausnitz, L. Brewer, Eds. (Princeton University Press, Princeton, ed. 1, 1984), pp. 39–77.

169. T. L. Hill, *Introduction to Statistical Thermodynamics* (Addison-Wesley, Reading, Massachusetts, 1960).

170. O. A. Hougen, K. M. Watson, Solid Catalysts and Reaction Rates - General Principles. *Ind. Eng. Chem.* **35**, 529–541 (1943).

171. O. Hinrichsen, R. Rosowski, M. Muhler, G. Ertl, The microkinetics of ammonia

synthesis catalyzed by cesium-promoted ruthenium. *Chem. Eng. Sci.* **51**, 1683–1690 (1996).

172. B. L. Foley, A. Bhan, Thermodynamically consistent forward and reverse degrees of rate control in reversible reactions. *J. Catal.* **389**, 566–577 (2020).

173. A. Hussain Motagamwala, J. A. Dumesic, Analysis of reaction schemes using maximum rates of constituent steps. *Proc. Natl. Acad. Sci.* **113**, E2879–E2888 (2016).

174. C. Reece, R. J. Madix, Moving from Fundamental Knowledge of Kinetics and Mechanisms on Surfaces to Prediction of Catalyst Performance in Reactors. *ACS Catal.* **11**, 3048–3066 (2021).

175. C. T. Campbell, J. M. Campbell, P. J. Dalton, F. C. Henn, J. A. Rodriguez, S. G. Seimanides, Probing Ensemble Effects in Surface Reactions. 1. Site-Size Requirements for the Dehydrogenation of Cyclic Hydrocarbons on Pt(111) Revealed by Bismuth Site Blocking. *J. Phys. Chem*. **93**, 806–814 (1989).

176. W. M. H. Sachtler, R. A. van Santen, Surface Composition and Selectivity of Alloy Catalysts. *Adv. Catal.* **26**, 69–119 (1977).

177. A. Kumar, A. Bhan, Oxygen content as a variable to control product selectivity in hydrodeoxygenation reactions on molybdenum carbide catalysts. *Chem. Eng. Sci.* **197**, 371–378 (2019).

178. C. H. Lien, J. W. Medlin, Promotion of activity and selectivity by alkanethiol monolayers for Pd-catalyzed benzyl alcohol hydrodeoxygenation. *J. Phys. Chem. C*. **118**, 23783–23789 (2014).

179. S. Wang, E. Iglesia, Entropy-Driven High Reactivity of Formaldehyde in

Nucleophilic Attack by Enolates on Oxide Surfaces. *J. Am. Chem. Soc.* **140**, 775–782 (2018).

180. W. Tu, Y.-H. (Cathy) Chin, Catalytic Consequences of Chemisorbed Oxygen during Methanol Oxidative Dehydrogenation on Pd Clusters. *ACS Catal.* **5**, 3375–3386 (2015).

181. K.-I. Fujimoto, F. H. Ribeiro, M. Avalos-Borja, E. Iglesia, Structure and Reactivity of PdOx/ZrO2 Catalysts for Methane Oxidation at Low Temperatures. *J. Catal.* **179**, 431–442 (1998).

182. W. Tu, M. Ghoussoub, C. Veer Singh, Y.-H. (Cathy) Chin, Consequences of Surface Oxophilicity of Ni, Ni-Co, and Co Clusters on Methane Activation. *J. Am. Chem. Soc.* **139**, 6928–6945 (2017).

183. N. Cardona-Martinez, J. A. Dumesic, Applications of Adsorption Microcalorimetry to the Study of Heterogeneous Catalysis. *Adv. Catal.* **38**, 149–244 (1992).

184. K. Liu, A. Wang, W. Zhang, J. Wang, Y. Huang, X. Wang, J. Shen, T. Zhang, Microkinetic Study of CO Oxidation and PROX on Ir-Fe Catalyst. *Ind. Eng. Chem. Res.* **50**, 758–766 (2011).

185. J. Shen, J. M. Hill, R. M. Watwe, B. E. Spiewak, J. A. Dumesic, Microcalorimetric, infrared spectroscopic, and DFT studies of ethylene adsorption on Pt/SiO_2 and $Pt-Sn/SiO_2$ catalysts. *J. Phys. Chem. B*. **103**, 3923–3934 (1999).

186. J. B. Miller, H. R. Siddiqui, S. M. Gates, J. N. Russell, J. T. Yates, J. C. Tully, M. J. Cardillo, Extraction of kinetic parameters in temperature programmed desorption: A comparison of methods. *J. Chem. Phys.* **87**, 6725–6732 (1987).

187. P. Azadi, G. Brownbridge, I. Kemp, S. Mosbach, J. S. Dennis, M. Kraft,

Microkinetic modeling of the Fischer-Tropsch synthesis over cobalt catalysts. *ChemCatChem*. **7**, 137–143 (2015).

188. R. A. Van Santen, A. J. Markvoort, I. A. W. Filot, M. M. Ghouri, E. J. M. Hensen, Mechanism and microkinetics of the Fischer-Tropsch reaction. *Phys. Chem. Chem. Phys.* **15**, 17038 (2013).

189. S. Storsaeter, D. Chen, A. Holmen, Microkinetic modelling of the formation of C_1 and C_2 products in the Fischer-Tropsch synthesis over cobalt catalysts. *Surf. Sci.* **600**, 2051–2063 (2006).

190. S. A. Goddard, R. D. Cortright, J. A. Dumesic, Deuterium Tracing Studies and Microkinetic Analysis of Ethylene Hydrogenation over Platinum. *J. Catal.* **137**, 186–198 (1992).

191. J. E. Rekoske, R. D. Cortright, S. A. Goddard, S. B. Sharma, J. A. Dumesic, Microkinetic Analysis of Diverse Experimental Data for Ethylene Hydrogenation on Platinum. *J. Phys. Chem*. **96**, 1880–1888 (1992).

192. D. Duca, L. Botar, T. Vidoczy, Monte Carlo Simulation of Ethylene Hydrogenation on Pt Catalysts. *J. Catal.* **162**, 260–267 (1996).

193. E. Iglesia, S. L. Soled, R. A. Fiato, G. H. Via, Bimetallic Synergy in Cobalt Ruthenium Fischer-Tropsch Synthesis Catalysts. *J. Catal.* **143**, 345–368 (1993).

194. A. K. Datye, J. Schwank, Fischer-Tropsch synthesis on bimetallic ruthenium-gold catalysts. *J. Catal.* **93**, 256–269 (1985).

195. J. Newman, K. E. Thomas-Alyea, *Electrochemical Systems* (Wiley-Interscience, Third., 2004).

196. A. J. Bard, L. R. Faulkner, *Electrochemical Methods: Fundamentals and*

Applications (John Wiley & Sons, Second., 2001).

197. A. Baz, A. Holewinski, Predicting macro-kinetic observables in electrocatalysis using the generalized degree of rate control. *J. Catal.* **397**, 233–244 (2021).

198. R. Guidelli, R. G. Compton, J. M. Feliu, E. Gileadi, J. Lipkowski, W. Schmickler, S. Trasatti, Defining the transfer coefficient in electrochemistry: An assessment (IUPAC Technical Report). *Pure Appl. Chem.* **86**, 245–258 (2014).

199. J. C. R. Reis, Thermodynamic analysis of the symmetry factor and the transfer coefficient in electrode kinetics. *J. Electrochem. Soc.* . **144**, 2404–2409 (1997).

200. Nian-Tzu Suen, Sung-Fu Hung, Quan Quan, Nan Zhang, Yi-Jun Xu, H. Ming Chen, Electrocatalysis for the oxygen evolution reaction: recent development and future perspectives. *Chem. Soc. Rev.* **46**, 337–365 (2017).

201. M. Boudart, Virtual pressure and virtual fugacity in catalysis and electrocatalysis. *Catal. Letters*. **3**, 111–115 (1989).

202. Z. J. Schiffer, N. Lazouski, N. Corbin, K. Manthiram, Nature of the First Electron Transfer in Electrochemical Ammonia Activation in a Nonaqueous Medium. *J. Phys. Chem. C*. **123**, 9713–9720 (2019).

203. A. Holewinski, S. Linic, Elementary Mechanisms in Electrocatalysis: Revisiting the ORR Tafel Slope. *J. Electrochem. Soc.* **159**, 864–870 (2012).

204. J. O. Bockris, Z. Nagy, Symmetry Factor and Transfer Coefficient A source of confusion in electrode kinetics. *J. Chem. Educ.* **50**, 839–843 (1973).

205. K. S. Exner, I. Sohrabnejad-Eskan, H. Over, A Universal Approach To Determine the Free Energy Diagram of an Electrocatalytic Reaction. *ACS Catal.* **8**, 1864–1879 (2018).

206. H. Ha, K. Jin, S. Park, K. G. Lee, K. H. Cho, H. Seo, H. Y. Ahn, Y. H. Lee, K. T. Nam, Highly Selective Active Chlorine Generation Electrocatalyzed by Co_3O_4 Nanoparticles: Mechanistic Investigation through in Situ Electrokinetic and Spectroscopic Analyses. *J. Phys. Chem. Lett.* **10**, 1226–1233 (2019).

207. E. J. F. Dickinson, A. J. Wain, The Butler-Volmer equation in electrochemical theory: Origins, value, and practical application. *J. Electroanal. Chem.* **872**, 114145 (2020).

208. T. Shinagawa, A. T. Garcia-Esparza, K. Takanabe, Insight on Tafel slopes from a microkinetic analysis of aqueous electrocatalysis for energy conversion. *Sci. Rep.* **5** (2015), doi:10.1038/srep13801.

209. S. Fletcher, Tafel slopes from first principles. *J. Solid State Electrochem.* **13**, 537–549 (2009).

210. A. Calderón-Cárdenas, E. A. Paredes-Salazar, H. Varela, Apparent Activation Energy in Electrochemical Multistep Reactions: A Description via Sensitivities and Degrees of Rate Control. *ACS Catal.* **10**, 9336–9345 (2020).

211. R. C. Tolman, The Principle of Microscopic Reversibility. *Proc. Natl. Acad. Sci.* **11**, 436–439 (1925).

212. R. M. Krupka, H. Kaplan, K. J. Laidler, Kinetic consequences of the principle of microscopic reversibility. *Trans. Faraday Soc.* **62**, 2754–2859 (1966).

213. A. T. Marshall, L. Vaisson-Béthune, Avoid the quasi-equilibrium assumption when evaluating the electrocatalytic oxygen evolution reaction mechanism by Tafel slope analysis. *Electrochem. commun.* **61**, 23–26 (2015).

214. D. B. Sepa, M. V. Vojnovic, L. M. Vracar, A. Damjanovic, Different views

regarding the kinetics and mechanisms of oxygen reduction at Pt and Pd electrodes. *Electrochim. Acta*. **32**, 129–134 (1987).

215. G. F. Wei, Y. H. Fang, Z. P. Liu, First principles tafel kinetics for resolving key parameters in optimizing oxygen electrocatalytic reduction catalyst. *J. Phys. Chem. C*. **116**, 12696–12705 (2012).

216. B. V. Tilak, C. P. Chen, Generalized analytical expressions for Tafel slope, reaction order and a.c. impedance for the hydrogen evolution reaction (HER): mechanism of HER on platinum in alkaline media. *J. Appl. Electrochem.* **23**, 631–640 (1993).

217. B. E. Conway, L. Bai, Determination of adsorption of OPD H species in the cathodic hydrogen evolution reaction at Pt in relation to electrocatalysis. *J. Electroanal. Chem.* **198**, 149–175 (1986).

218. B. E. Conway, L. Bai, H_2 evolution kinetics at high activity Ni-Mo-Cd electrocoated cathodes and its relation to potential dependence of sorption of H*. *Int. J. Hydrogen Energy*. **11**, 533–540 (1986).

219. N. M. Marković, B. N. Grgur, P. N. Ross, Temperature-dependent hydrogen electrochemistry on platinum low-index single-crystal surfaces in acid solutions. *J. Phys. Chem. B*. **101**, 5405–5413 (1997).

220. E. Mostafa, H. Baltruschat, Apparent transfer coefficient for ORR at polycrystalline platinum under convection conditions: A potential modulation study. *J. Solid State Electrochem.* **17**, 1861–1867 (2013).

221. A. Damjanovic, M. A. Genshaw, J. O. M. Bockris, Hydrogen peroxide formation in oxygen reduction at gold electrodes. II. Alkaline solution. *J. Electroanal. Chem.* **15**, 173–180 (1967).

222. K. S. Exner, J. Anton, T. Jacob, H. Over, Full Kinetics from First Principles of the Chlorine Evolution Reaction over a RuO_2(110) Model Electrode. *Angew. Chemie - Int. Ed.* **55**, 7501–7504 (2016).

223. K. S. Exner, H. Over, Kinetics of Electrocatalytic Reactions from First-Principles: A Critical Comparison with the Ab Initio Thermodynamics Approach. *Acc. Chem. Res.* **50**, 1240–1247 (2017).

224. J. O'M Bockris, I. A. Ammar, A. K. M. S. Huq, The mechanism of the hydrogen evolution reaction on platinum, silver, and tungsten surfaces in acid solutions. *J. Phys. Chem.* **61**, 879–886 (1957).

225. J. S. Spendelow, J. D. Goodpaster, P. J. A. Kenis, A. Wieckowski, Mechanism of CO oxidation on Pt(111) in alkaline media. *J. Phys. Chem. B*. **110**, 9545–9555 (2006).

226. A. Baz, A. Holewinski, Understanding the interplay of bifunctional and electronic effects: Microkinetic modeling of the CO electro-oxidation reaction. *J. Catal.* **384**, 1–13 (2020).

227. T. Cheng, H. Xiao, W. A. Goddard, Full atomistic reaction mechanism with kinetics for CO reduction on Cu(100) from ab initio molecular dynamics free-energy calculations at 298 K. *Proc. Natl. Acad. Sci. U. S. A.* **114**, 1795–1800 (2017).

228. M. Schreier, Y. Yoon, M. N. Jackson, Y. Surendranath, Competition between H and CO for Active Sites Governs Copper-Mediated Electrosynthesis of Hydrocarbon Fuels. *Angew. Chemie - Int. Ed.* **57**, 10221–10225 (2018).

229. K. P. Kuhl, E. R. Cave, D. N. Abram, T. F. Jaramillo, New insights into the electrochemical reduction of carbon dioxide on metallic copper surfaces. *Energy*

Environ. Sci. **5**, 7050–7059 (2012).

230. A. J. Garza, A. T. Bell, M. Head-Gordon, Mechanism of CO_2 Reduction at Copper Surfaces: Pathways to C_2 Products. *ACS Catal.* **8**, 1490–1499 (2018).

231. A. Nielsen, J. Kjaer, B. Hansen, Rate Equation and Mechanism of Ammonia Synthesis at Industrial Conditions. *J. Catal.* **3**, 68–79 (1964).

A Supporting Information for Controlling kinetic and diffusive length-scales during absorptive hydrogen removal in methane dehydroaromatization on MoCx/H-ZSM-5 catalysts

A.1 Simulation of CH_4 aromatization with in-situ hydrogen abstraction for ideal plug flow reactor

The reaction-transport model presented in Section 2.3.2 was used to predict the hydrogen partial pressure profile and methane single-pass conversion along the axial coordinate of the catalyst bed for an ideal plug flow reactor with Pe = 100. The results of the simulation are shown in Figure A.1 below. The predominance of convective mass transport as Pe → ∞ or Pe >> Da limits the capacity of neighboring fluid elements to transfer matter axially, preventing bed-scale suppression of H_2 partial pressure (Figure A.1(a)) and enhancement in methane conversion (Figure A.1(b)).

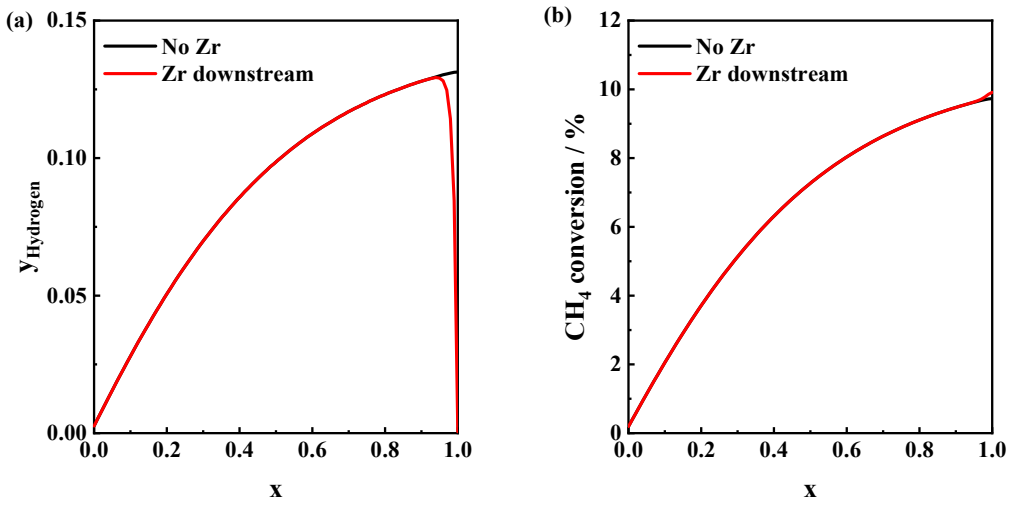

Figure A.1: (a) Hydrogen partial pressure and (b) maximum single-pass (steady-state) methane conversion along non-dimensional axial coordinate of catalyst bed, x, for an ideal plug flow reactor with Pe = 100 as predicted by simulation of the kinetic-transport model for MoCx/H-ZSM-5 only (No Zr) and Zr packed downstream of MoC_x/H-ZSM-5. Reaction conditions: 973 K, MoC_x/H-ZSM-5 ≈ 1.2 g, Zr ≈ 2.4 g, feed flow rate ≈ 0.21 $cm^3\ s^{-1}$ (90 vol% CH_4).

A.2 Calculation of H_2 Mutual Diffusion Coefficients from Correlative Relations

Matsunaga, Hori, and Nagashima (*51*) report mutual diffusion coefficients of dilute H_2 in air, N_2, and O_2 at atmospheric pressure over a wide range of temperature (303 K – 503 K). Data are fit to correlations resembling power-law dependences predicted by the kinetic theory of gases

$$D = AT^B \qquad \textbf{[A.1]}$$

where A and B are fitting parameters listed below.

Table A.1: Diffusion-coefficient correlation parameters from Matsunaga, et al. (*51*) for intermolecular bulk counter diffusion of H_2 and various gases or gaseous mixtures.

System	A / [$cm^2 K^{-B} s^{-1}$]	B
H_2-air	$4.19 \cdot 10^{-5}$	1.73
H_2-N_2	$4.68 \cdot 10^{-5}$	1.71
H_2-O_2	$3.68 \cdot 10^{-5}$	1.76

Using the reported values gives an average diffusion coefficient D (973 K)=6.3 ± 0.2 $cm^2\ s^{-1}$ across the three studied systems.

A.3 Reaction-Transport Simulations: Effects of Damköhler and Péclet Number

Section 2.3.4 examines the key interplay of kinetic, convective, and diffusive length-scales in catalyst-absorbent mixtures for methane DHA by systematic change of catalyst bed-length, L, and linear velocity, u. Figures A.2 and A.3 are surface plots of B+N yield as a function of Da_B and Pe, with and without Zr, respectively. Da_B and Da_N are increased in concert such that the condition $Da_B/Da_N = k_B/k_N$ holds for all values of Da_B. Figure A.3 demonstrates that, without introduction of a hydrogen removal function, increase of Da or Pe^{-1} is unable to effect enhancement of B+N yield or methane conversion beyond limits

prescribed by equilibrium. Addition of Zr in Figure A.2 permits rapid increase of B+N yield as kinetic limits and resistance to dispersive H_2 transport are relaxed with increase of Da and Pe^{-1}, respectively.

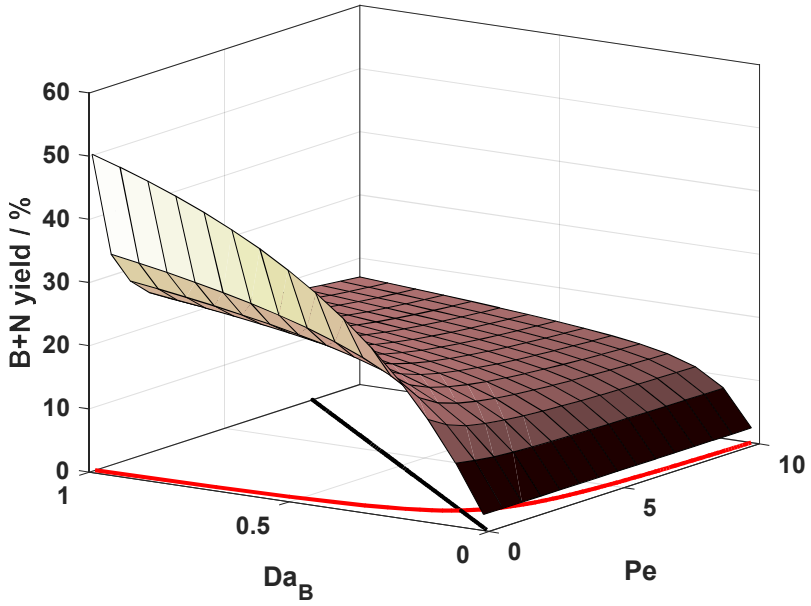

Figure A.2: Surface plot of maximum single-pass B+N yield as a function of Da_B and Pe with downstream Zr bed per simulation of the reaction-transport model. The red curve is the path parameterized by change of linear velocity, u. The black line is the path parameterized by change of bed length, L. The projection of the surface plot onto the red curve is shown as a dashed line in Figure 2.4a of the main text. The projection of the surface plot onto the black line is shown as a dashed line in Figure 2.4b of the main text.

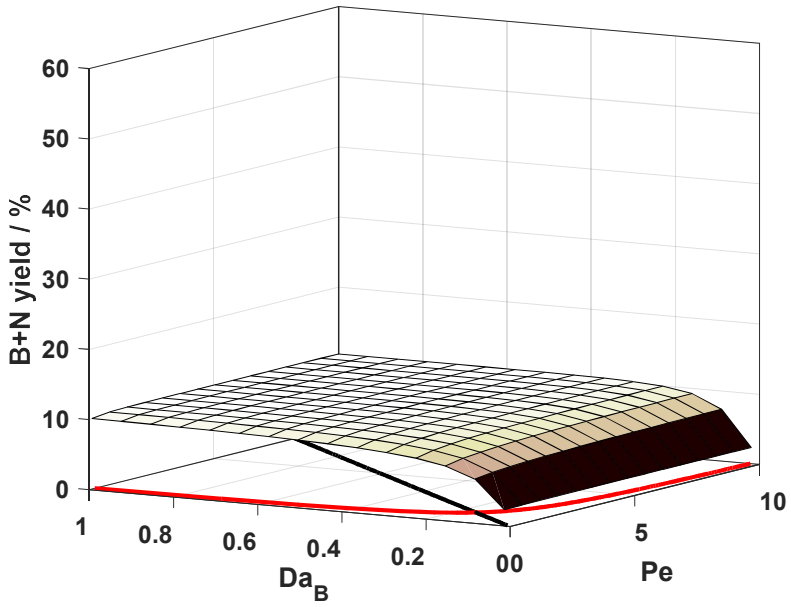

Figure A.3: Surface plot of maximum single-pass B+N yield as a function of Da_B and Pe without Zr per simulation of the reaction-transport model. The red curve is the path parameterized by change of linear velocity, u. The black line is the path parameterized by change of bed length, L. The projection of the surface plot onto the red curve is shown as a solid line in Figure 2.4a of the main text. The projection of the surface plot onto the black line is shown as a solid line in Figure 2.4b of the main text.

B Supporting Information for Influence of ethylene and acetylene on the rate and reversibility of methane dehydroaromatization on Mo/H-ZSM-5 catalysts

B.1 Rates of Acetylene and Methane Aromatization

All carburized MoC_x/H-ZSM-5 catalysts used for experiments reported in this work were synthesized under identical flow conditions. Oxidic pre-catalysts were exposed to CH_4/Ar (90 vol% CH_4 and 10 vol% Ar, total feed flow rate 0.21 cm^3 s^{-1}, UHP, Matheson Tri-Gas) at 973 K until carburization was complete – as indicated by closure of carbon balance. An example is shown in Figure B.1 which depicts methane conversion as a function of time-on-stream for 0.150 g fresh oxidic pre-catalyst exposed to the reaction mixture.

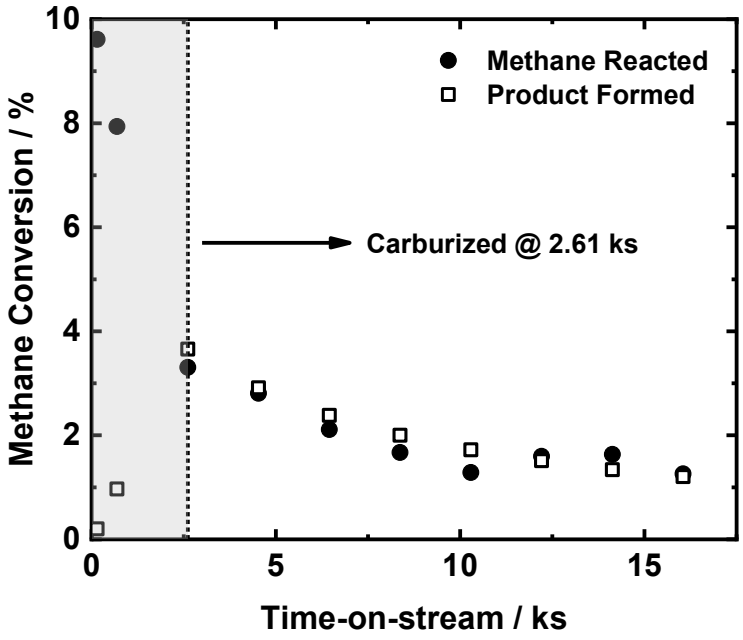

Figure B.1: Methane conversion of 0.150 g Mo/H-ZSM-5 catalyst (Mo/Al = 0.25, Si/Al = 11.5) exposed to 0.21 cm^3 s^{-1} 90% CH_4, 10% Ar at ~115 kPa total pressure and 973 K.

Methane conversion is calculated based on reacted methane

$$f = \frac{F_{CH_4,in} - F_{CH_4,out}}{F_{CH_4,in}} \quad \textbf{[B.1]}$$

and carbon in effluent products

$$f = \frac{1}{F_{CH_4,in}} \sum_{j=products} n_j F_j \quad \textbf{[B.2]}$$

where n_j is the carbon number of product j. Carburization is complete once these values agree within experimental error – demonstrating carbon balance has closed (> 2.61 ks in Fig. B.1). After this period, DHA reactions were either continued under 0.21 cm^3 s^{-1} total flow or were performed at identical composition, but varied flow range, after ~30 minutes flush of reactor lines in He flow (~ 0.33 cm^3 s^{-1}) as reaction feed flow stabilized.

Acetylene aromatization rates shown in Fig. B.2 were measured on 0.150 g Mo/H-ZSM-5 carburized in 0.21 cm^3 s^{-1} 90% CH_4 / 10% Ar flow at 973 K and ~115 kPa total pressure. Once steady-state benzene rates were achieved, reaction feed was switched to 1.46 cm^3 s^{-1} 0.75% C_2H_2 / balance Ar after ~30 minutes flush of reactor lines in He flow (~ 0.33 cm^3 s^{-1}) as reaction feed flow stabilized. The content of acetylene in feed mixture corresponds to the calculated equilibrium concentration of acetylene for complete conversion of 103 kPa CH_4 to C_2H_2 and H_2 at 973 K.

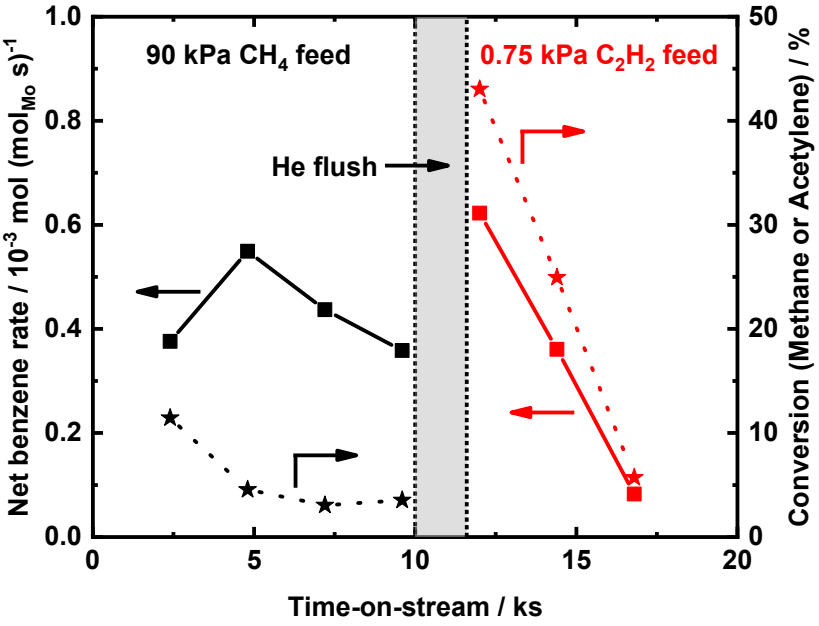

Figure B.2: Net benzene synthesis rates and methane and acetylene conversion on 0.15g Mo/H-ZSM-5 catalyst (Mo/Al = 0.25, Si/Al = 11.5) exposed to 13 cm^3 s^{-1} 90% CH_4, 10% Ar and then 0.75% C_2H_2 / balance Ar at ~115 kPa total pressure and 973 K.

Equilibrium conversion of 0.86 kPa acetylene to benzene is >99% and, as such, overall approach to equilibrium of acetylene to benzene formation never exceeds 0.02 during aromatization reactions with 0.86 kPa C_2H_2 feed. Thus, measured net benzene synthesis rates are equivalent to length-averaged forward rates of acetylene to benzene synthesis. Forward rates of the acetylene to benzene reaction during PSS methane DHA can be calculated using De Donder relations as

$$\vec{r}_D = \frac{F_{C_6H_6} + F_{C_{10}H_8}}{< 1 - Z_D^{2/3} >} \qquad \textbf{[B.3]}$$

taking the net length-averaged rate of benzene formation to be the sum of benzene and naphthalene effluent flow rates. Fig. B.3 shows forward rates of acetylene to benzene synthesis as a function of contact-time during methane DHA reactions per Eq. **B.3**.

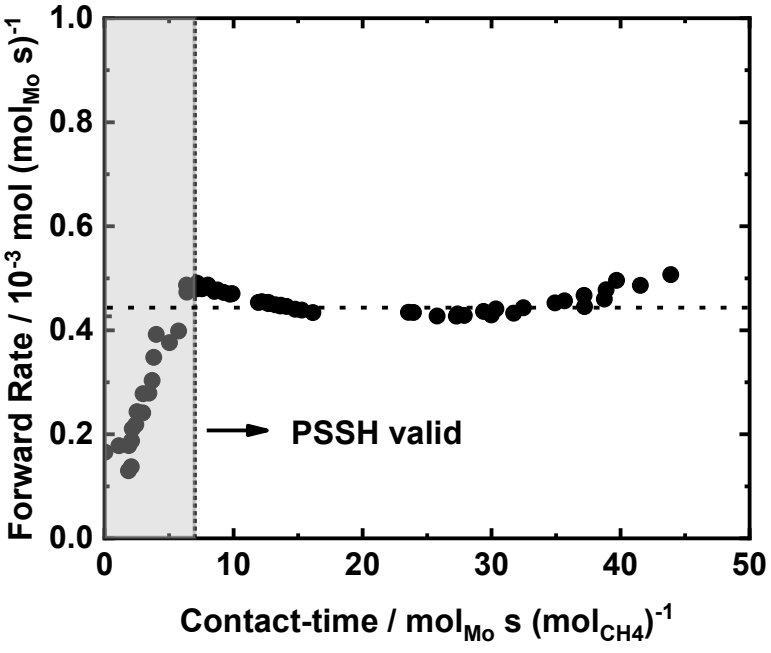

Figure B.3: Forward rate of the acetylene to benzene reaction [=] $mol_{benzene}$ $(mol_{Mo}\ s)^{-1}$ as a function of contact-time varied by extent of deactivation at 973 K.

The steady-state forward rate of acetylene to benzene formation during methane DHA is $4.4 \cdot 10^{-4}$ mol $(mol_{Mo}\ s)^{-1}$ and is comparable to the maximum measured length-averaged forward rate with acetylene feed of $6.2 \cdot 10^{-4}$ mol $(mol_{Mo}\ s)^{-1}$. These findings corroborate Scheme 3.1 and 3.2 which posit acetylene is an intermediate to benzene formation.

B.2 Kinetics of Methane DHA Proceeding through Ethylene Oligomerization

Despite the body of evidence which suggests acetylene is an intermediate of aromatic formation, we cannot unequivocally eliminate the possibility that acetylene is a side-product of ethane/ethylene dehydrogenation and that benzene formation proceeds directly from ethylene coupling. In such a case, the reaction network is summarized by Scheme B.1 and B.2.

Scheme B.1: Alternative methane DHA reaction pathway

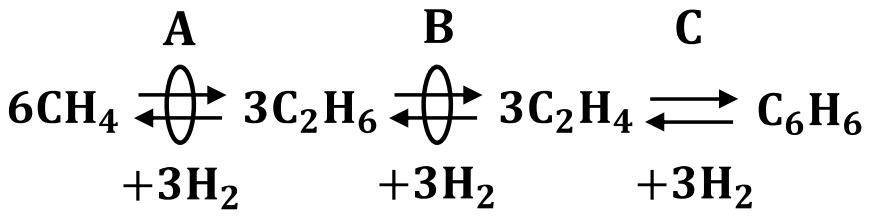

Methane, ethane, and ethylene form a quasi-equilibrated pool catalyzed by carbidic Mo sites for sufficient contact-times (> 7 mol_{Mo} s mol_{CH4}^{-1}). Subsequent ethylene aromatization may be catalyzed by Mo or zeolitic Brønsted acid sites.

Scheme B.2: Alternative methane DHA reaction sequence with pseudo-elementary steps

	Reaction	σ	σ^*
(A.1)	**$CH_4 \rightleftharpoons CH_3 + ½\ H_2$**		**6**
(A.2)	$2CH_3 \rightleftharpoons C_2H_6$	3	
(A)	$2CH_4 \rightleftharpoons C_2H_6 + H_2$	3	
(B.1)	**$C_2H_6 \rightleftharpoons C_2H_5 + ½\ H_2$**		**3**
(B.2)	$C_2H_5 \rightleftharpoons C_2H_4 + ½\ H_2$	3	
(B)	$C_2H_6 \rightleftharpoons C_2H_4 + H_2$	3	
(C.1)	**$2C_2H_4 \rightleftharpoons C_4H_8$**		**1.5**
(C.2)	$C_2H_4 + C_4H_8 \rightleftharpoons C_6H_6 + 3H_2$	1	
(C)	$3C_2H_4 \rightleftharpoons C_6H_6 + 3H_2$	1	

overall	$6CH_4 \rightleftharpoons C_6H_6 + 9H_2$	1

Bolded entries indicate rate-determining elementary steps within each gas-phase global reaction (A, B, and C).

The alternative methane DHA single-path reaction sequence depicted in Schemes B.1 and B.2 gives rise to altered total approach to equilibrium of global gas-phase reactions and approach to equilibrium of rate-determining elementary steps within each global gas-phase reaction for the portion of the reaction sequence succeeding steps A and B. Figures B.4a and B.4b show $Z_{i = A,B,C}$ and $z^{*}_{i = A,B,C}$.

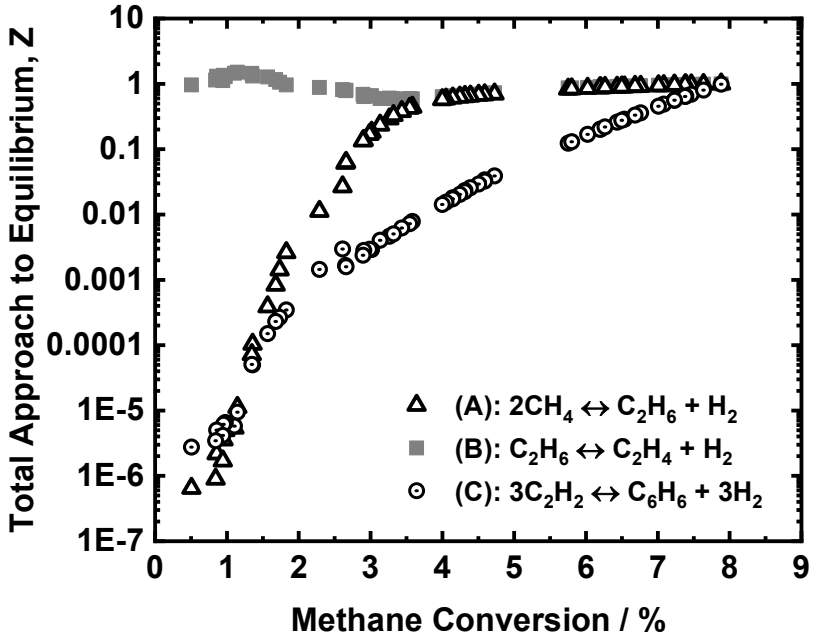

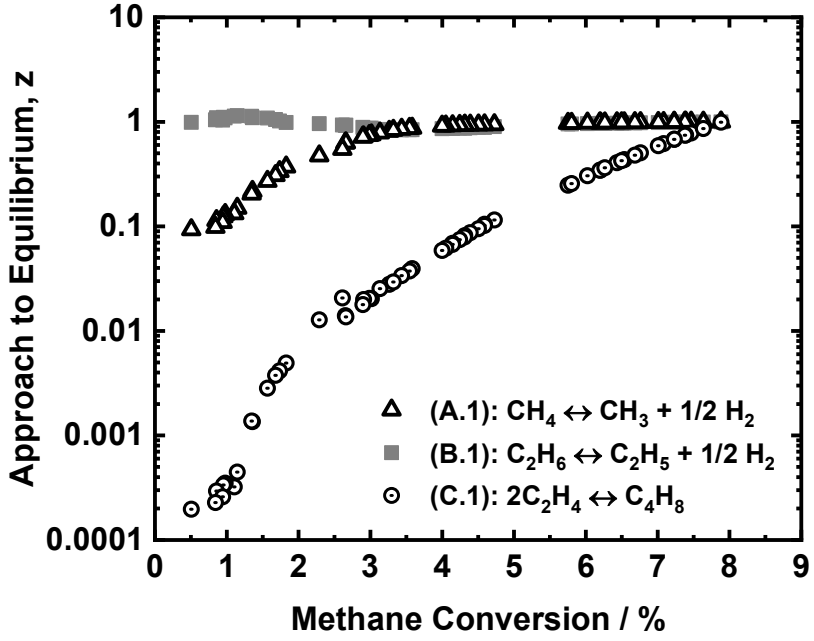

Figure B.4: (a) Total approach to equilibrium of global gas-phase DHA reactions, as listed in Scheme B.1 on a one benzene molecule basis. (b) Approach to equilibrium of rate-determining elementary steps within each global gas-phase DHA reaction, as listed in Scheme B.2. Reaction conditions: 973 K, ~115 kPa total pressure, 90% CH_4, 10% Ar, 0.21-2.1 $cm^3\ s^{-1}$. 0.1-1.2 g Mo/H-ZSM-5

Changes in the approach to equilibrium of global gas-phase reactions and their constituent rate-determining steps manifests changes in the degree of rate control and degree of reversibility control of each step, per Eqs. **3.9** and equations analogous to Eqs. **3.13**-**3.16**. Figures B.5a and B.5b show X_{RC} and X_{ZC} per the reaction sequence in Schemes B.1 and B.2.

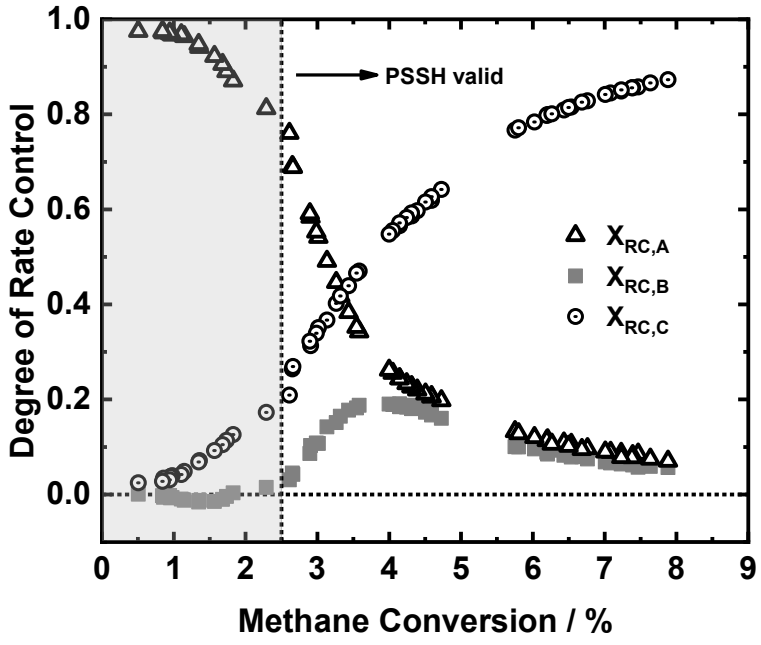

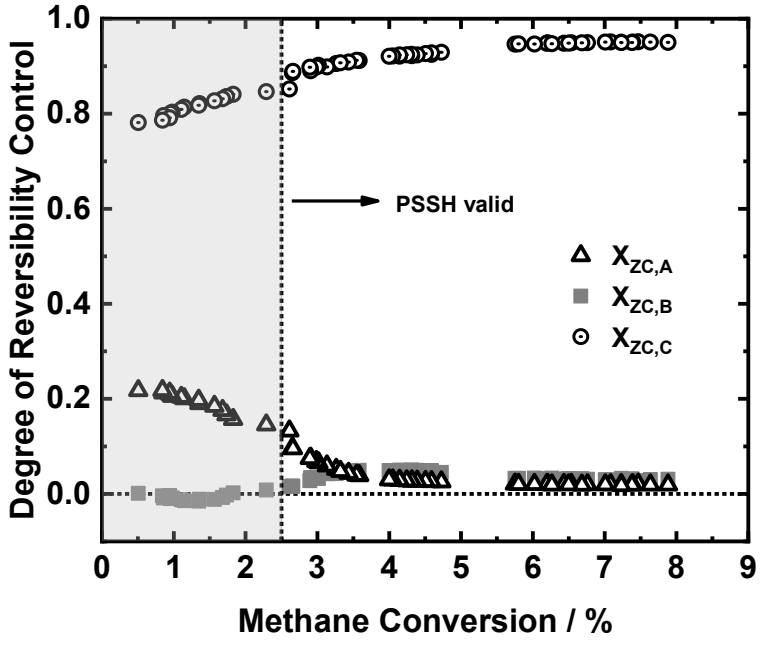

Figure B.5: Degree of rate control (a) and reversibility control (b) of rate-determining elementary steps in global gas-phase reactions A-C (Scheme B.2) from 0.5-8% methane conversion.

Figure B.5 shows steps succeeding ethylene formation are rate and reversibility determining once the reaction sequence achieves a pseudo steady-state upon equilibration of methane, ethane, and ethylene.

Lastly, changes in the reaction network discussed in this section influence $\bar{\sigma}$, the affinity-averaged stoichiometric number, and therefore affect calculation of forward rates. Figure B.6 shows overall forward rate of benzene formation per Schemes B.1 and B.2.

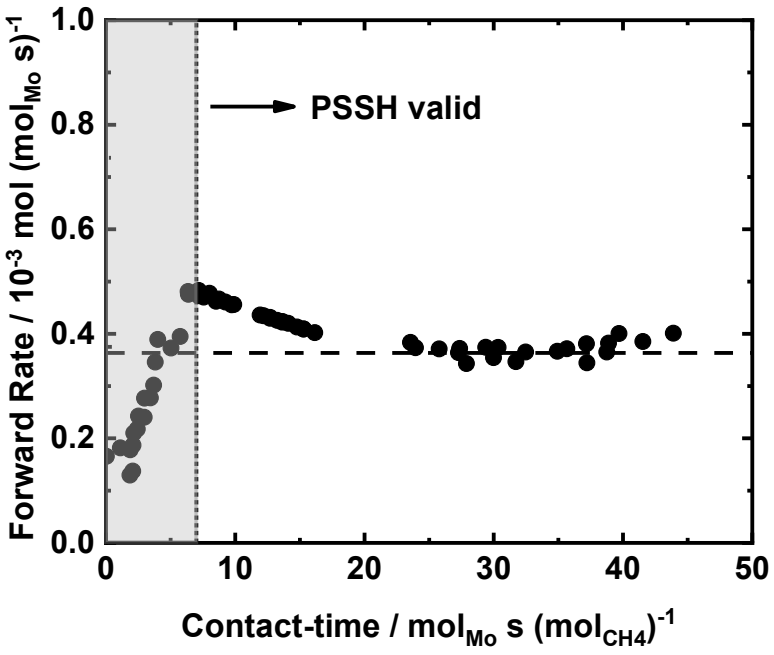

Figure B.6: Forward rates of benzene synthesis [=] $mol_{benzene}$ $(mol_{Mo}\ s)^{-1}$ as a function of contact-time varied by extent of deactivation at T = 973 K. Reaction conditions: 973 K, ~115 kPa total pressure, 90% CH_4, 10% Ar, 0.21-2.1 $cm^3\ s^{-1}$. 0.1-1.2 g Mo/H-ZSM-5.

The forward rate in Fig. B.6 approaches a steady value of $0.36 \cdot 10^{-3}$ mol $(mol_{Mo}\ s)^{-1}$, as indicated by the dashed line, and is comparable to the forward rate per Scheme 3.1 and 3.2 of $0.39 \cdot 10^{-3}$ mol $(mol_{Mo}\ s)^{-1}$ shown in Fig. 3.6. The identity of acetylene as an intermediate therefore has little bearing on the magnitude of the forward rate.

B.3 De Donder Relations, The Degree of Reversibility Control, and Relation of Thermodynamic Quantities to Reversibility of Global Gas-Phase Reactions

B.3.1 The Degree of Reversibility Control

The degree of reversibility control of elementary step i is defined as

$$X_{ZC,i} \equiv \left(\frac{\partial \ln \ln(z_{eff})}{\partial \ln \ln(z_i)}\right)_{z_j \neq i} = \frac{A_i}{\sum_j A_j} \qquad \textbf{[3.9]}$$

where index j refers to all elementary steps in the considered single-path reaction sequence. Expanding the definition in Eq. **3.9**,

$$\left(\frac{\partial \ln \ln(z_{eff})}{\partial \ln \ln(z_i)}\right)_{z_j \neq i} = \frac{\ln(z_i)}{\ln(z_{eff})}\left(\frac{\partial \ln(z_{eff})}{\partial \ln(z_i)}\right)_{z_j \neq i} = \frac{\ln(z_i)}{\ln(z_{eff})}\left(\frac{\partial \sum_j \ln(z_j)}{\partial \ln(z_i)}\right)_{z_j \neq i} \qquad \textbf{[B.4]}$$

From the definition of z_{eff}

$$z_{eff} = \prod_j z_j = z_{ov}^{1/\bar{\sigma}} \qquad \textbf{[3.8]}$$

Thus,

$$\left(\frac{\partial \ln \ln(z_{eff})}{\partial \ln \ln(z_i)}\right)_{z_j \neq i} = \frac{\ln(z_i)}{\ln(z_{eff})} = \frac{A_i}{\sum_j A_j} = X_{ZC,i} \qquad \textbf{[B.5]}$$

Inspection of Eq. **3.8** suggests there is also a relation between $X_{ZC,i}$ and the contribution of each step to $\bar{\sigma}$. Indeed,

$$X_{ZC,i} \equiv \left(\frac{\partial \ln \ln(z_{eff})}{\partial \ln \ln(z_i)}\right)_{z_j \neq i} = -\left(\frac{\partial \ln(\bar{\sigma} - \sigma_i)}{\partial \ln(A_i)}\right)_{A_j \neq i} \qquad \textbf{[B.6]}$$

This is confirmed in the following. Consider

$$-\left(\frac{\partial \ln(\bar{\sigma} - \sigma_i)}{\partial \ln(A_i)}\right)_{A_j \neq i} = -\frac{A_i}{\bar{\sigma} - \sigma_i}\left(\frac{\partial \bar{\sigma}}{\partial A_i}\right)_{A_j \neq i} \qquad \textbf{[B.7]}$$

So,

$$-\left(\frac{\partial \ln(\bar{\sigma} - \sigma_i)}{\partial \ln(A_i)}\right)_{A_j \neq i} = -\frac{A_i}{\bar{\sigma} - \sigma_i}\left(\frac{\partial}{\partial A_i}\frac{\sum_i \sigma_i A_i}{\sum_i A_i}\right)_{A_j \neq i} \qquad \textbf{[B.8]}$$

Giving,

$$-\left(\frac{\partial \ln(\overline{\sigma}-\sigma_i)}{\partial \ln(A_i)}\right)_{A_j\neq i} = -\frac{A_i}{\overline{\sigma}-\sigma_i}\,\frac{1}{\sum_i A_i}\,\frac{\sigma_i\sum_i A_i - \sum_i \sigma_i A_i}{\sum_i A_i}. \qquad \textbf{[B.9]}$$

or, with simplification,

$$-\left(\frac{\partial \ln(\overline{\sigma}-\sigma_i)}{\partial \ln(A_i)}\right)_{A_j\neq i} = -\frac{A_i}{\overline{\sigma}-\sigma_i}\,\frac{(\sigma_i-\overline{\sigma})}{\sum_i A_i} = \frac{A_i}{\sum_j A_j} = X_{ZC,i} \qquad \textbf{[B.10]}$$

Thus, the degree of reversibility control is a quantitative measure of the extent to which the reversibility of a given step exerts influence on $\overline{\sigma}$, or, more particularly, on $\overline{\sigma}-\sigma_i$. In fact,

$$\overline{\sigma} = \sum_{i=\text{steps}} \sigma_i X_{ZC,i} \qquad \textbf{[B.11]}$$

where index i refers to all elementary steps.

B.3.2 Relation of Thermodynamic Quantities to Total Approach to Equilibrium of Global-Gas Phase Reactions

Section 3.4.3 uses assignment of the stoichiometric number of the rate-determining elementary step within each global gas-phase reaction, σ_i^*, to calculate degrees of rate control, degrees of reversibility control, and forward rate solely from total approach to equilibrium of global gas-phase reactions. This section details those calculations.

As reported in Scheme 3.2, $\sigma_A^*= 6$, $\sigma_B^*= \sigma_C^*= 3$, and $\sigma_D^* = 1.5$. Thus, z_i^* are calculable by Eq. **3.12** from Z_i reported in Fig. 3.3. Application of Eq. **3.7** then gives $\overline{\sigma}$ as

$$\overline{\sigma} = \frac{\sum_{i=A,B,C,D} \sigma_i^* \ln(z_i^*)}{\sum_{i=A,B,C,D} \ln(z_i^*)} \qquad \textbf{[B.12]}$$

which is reported in Fig. B.7

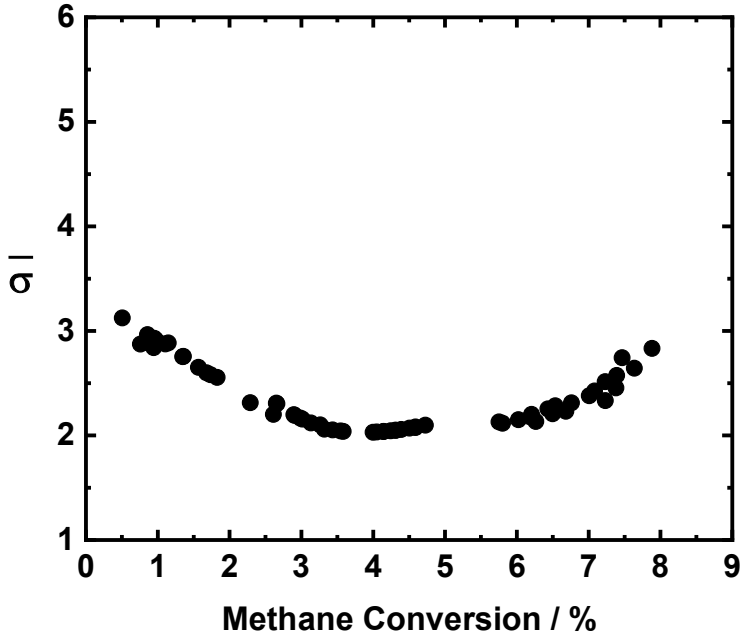

Figure B.7: Affinity-averaged stoichiometric number as a function of methane conversion calculated by Eq. **3.7** using reversibility data shown in Figs. 3.3 and 3.4.

The forward rate per Eq. **3.6** may now be calculated by

$$\vec{R} = \frac{R}{1 - \prod_{i=A,B,C,D} z_i^*} = \frac{R}{1 - z_{ov}^{1/\bar{\sigma}}} \qquad \textbf{[B.13]}$$

and appropriate length-averaging described in Section 3.4.4.

The degree of reversibility control per Eq. **3.9** is also calculated directly from $z_i^* = Z_i^{1/\sigma_i^*}$ as

$$X_{ZC,i} = \frac{\ln(z_i^*)}{\sum_{j=A,B,C,D} \ln(z_j^*)} \qquad \textbf{[B.14]}$$

B.3.3 Relation of Thermodynamic Quantities to Degree of Rate Control

We derive Eqs. **3.13-3.16** from the pseudo-elementary steps in Scheme 3.2 following formalisms developed recently by Foley and Bhan (*88*). These authors prove that for all intermediates j in a single-path reaction sequence which are either in the fluid-phase or have surface coverages much less than unity

$$\sum_{i=steps} \nu_{ij} s_i [\nu_{ij} < 0] = 0 \qquad \textbf{[B.15]}$$

where ν_{ij} is the stoichiometric coefficient of intermediate j in step i. The brackets in Eq. **B.15** are per Iverson Bracket notation where $[\nu_{ij} < 0]$ is equal to unity if true and zero if false. Cortright and Dumesic (*85*) define s_i as the sensitivity of step i

$$s_i = \left(\frac{\partial \ln r}{\partial \ln \vec{k}_i}\right)_{k_{j\neq i}} \qquad \textbf{[B.16]}$$

and

$$s_{-i} = \left(\frac{\partial \ln r}{\partial \ln \overleftarrow{k}_i}\right)_{k_{j\neq i}} \qquad \textbf{[B.17]}$$

which are related by

$$s_{-i} = -z_i s_i \qquad \textbf{[B.18]}$$

and are related to the degree of rate control by

$$X_{RC,i} = s_i + s_{-i} = s_i(1 - z_i). \qquad \textbf{[B.19]}$$

Scheme B.3 lists the result of application of Eq. **B.15** to each carbon-containing intermediate in the methane DHA reaction per Scheme 3.2

Scheme B.3: Application of Eq. **B.15** to each carbon-containing intermediate in Scheme 3.2

Species	**Eq. B.15**
CH_3	$s_{-(A.1)} + \frac{\sigma_A^*}{\sigma_B^*} s_{(A.2)} = 0$
C_2H_6	$s_{-(A.2)} + s_{(B.1)} = 0$
C_2H_5	$s_{-(B.1)} + s_{(B.2)} = 0$

C_2H_4	$s_{-(B.2)} + s_{(C.1)} = 0$
C_2H_3	$s_{-(C.1)} + s_{(C.2)} = 0$
C_2H_2	$s_{-(C.2)} + \frac{\sigma_C^*}{\sigma_D^*} s_{(D.1)} + s_{(D.2)} = 0$
C_4H_4	$s_{-(D.1)} + s_{(D.2)} = 0$

Applying Eqs. **B.16-B.19** to the set of relations in Scheme B.3 then gives, upon rearrangement,

$$s_B^* = \frac{\sigma_B^*}{\sigma_A^*} z_A^* s_A^* \quad \textbf{[B.20]}$$

$$s_C^* = \frac{\sigma_C^*}{\sigma_A^*} z_A^* z_B^* s_A^* \quad \textbf{[B.21]}$$

$$s_D^* = \frac{\frac{\sigma_D^*}{\sigma_A^*} z_A^* z_B^* z_C^*}{\left(1 + \frac{\sigma_C^*}{\sigma_D^*} z_D^*\right)} s_A^* \quad \textbf{[B.22]}$$

where s_i^* is the sensitivity of the rate-determining elementary step within each global gas-phase reaction i (i.e. $s_i^* = s_{(i.1)}$ for all i per Scheme 3.2). We only list sensitivities of rate-determining elementary steps in Eqs. **B.20**-**B.22** since the degree of rate control for all other steps will be zero per Eq. **B.19**. Imposing

$$\sum_{i=\text{steps}} X_{RC,i} = 1 \quad \textbf{[B.23]}$$

as proven by Foley and Bhan (*88*) then gives Eqs. **3.13**-**3.16** upon rearrangement of Eqs. **B.19**-**B.23**.

B.4 Measuring Turnover Frequencies, Controlling Contact-Time, and evaluating PSSH in Ideal and Non-Ideal Flow Reactors

B.4.1 Measuring Net Rates in Dispersed Flow Reactors

As we have recently shown (*47*), laboratory-scale methane DHA flow reactors are characterized by significant axial dispersion owing to large contact-times and high temperatures required for appreciable conversion of methane to aromatics. Residence-time distribution experiments and the fidelity of reaction-transport models to capture the critical role of dispersive H_2 transport in polyfunctional catalyst-absorbent flow configurations demonstrates packed-bed reactors of Mo/H-ZSM-5 are axially-dispersed flow reactors characterized by closed-closed Danckwerts boundary conditions. In the following we will show that

$$F_j = \frac{1}{\int_0^X dx} \cdot \int_0^X \sum_i \nu_{ij} r_i \, dx = \sum_i \nu_{ij} < r_i > \qquad \textbf{[3.17]}$$

in axially dispersed flow reactors, as well as ideal PFRs. First, consider a mole balance for an axially-dispersed flow reactor (*48*)

$$D\frac{d^2C_j}{dz^2} - u\frac{dC_j}{dz} + \sum_i \nu_{ij} r_i = 0 \qquad \textbf{[B.24]}$$

where D is the dispersion coefficient, u is the linear flow velocity, z is the axial coordinate, C_j is the concentration of species j, ν_{ij} is the stoichiometric coefficient of species j in reaction i, and r_i is the net rate of reaction i. Closed-closed boundary conditions are

$$uC_j(z = 0^-) = uC_j(z = 0^+) - D\frac{dC_j}{dz}\bigg|_{z=0^+} \qquad \textbf{[B.25]}$$

and

$$\frac{dC_j}{dz}\bigg|_{z=L} = 0 \qquad \textbf{[B.26]}$$

Integrating Eq. **B.24** from z = 0 to z = L, the outlet of the packed-bed, gives

$$D\left(\left.\frac{dC_j}{dz}\right|_{z=L} - \left.\frac{dC_j}{dz}\right|_{z=0^+}\right) - u\left(C_j(z=L) - C_j(z=0^+)\right) + L\sum_i \nu_{ij} < r_i > = 0 \quad \textbf{[B.27]}$$

Substituting the closed-closed boundary conditions gives

$$u\left(C_j(z=0^-) - C_j(z=0^+)\right) - u\left(C_j(z=L) - C_j(z=0^+)\right) + L\sum_i \nu_{ij} < r_i > = 0 \quad \textbf{[B.28]}$$

Rearranging,

$$\frac{u\left(C_j(z=L) - C_j(z=0^-)\right)}{L} = \sum_i \nu_{ij} < r_i > \quad \textbf{[B.29]}$$

which, for a species not in the reaction feed mixture, gives

$$F_j = \frac{1}{\int_0^L dz} \cdot \int_0^L \sum_i \nu_{ij} r_i \, dz = \sum_i \nu_{ij} < r_i > \quad \textbf{[B.30]}$$

identically to Eq. **3.12**. Thus, provided boundary conditions are closed-closed, effluent flow rates reflect length-average rates in axially dispersed PFRs identically to ideal plug-flow reactors because closed-closed boundary conditions manifest total change in species content from within the packed-bed is resultant from reaction – regardless of axial re-distribution of species by dispersive transport. In other words, axial dispersion does not affect the calculated of rates provided boundary conditions are closed-closed because all the chemical conversion occurs within the catalyst bed.

B.4.2 One-to-oneness of Contact-Time and Conversion in Flow Reactors

Fig. B.8 shows steady-state methane conversion at various contact-times in methane DHA reactors over Mo/H-ZSM-5 catalysts.

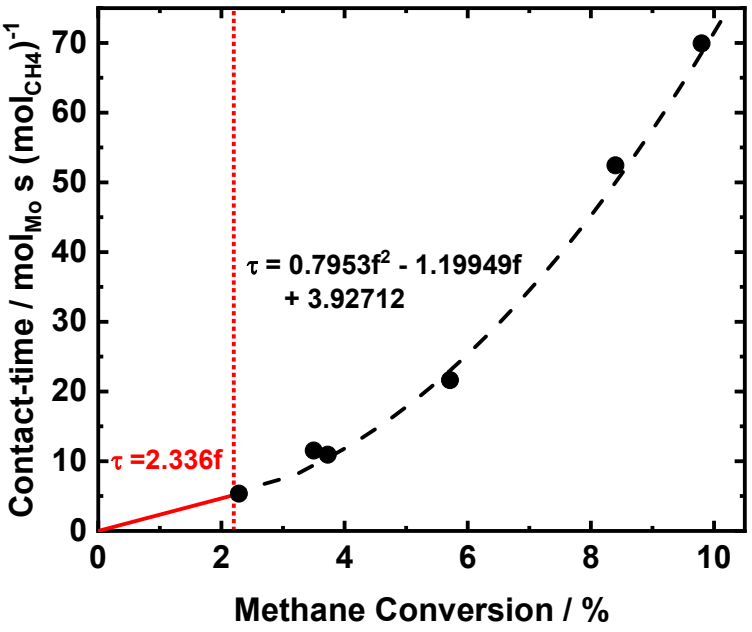

Figure B.8: Steady-state methane conversion as a function of contact-time conversion over several Mo/H-ZSM-5 catalysts (Mo/Al = 0.25, Si/Al = 11.5). Reaction conditions: 973 K, ~115 kPa total pressure, 90% CH_4, 10% Ar, 0.21-2.1 cm^3 s^{-1}, 0.1-1.2 g Mo/H-ZSM-5. Dashed black line and solid red line are heuristic fits used together as a continuous, piecewise mapping of conversion to contact-time.

The continuous, piecewise polynomial in Fig. B.8 is used to length-average reaction reversibilities in order to calculate forward rates in Section 3.4.4.

The equality of f(τ) by deactivation or change of catalyst loading at steady-state (i.e. the one-to-oneness of f(τ)) is not strictly true in dispersed flow reactors. The significance of dispersive transport in axially-dispersed reactors is captured by Péclet number

$$\mathrm{Pe} = \frac{\mathrm{uL}}{\mathrm{D}} = \frac{\text{rate of convection}}{\text{rate of dispersion}} \qquad \textbf{[B.31]}$$

where u is the linear velocity, L is the catalyst bed-length, and D is the dispersion coefficient. The one-to-oneness of f(τ) is exactly true in ideal PFR reactors wherein Pe → ∞. We recently (*47*) demonstrated that the slow kinetics of DHA on Mo/H-ZSM-5 demands flow reactors be operated with Pe = $\mathcal{O}(1)$ to achieve near-equilibrium conversions. The

recent work developed a reaction-transport model based on a non-dimensional version of the mole balance in Eq. **B.24**

$$\frac{1}{Pe}\frac{d^2y_j}{dx^2} - \frac{dy_j}{dx} + y_{CH4}^{0.7}\sum_{i=B,N}\nu_{ij}Da_i\left(1 - z_{ov,i}^{1/\bar{\sigma}_i}\right) = 0 \qquad \textbf{[B.32]}$$

where y_j is the partial pressure of species j normalized by 1 bar, x = z/L, and $Da_i = k_iL/u$ is the Damköhler number of reaction i = B,N for benzene (B) and naphthalene (N) formation with forward rate equations determined by the De Donder formalism. Benzene and naphthalene constitute >90% of carbon selectivity at PSS and are the only product hydrocarbon species considered in the reaction-transport model. Methane, molecular hydrogen, and argon complete the considered gas-phase species. $\bar{\sigma}$ is fixed at 2.5 for both benzene and naphthalene synthesis reactions since $\bar{\sigma} \approx 2.5$ for all methane conversion during PSS (Fig. B.7). $f(\tau)$ is essentially one-to-one function if (i) $f(L/L_0)$, (ii) $f(u_0/u)$, and (iii) $f(Da/Da_0)$ are nearly identical. $f(L/L_0)$ is methane conversion as a function of contact-time changed by catalyst bed-length. $f(u_0/u)$ is methane conversion as a function of contact-time changed by total flow-rate. $f(Da/Da_0)$ is methane conversion as a function of contact-time changed by extent of deactivation (i.e. density of active sites). Fig. B.9 shows conversion vs contact-time changed by each metric.

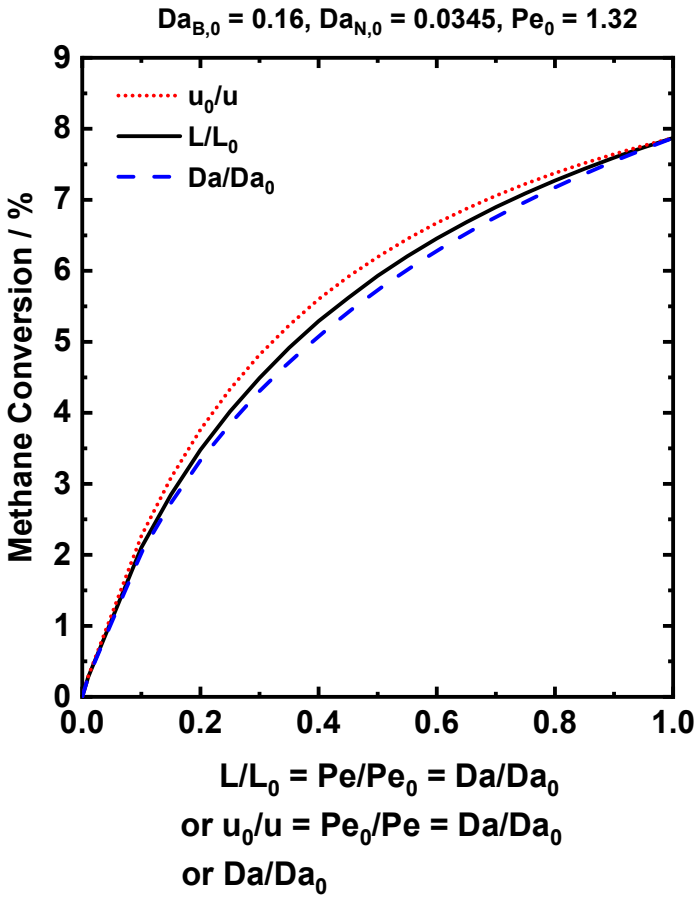

Figure B.9: Steady-state methane conversion to benzene and naphthalene per simulation of Eq. **B.24**.

Fig. B.9 shows variation of contact-time by (i) change of catalyst loading, (ii) change of total flow-rate, or (iii) extent of deactivation gives nearly identical conversion vs. contact-time profiles, demonstrating f(τ) is essentially a one-to-one function. Difference in each profile is close to the experimental error in quantifying methane conversion (~5% of the magnitude of conversion).

B.4.3 Evaluating PSSH in Flow Reactors

The pseudo-steady state hypothesis (PSSH) allows the concentration of reactive intermediates in a flow reactor to be determined arithmetically by reactants and products of an overall reaction sequence provided

$$\frac{d\dot{n}_I}{d\zeta} \ll \frac{d\dot{n}_R}{d\zeta} \qquad \textbf{[B.33]}$$

where $\dot{n}$ [=] mol s^{-1} is molar flow rate, subscript I refers to reactive intermediates, subscript R refers to reactants, and ζ is the axial coordinate along the catalyst bed in units of moles of active site. Assessing the veracity of Eq. **B.33** requires differentiating effluent flow rates, $\dot{n}_I$, of all intermediates with respect to ζ which we determine from the one-to-one function of methane conversion and contact-time since $\zeta = \tau \cdot \dot{n}_{CH_4,Inlet}$ is simply contact-time adjusted by a constant, $\dot{n}_{CH_4,Inlet}$. In the case of the single-path methane DHA reaction per Scheme 3.1 and 3.2, $\dot{n}_I$ is the carbon molar flow rates of all C_2 hydrocarbons and $\dot{n}_R$ is the molar flow rate of methane. Figure B.10 shows methane and C_2 molar flow rates as a function of ζ

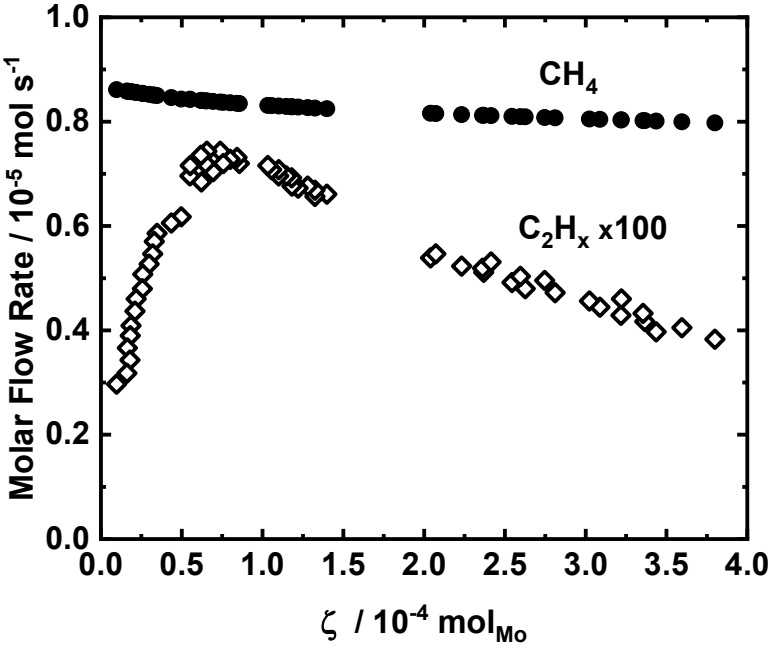

Figure B.10: Effluent molar flow rates of methane and all C_2H_x hydrocarbons as a function of active Mo determined from the one-to-one function of methane conversion to contact-time.

Differentiating the effluent molar flow rates of methane and all C_2H_x hydrocarbons with respect to ζ and taking the ratio defined in Eq. **B.34** gives a quantitative metric for the applicability of the PSSH

$$\mathrm{P} \equiv \left| \frac{\mathrm{d}\dot{n}_\mathrm{I}}{\mathrm{d}\zeta} \Big/ \frac{\mathrm{d}\dot{n}_\mathrm{R}}{\mathrm{d}\zeta} \right| \ll 1. \qquad \textbf{[B.34]}$$

Figure B.11 shows this metric as a function of τ for ease of comparison to figures throughout the text

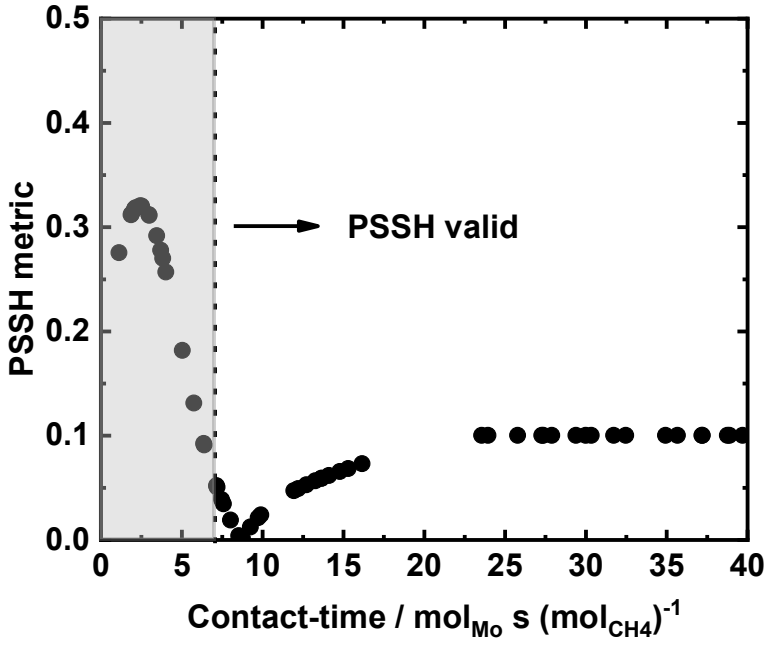

Figure B.11: $\mathbf{P \equiv \left| \frac{d\dot{n}_I}{d\zeta} \Big/ \frac{d\dot{n}_R}{d\zeta} \right|}$ against contact time varied by extent of non-selective deactivation.

B.5 Pertinence of Spatial-Averaging, Affinity-Averaging, and the Pseudo-Steady-State Hypothesis (PSSH) to Methane DHA

B.5.1 Spatial-Averaging and Affinity-Averaging Forward Rates in Methane DHA

Our previous attempts to calculate forward rates of benzene formation in methane DHA (*19*) serendipitously give similar values to calculations in this work due to a balance of incorrect length- and affinity-averaging which overestimate and underestimate forward rates, respectively. Fig. B.12 shows forward rates calculated with and without length- and affinity-averaging.

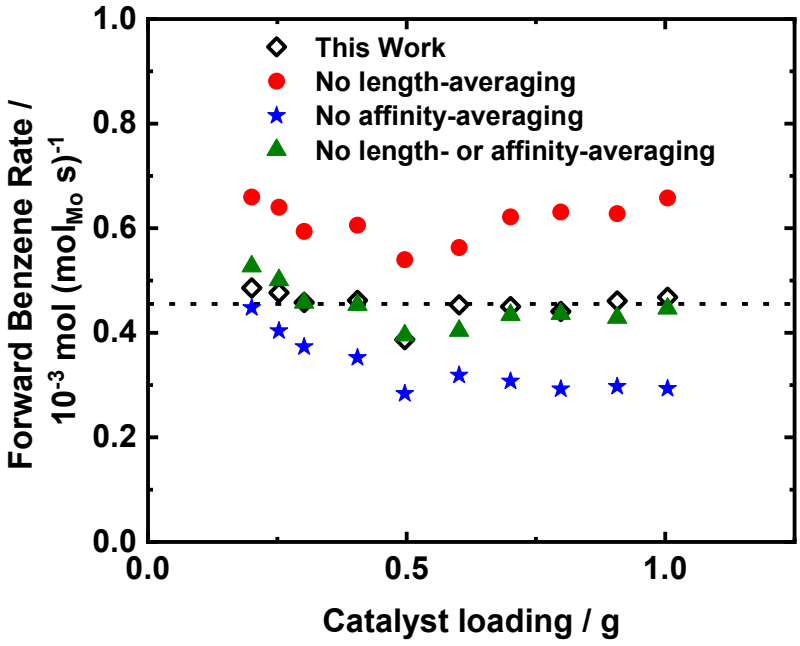

Figure B.12: Forward rate of benzene synthesis [=] $mol_{benzene}$ $(mol_{Mo}\ s)^{-1}$ as a function of catalyst loading during steady-state catalysis. Reaction conditions: 950 K, atmospheric pressure, 0.21 $cm^3\ s^{-1}$ 90 kPa CH_4, 10 kPa Ar. All data taken from Bedard et al., *J. Catal.* **2013**, *306*, 58–67. (▲) follow the analysis of Bedard et al., *J. Catal.* **2013**, *306*, 58–67.

The agreement between the approach of Bedard et al., (*19*) (▲) and the formalism we outline in Sections 3.4.1-3.4.4 (◊) is a coincidence dependent on the particular values in question and the fortuitous balance of incorrect length- and affinity-averaging and is not meant to encourage use of the formalism of Bedard et al., (*19*).

B.5.2 Forward Rate Calculations Away From the PSSH Regime

Deviation from the PSS regime invalidates the assumption of constant forward rate used to derive Eq. **3.19** from Eq. **3.18**. However, Fig. B.13 shows that, during deviation from PSS for $\tau < 7$ mol_{Mo} s $(mol_{CH4})^{-1}$, net rates and forward rates are nearly identical so that values of $\vec{R}$ are reasonably accurate despite rigorously incorrect assumptions made in their calculation.

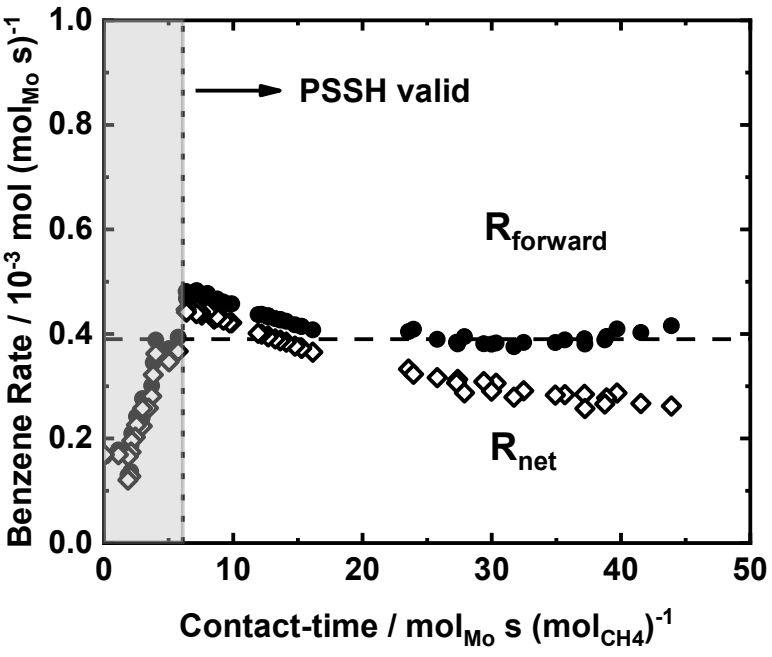

Figure B.13: Net rate (◊) and forward rate (●) of benzene synthesis [=] $mol_{benzene}$ $(mol_{Mo}$ $s)^{-1}$ as a function of contact-time varied by extent of deactivation. Reaction conditions: 973 K, ~115 kPa total pressure, 0.21-2.1 cm^3 s^{-1} 90% CH_4, 10% Ar, 1.0-1.2 g Mo/H-ZSM-5 (Mo/Al = 0.25, Si/Al = 11.5).

C Supporting Information for Carbidic Mo is the sole kinetically-relevant active site for catalytic methane dehydroaromatization on Mo/H-ZSM-5

C.1 DHA on steady-state and deactivating Mo/H-ZSM-5 catalysts

All carburized MoC_x/H-ZSM-5 catalysts used for experiments reported in this work were synthesized under identical flow conditions (0.21 cm^3 s^{-1}, 90% CH_4, 10% Ar, ~115 kPa, 973 K). We define steady state to be the time of cessation of carburization and onset of catalysis – indicated by closure of carbon balance and coincidence of product distribution with non-selective deactivation profiles. An example is shown in Figures C.1 and C.2 which show methane conversion as a function of time-on-stream and corresponding product distribution for 0.78g Mo/H-ZSM-5 (Mo/Al = 0.10, Si/Al = 11.5) exposed to the reaction mixture. Note the first datum in Fig. C.2 has product selectivities which deviate from the non-selective deactivation profiles.

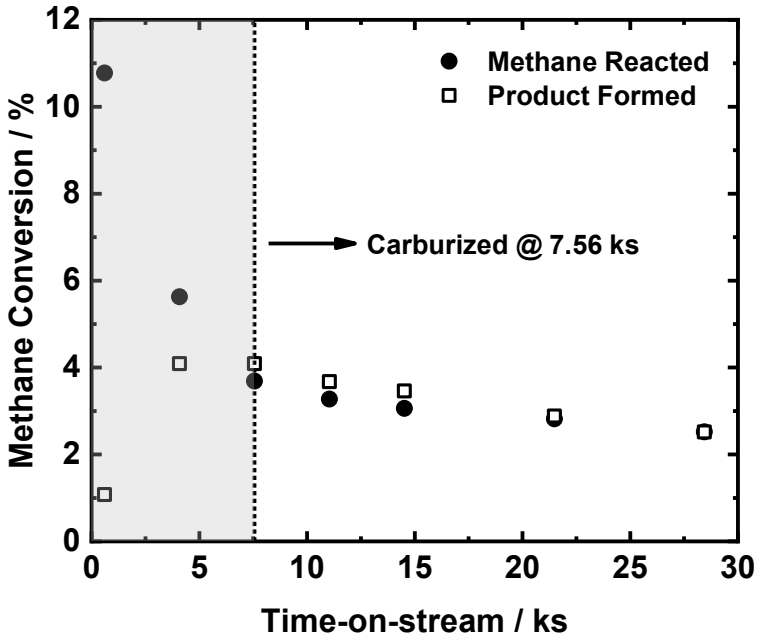

Figure C.1: Methane conversion during DHA on 0.78 g Mo/H-ZSM-5 catalyst (Mo/Al = 0.10, Si/Al = 11.5) exposed to 0.21 cm^3 s^{-1} 90% CH_4, 10% Ar at ~115 kPa total pressure and 973 K.

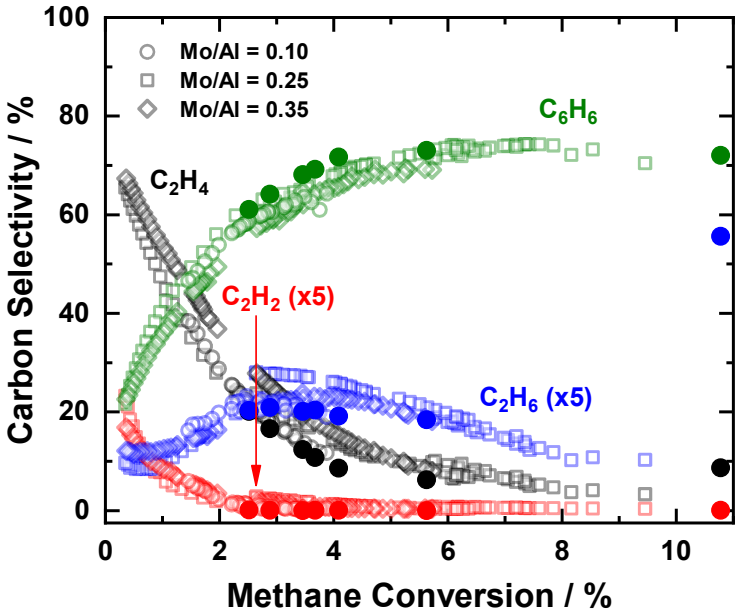

Figure C.2: Product selectivities (●) during DHA on 0.78 g Mo/H-ZSM-5 catalyst (Mo/Al = 0.10, Si/Al = 11.5) exposed to 0.21 cm^3 s^{-1} 90% CH_4, 10% Ar at ~115 kPa total pressure and 973 K. Transparent symbols are reproduced from Fig. 4.2 used to evince non-selective deactivation.

Figure C.3 shows characteristic data for methane conversion and benzene formation rate during catalytic DHA at steady state (0 – 10 ks) and during deactivation (> 10 ks) on a catalyst sample of distinct Mo-to-Al ratio and catalyst mass loading to that in Figs. C.1 and C.2.

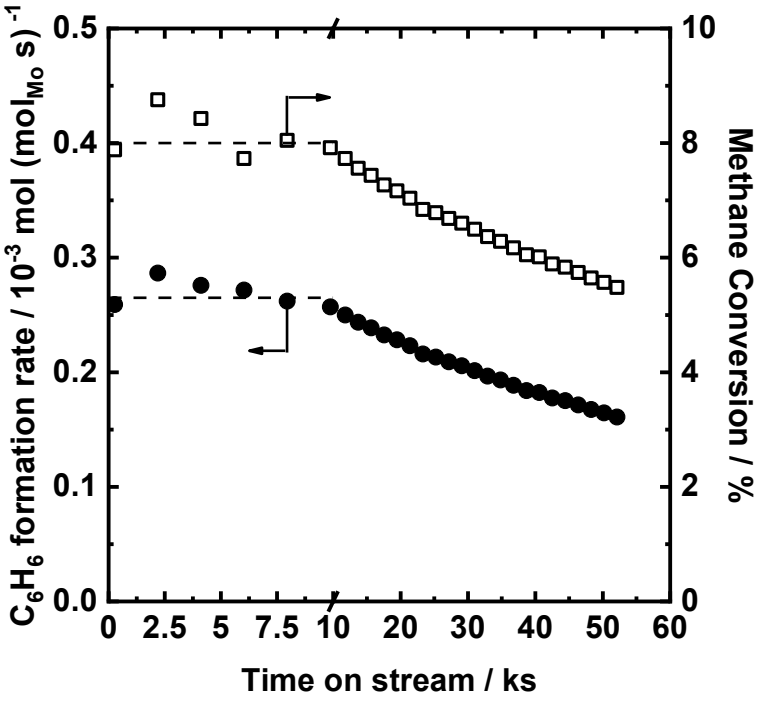

Figure C.3: Net benzene formation rate (●) and methane conversion (□) as a function of time on stream during catalytic methane DHA. Reaction conditions: 1.20 g Mo/H-ZSM-5 catalyst (Mo/Al = 0.25, Si/Al = 11.5); 0.21 cm^3 s^{-1} 90% CH_4, 10% Ar at ~115 kPa total pressure and 973 K.

Figures C.4-C.6 show deactivation profiles in methane conversion and product distribution used to construct conversion-selectivity profiles in Figures 4.2 and C.2. All data in Figures 4.2 and C.2 are shown as a function of time on stream in Figures C.4-C.6.

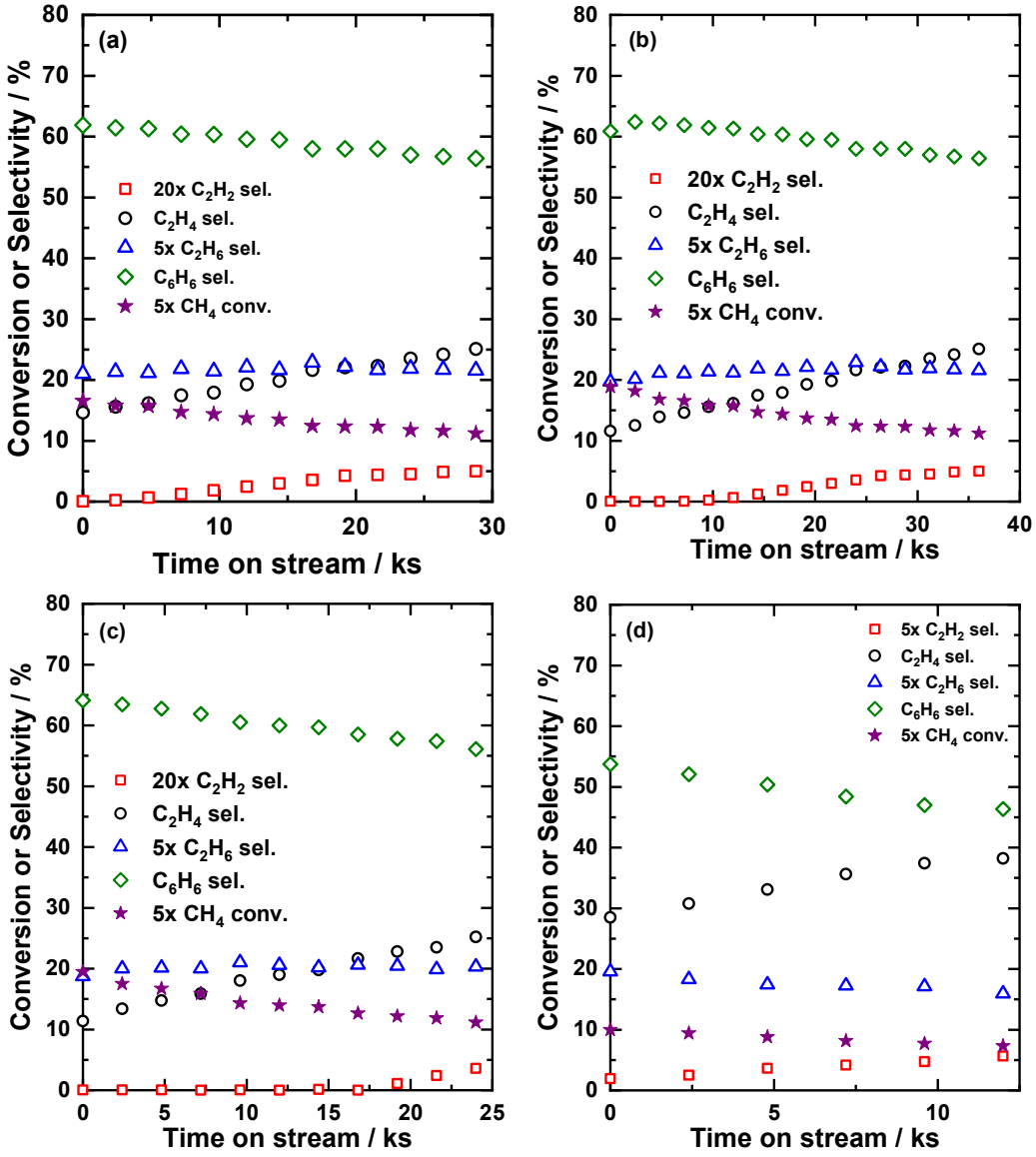

Figure C.4: Methane conversion and product selectivities as a function on time on stream over deactivating Mo/H-ZSM-5 catalysts with Mo/Al = 0.10. Reaction conditions: 973 K, ~115 kPa total pressure, total flow of 0.21 – 2.1 $cm^3\ s^{-1}$ with composition 90% CH_4/10% Ar. Mo/Al = 0.10, g_{cat} = 0.75 – 1.20.

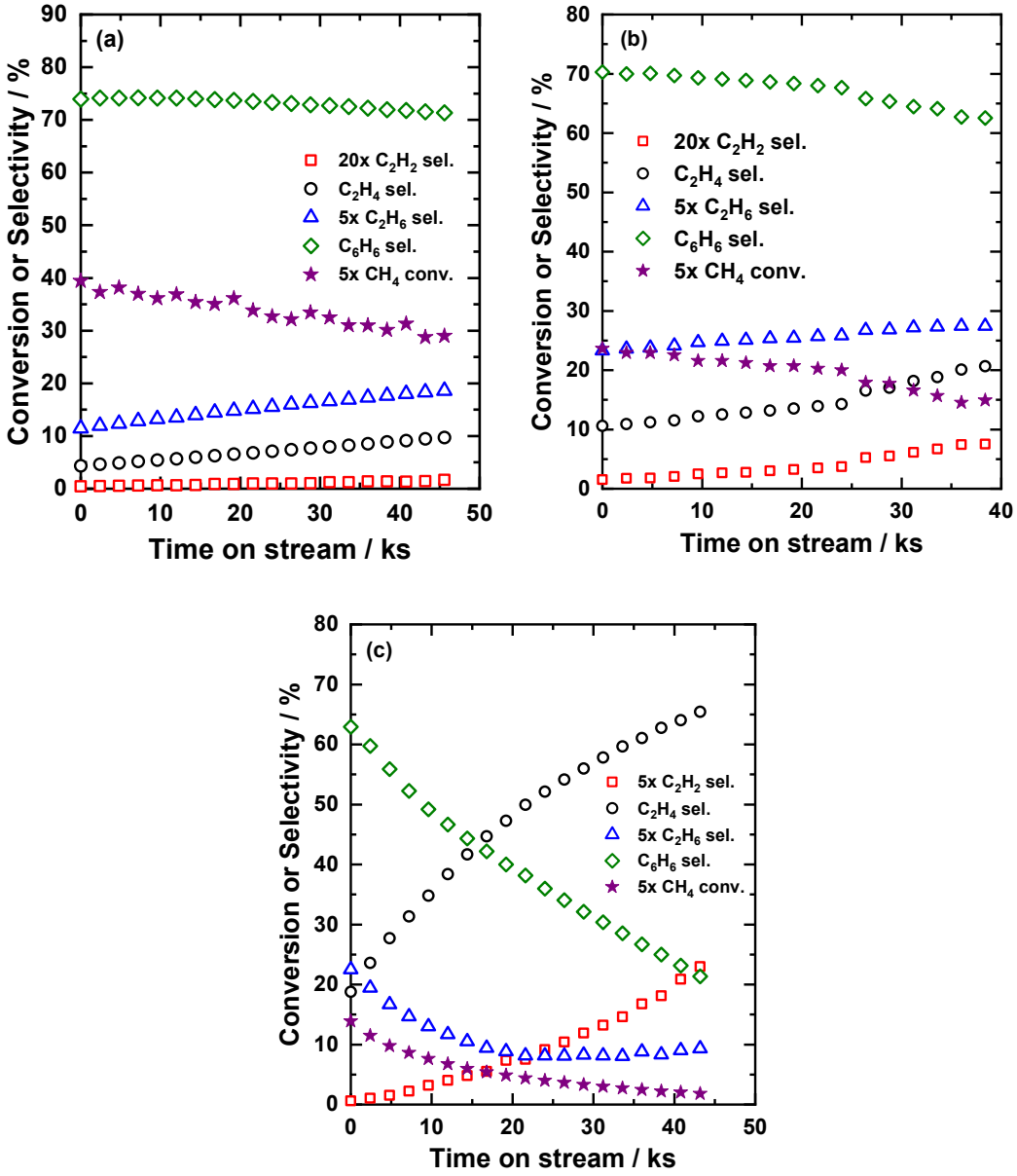

Figure C.5: Methane conversion and product selectivities as a function on time on stream over deactivating Mo/H-ZSM-5 catalysts with Mo/Al = 0.25. Reaction conditions: 973 K, ~115 kPa total pressure, total flow of 0.21 – 2.1 cm^3 s^{-1} with composition 90% CH_4/10% Ar. Mo/Al = 0.10, g_{cat} = 0.10 – 1.20.

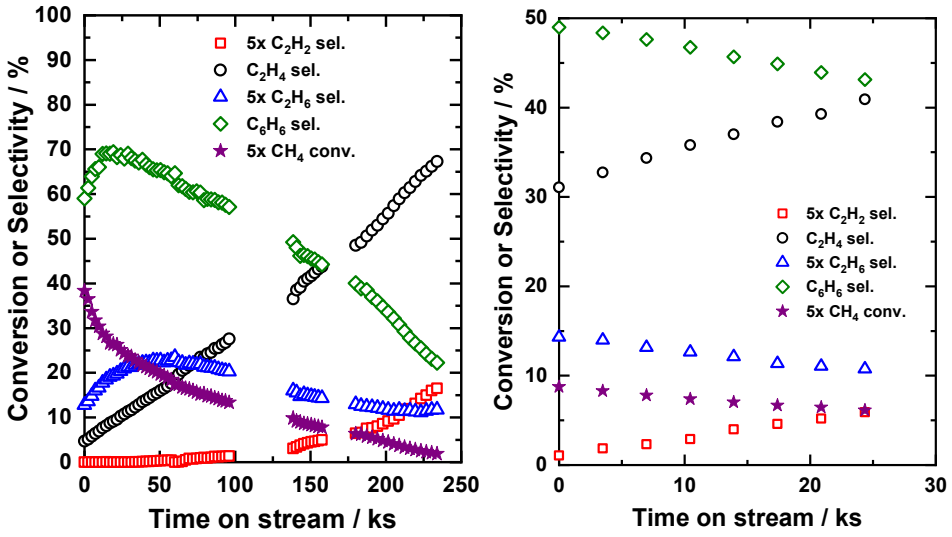

Figure C.6: Methane conversion and product selectivities as a function on time on stream over deactivating Mo/H-ZSM-5 catalysts with Mo/Al = 0.35. Reaction conditions: 973 K, ~115 kPa total pressure, total flow of 0.21 – 2.1 $cm^3\ s^{-1}$ with composition 90% CH_4/10% Ar. Mo/Al = 0.35, g_{cat} = 0.15 – 0.75.

C.1.1 Relationship between methane conversion and contact time

We discuss the relationship between f and τ_{Mo} (see Fig. 4.3) in the context of the PFR design equation. The general differential PFR molar balance for methane in catalytic DHA is

$$r_{CH_4} = \frac{df}{d\tau} \qquad \textbf{[C.1]}$$

where r_{CH_4} [=] $mol_C\ (mol_{site}\ s)^{-1}$ is the instantaneous rate of methane consumption, f is methane conversion, and τ [=] $mol_{site}\ s\ mol_C^{-1}$ is the contact time. The basis of contact time and basis for normalization of rate must correspond and are arbitrary (e.g. per gram catalyst, per m^2 surface area, per mol H^+). For all PFR reactions performed at identical conditions and on identical catalyst samples, f and τ are ostensibly a one-to-one function. Across a series of catalytic materials with different densities of possible active sites, f and τ will only have a one-to-one correspondence if the basis for τ and r_{CH_4} is the only kinetically-relevant active site – making r_{CH_4} solely a function of f or, interchangeably, τ

(conversion must increase monotonically with the number of sites, or equivalently, with τ). For example, Figure C.7 shows steady-state methane conversion as a function of contact time on a per gram basis, rather than an active Mo basis as in Fig. 4.3.

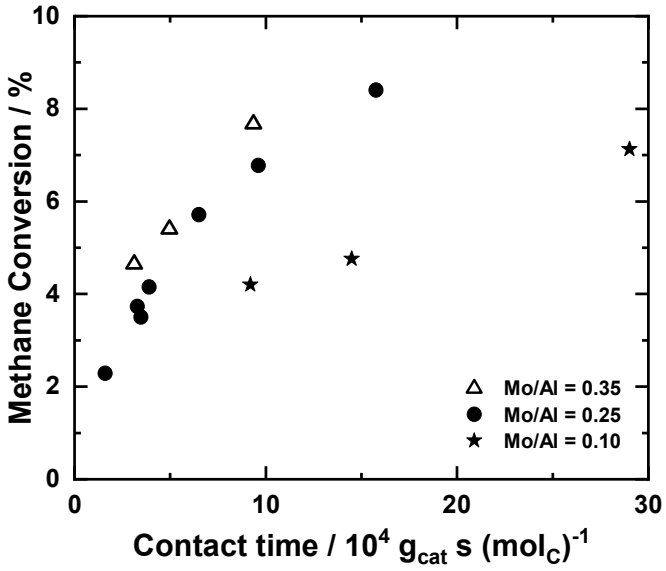

Figure C.7: Steady-state methane conversion as a function of contact time based on catalyst mass. Reaction conditions: 973 K, ~115 kPa total pressure, total flow of 0.21 – 2.1 cm^3 s^{-1} with composition 90% CH_4/10% Ar, and 0.10 – 1.20 g Mo/H-ZSM-5. Data are from Fig. 4.3 and C.7 are from the same experiments.

Steady-state methane conversions for each Mo-to-Al ratio are ostensibly one-to-one functions of τ on a gram basis; however, across Mo/Al = 0.10 – 0.35, the data show no quantitative correspondence, demonstrating the number of active sites is not directly correspondent with catalyst mass.

C.2 Characteristic data for dimethyl ether titration and ethane hydrogenolysis

Figure C.8 shows characteristic time-on-stream data for the evolution of dimethyl ether (DME) following breakthrough of DME pulses. All doses of DME prior to data shown in Fig. C.8 are completely -sorbed by Mo/H-ZSM-5. The total amount of DME which titrates Brønsted acid sites is determined by the difference in total dosed DME and DME subsequently desorbed in He flow, as shown on the right ordinate axis in Fig. C.8.

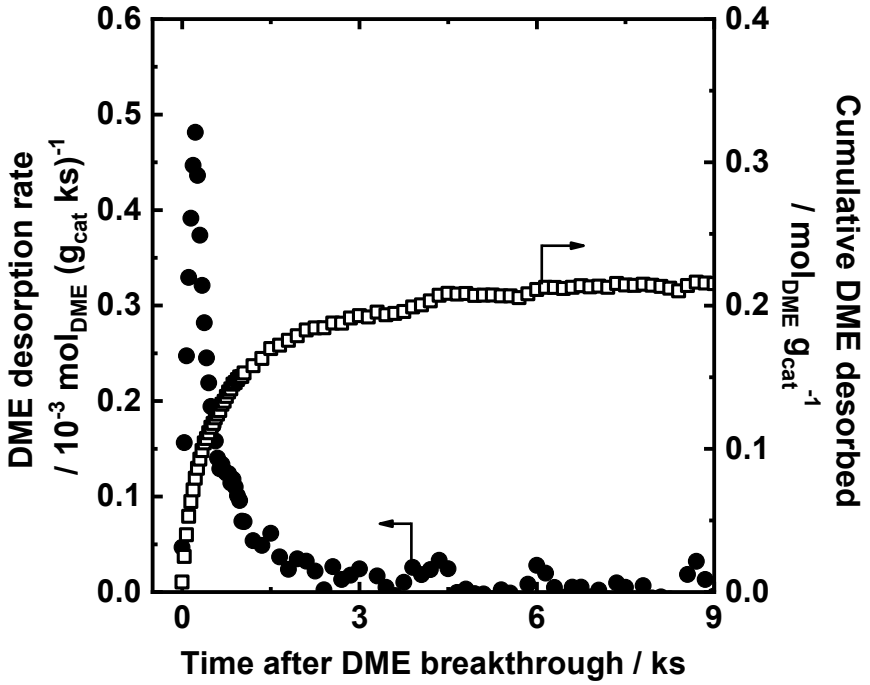

Figure C.8: DME desorption rate (●) and cumulative DME desorbed (□) as a function of time after DME breakthrough on 0.15 g Mo/H-ZSM-5 catalyst (Mo/Al = 0.35, Si/Al = 11.5) DHA-deactivated for 6.3 ks. DHA reaction conditions: 973 K, ~115 kPa total pressure, total flow of 0.21 cm^3 s^{-1} with composition 90% CH_4/10% Ar). Dimethyl ether titration conditions: 423 K, ~120 kPa total pressure, total flow of 0.50 cm^3 s^{-1} with composition 96% He/4% Ar and 0.25 cm^3 doses of dimethyl ether.

Figure C.9 shows characteristic time on stream data for ethane hydrogenolysis reactions performed on DHA-deactivated Mo/H-ZSM-5 catalysts. Ethane conversion is in the range 0.48 – 0.72% with the maximum conversion observed at steady state (12 – 15 ks).

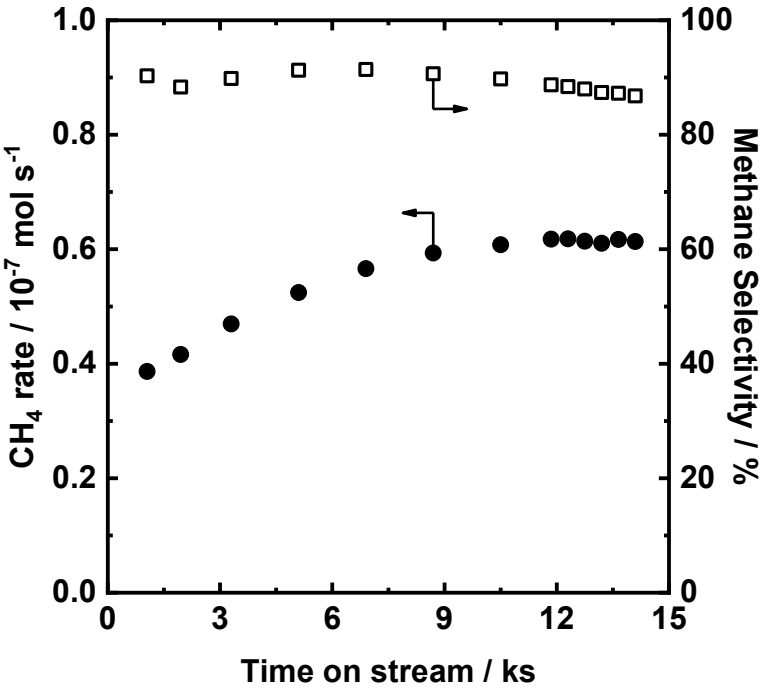

Figure C.9: Methane formation rate (●) and selectivity (□) as a function of duration of ethane hydrogenolysis on 0.30 g Mo/H-ZSM-5 catalyst (Mo/Al = 0.25, Si/Al = 11.5) measured after cessation of DHA catalysis. DHA reaction conditions: 973 K, ~115 kPa total pressure, total flow of 0.21 cm^3 s^{-1} with composition 90% CH_4/10% Ar). Ethane hydrogenolysis reaction conditions: 750 K, ~120 kPa total pressure, total flow of 0.49 cm^3 s^{-1} with composition 46% C_2H_6/49% H_2/balance Ar

C.3 Effect of Mo loading on H^+ density

Figure C.10 shows separate linear fits to the data of Borry et al. (*42*) and those presented herein are quantitatively similar for the correlation between Mo/Al and H^+/Al. We recognize the degree of quantitative agreement in separate linear fits is, to some extent, fortuitous given the scatter in each set of data.

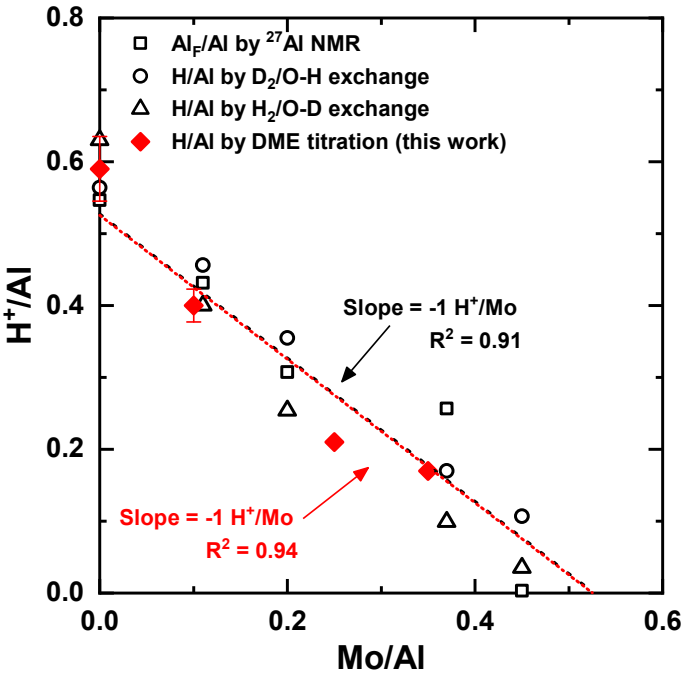

Figure C.10: The number of Brønsted-acid sites (H^+) or framework Al atoms (Al_F) per total Al in (Mo/)H-ZSM-5 samples treated to 973 K in dry air. Empty symbols and black line are data and corresponding fit per the work of Borry et al. (*42*) Red diamonds and red line are data and corresponding fit per DME titration presented in this work.

C.4 Active site normalization of DHA rates during catalyst deactivation

In catalytic flow reactions, the spatially-averaged net site-time yield, R_{net} [=] mol $(mol_{site}\ s)^{-1}$, is calculated from measured effluent molar flow rates of species i, N_i [=] mol_i s^{-1}, and the active site count, L [=] mol_{site}, per the integral PFR molar balance. For example, the net formation rate of a terminal product species i, $R_{net,i}$, is given by

$$R_{net,i} = \frac{N_i}{L} \qquad \textbf{[C.2]}$$

Eq. **C.2** can be re-written in terms of (active-site)-based contact time, τ [=] mol_{site} s mol_{feed}^{-1}, as

$$R_{net,i} = \frac{y_i}{\tau} \qquad \textbf{[C.3]}$$

where y_i [=] mol_i/mol_{feed}. In this work we are interested in determining the net Mo-based site-time yield of methane aromatization, referred to as R in Eqs. **4.3** and **4.6**. We calculate

the aromatization rate from the sum of effluent molar fractions of benzene and naphthalene, $y_{C_6H_6} + y_{C_{10}H_8}$, to account for the benzene consumption pathways. Per Eq. **C.3**, the net rate is

$$R = \frac{y_{C_6H_6} + y_{C_{10}H_8}}{\tau_{Mo}} \qquad \textbf{[C.4]}$$

where τ_{Mo} [=] mol_{Mo} s mol_C^{-1} is the contact time based on Mo content and inlet carbon flow. Eq. **C.4** is identical to numerator of Eq. **4.6**, since $F_i = y_i/\tau_{Mo}$.

The deactivation of Mo/H-ZSM-5 catalysts during DHA reactions results in decay of τ_{Mo} with time on stream as Mo active sites are lost. To calculate the *active* site-time yield, we determine instantaneous values of τ_{Mo} from measurement of instantaneous methane conversion and the one-to-one function $f(\tau_{Mo})$. Figures C.11-C.13 explicate the procedure by which we (i) obtain instantaneous values of τ_{Mo} and (ii) re-normalize rates by the contemporaneous, rather than initial, value of τ_{Mo}.

Methane conversion, shown on the right ordinate axis of Fig. C.11, is measured in the effluent; and, the contemporaneous *active* Mo-based contact time, shown on the left ordinate axis of Fig. C.11, is determined from methane conversion and $f(\tau_{Mo})$ shown and constructed from data in Fig. 4.3.

Figure C.12 shows R calculated from (i) $\tau_{Mo,initial}$ per the total number of Mo atoms charged to the reactor bed and (ii) the deactivation-corrected, instantaneous τ_{Mo} determined in Figure C.11. R normalized by $\tau_{Mo,initial}$ monotonically decay with time on stream due to the loss of active sites during deactivation and the uncorrected, overestimated Mo-based contact time. R normalized by the contemporaneous active site count increase from 0 – 80 ks because the deactivation of Mo/H-ZSM-5 results in decreased conversion and therefore decreased thermodynamic barriers to DHA (i.e. decreased z_{eff}). At longer times on stream

(i.e. > 80 ks), R normalized by τ_{Mo} decay because $\tau_{Mo} < 7$ mol_{Mo} s mol_C^{-1} and the DHA network is no longer at a PSS and R increases with τ_{Mo} (see Figs. 4.4, 4.5, C.13). Figure C.13 shows R normalized by $\tau_{Mo,initial}$ and τ_{Mo} as a function of τ_{Mo} to demonstrate the utility of contemporaneous active site normalization in constructing axial rate profiles from time-on-stream data.

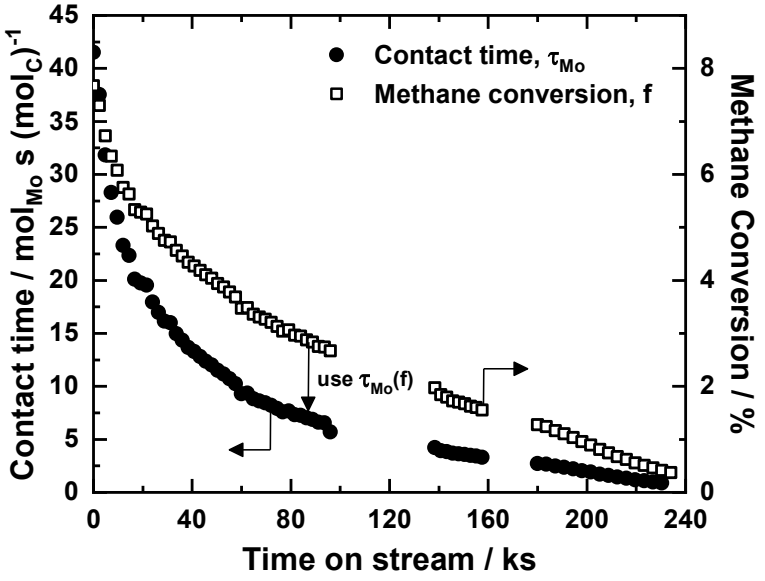

Figure C.11: Mo-based contact time (●) and methane conversion (□) as a function of time on stream during catalytic methane DHA. Reaction conditions: 0.75 g Mo/H-ZSM-5 catalyst (Mo/Al = 0.35, Si/Al = 11.5); 0.21 cm^3 s^{-1} 90% CH_4, 10% Ar at ~115 kPa total pressure and 973 K. Data from Figs. C.11-C.13 are from the same experiment.

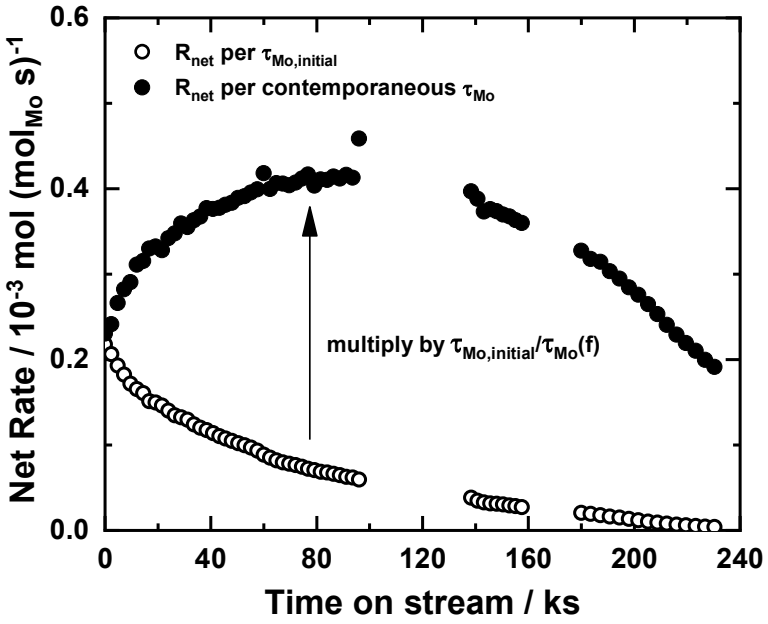

Figure C.12: Net benzene formation rate normalized by $\tau_{Mo,initial}$ (●) and contemporaneous τ_{Mo} (○) as a function of time on stream during catalytic methane DHA. Reaction conditions: 0.75 g Mo/H-ZSM-5 catalyst (Mo/Al = 0.35, Si/Al = 11.5); 0.21 cm^3 s^{-1} 90% CH_4, 10% Ar at ~115 kPa total pressure and 973 K. Data from Figs. C.11-C.13 are from the same experiment.

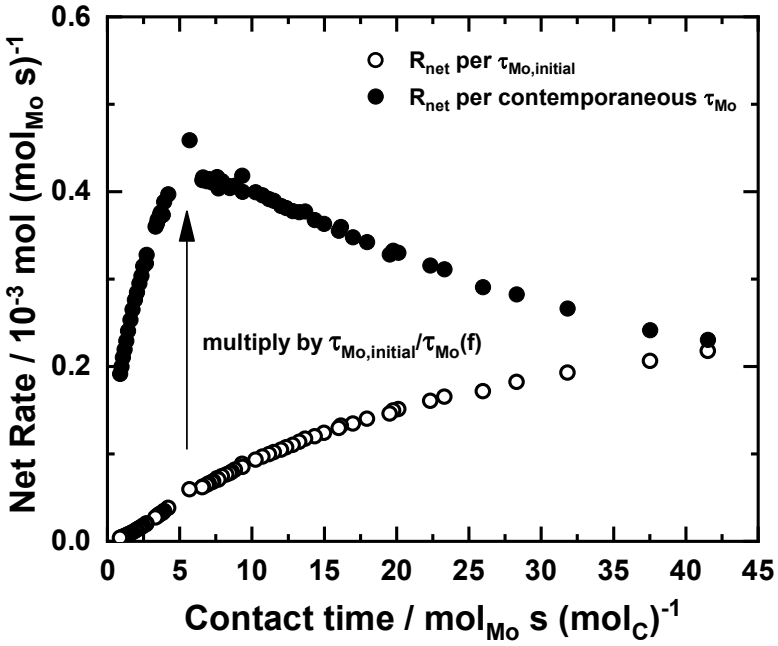

Figure C.13: Net benzene formation rate normalized by $\tau_{Mo,initial}$ (●) and contemporaneous τ_{Mo} (○) as a function of *active* Mo-based contact time, τ_{Mo}, during catalytic methane DHA. Reaction conditions: 0.75 g Mo/H-ZSM-5 catalyst (Mo/Al = 0.35, Si/Al = 11.5); 0.21 cm^3

s^{-1} 90% CH_4, 10% Ar at ~115 kPa total pressure and 973 K. Data from Figs. C.11-C.13 are from the same experiment.

C.5 Calculation of forward rate from De Donder relations

Our recent work (*95*) details use of De Donder relations to calculate forward rate from measurement of net rate and partial pressure of gas-phase intermediates and products. In brief, we identify methane DHA proceeds through a sequential reaction pathway with gas-phase and pseudo-elementary steps shown in Scheme C.1 and C.2. The steps in Scheme C.2 are not meant to faithfully describe molecular catalytic events, but simply to identify the stoichiometric number and the connectivity of the constituent elementary steps in the overall methane to benzene reaction. Scheme C.1 and C.2 are reproduced from our prior work (*95*).

Scheme C.1: Proposed methane DHA reaction pathway

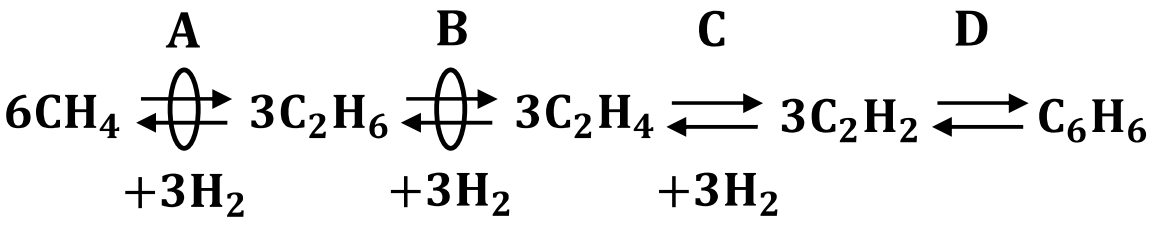

Methane, ethane, and ethylene form a quasi-equilibrated pool catalyzed by carbidic Mo sites for sufficient contact-times (> 7 mol_{Mo} s mol_C^{-1}).

Scheme C.2: Methane DHA reaction sequence with pseudo-elementary steps

	Reaction	σ	σ*
(A.1)	**$CH_4 \rightleftharpoons CH_3 + ½\ H_2$**		**6**
(A.2)	$2CH_3 \rightleftharpoons C_2H_6$	3	

(A)	$2CH_4 \rightleftharpoons C_2H_6 + H_2$	3	
(B.1)	**$C_2H_6 \rightleftharpoons C_2H_5 + ½\ H_2$**		**3**
(B.2)	$C_2H_5 \rightleftharpoons C_2H_4 + ½\ H_2$	3	
(B)	$C_2H_6 \rightleftharpoons C_2H_4 + H_2$	3	
(C.1)	**$C_2H_4 \rightleftharpoons C_2H_3 + ½\ H_2$**		**3**
(C.2)	$C_2H_3 \rightleftharpoons C_2H_2 + ½\ H_2$	3	
(C)	$C_2H_4 \rightleftharpoons C_2H_2 + H_2$	3	
(D.1)	**$2C_2H_2 \rightleftharpoons C_4H_4$**		**1.5**
(D.2)	$C_2H_2 + C_4H_4 \rightleftharpoons C_6H_6$	1	
(D)	$3C_2H_2 \rightleftharpoons C_6H_6$	1	
overall	$6CH_4 \rightleftharpoons C_6H_6 + 9H_2$	1	

Bolded entries indicate rate-determining elementary steps within each gas-phase global reaction (A, B, C, and D).

Within each global-phase reaction (A,B,C,D), we assign a rate-determining elementary step and identify the corresponding stoichiometric number, $\sigma^{*}_{i=A,B,C,D}$, in relation to the overall methane to benzene reaction. The reversibility of the identified rate-determining elementary step, $z^{*}_{i=A,B,C,D}$, is then calculated by the measured total reversibility of the corresponding global gas-phase reaction, $Z_{i=A,B,C,D}$

$$z_i^* = Z_i^{1/\sigma_i^*} \qquad \textbf{[C.5]}$$

The affinity-averaged stoichiometric number is then calculated as

$$\overline{\sigma} = \frac{\sum_{i=A,B,C,D} \sigma_i^* \ln(z_i^*)}{\sum_{i=A,B,C,D} \ln(z_i^*)} \qquad \textbf{[C.6]}$$

which is reported as a function of methane conversion on Mo/Al = 0.25 catalysts in Fig. C.14

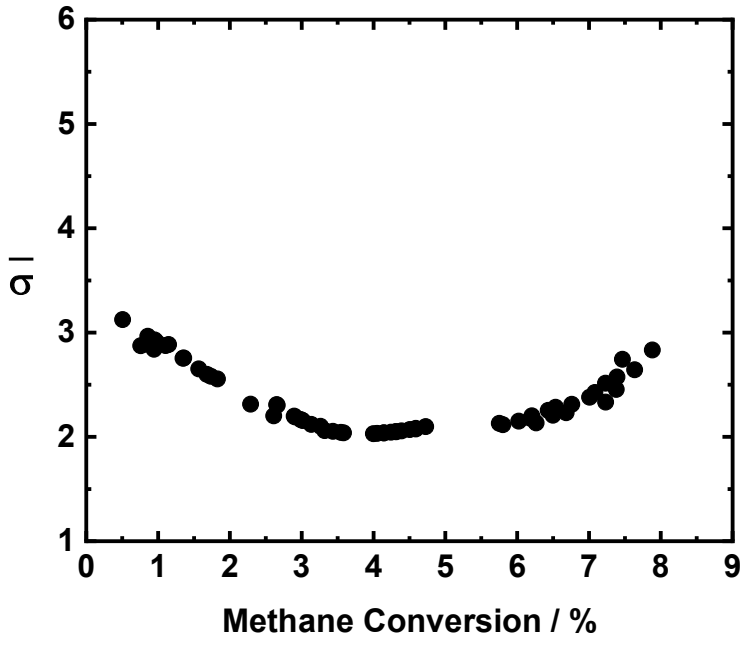

Figure C.14: Affinity-averaged stoichiometric number as a function of methane conversion calculated by Eq**. C.6.**

The forward rate may now be calculated by

$$\vec{R} = \frac{R}{1 - \prod_{i=A,B,C,D} z_i^*} = \frac{R}{1 - z_{ov}^{1/\overline{\sigma}}} \qquad \textbf{[C.7]}$$

and appropriate spatial-averaging described in Section 3.4 in our previous report (*95*).

Spatial averaging of $z_{ov}^{1/\overline{\sigma}}$, as is necessary for flow reactors, gives Eq. **C.6**, a particular form of Eq. **C.7** which holds provided that for all τ_{Mo} at least one of the following is true:

(i) $< z_{ov}^{1/\bar{\sigma}} > \ll 1$ and/or (ii) $d\vec{R}/d\tau_{Mo} \sim 0$. Inspection of Figs. 4.4 and 4.5 show these conditions hold for all τ_{Mo}; $\vec{R} \sim R$ in the non-pseudo-steady state regime and $\vec{R}$ is essentially constant once the DHA network achieves a PSS. In general, we surmise forward rate is calculable by Eq. **4.6** provided $z_{eff} << 1$ and/or kinetic product inhibition is weak compared to thermodynamic product inhibition (i.e. the influence of z_{eff}).

C.6 Ethane hydrogenolysis on H-ZSM-5 zeolite

Figure C.15 shows time on stream data for ethane hydrogenolysis reactions performed on H-ZSM-5 zeolite at identical conditions as performed on DHA-deactivated Mo/H-ZSM-5 catalysts. The steady-state H^+-catalyzed ethane hydrogenolysis turnover rate is $1.25 \cdot 10^{-5}$ mol_C $(mol_{H+}\ s)^{-1}$, 0.56% of the Mo-normalized ethane hydrogenolysis turnover rate, $2.24 \cdot 10^{-3}$ mol_C $(mol_{Mo}\ s)^{-1}$, determined from data presented in Figs. 4.6 and 4.7. The maximum contribution of Brønsted-acid catalysis to measured ethane hydrogenolysis rate is calculable from the maximum measured H^+-to-Mo ratio and is $0.56\% \cdot (H^+/Mo)_{max} \sim 6\%$, which we regard negligible.

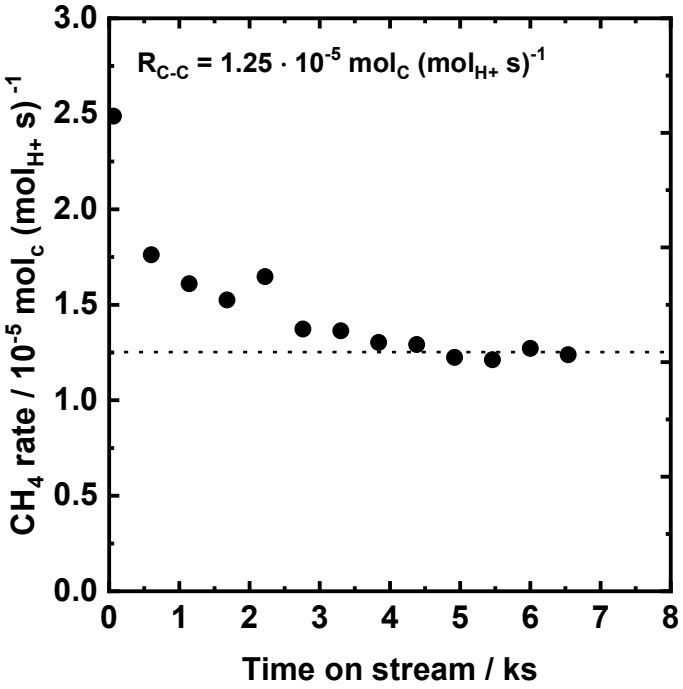

Figure C.15: Methane formation rate (●) as a function of duration of ethane hydrogenolysis on 0.10 g H-ZSM-5 (Si/Al = 11.5, $[H^+] = 7.9 \cdot 10^{-4}$ mol_{H+} g^{-1} per DME titration). Reaction conditions: 750 K, ~120 kPa total pressure, total flow of 0.49 cm^3 s^{-1} with composition 46% C_2H_6/49% H_2/balance Ar.

C.7 Regeneration of Mo/H-ZSM-5 catalysts

Mo/H-ZSM-5 catalysts are regenerated in 1%O_2/He for re-use in DHA reactions and subsequent ethane hydrogenolysis or DME titration. Figs. C.16 and C.17 show that time-on-stream behavior and product distribution of Mo/H-ZSM-5 catalysts is reproducibly regenerable.

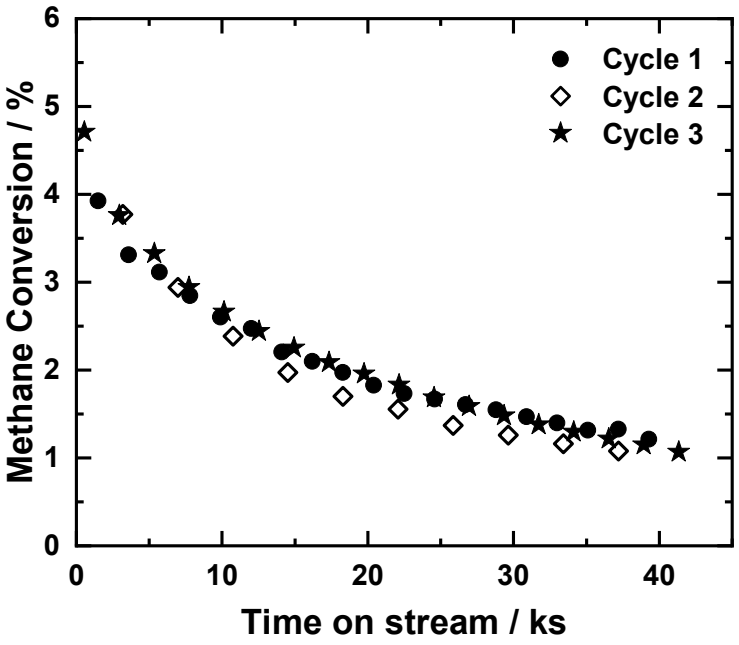

Figure C.16: Methane conversion as a function of duration DHA catalysis. Reaction conditions: 973 K, ~115 kPa total pressure, total flow of 0.21 cm^3 s^{-1} with composition 90% CH_4/10% Ar. Mo/Al = 0.25, g_{cat} = 0.30. Different symbol shapes indicate separate DHA reactions after O_2-regeneration.

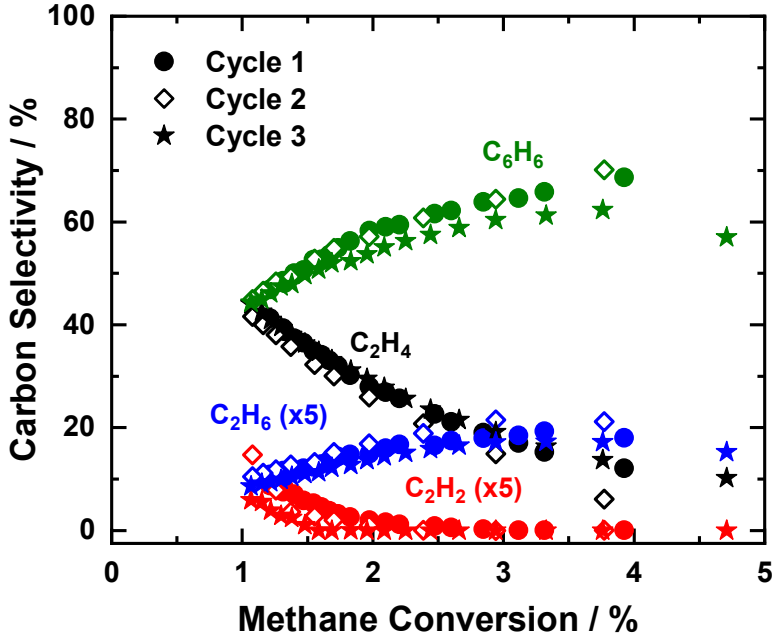

Figure C.17: Carbon selectivity of C_2 hydrocarbons and benzene as a function of methane conversion over deactivating Mo/H-ZSM-5 catalysts with time-on-stream behavior shown in Fig. C.10. Reaction conditions: 973 K, ~115 kPa total pressure, total flow of 0.21 cm^3 s^{-}

[1] with composition 90% CH_4/10% Ar. Mo/Al = 0.25, g_{cat} = 0.30. Different symbol shapes indicate separate DHA reactions after O_2-regeneration.

D Supporting Information for Kinetic description of site ensembles on catalytic surfaces

D.1 1st-order descriptions of rate equations reaction sensitivity and related kinetic descriptors

Tables D.1-D.5 list 1st-order rate equations for heterogeneous two-site events on a 2D square lattice.

Table D.1: Rate equations for monomer -sorption ($M_{(g)} + o \rightleftharpoons m$) in the presence of spectators, s^*

Monomer adsorption ($o \rightarrow m$)		**Monomer desorption ($m \rightarrow o$)**	
One-site rate equations			
$\boldsymbol{\frac{d\theta_m}{d\tau} = -\frac{d\theta_o}{d\tau} = \theta_o \qquad \frac{d\theta_s}{d\tau} = 0}$		$\frac{d\theta_m}{d\tau} = -\frac{d\theta_o}{d\tau} = -\theta_m \qquad \frac{d\theta_s}{d\tau} = 0$	
Two-site rate equations			
$\boldsymbol{\frac{d\theta_{mm}}{d\tau} = 2\theta_{mo}}$	$\frac{d\theta_{mo}}{d\tau} = \theta_{oo} - \theta_{mo}$	$\frac{d\theta_{mm}}{d\tau} = -2\theta_{mm}$	$\frac{d\theta_{mo}}{d\tau} = \theta_{mm} - \theta_{mo}$
$\boldsymbol{\frac{d\theta_{oo}}{d\tau} = -2\theta_{oo}}$	$\frac{d\theta_{so}}{d\tau} = -\theta_{so}$	$\frac{d\theta_{oo}}{d\tau} = 2\theta_{mo}$	$\frac{d\theta_{so}}{d\tau} = \theta_{ms}$
$\boldsymbol{\frac{d\theta_{ss}}{d\tau} = 0}$	$\frac{d\theta_{ms}}{d\tau} = \theta_{so}$	$\frac{d\theta_{ss}}{d\tau} = 0$	$\frac{d\theta_{ms}}{d\tau} = -\theta_{ms}$
Rate balances (Eq. 5.17)			
$\boldsymbol{\sum_j \frac{d\theta_{mj}}{d\tau} = \sum_j \theta_{jo} = \theta_o = \frac{d\theta_m}{d\tau} = -\frac{d\theta_o}{d\tau}}$		$\sum_j \frac{d\theta_{mj}}{d\tau} = -\sum_j \theta_{mj} = -\theta_m = \frac{d\theta_m}{d\tau} = -\frac{d\theta_o}{d\tau}$	

Table D.2: Rate equations for dimer -sorption ($D_{2(g)} + oo \rightleftharpoons dd$) in the presence of spectators, s^*

Homogeneous dimer adsorption ($oo \rightarrow dd$)		**Homogeneous dimer desorption ($dd \rightarrow oo$)**	
One-site rate equations			
$\boldsymbol{\frac{d\theta_d}{d\tau} = -\frac{d\theta_o}{d\tau} = 4\theta_{oo} \qquad \frac{d\theta_s}{d\tau} = 0}$		$\frac{d\theta_d}{d\tau} = -\frac{d\theta_o}{d\tau} = -4\theta_{dd} \qquad \frac{d\theta_s}{d\tau} = 0$	
Two-site rate equations			
$\boldsymbol{\frac{d\theta_{dd}}{d\tau} = \theta_{oo}\left(1 + \frac{6\theta_{do}}{\theta_o}\right)}$	$\frac{d\theta_{do}}{d\tau} = 3\theta_{oo}\left(\frac{\theta_{oo}}{\theta_o} - \frac{\theta_{do}}{\theta_o}\right)$	$\frac{d\theta_{dd}}{d\tau} = -\theta_{dd}\left(1 + \frac{6\theta_{dd}}{\theta_d}\right)$	$\frac{d\theta_{do}}{d\tau} = 3\theta_{dd}\left(\frac{\theta_{dd}}{\theta_d} - \frac{\theta_{do}}{\theta_d}\right)$

$\frac{d\boldsymbol{\theta_{oo}}}{d\boldsymbol{\tau}} = -\boldsymbol{\theta_{oo}}\left(\mathbf{1}+\frac{\mathbf{6}\boldsymbol{\theta_{oo}}}{\boldsymbol{\theta_o}}\right)$	$\frac{d\theta_{so}}{d\tau} = -3\theta_{oo}\frac{\theta_{so}}{\theta_o}$	$\frac{d\theta_{oo}}{d\tau} = \theta_{dd}\left(1+\frac{6\theta_{do}}{\theta_d}\right)$	$\frac{d\theta_{so}}{d\tau} = 3\theta_{dd}\frac{\theta_{ds}}{\theta_d}$
$\frac{d\boldsymbol{\theta_{ss}}}{d\boldsymbol{\tau}} = \mathbf{0}$	$\frac{d\theta_{ds}}{d\tau} = 3\theta_{oo}\frac{\theta_{so}}{\theta_o}$	$\frac{d\theta_{ss}}{d\tau} = 0$	$\frac{d\theta_{ds}}{d\tau} = -3\theta_{dd}\frac{\theta_{ds}}{\theta_d}$
Rate balances (Eq. 5.17)			
$\sum_j \frac{d\boldsymbol{\theta_{dj}}}{d\boldsymbol{\tau}} = \boldsymbol{\theta_{oo}}\left(\mathbf{1}+\mathbf{3}\frac{\sum_j \boldsymbol{\theta_{jo}}}{\boldsymbol{\theta_o}}\right) = \frac{d\boldsymbol{\theta_d}}{d\boldsymbol{\tau}} = -\frac{d\boldsymbol{\theta_o}}{d\boldsymbol{\tau}}$		$\sum_j \frac{d\theta_{dj}}{d\tau} = -\theta_{dd}\left(1+3\frac{\sum_j \theta_{dj}}{\theta_d}\right) = \frac{d\theta_d}{d\tau} = -\frac{d\theta_o}{d\tau}$	

*Time, *t*, is made non-dimensional; τ = *kt* where *k* is the rate constant of the considered process. *s* generally refers to all spectators.

Table D.3: Rate equations for dimer -sorption ($BD_{(g)}$ + *oo* ⇌ *bd*) in the presence of spectators, *s*[*]

Heterogeneous dimer adsorption (*oo* → *bd*)		**Heterogeneous dimer desorption (*bd* → *oo*)**	
One-site rate equations			
$\frac{d\boldsymbol{\theta_o}}{d\boldsymbol{\tau}} = -\mathbf{2}\frac{d\boldsymbol{\theta_b}}{d\boldsymbol{\tau}} = -\mathbf{2}\frac{d\boldsymbol{\theta_d}}{d\boldsymbol{\tau}} = -\mathbf{8}\boldsymbol{\theta_{oo}};\quad \frac{d\boldsymbol{\theta_s}}{d\boldsymbol{\tau}} = \mathbf{0}$		$\frac{d\theta_o}{d\tau} = -2\frac{d\theta_b}{d\tau} = -2\frac{d\theta_d}{d\tau} = 8\theta_{bd};\quad \frac{d\theta_s}{d\tau} = 0$	
Two-site rate equations			
$\frac{d\boldsymbol{\theta_{bb}}}{d\boldsymbol{\tau}} = \mathbf{6}\boldsymbol{\theta_{oo}}\frac{\boldsymbol{\theta_{bo}}}{\boldsymbol{\theta_o}}$	$\frac{d\theta_{dd}}{d\tau} = 6\theta_{oo}\frac{\theta_{do}}{\theta_o}$	$\frac{d\theta_{bb}}{d\tau} = -6\theta_{bd}\frac{\theta_{bb}}{\theta_b}$	$\frac{d\theta_{dd}}{d\tau} = -6\theta_{bd}\frac{\theta_{dd}}{\theta_d}$
$\frac{d\boldsymbol{\theta_{bo}}}{d\boldsymbol{\tau}} = \boldsymbol{\theta_{oo}}\left(\frac{\mathbf{3}\boldsymbol{\theta_{oo}}}{\boldsymbol{\theta_o}}-\frac{\mathbf{6}\boldsymbol{\theta_{bo}}}{\boldsymbol{\theta_o}}\right)$	$\frac{d\theta_{do}}{d\tau} = \theta_{oo}\left(\frac{3\theta_{oo}}{\theta_o}-\frac{6\theta_{do}}{\theta_o}\right)$	$\frac{d\theta_{bo}}{d\tau} = 3\theta_{bd}\left(\frac{\theta_{bb}}{\theta_b}+\frac{\theta_{bd}}{\theta_d}-\frac{\theta_{bo}}{\theta_b}\right)$	$\frac{d\theta_{do}}{d\tau} = 3\theta_{bd}\left(\frac{\theta_{dd}}{\theta_d}+\frac{\theta_{bd}}{\theta_b}-\frac{\theta_{do}}{\theta_d}\right)$
$\frac{d\boldsymbol{\theta_{ds}}}{d\boldsymbol{\tau}} = \mathbf{3}\boldsymbol{\theta_{oo}}\frac{\boldsymbol{\theta_{so}}}{\boldsymbol{\theta_o}}$	$\frac{d\theta_{bs}}{d\tau} = 3\theta_{oo}\frac{\theta_{so}}{\theta_o}$	$\frac{d\theta_{ds}}{d\tau} = -3\theta_{bd}\frac{\theta_{ds}}{\theta_d}$	$\frac{d\theta_{bs}}{d\tau} = -3\theta_{bd}\frac{\theta_{bs}}{\theta_b}$
$\frac{d\boldsymbol{\theta_{ss}}}{d\boldsymbol{\tau}} = \mathbf{0}$	$\frac{d\theta_{so}}{d\tau} = -6\theta_{oo}\frac{\theta_{so}}{\theta_o}$	$\frac{d\theta_{ss}}{d\tau} = 0$	$\frac{d\theta_{so}}{d\tau} = 3\theta_{bd}\left(\frac{3\theta_{bs}}{\theta_b}+\frac{3\theta_{ds}}{\theta_d}\right)$
$\frac{d\boldsymbol{\theta_{oo}}}{d\boldsymbol{\tau}} = -\boldsymbol{\theta_{oo}}\left(\mathbf{2}+\frac{\mathbf{12}\boldsymbol{\theta_{oo}}}{\boldsymbol{\theta_o}}\right)$	$\frac{d\theta_{bd}}{d\tau} = \theta_{oo}\left(1+\frac{3\theta_{bo}}{\theta_o}+\frac{3\theta_{do}}{\theta_o}\right)$	$\frac{d\theta_{oo}}{d\tau} = \theta_{bd}\left(2+\frac{6\theta_{bo}}{\theta_b}+\frac{6\theta_{do}}{\theta_d}\right)$	$\frac{d\theta_{bd}}{d\tau} = -\theta_{bd}\left(1+\frac{3\theta_{bd}}{\theta_b}+\frac{3\theta_{bd}}{\theta_d}\right)$
Rate balances (Eq. 5.17)			
$\sum_j \frac{d\boldsymbol{\theta_{bj}}}{d\boldsymbol{\tau}} = \boldsymbol{\theta_{oo}}\left(\mathbf{1}+\mathbf{3}\frac{\sum_j \boldsymbol{\theta_{jo}}}{\boldsymbol{\theta_o}}\right) = \mathbf{4}\boldsymbol{\theta_{oo}} = \frac{d\boldsymbol{\theta_b}}{d\boldsymbol{\tau}}$		$\sum_j \frac{d\theta_{bj}}{d\tau} = -\theta_{bd}\left(1+3\frac{\sum_j \theta_{bj}}{\theta_b}\right) = -4\theta_{bd} = \frac{d\theta_b}{d\tau}$	

$\sum_j \frac{d\boldsymbol{\theta}_{dj}}{d\boldsymbol{\tau}} = \boldsymbol{\theta}_{oo}\left(\mathbf{1} + \mathbf{3}\frac{\sum_j \boldsymbol{\theta}_{jo}}{\boldsymbol{\theta}_o}\right) = \mathbf{4}\boldsymbol{\theta}_{oo} = \frac{d\boldsymbol{\theta}_d}{d\boldsymbol{\tau}}$	$\sum_j \frac{d\theta_{dj}}{d\tau} = -\theta_{bd}\left(1 + 3\frac{\sum_j \theta_{dj}}{\theta_d}\right) = -4\theta_{bd} = \frac{d\theta_d}{d\tau}$
$\sum_j \frac{d\boldsymbol{\theta}_{jo}}{d\boldsymbol{\tau}} = -\boldsymbol{\theta}_{oo}\left(\mathbf{2} + \mathbf{6}\frac{\sum_j \boldsymbol{\theta}_{jo}}{\boldsymbol{\theta}_o}\right) = \frac{d\boldsymbol{\theta}_o}{d\boldsymbol{\tau}}$	$\sum_j \frac{d\theta_{jo}}{d\tau} = \theta_{bd}\left(2 + 3\frac{\sum_j \theta_{bj}}{\theta_b} + 3\frac{\sum_j \theta_{dj}}{\theta_d}\right) = \frac{d\theta_o}{d\tau}$

*Time, t, is made non-dimensional; $\tau = kt$ where k is the rate constant of the considered process. s generally refers to all spectators.

Table D.4: Rate equations for reaction *ab* → *co* in the presence of spectators, *s*

Doubly-heterogeneous two-site reaction (*ab* → *co*)	
One-site rate equations	
$\frac{d\theta_a}{d\tau} = \frac{d\theta_b}{d\tau} = -\frac{d\theta_c}{d\tau} = -\frac{d\theta_o}{d\tau} = -4\theta_{ab}$; $\quad \frac{d\theta_s}{d\tau} = 0$	
Two-site rate equations	
$\frac{d\theta_{aa}}{d\tau} = -6\theta_{ab}\frac{\theta_{aa}}{\theta_a}$	$\frac{d\theta_{cc}}{d\tau} = 6\theta_{ab}\frac{\theta_{ac}}{\theta_a}$
$\frac{d\theta_{ac}}{d\tau} = 3\theta_{ab}\left(\frac{\theta_{aa}}{\theta_a} - \frac{\theta_{ac}}{\theta_a}\right)$	$\frac{d\theta_{bb}}{d\tau} = -6\theta_{ab}\frac{\theta_{bb}}{\theta_b}$
$\frac{d\theta_{bo}}{d\tau} = 3\theta_{ab}\left(\frac{\theta_{bb}}{\theta_b} - \frac{\theta_{bo}}{\theta_b}\right)$	$\frac{d\theta_{oo}}{d\tau} = 6\theta_{ab}\frac{\theta_{bo}}{\theta_b}$
$\frac{d\theta_{ao}}{d\tau} = 3\theta_{ab}\left(\frac{\theta_{ab}}{\theta_b} - \frac{\theta_{ao}}{\theta_a}\right)$	$\frac{d\theta_{bc}}{d\tau} = 3\theta_{ab}\left(\frac{\theta_{ab}}{\theta_a} - \frac{\theta_{bc}}{\theta_b}\right)$
$\frac{d\theta_{ab}}{d\tau} = -\theta_{ab}\left(1 + \frac{3\theta_{ab}}{\theta_a} + \frac{3\theta_{ab}}{\theta_b}\right)$	$\frac{d\theta_{co}}{d\tau} = \theta_{ab}\left(1 + \frac{3\theta_{ao}}{\theta_a} + \frac{3\theta_{bc}}{\theta_b}\right)$
$\frac{d\theta_{as}}{d\tau} = -3\theta_{ab}\frac{\theta_{as}}{\theta_a}$	$\frac{d\theta_{bs}}{d\tau} = -3\theta_{ab}\frac{\theta_{bs}}{\theta_b}$
$\frac{d\theta_{cs}}{d\tau} = 3\theta_{ab}\frac{\theta_{as}}{\theta_a}$	$\frac{d\theta_{so}}{d\tau} = 3\theta_{ab}\frac{\theta_{bs}}{\theta_b}$
$\frac{d\theta_{ss}}{d\tau} = 0$	--
Rate balances (Eq. 5.17)	
$\sum_j \frac{d\theta_{aj}}{d\tau} = -\theta_{ab}\left(1 + 3\frac{\sum_j \theta_{aj}}{\theta_a}\right) = -4\theta_{ab} = \frac{d\theta_a}{d\tau}$	$\sum_j \frac{d\theta_{cj}}{d\tau} = \theta_{ab}\left(1 + 3\frac{\sum_j \theta_{aj}}{\theta_a}\right) = 4\theta_{ab} = \frac{d\theta_c}{d\tau}$
$\sum_j \frac{d\theta_{bj}}{d\tau} = -\theta_{ab}\left(1 + 3\frac{\sum_j \theta_{bj}}{\theta_b}\right) = -4\theta_{ab} = \frac{d\theta_b}{d\tau}$	$\sum_j \frac{d\theta_{jo}}{d\tau} = \theta_{ab}\left(1 + 3\frac{\sum_j \theta_{bj}}{\theta_b}\right) = 4\theta_{ab} = \frac{d\theta_o}{d\tau}$

*Time, *t*, is made non-dimensional; τ = *kt* where *k* is the rate constant of the considered process. *s* generally refers to all spectators.

Table D.5: Rate equations for surface diffusion *ao* → *oa* in the presence of spectators, *s*

Surface diffusion (*ao* → *oa*)	
One-site rate equations	
$\boldsymbol{\frac{d\theta_a}{d\tau} = \frac{d\theta_o}{d\tau} = \frac{d\theta_s}{d\tau} = 0}$	
Two-site rate equations	
$\boldsymbol{\frac{d\theta_{aa}}{d\tau} = 6\theta_{ao}\left(\frac{\theta_{ao}}{\theta_o} - \frac{\theta_{aa}}{\theta_a}\right)}$	$\frac{d\theta_{oo}}{d\tau} = 6\theta_{ao}\left(\frac{\theta_{ao}}{\theta_a} - \frac{\theta_{oo}}{\theta_o}\right)$
$\boldsymbol{\frac{d\theta_{ao}}{d\tau} = 3\theta_{ao}\left(\frac{\theta_{aa}}{\theta_a} + \frac{\theta_{oo}}{\theta_o} - \frac{\theta_{ao}}{\theta_a} - \frac{\theta_{ao}}{\theta_o}\right)}$	$\frac{d\theta_{as}}{d\tau} = 3\theta_{ao}\left(\frac{\theta_{so}}{\theta_o} - \frac{\theta_{as}}{\theta_a}\right)$
$\boldsymbol{\frac{d\theta_{so}}{d\tau} = 3\theta_{ao}\left(\frac{\theta_{as}}{\theta_a} - \frac{\theta_{so}}{\theta_o}\right)}$	$\frac{d\theta_{ss}}{d\tau} = 0$
Rate balances (Eq. 5.17)	
$\boldsymbol{\sum_j \frac{d\theta_{aj}}{d\tau} = \theta_{ao}\left(3\frac{\sum_j \theta_{jo}}{\theta_o} - 3\frac{\sum_j \theta_{aj}}{\theta_a}\right) = 0 = \frac{d\theta_a}{d\tau}}$	$\sum_j \frac{d\theta_{jo}}{d\tau} = \theta_{ao}\left(3\frac{\sum_j \theta_{aj}}{\theta_a} - 3\frac{\sum_j \theta_{jo}}{\theta_o}\right) = 0 = \frac{d\theta_o}{d\tau}$

*Time, *t*, is made non-dimensional; $\tau = kt$ where *k* is the rate constant of the considered process. *s* generally refers to all spectators.

The sensitivity of step *i* is the fractional change in turnover rate, *r*, per fractional change in rate constant k_i

$$s_i = \left(\frac{\partial ln\, r}{\partial ln\, k_i}\right)_{k_{j\neq i}} \qquad \textbf{[D.1.1]}$$

The sum of the forward and reverse sensitivity of step *i* is the kinetic degree of rate control, $X_{RC,i}$, of the shared transition state, *TS,i*, given by

$$s_i + s_{-i} = X_{RC,i} = \left(\frac{\partial ln\, r}{\partial(-G^0_{TS,i}/k_BT)}\right)_{G^0_{TS,j\neq TS,i}} \qquad \textbf{[D.1.2]}$$

Recall, the reaction order of species *j*, given by

$$\Psi_j = \left(\frac{\partial ln\, r}{\partial ln\, a_j}\right)_{a_{k\neq j}} \qquad \textbf{[D.1.3]}$$

is the fractional change in turnover rate per fractional change in the thermodynamic activity (ideally, partial pressure) of species *j*, a_j. The reaction order is readily calculated from sensitivities by

$$\Psi_j = -\sum_{i=steps} s_i \nu_{ij}[\nu_{ij} < 0] \qquad \textbf{[D.1.4]}$$

where ν_{ij} is the stoichiometric coefficient of species *j* in step *i* and brackets in Eq. **D.1.4** are per Iverson Bracket notation where $[\nu_{ij} < 0]$ is unity if the enclosed inequality is true and zero if false (*140*).

The reversibility of step *i* in a fluid-phase or Langmuir-Hinshelwood reaction is related to the forward and reverse sensitivity of step *i* by the relation

$$\frac{-s_{-i}}{s_i} = z_i \qquad \textbf{[D.1.5]}$$

Proof of Eq. **D.1.5** (*140*), however, requires that s_i and s_{-i} refer to a single reversible rate expression for all instances of k_i and k_{-i} – which is not true in models of order greater than

zero since distinct $r_{i,[j]}$ engender distinct attendant $k_{i,[j]}$. Therefore, we surmise there must be a unique sensitivity identifiable for each independent $k_{i,[j]}$ and $k_{-i,[j]}$. We note here that $k_{i,[j]}$ are numerically-equivalent for all j and are distinct only in the sense that each $k_{i,[j]}$ refers to a rate expression unique to site ensemble j. The only site ensembles which share identical rate expressions are single-site configurations j^1 – the only configurations considered by the Langmuir-Hinshelwood model.

We derive the distinct sensitivities $s_{i,[j]}$ in the following. The reaction sensitivity may be re-expressed using the chain rule as

$$s_i = \left(\frac{\partial ln\, r}{\partial ln\, k_i}\right)_{k_{j\neq i}} = \sum_{\substack{m=rate\\process}} \left(\frac{\partial ln\, r}{\partial ln\, r_m}\right)_{r_{n\neq m}} \left(\frac{\partial ln\, r_m}{\partial ln\, k_i}\right)_{k_{j\neq i}} \quad \textbf{[D.1.6]}$$

where m is an index over all rate processes, or elementary steps (*140*). In the Langmuir-Hinshelwood formalism, all stoichiometric coefficients are numeric, and, therefore, all instances of k_i refer to a single, degenerate rate expression for step i

$$s_i = \sum_{\substack{m=rat\\process}} \left(\frac{\partial ln\, r}{\partial ln\, r_m}\right)_{r_{n\neq m}} \delta_{im} = \left(\frac{\partial ln\, r}{\partial ln\, r_i}\right)_{r_{n\neq i}} \quad \textbf{[D.1.7]}$$

We therefore conclude

$$\left(\frac{\partial ln\, r}{\partial ln\, k_i}\right)_{k_{j\neq i}} = \left(\frac{\partial ln\, r}{\partial ln\, r_i}\right)_{r_{n\neq i}} \quad \textbf{[D.1.8]}$$

as is also derived from the limit definition of the derivative in the Supporting Information of the recent work of Foley and Bhan (*140*). In higher-order models, we must re-write Eq. **D.1.6** in terms of the distinct $r_{i,[j]}$ and $k_{i,[j]}$

$$s_i = \sum_{m,n,j} \left(\frac{\partial ln\, r}{\partial ln\, r_{m,[n]}}\right)_{r_{v,[w]\neq m,[n]}} \left(\frac{\partial ln\, r_{m,[n]}}{\partial ln\, k_{i,[j]}}\right)_{k_{p,[q]\neq i,[j]}}$$

$$= \sum_{m,n,j} \left(\frac{\partial ln\, r}{\partial ln\, r_{m,[n]}} \right)_{r_{v,[w]\neq m,[n]}} \delta_{im}\delta_{jn} = \sum_{j} \left(\frac{\partial ln\, r}{\partial ln\, r_{i,[j]}} \right)_{r_{v,[w]\neq i,[j]}}$$

$$= \sum_{j} \left(\frac{\partial ln\, r}{\partial ln\, k_{i,[j]}} \right)_{k_{p,[q]\neq i,[j]}} = \sum_{\substack{j=independen \\ site\ configs.}} s_{i,[j]} \qquad \textbf{[D.1.9]}$$

where index *j* refers to all *independent* site configurations to avoid over-specification of the reaction system. We note here that the contribution of independent site ensemble *j* to the degree of rate control of step *i* may simply be defined by

$$X_{RC,i,[j]} = s_{i,[j]} + s_{-i,[j]} = \left(\frac{\partial ln\, r}{\partial ln\, k_{i,[j]}} \right)_{k_{p,[q]\neq i,[j]},K_i} \qquad \textbf{[D.1.10]}$$

From Eq. **D.1.9**, we see that the sensitivity of reaction, s_i, is a sum of sensitivities of the reaction with respect to each site configuration, $s_{i,[j]}$. Eq. **D.1.5** may now be correctly reformulated in terms of distinct reversibilities and sensitivities

$$\frac{-s_{-i,[j]}}{s_{i,[j]}} = z_{i,[j]} \qquad \textbf{[D.1.11]}$$

From Eq. **D.1.11** we see that z_i, the reversibility for all single-site configurations, is not generally equal to the ratio of $-s_{-i}$ and s_i – which are now sums over sensitivities of all independent site configurations. Section D.3 hereinafter will demonstrate the veracity of Eqs. **D.1.9** and **D.1.11** and the ostensible violation of Eq. **D.1.5** when combinatorial non-idealities are accounted for in the 1st-order model and kMC method.

D.2 Incorporating adsorbate interactions into 1st-order kinetic descriptions

The 1st-order description of catalysis of mobile Langmuirian adsorbates is readily modified to include lateral adsorbate interactions. Considering thermodynamic non-idealities leaves only two conditions of the Langmuirian adsorption on which the 1st-order formalism relies

(I) The absorbent is a perfect, flat 2-D lattice

(II) Each adsorption site can be occupied by at most one occupant

Condition (I) can be relaxed by quantitative consideration of surface heterogeneity following the work of Boudart and Djega-Mariadassou (*76*) which considers catalysis to occur over a distribution of energetically-distinct active sites. Since rate equations, including those for multi-site ensembles, are linearly proportional to the pertinent active site density, the formalism detailed by Boudart and Djega-Mariadassou is applicable to the higher-order kinetic description presented herein.

Condition (II) can be readily relaxed by enumerating rate equations for multi-layer adsorption; each adsorption layer will be associated with layer-specific overall and component site balances which are coupled to site balances for the layers immediately above and below.

Condition (III) of the Langmuir adsorption model – that the surface is thermodynamically ideal – can be relaxed by inclusion of any local or mean-field adsorbate interaction model into the 1st-order formalism. Change of adsorption or activation enthalpies with total coverage is readily incorporated in the same fashion as in modified Langmuir-Hinshelwood mechanisms, and nearest-neighbor adsorbate interaction energies can be accounted for by re-derivation of 1st-order rate equations tabulated in Section D.1 with special attention paid to statistical distribution of site occupants which are nearest

neighbors to the -sorptive/reactive/diffusive configuration. In this section, in the context of Case Studies I and II, we first explicate the procedure by which 1st-order lateral adsorbate interaction terms are derived, then compute the consequences of nearest-neighbor adsorbate interactions.

Table D.6 summarizes the reaction network of the $A + A \rightarrow A_2$ reaction discussed in Case Studies I and II.

Table D.6: Homogeneous bimolecular catalytic reaction

#	Step	Rate constants
1	$A_{(g)} + o \rightarrow a$	k_{ads}*
–1	$a \rightarrow A_{(g)} + o$	k_{des}
2	$aa \rightarrow oo + A_{2(g)}$	k_r
n/a	$ao \rightarrow oa$	k_{diff}

*k_{ads} is the product of the rate constant of adsorption and the thermodynamic activity (ideally, partial pressure) of $A_{(g)}$.

D.2.1 Single-site rate equations

We first derive single-site rate equations for $A_{(g)}$ desorption in the $A + A \rightarrow A_2$ reaction system (Table D.6). Recall that, in the absence of adsorbate interactions, the desorption rate is simply

$$-\frac{d\theta_a}{dt} = \frac{d\theta_o}{dt} = k_{des}\theta_a \qquad \textbf{[D.2.1]}$$

In order to explicate the effect of adsorbate interactions on rate, we re-express k_{des} in terms of the pre-exponential factor A_{des} and activation energy barrier E_{des}

$$-\frac{d\theta_a}{dt} = \frac{d\theta_o}{dt} = A_{des}e^{-\frac{E_{des}}{k_BT}}\theta_a \qquad \textbf{[D.2.2]}$$

where k_B is the Boltzmann constant, T is temperature, and E_{des} is the activation energy of desorption *in the absence of lateral interactions*. Nearest-neighbor interactions affect

reaction kinetics by (de-)stabilizing initial and transition states – thereby changing the effective activation energy of each elementary step and biasing the distribution of surface species (i.e. effecting adsorbate clustering and/or isolation). We refer to the interaction energy between any two nearest-neighbor site occupants i and j as ε_{ij}; and, we refer to the interaction energy between a site occupant i and nearest-neighboring transition state $j^{\ddagger}$ as $\varepsilon_{ij}{}^{\ddagger}$. For example, we refer to the -sorption transition state as $a^{\ddagger}$; so, the interaction energy between nearest-neighbor a species and the -sorption transition state is $\varepsilon_{aa}{}^{\ddagger}$.

We now re-derive Eq. **D.2.1** by enumerating all configurations relevant to desorption

$$-\frac{d\theta_a}{dt}=\frac{d\theta_o}{dt}=A_{des}e^{-\frac{E_{des}}{k_BT}}\left[\theta_{\substack{a\\ aaa\\ a}}+4\theta_{\substack{a\\ aaa\\ o}}+6\theta_{\substack{a\\ aao\\ o}}+4\theta_{\substack{a\\ oao\\ o}}+\theta_{\substack{o\\ oao\\ o}}\right] \qquad \textbf{[D.2.3]}$$

where the desorbing a-species is highlighted in red and each ensemble in the bracketed sum represents all configurations with the same number of a-neighbors. The numeric factor adjoining each bracketed term is the number of distinct configurations with the same number of a species nearest-neighboring the desorbing a species. For example, there are six distinct microstates in which the desorbing a species is neighbored by exactly two a and two o species. The bracketed sum is simplified in terms of coverages of one- and two-site configurations by executing the 1st-order truncation scheme. We explicate this procedure for a select bracketed term, $\theta_{\substack{a\\ aao\\ o}}$, *for the reader's reference*

$$\theta_{\substack{a\\ aao\\ o}}=\theta_{\substack{a\\ aa\\ o}}\chi_{\substack{\alpha\\ \alpha ao\\ \phi}}\overset{truncate}{\Longrightarrow}\theta_{\substack{a\\ aa\\ o}}\chi_{\alpha o}=\theta_{\substack{a\\ aa\\ o}}\frac{\theta_{ao}}{\theta_a}$$

$$=\theta_{\substack{a\\ aa}}\chi_{\substack{\alpha\\ \alpha a\\ o}}\frac{\theta_{ao}}{\theta_a}\overset{truncate}{\Longrightarrow}\theta_{\substack{a\\ aa}}\chi_{\substack{\alpha\\ o}}\frac{\theta_{ao}}{\theta_a}=\theta_{\substack{a\\ aa}}\left(\frac{\theta_{ao}}{\theta_a}\right)^2 \qquad \textbf{[D.2.4]}$$

$$= \theta_{aa}\chi_{\alpha\alpha}^{\ a}\left(\frac{\theta_{ao}}{\theta_a}\right)^2 \xrightarrow{truncate} \theta_{aa}\chi_{\alpha}^{a}\left(\frac{\theta_{ao}}{\theta_a}\right)^2 = \theta_{aa}\left(\frac{\theta_{ao}}{\theta_a}\right)^2\frac{\theta_{aa}}{\theta_a}$$

$$= \frac{\theta_a}{\theta_a} \times \theta_{aa}\left(\frac{\theta_{ao}}{\theta_a}\right)^2\frac{\theta_{aa}}{\theta_a} = \theta_a \times \frac{\theta_{aa}^2\theta_{ao}^2}{\theta_a^4}$$

In general, each bracketed coverage term in Eq. **D.2.3** with *n* nearest *a* neighbors reduces to $\theta_a \times \theta_{aa}{}^n\theta_{ao}{}^{4-n}\theta_a{}^{-4}$. *Therefore,* Eq. **D.2.3** becomes

$$-\frac{d\theta_a}{dt} = \frac{d\theta_o}{dt} = A_{des}e^{-\frac{E_{des}}{k_BT}}\theta_a\left[\frac{\theta_{aa}^4 + 4\theta_{aa}^3\theta_{ao} + 6\theta_{aa}^2\theta_{ao}^2 + 4\theta_{aa}\theta_{ao}^3 + \theta_{ao}^4}{\theta_a^4}\right] \quad \textbf{[D.2.5]}$$

The bracketed term is recognized as a binomial expansion; therefore,

$$\left[\frac{\theta_{aa}^4 + 4\theta_{aa}^3\theta_{ao} + 6\theta_{aa}^2\theta_{ao}^2 + 4\theta_{aa}\theta_{ao}^3 + \theta_{ao}^4}{\theta_a^4}\right] = \left(\frac{\theta_{aa} + \theta_{ao}}{\theta_a}\right)^4 = 1 \quad \textbf{[D.2.6]}$$

since $\theta_a = \theta_{aa} + \theta_{ao}$. If we include nearest-neighbor interactions, however, each nearest neighbor *j* to the desorption center carries an energetic contribution

$$\Delta\epsilon_{des,j} = \epsilon_{a^{\ddagger}j} - \epsilon_{aj} \quad \textbf{[D.2.7]}$$

which is the difference in the interaction energy contributions in the transition state and in the initial state. Accounting for these energetic contributions, Eq. **D.2.3** is now

$$-\frac{d\theta_a}{dt} = \frac{d\theta_o}{dt} = A_{des}e^{-\frac{E_{des}}{k_BT}}\theta_a\left[\frac{\theta_{aa}e^{-\frac{\Delta\epsilon_{des,a}}{k_BT}} + \theta_{ao}e^{-\frac{\Delta\epsilon_{des,o}}{k_BT}}}{\theta_a}\right]^4 \quad \textbf{[D.2.8]}$$

The bracketed term compendiously captures the propensity of lateral adsorbate interactions to affect the activation energy of desorption and is referred to in the following as

$$\Gamma_{des} = \frac{\theta_{aa}e^{-\frac{\Delta\epsilon_{des,a}}{k_BT}} + \theta_{ao}e^{-\frac{\Delta\epsilon_{des,o}}{k_BT}}}{\theta_a} \quad \textbf{[D.2.9]}$$

Eqs. **D.2.8** and **D.2.9** demonstrate that accurately accounting for lateral adsorbate interactions requires a rigorous means of counting site pairs. Attractive (repulsive)

energetic interactions will naturally bias clustering (isolation) of surface species, rendering the Hinshelwood assumption incompatible with the inclusion of adsorbate interactions. In the limit of infinitely-fast surface diffusion, the distribution of interacting adsorbates is not random (i.e. $\mu_{ij} \neq 1$); rather, site occupants energetically-equilibrate in accordance with nearest-neighbor interaction energies, giving site pair coverages determined by ε_{ij}. The quasi-chemical approximation (QCA) describes exactly this case by assuming diffusion events such as

$$aa + oo \leftrightarrow 2ao \qquad \textbf{[D.2.10]}$$

are equilibrated. Equilibration of Eq. **D.2.10** algebraically constrains coverages of *aa*, *oo*, and *ao* site pairs based on the energy change of the diffusion event

$$\frac{\theta_{ao}^2}{\theta_{aa}\theta_{oo}} = e^{-(2\epsilon_{ao}-\epsilon_{oo}-\epsilon_{aa})/k_BT} \qquad \textbf{[D.2.11]}$$

If we regard vacant sites as non-interacting, as is most common, Eq. **D.2.11** simplifies to

$$\frac{\theta_{ao}^2}{\theta_{aa}\theta_{oo}} = e^{\epsilon_{aa}/k_BT} \qquad \textbf{[D.2.12]}$$

We note that if $\varepsilon_{aa} = 0$ (i.e. if all adsorbates are non-interacting), then the QCA collapses exactly to the Hinshelwood assumption. In this sense, the Hinshelwood assumption is a special case of the QCA – both of which rely on surface diffusion of each species being arbitrarily-fast compared to all -sorption/reaction events.

Use of the QCA provides an algebraic constraint on site-pair coverages which permits calculation of steady-state coverages and rates without the need for explicit rate equations for multi-site ensembles. Much like the Hinshelwood assumption, however, the QCA is inappropriate if diffusion is not arbitrarily-fast and results in miscalculated rates,

coverages, reaction orders, and degrees of rate control – as we demonstrate in the context of the $A + A \rightarrow A_2$ reaction in this section.

In the succeeding subsection, we derive single-site rate equations for adsorption and reaction – identical in both the 1st-order and QCA formalism. We will then derive two-site rate equations inaccessible to the QCA formalism and compare the predictions of the 1st-order method with those calculated by use of the Hinshelwood approximation and QCA.

D.2.1.1 Single-site adsorption rate equations

The single-site rate equations for adsorption are derived similarly to those for desorption with appropriate change of occupant at the -sorptive center from *a* to *o*. The interaction energy change from the initial to the transition state contributed by each nearest neighbor $j = \{a, o\}$ is

$$\Delta\epsilon_{ads,j} = \epsilon_{a^{\ddagger}j} - \epsilon_{oj} \qquad \textbf{[D.2.13]}$$

where $\varepsilon_{a^{\ddagger}j}$ is identical in the adsorption and desorption rate equations because the directional steps share a transition state. We now derive the single-site rate equations by enumeration of all adsorptive configurations

$$\frac{d\theta_a}{dt} = -\frac{d\theta_o}{dt} = A_{ads}e^{-\frac{E_{ads}}{k_BT}}\left[\theta_{\substack{a\\aoa\\a}} e^{-\frac{4\Delta\epsilon_{ads,a}}{k_BT}} + 4\theta_{\substack{o\\aoa\\a}} e^{-\frac{3\Delta\epsilon_{ads,a}+\Delta\epsilon_{ads,o}}{k_BT}} + 6\theta_{\substack{o\\aoo\\a}} e^{-\frac{2\Delta\epsilon_{ads,a}+2\Delta\epsilon_{ads,o}}{k_BT}} + 4\theta_{\substack{o\\aoo\\o}} e^{-\frac{\Delta\epsilon_{ads,a}+3\Delta\epsilon_{ads,o}}{k_BT}} + \theta_{\substack{o\\ooo\\o}} e^{-\frac{4\Delta\epsilon_{ads,o}}{k_BT}}\right] \qquad \textbf{[D.2.14]}$$

Truncating each five-site coverage term to the 1st-order, we find

$$\frac{d\theta_a}{dt} = -\frac{d\theta_o}{dt} = A_{ads} e^{-\frac{E_{ads}}{k_B T}} \theta_o \left[\theta_o^{-4} \left(\theta_{ao}^4 e^{-\frac{4\Delta\epsilon_{ads,a}}{k_B T}} \right.\right.$$

$$+ 4\theta_{ao}^3 \theta_{oo} e^{-\frac{3\Delta\epsilon_{ads,a}+\Delta\epsilon_{ads,o}}{k_B T}} + 6\theta_{ao}^2 \theta_{oo}^2 e^{-\frac{2\Delta\epsilon_{ads,a}+2\Delta\epsilon_{ads,o}}{k_B T}} \qquad \textbf{[D.2.15]}$$

$$\left.\left. + 4\theta_{ao} \theta_{oo}^3 e^{-\frac{\Delta\epsilon_{ads,a}+3\Delta\epsilon_{ads,o}}{k_B T}} + \theta_{oo}^4 e^{-\frac{4\Delta\epsilon_{ads,o}}{k_B T}} \right) \right]$$

The bracketed term is again a binomial expansion; therefore, Eq. **D.2.15** simplifies to

$$\frac{d\theta_a}{dt} = -\frac{d\theta_o}{dt} = A_{ads} e^{-\frac{E_{ads}}{k_B T}} \theta_o \left[\frac{\theta_{ao} e^{-\frac{\Delta\epsilon_{ads,a}}{k_B T}} + \theta_{oo} e^{-\frac{\Delta\epsilon_{ads,o}}{k_B T}}}{\theta_o} \right]^4 \qquad \textbf{[D.2.16]}$$

$$= A_{ads} e^{-\frac{E_{ads}}{k_B T}} \theta_o \Gamma_{ads}^4$$

where Γ_{ads} is identified as the compendious measure of the influence of lateral adsorbate interactions. We note that $\Gamma_{ads} = 1$ if all site-occupants are non-interacting – giving the canonical Langmuirian rate expression for monomer adsorption.

D.2.1.2 Single-site surface reaction rate equations

The single-site rate equations for surface reaction again require enumeration of all reactive configurations and the attendant energetic contribution of nearest-neighbor interactions. Each nearest neighbor $j = \{a, o\}$ to a reacting a species carries energetic contribution

$$\Delta\epsilon_{rxn,j} = \epsilon_{r^\ddagger j} - \epsilon_{aj} \qquad \textbf{[D.2.17]}$$

where $r^\ddagger$ indicates the transition state of the surface reaction event. We distinguish $r^\ddagger$ and $a^\ddagger$ because lateral interactions with transition states for surface reaction and -sorption events are not necessarily the same – even if both transition states are composed exclusively of a species.

Each surface reaction event also inherently carries a contribution

$$\epsilon_{rxn} = \epsilon_{r^{\ddagger}r^{\ddagger}} - \epsilon_{aa} \qquad \textbf{[D.2.18]}$$

which we consider accounted for by E_{rxn} since this energy contribution is intrinsic to the elementary step activation energy barrier.

Enumerating reactive configuration and the pertinent energetic contributions gives

$$-\frac{d\theta_a}{dt} = \frac{d\theta_o}{dt} = 4A_{rxn}e^{-\frac{E_{rxn}}{k_BT}}\left[\theta_{\substack{aa\\aaaa\\aa}} e^{-\frac{6\Delta\epsilon_{rxn,a}}{k_BT}} + 6\theta_{\substack{ao\\aaaa\\aa}} e^{-\frac{5\Delta\epsilon_{rxn,a}+\Delta\epsilon_{rxn,o}}{k_BT}}\right.$$
$$+ 15\theta_{\substack{ao\\aaao\\aa}} e^{-\frac{4\Delta\epsilon_{rxn,a}+2\Delta\epsilon_{rxn,o}}{k_BT}} + 20\theta_{\substack{ao\\aaao\\ao}} e^{-\frac{3\Delta\epsilon_{rxn,a}+3\Delta\epsilon_{rxn,o}}{k_BT}}$$
$$+ 15\theta_{\substack{ao\\aaao\\oo}} e^{-\frac{2\Delta\epsilon_{rxn,a}+4\Delta\epsilon_{rxn,o}}{k_BT}} + 6\theta_{\substack{ao\\oaao\\oo}} e^{-\frac{\Delta\epsilon_{rxn,a}+5\Delta\epsilon_{rxn,o}}{k_BT}}$$
$$\left. + \theta_{\substack{oo\\oaao\\oo}} e^{-\frac{6\Delta\epsilon_{rxn,o}}{k_BT}}\right] \qquad \textbf{[D.2.19]}$$

Executing the 1st-order truncation scheme and recognizing the bracketed term is, again, a binomial expansion, Eq. **D.2.19** simplifies to

$$-\frac{d\theta_a}{dt} = \frac{d\theta_o}{dt} = 4A_{rxn}e^{-\frac{E_{rxn}}{k_BT}}\theta_{aa}\left[\frac{\theta_{aa}e^{-\frac{\Delta\epsilon_{rxn,a}}{k_BT}} + \theta_{ao}e^{-\frac{\Delta\epsilon_{rxn,o}}{k_BT}}}{\theta_a}\right]^6$$
$$= 4A_{rxn}e^{-\frac{E_{rxn}}{k_BT}}\theta_{aa}\Gamma_{rxn}^6 \qquad \textbf{[D.2.20]}$$

which a stronger function of lateral adsorbate interactions than single-site rate equations for $A_{(g)}$ -sorption steps which only require one site and therefore have four, rather than six, nearest neighbors with which to interact.

D.2.1.3 Single-site surface diffusion rate equations

Surface diffusion events do not affect the coverage of single-site configurations; therefore, all single-site rate equations are equal to zero in all kinetic descriptions.

The single-site rate equations derived in this section – along with the appropriate site-pair coverage algebraic constraints – complete Langmuir-Hinshelwood and QCA descriptions of the $A + A \rightarrow A_2$ reaction. Explicitly treating site pair coverages requires re-derivation of two-site rate equations following an analogous procedure by which we derived thermodynamically non-ideal one-site rate equations.

D.2.2 Two-site rate equations

The following subsections derive two-site rate equations for *aa*, *ao*, and *oo* site pairs in the $A + A \rightarrow A_2$ reaction. We intend to re-derive all general rate equations tabulated in Section D.1 with the consideration of nearest-neighbor lateral interactions in a subsequent study.

D.2.2.1 Two-site adsorption rate equations

Recall the two-site rate equation for $A_{(g)}$ adsorption in the absence of thermodynamic non-idealities

$$\frac{d\theta_{aa}}{dt} = 2k_{ads}\theta_{ao} \qquad \textbf{[D.2.21]}$$

$$\frac{d\theta_{ao}}{dt} = k_{ads}(\theta_{oo} - \theta_{ao}) \qquad \textbf{[D.2.22]}$$

$$\frac{d\theta_{oo}}{dt} = -2k_{ads}\theta_{oo} \qquad \textbf{[D.2.23]}$$

Incorporating lateral interactions requires enumerating all adsorptive configurations which contain the ensembles relevant to each ensemble-specific rate equation. For example $d\theta_{aa}/dt$ is only concerned with adsorptive configurations with at least one *a* species neighboring the adsorption center. The rate equation for *aa* pairs is thusly

$$\frac{d\theta_{aa}}{dt} = 2A_{ads}e^{-\frac{E_{ads}}{k_BT}}\left[\theta_{\substack{a\\aoa\\a}}e^{-\frac{4\Delta\epsilon_{ads,a}}{k_BT}} + 3\theta_{\substack{o\\aoa\\a}}e^{-\frac{3\Delta\epsilon_{ads,a}+\Delta\epsilon_{ads,o}}{k_BT}}\right.$$

$$\left. + 3\theta_{\substack{o\\aoo\\a}}e^{-\frac{2\Delta\epsilon_{ads,a}+2\Delta\epsilon_{ads,o}}{k_BT}} + \theta_{\substack{o\\aoo\\o}}e^{-\frac{\Delta\epsilon_{ads,a}+3\Delta\epsilon_{ads,o}}{k_BT}}\right] \quad \textbf{[D.2.24]}$$

which does not include the five-site configuration exclusively populated by vacant sites. Each term in Eq. **D.2.24** contains an energetic contribution $e^{-\frac{\Delta\epsilon_{\mathrm{ads},a}}{k_BT}}$ because each configuration is required to have at least one ao pair. Executing the 1st-order truncation scheme, separating the term $e^{-\frac{\Delta\epsilon_{ads,a}}{k_BT}}$, and simplifying the binomial expansion gives

$$\frac{d\theta_{aa}}{dt} = 2A_{ads}e^{-\frac{E_{ads}}{k_BT}}e^{-\frac{\Delta\epsilon_{ads,a}}{k_BT}}\theta_{ao}\left[\frac{\theta_{ao}e^{-\frac{\Delta\epsilon_{ads,a}}{k_BT}} + \theta_{oo}e^{-\frac{\Delta\epsilon_{ads,o}}{k_BT}}}{\theta_o}\right]^3 \quad \textbf{[D.2.25]}$$

$$= 2A_{ads}e^{-\frac{E_{ads}}{k_BT}}e^{-\frac{\Delta\epsilon_{ads,a}}{k_BT}}\theta_{ao}\Gamma_{ads}^3$$

which, as we expect, collapses to Eq. **D.2.21** if adsorbates are non-interacting. Eq. **D.2.25** explicates the distinct, ensemble-specific kinetic description proffered by the 1st-order formalism. Retaining terms of the 1st-order captures the unique omnipresence of the energetic term $e^{-\frac{\Delta\epsilon_{\mathrm{ads},a}}{k_BT}}$ in adsorption rate equations for the aa ensemble. Pairs of a species can only be generated by adsorption if the adsorption center neighbors an *a* adatom; therefore, the rate equation for the aa ensemble must always carry a contribution $e^{-\frac{\Delta\epsilon_{\mathrm{ads,a}}}{k_BT}}$ – regardless of the occupancy of the three remaining nearest-neighbor sites. Ensemble-specific lateral interaction terms such as these enable description of catalysis of thermodynamically non-ideal adsorbates without the requirement that surface diffusion be equilibrated with respect to each ensemble.

The adsorption rate equation for *oo* pairs is derived similarly to that for *aa* with the requirement that each adsorptive configuration contain at least one vacant site neighboring the adsorption center.

$$\frac{d\theta_{oo}}{dt} = -2A_{ads}e^{-\frac{E_{ads}}{k_BT}}\left[\theta_{\substack{o\\ aoa\\ a}}e^{-\frac{3\Delta\epsilon_{ads,a}+\Delta\epsilon_{ads,o}}{k_BT}} + 3\theta_{\substack{o\\ aoo\\ a}}e^{-\frac{2\Delta\epsilon_{ads,a}+2\Delta\epsilon_{ads,o}}{k_BT}}\right.$$

$$\left. + 3\theta_{\substack{o\\ aoo\\ o}}e^{-\frac{\Delta\epsilon_{ads,a}+3\Delta\epsilon_{ads,o}}{k_BT}} + \theta_{\substack{o\\ ooo\\ o}}e^{-\frac{4\Delta\epsilon_{ads,o}}{k_BT}}\right] \qquad \textbf{[D.2.26]}$$

which does not include the five-site configuration populated by four *a* species. Each term in Eq. **D.2.26** contains an energetic contribution $e^{-\frac{\Delta\epsilon_{ads,o}}{k_BT}}$ because each configuration is required to have at least one *oo* pair. Executing the 1st-order truncation scheme, separating the term $e^{-\frac{\Delta\epsilon_{ads,o}}{k_BT}}$, and simplifying the binomial expansion gives

$$\frac{d\theta_{oo}}{dt} = -2A_{ads}e^{-\frac{E_{ads}}{k_BT}}e^{-\frac{\Delta\epsilon_{ads,o}}{k_BT}}\theta_{oo}\left[\frac{\theta_{ao}e^{-\frac{\Delta\epsilon_{ads,a}}{k_BT}} + \theta_{oo}e^{-\frac{\Delta\epsilon_{ads,o}}{k_BT}}}{\theta_o}\right]^3 \qquad \textbf{[D.2.27]}$$

$$= -2A_{ads}e^{-\frac{E_{ads}}{k_BT}}e^{-\frac{\Delta\epsilon_{ads,o}}{k_BT}}\theta_{oo}\Gamma_{ads}^3$$

The adsorption rate equation for ao pairs is simply the sum of the adsorption rate equations for aa and oo pairs multiplied by a factor of – ½ since (i) each annihilation of an *oo* pair generates an *ao* or *oa* pair, (ii) each generation of an aa pair annihilates an ao or oa pair, and (iii) the *ao* configuration is heterogeneous and is therefore only counted in half of adsorption events, with the other half affecting the oa pair. Enumerating all the relevant configurations gives

$$\frac{d\theta_{ao}}{dt} = A_{ads}e^{-\frac{E_{ads}}{k_BT}}\left[\left(\theta_{\substack{o\\aoa\\a}}e^{-\frac{3\Delta\epsilon_{ads,a}+\Delta\epsilon_{ads,o}}{k_BT}} + 3\theta_{\substack{o\\aoo\\a}}e^{-\frac{2\Delta\epsilon_{ads,a}+2\Delta\epsilon_{ads,o}}{k_BT}}\right.\right.$$

$$\left. + 3\theta_{\substack{o\\aoo\\o}}e^{-\frac{\Delta\epsilon_{ads,a}+3\Delta\epsilon_{ads,o}}{k_BT}} + \theta_{\substack{o\\ooo\\o}}e^{-\frac{4\Delta\epsilon_{ads,o}}{k_BT}}\right)$$

$$-\left(\theta_{\substack{a\\aoa\\a}}e^{-\frac{4\Delta\epsilon_{ads,a}}{k_BT}} + 3\theta_{\substack{o\\aoa\\a}}e^{-\frac{3\Delta\epsilon_{ads,a}+\Delta\epsilon_{ads,o}}{k_BT}}\right.$$

$$\left.\left. + 3\theta_{\substack{o\\aoo\\a}}e^{-\frac{2\Delta\epsilon_{ads,a}+2\Delta\epsilon_{ads,o}}{k_BT}} + \theta_{\substack{o\\aoo\\o}}e^{-\frac{\Delta\epsilon_{ads,a}+3\Delta\epsilon_{ads,o}}{k_BT}}\right)\right] \qquad \textbf{[D.2.28]}$$

Executing the 1st-order truncation procedure and collecting terms gives

$$\frac{d\theta_{ao}}{dt} = A_{ads}e^{-\frac{E_{ads}}{k_BT}}\Gamma_{ads}^3\left(e^{-\frac{\Delta\epsilon_{ads,o}}{k_BT}}\theta_{oo} - e^{-\frac{\Delta\epsilon_{ads,a}}{k_BT}}\theta_{ao}\right) \qquad \textbf{[D.2.29]}$$

We demonstrate the two-site rate equations conform to component rate balance by sum of $d\theta_{aa}/dt$ and $d\theta_{ao}/dt$

$$\frac{d\theta_{aa}}{dt} + \frac{d\theta_{ao}}{dt} = A_{ads}e^{-\frac{E_{ads}}{k_BT}}\Gamma_{ads}^3\left(2e^{-\frac{\Delta\epsilon_{ads,a}}{k_BT}}\theta_{ao} + e^{-\frac{\Delta\epsilon_{ads,o}}{k_BT}}\theta_{oo}\right.$$

$$\left. - e^{-\frac{\Delta\epsilon_{ads,a}}{k_BT}}\theta_{ao}\right)$$

$$= A_{ads}e^{-\frac{E_{ads}}{k_BT}}\Gamma_{ads}^3\left(e^{-\frac{\Delta\epsilon_{ads,a}}{k_BT}}\theta_{ao} + e^{-\frac{\Delta\epsilon_{ads,o}}{k_BT}}\theta_{oo}\right)$$

$$= A_{ads}e^{-\frac{E_{ads}}{k_BT}}\Gamma_{ads}^3\theta_o\left(\frac{e^{-\frac{\Delta\epsilon_{ads,a}}{k_BT}}\theta_{ao} + e^{-\frac{\Delta\epsilon_{ads,o}}{k_BT}}\theta_{oo}}{\theta_o}\right)$$

$$= A_{ads}e^{-\frac{E_{ads}}{k_BT}}\Gamma_{ads}^4\theta_o = \frac{d\theta_a}{dt} \qquad \textbf{[D.2.30]}$$

which agrees with Eq. **D.2.16**.

D.2.2.2 Two-site desorption rate equations

Desorption rate equations can be derived from adsorption rate equations by subscript interchange of '*o*' and '*a*' and by replacement of subscript '*ads*' with '*des*'. We also provide explicit derivation of two-site rate equations for desorption if the reader is not satisfied with the subscript interchange method.

Recall the two-site rate equation for $A_{(g)}$ desorption in the absence of thermodynamic non-idealities.

$$\frac{d\theta_{aa}}{dt} = -2k_{des}\theta_{aa} \quad \textbf{[D.2.31]}$$

$$\frac{d\theta_{ao}}{dt} = k_{des}(\theta_{aa} - \theta_{ao}) \quad \textbf{[D.2.32]}$$

$$\frac{d\theta_{oo}}{dt} = 2k_{des}\theta_{ao} \quad \textbf{[D.2.33]}$$

We modify these rate equations by incorporation of lateral interactions dependent on the occupancy of sites neighboring the desorbing *a* species. Each site ensemble is associated with a unique set of desorptive configurations relevant to the annihilation and/or creation of the considered ensemble.

For example, the desorption rate equation for *aa* pairs is derived by considering all desorption events in which there is at least one *aa* pair annihilated by desorption

$$\frac{d\theta_{aa}}{dt} = -2A_{des}e^{-\frac{E_{des}}{k_BT}}\left[\theta_{\substack{a\\aaa\\a}}e^{-\frac{4\Delta\epsilon_{des,a}}{k_BT}} + 3\theta_{\substack{o\\aaa\\a}}e^{-\frac{3\Delta\epsilon_{des,a}+\Delta\epsilon_{des,o}}{k_BT}} + 3\theta_{\substack{o\\aao\\a}}e^{-\frac{2\Delta\epsilon_{des,a}+2\Delta\epsilon_{des,o}}{k_BT}} + \theta_{\substack{o\\aao\\o}}e^{-\frac{\Delta\epsilon_{des,a}+3\Delta\epsilon_{des,o}}{k_BT}}\right] \quad \textbf{[D.2.34]}$$

Each term in Eq. **D.2.34** contains an energetic contribution $e^{-\frac{\Delta\epsilon_{des,a}}{k_BT}}$ because each configuration is required to have at least one *aa* pair. Executing the 1st-order truncation scheme and collecting terms gives

$$\frac{d\theta_{aa}}{dt} = -2A_{des}e^{-\frac{E_{des}}{k_BT}}e^{-\frac{\Delta\epsilon_{des,a}}{k_BT}}\theta_{aa}\left[\frac{\theta_{aa}e^{-\frac{\Delta\epsilon_{des,a}}{k_BT}} + \theta_{ao}e^{-\frac{\Delta\epsilon_{des,o}}{k_BT}}}{\theta_a}\right]^3 \qquad \textbf{[D.2.35]}$$

$$= -2A_{des}e^{-\frac{E_{des}}{k_BT}}e^{-\frac{\Delta\epsilon_{des,a}}{k_BT}}\theta_{aa}\Gamma_{des}^3$$

The rate equation for *oo* pairs is derived similarly to that for *aa* with the requirement that each desorptive configuration contain at least one vacant site neighboring the desorption center.

$$\frac{d\theta_{oo}}{dt} = 2A_{des}e^{-\frac{E_{des}}{k_BT}}\left[\theta_{\substack{o\\aaa\\a}}e^{-\frac{3\Delta\epsilon_{des,a}+\Delta\epsilon_{des,o}}{k_BT}} + 3\theta_{\substack{o\\aao\\a}}e^{-\frac{2\Delta\epsilon_{des,a}+2\Delta\epsilon_{des,o}}{k_BT}}\right.$$

$$\left. + 3\theta_{\substack{o\\aao\\o}}e^{-\frac{\Delta\epsilon_{des,a}+3\Delta\epsilon_{des,o}}{k_BT}} + \theta_{\substack{o\\oao\\o}}e^{-\frac{4\Delta\epsilon_{des,o}}{k_BT}}\right] \qquad \textbf{[D.2.36]}$$

Each term in Eq. **D.2.36** contains an energetic contribution $e^{-\frac{\Delta\epsilon_{des,o}}{k_BT}}$ because each configuration is required to have at least one ao pair. Executing the 1st-order truncation scheme and collecting terms gives

$$\frac{d\theta_{oo}}{dt} = 2A_{des}e^{-\frac{E_{des}}{k_BT}}e^{-\frac{\Delta\epsilon_{des,o}}{k_BT}}\theta_{ao}\left[\frac{\theta_{aa}e^{-\frac{\Delta\epsilon_{des,a}}{k_BT}} + \theta_{ao}e^{-\frac{\Delta\epsilon_{des,o}}{k_BT}}}{\theta_a}\right]^3 \qquad \textbf{[D.2.37]}$$

$$= 2A_{des}e^{-\frac{E_{des}}{k_BT}}e^{-\frac{\Delta\epsilon_{des,o}}{k_BT}}\theta_{ao}\Gamma_{des}^3$$

The desorption rate equation for ao pairs is simply the sum of the rate equations for aa and oo pairs multiplied by a factor of – ½ since (i) each annihilation of an aa pair generates an ao or oa pair, (ii) each generation of an oo pair annihilates an ao or oa pair, and (iii) the

ao configuration is heterogeneous and is therefore only counted in half of desorption events, with the other half affecting the oa pair. Enumerating all the relevant configurations gives

$$\frac{d\theta_{ao}}{dt} = A_{des}e^{-\frac{E_{des}}{k_BT}}\left[\left(\theta_{\substack{a\\aaa\\a}}e^{-\frac{4\Delta\epsilon_{des,a}}{k_BT}} + 3\theta_{\substack{o\\aaa\\a}}e^{-\frac{3\Delta\epsilon_{des,a}+\Delta\epsilon_{des,o}}{k_BT}} + 3\theta_{\substack{o\\aao\\a}}e^{-\frac{2\Delta\epsilon_{des,a}+2\Delta\epsilon_{des,o}}{k_BT}} + \theta_{\substack{o\\aao\\o}}e^{-\frac{\Delta\epsilon_{des,a}+3\Delta\epsilon_{des,o}}{k_BT}}\right)\right.$$
$$-\left(\theta_{\substack{o\\aaa\\a}}e^{-\frac{3\Delta\epsilon_{des,a}+\Delta\epsilon_{des,o}}{k_BT}} + 3\theta_{\substack{o\\aao\\a}}e^{-\frac{2\Delta\epsilon_{des,a}+2\Delta\epsilon_{des,o}}{k_BT}}\right.$$
$$\left.\left. + 3\theta_{\substack{o\\aao\\o}}e^{-\frac{\Delta\epsilon_{des,a}+3\Delta\epsilon_{des,o}}{k_BT}} + \theta_{\substack{o\\oao\\o}}e^{-\frac{4\Delta\epsilon_{des,o}}{k_BT}}\right)\right] \quad \textbf{[D.2.38]}$$

Executing the 1st-order truncation procedure and collecting terms gives

$$\frac{d\theta_{ao}}{dt} = A_{des}e^{-\frac{E_{des}}{k_BT}}\Gamma_{des}^3\left(e^{-\frac{\Delta\epsilon_{des,a}}{k_BT}}\theta_{aa} - e^{-\frac{\Delta\epsilon_{des,o}}{k_BT}}\theta_{ao}\right) \quad \textbf{[D.2.39]}$$

We demonstrate the two-site rate equations conform to component rate balance by sum of $d\theta_{aa}/dt$ and $d\theta_{ao}/dt$

$$\frac{d\theta_{aa}}{dt} + \frac{d\theta_{ao}}{dt} = A_{des}e^{-\frac{E_{des}}{k_BT}}\Gamma_{des}^3\left(-2e^{-\frac{\Delta\epsilon_{des,a}}{k_BT}}\theta_{aa} + e^{-\frac{\Delta\epsilon_{des,a}}{k_BT}}\theta_{aa} - e^{-\frac{\Delta\epsilon_{des,o}}{k_BT}}\theta_{ao}\right)$$
$$= -A_{des}e^{-\frac{E_{des}}{k_BT}}\Gamma_{des}^3\left(e^{-\frac{\Delta\epsilon_{des,a}}{k_BT}}\theta_{aa} + e^{-\frac{\Delta\epsilon_{des,o}}{k_BT}}\theta_{ao}\right)$$
$$= -A_{des}e^{-\frac{E_{des}}{k_BT}}\Gamma_{des}^3\theta_a\left(\frac{e^{-\frac{\Delta\epsilon_{des,a}}{k_BT}}\theta_{aa} + e^{-\frac{\Delta\epsilon_{des,o}}{k_BT}}\theta_{ao}}{\theta_a}\right) \quad \textbf{[D.2.40]}$$

$$= -A_{des} e^{-\frac{E_{des}}{k_B T}} \Gamma_{des}^4 \theta_a = \frac{d\theta_a}{dt}$$

which agrees with the rate equation for *a* species provided in Eq. **D.2.8**.

D.2.2.3 Two-site surface reaction rate equations

Two-site rate equations for *aa*, *ao*, and *oo* pairs are derived in the following by enumerating the pertinent reactive configurations for each site pair. First, recall the un-truncated form of thermodynamically-ideal surface reaction rate equations

$$\frac{d\theta_{aa}}{dt} = -k_r \left(\theta_{aa} + 2\theta_{aaa} + 4\theta_{aa}^{\ a} \right) \quad \textbf{[D.2.41]}$$

$$\frac{d\theta_{ao}}{dt} = k_r \left(\theta_{aaa} + 2\theta_{aa}^{\ a} - \theta_{aao} - 2\theta_{aa}^{\ o} \right) \quad \textbf{[D.2.42]}$$

$$\frac{d\theta_{oo}}{dt} = k_r \left(\theta_{aa} + 2\theta_{aao} + 4\theta_{aa}^{\ o} \right) \quad \textbf{[D.2.43]}$$

Site pairs *aa* and *oo* are respectively annihilated and created in each surface reaction event, giving rise to the θ_{aa} term in the rate equations for *aa* and *oo*. This term is identical to that in single-site rate equations and allows for any distribution of site occupants neighboring the reactive *aa* pair. All other coverage terms in Eqs. **D.2.41**-**D.2.43** describe populations of three-site configurations and capture the nearest-neighbor occupancy requirements for creation or annihilation of the considered ensemble. For example, the last two terms in the rate equation $d\theta_{aa}/dt$ are only concerned with reactive configurations with at least one *a* species neighboring the reactive center.

We modify Eq. **D.2.41** to capture nearest-neighbor lateral interaction effects by considering all configurations described by each term enclosed in parenthesis

$$\frac{d\theta_{aa}}{dt} = -A_{rxn}e^{-\frac{E_{rxn}}{k_BT}}\left[\theta_{\substack{aa\\aaaa\\aa}}e^{-\frac{6\Delta\epsilon_{rxn,a}}{k_BT}} + 6\theta_{\substack{ao\\aaaa\\aa}}e^{-\frac{5\Delta\epsilon_{rxn,a}+\Delta\epsilon_{rxn,o}}{k_BT}}\right.$$

$$+ 15\theta_{\substack{ao\\aaao\\aa}}e^{-\frac{4\Delta\epsilon_{rxn,a}+2\Delta\epsilon_{rxn,o}}{k_BT}} + 20\theta_{\substack{ao\\aaao\\ao}}e^{-\frac{3\Delta\epsilon_{rxn,a}+3\Delta\epsilon_{rxn,o}}{k_BT}}$$

$$+ 15\theta_{\substack{ao\\aaao\\oo}}e^{-\frac{2\Delta\epsilon_{rxn,a}+4\Delta\epsilon_{rxn,o}}{k_BT}} + 6\theta_{\substack{ao\\oaao\\oo}}e^{-\frac{\Delta\epsilon_{rxn,a}+5\Delta\epsilon_{rxn,o}}{k_BT}}$$

$$+ \theta_{\substack{oo\\oaao\\oo}}e^{-\frac{6\Delta\epsilon_{rxn,o}}{k_BT}}$$

$$+ (2+4)\left(\theta_{\substack{aa\\aaaa\\aa}}e^{-\frac{6\Delta\epsilon_{rxn,a}}{k_BT}} + 5\theta_{\substack{ao\\aaaa\\aa}}e^{-\frac{5\Delta\epsilon_{rxn,a}+\Delta\epsilon_{rxn,o}}{k_BT}}\right.$$

$$+ 10\theta_{\substack{ao\\aaao\\aa}}e^{-\frac{4\Delta\epsilon_{rxn,a}+2\Delta\epsilon_{rxn,o}}{k_BT}} + 10\theta_{\substack{ao\\aaao\\ao}}e^{-\frac{3\Delta\epsilon_{rxn,a}+3\Delta\epsilon_{rxn,o}}{k_BT}}$$

$$\left.\left. + 5\theta_{\substack{ao\\aaao\\oo}}e^{-\frac{2\Delta\epsilon_{rxn,a}+4\Delta\epsilon_{rxn,o}}{k_BT}} + \theta_{\substack{ao\\oaao\\oo}}e^{-\frac{\Delta\epsilon_{rxn,a}+5\Delta\epsilon_{rxn,o}}{k_BT}}\right)\right] \quad \textbf{[D.2.44]}$$

Executing the 1st-order truncation procedure and collecting terms, we have

$$\frac{d\theta_{aa}}{dt} = -A_{rxn}e^{-\frac{E_{rxn}}{k_BT}}\theta_{aa}\left[\Gamma_{rxn}^{6} + 6\frac{\theta_{aa}}{\theta_a}e^{-\frac{\Delta\epsilon_{rxn,a}}{k_BT}}\Gamma_{rxn}^{5}\right] \quad \textbf{[D.2.45]}$$

The rate equation for *oo* pairs is derived similarly to that for *aa* with the final two terms of Eq. **D.2.43** requiring at least one *ao* pair rather than requiring at least one *aa* pair

$$\frac{d\theta_{oo}}{dt} = A_{rxn}e^{-\frac{E_{rxn}}{k_BT}}\left[\theta_{\substack{aa\\aaaa\\aa}}e^{-\frac{6\Delta\epsilon_{rxn,a}}{k_BT}} + 6\theta_{\substack{ao\\aaaa\\aa}}e^{-\frac{5\Delta\epsilon_{rxn,a}+\Delta\epsilon_{rxn,o}}{k_BT}}\right.$$

$$+ 15\theta_{\substack{ao\\aaao\\aa}}e^{-\frac{4\Delta\epsilon_{rxn,a}+2\Delta\epsilon_{rxn,o}}{k_BT}} + 20\theta_{\substack{ao\\aaao\\ao}}e^{-\frac{3\Delta\epsilon_{rxn,a}+3\Delta\epsilon_{rxn,o}}{k_BT}}$$

$$+ 15\theta_{\substack{ao\\aaao\\oo}}e^{-\frac{2\Delta\epsilon_{rxn,a}+4\Delta\epsilon_{rxn,o}}{k_BT}} + 6\theta_{\substack{ao\\oaao\\oo}}e^{-\frac{\Delta\epsilon_{rxn,a}+5\Delta\epsilon_{rxn,o}}{k_BT}}$$

$$+ \theta_{\substack{oo\\oaao\\oo}}e^{-\frac{6\Delta\epsilon_{rxn,o}}{k_BT}}$$

$$+ (2+4)\left(\theta_{\substack{ao\\aaaa\\aa}}e^{-\frac{5\Delta\epsilon_{rxn,a}+\Delta\epsilon_{rxn,o}}{k_BT}}\right.$$

$$+ 5\theta_{\substack{ao\\aaao\\aa}}e^{-\frac{4\Delta\epsilon_{rxn,a}+2\Delta\epsilon_{rxn,o}}{k_BT}} + 10\theta_{\substack{ao\\aaao\\ao}}e^{-\frac{3\Delta\epsilon_{rxn,a}+3\Delta\epsilon_{rxn,o}}{k_BT}}$$

$$+ 10\theta_{\substack{ao\\aaao\\oo}}e^{-\frac{2\Delta\epsilon_{rxn,a}+4\Delta\epsilon_{rxn,o}}{k_BT}} + 5\theta_{\substack{ao\\oaao\\oo}}e^{-\frac{\Delta\epsilon_{rxn,a}+5\Delta\epsilon_{rxn,o}}{k_BT}}$$

$$\left.\left. + \theta_{\substack{oo\\oaao\\oo}}e^{-\frac{6\Delta\epsilon_{rxn,o}}{k_BT}}\right)\right] \qquad \textbf{[D.2.46]}$$

Executing the 1st-order truncation procedure and collecting terms, we have

$$\frac{d\theta_{oo}}{dt} = A_{rxn}e^{-\frac{E_{rxn}}{k_BT}}\theta_{aa}\left[\Gamma_{rxn}^{6} + 6\frac{\theta_{ao}}{\theta_a}e^{-\frac{\Delta\epsilon_{rxn,o}}{k_BT}}\Gamma_{rxn}^{5}\right] \qquad \textbf{[D.2.47]}$$

The surface reaction rate equation for ao pairs is simply the sum of the rate equations for aa and oo pairs multiplied by a factor of – ½ since (i) each annihilation of an aa pair generates an ao or oa pair, (ii) each generation of an oo pair annihilates an ao or oa pair, and (iii) the ao configuration is heterogeneous and is therefore only counted in half of surface reaction events, with the other half affecting the oa pair. Enumerating all the relevant configurations gives

$$\frac{d\theta_{ao}}{dt} = A_{rxn}e^{-\frac{E_{rxn}}{k_BT}}\left[(1+2)\left(\theta_{\substack{aa\\aaaa\\aa}}e^{-\frac{6\Delta\epsilon_{rxn,a}}{k_BT}} + 5\theta_{\substack{ao\\aaaa\\aa}}e^{-\frac{5\Delta\epsilon_{rxn,a}+\Delta\epsilon_{rxn,o}}{k_BT}}\right.\right.$$
$$+ 10\theta_{\substack{ao\\aaao\\aa}}e^{-\frac{4\Delta\epsilon_{rxn,a}+2\Delta\epsilon_{rxn,o}}{k_BT}} + 10\theta_{\substack{ao\\aaao\\ao}}e^{-\frac{3\Delta\epsilon_{rxn,a}+3\Delta\epsilon_{rxn,o}}{k_BT}}$$
$$\left.+ 5\theta_{\substack{ao\\aaao\\oo}}e^{-\frac{2\Delta\epsilon_{rxn,a}+4\Delta\epsilon_{rxn,o}}{k_BT}} + \theta_{\substack{ao\\oaao\\oo}}e^{-\frac{\Delta\epsilon_{rxn,a}+5\Delta\epsilon_{rxn,o}}{k_BT}}\right) - (1$$
$$+ 2)\left(\theta_{\substack{ao\\aaaa\\aa}}e^{-\frac{5\Delta\epsilon_{rxn,a}+\Delta\epsilon_{rxn,o}}{k_BT}} + 5\theta_{\substack{ao\\aaao\\aa}}e^{-\frac{4\Delta\epsilon_{rxn,a}+2\Delta\epsilon_{rxn,o}}{k_BT}}\right.$$
$$+ 10\theta_{\substack{ao\\aaao\\ao}}e^{-\frac{3\Delta\epsilon_{rxn,a}+3\Delta\epsilon_{rxn,o}}{k_BT}} + 10\theta_{\substack{ao\\aaao\\oo}}e^{-\frac{2\Delta\epsilon_{rxn,a}+4\Delta\epsilon_{rxn,o}}{k_BT}}$$
$$\left.\left.+ 5\theta_{\substack{ao\\oaao\\oo}}e^{-\frac{\Delta\epsilon_{rxn,a}+5\Delta\epsilon_{rxn,o}}{k_BT}} + \theta_{\substack{oo\\oaao\\oo}}e^{-\frac{6\Delta\epsilon_{rxn,o}}{k_BT}}\right)\right] \qquad \textbf{[D.2.48]}$$

Executing the 1st-order truncation procedure and collecting terms, we have

$$\frac{d\theta_{ao}}{dt} = A_{rxn}e^{-\frac{E_{rxn}}{k_BT}}\theta_{aa}\left[3\frac{\theta_{aa}}{\theta_a}e^{-\frac{\Delta\epsilon_{rxn,a}}{k_BT}}\Gamma_{rxn}^5 - 3\frac{\theta_{ao}}{\theta_a}e^{-\frac{\Delta\epsilon_{rxn,o}}{k_BT}}\Gamma_{rxn}^5\right] \qquad \textbf{[D.2.49]}$$

We demonstrate the two-site rate equations conform to component rate balance by sum of $d\theta_{aa}/dt$ and $d\theta_{ao}/dt$

$$\frac{d\theta_{aa}}{dt} + \frac{d\theta_{ao}}{dt} = A_{rxn}e^{-\frac{E_{rxn}}{k_BT}}\theta_{aa}\left(-\Gamma_{rxn}^6 - 6\frac{\theta_{aa}}{\theta_a}e^{-\frac{\Delta\epsilon_{rxn,a}}{k_BT}}\Gamma_{rxn}^5\right.$$
$$\left.+ 3\frac{\theta_{aa}}{\theta_a}e^{-\frac{\Delta\epsilon_{rxn,a}}{k_BT}}\Gamma_{rxn}^5 - 3\frac{\theta_{ao}}{\theta_a}e^{-\frac{\Delta\epsilon_{rxn,o}}{k_BT}}\Gamma_{rxn}^5\right)$$
$$= A_{rxn}e^{-\frac{E_{rxn}}{k_BT}}\theta_{aa}\left(-\Gamma_{rxn}^6 - 3\frac{\theta_{aa}}{\theta_a}e^{-\frac{\Delta\epsilon_{rxn,a}}{k_BT}}\Gamma_{rxn}^5 - 3\frac{\theta_{ao}}{\theta_a}e^{-\frac{\Delta\epsilon_{rxn,o}}{k_BT}}\Gamma_{rxn}^5\right)$$
$$= A_{rxn}e^{-\frac{E_{rxn}}{k_BT}}\theta_{aa}\left(-\Gamma_{rxn}^6 - 3\Gamma_{rxn}^5\left(\frac{\theta_{aa}}{\theta_a}e^{-\frac{\Delta\epsilon_{rxn,a}}{k_BT}} + \frac{\theta_{ao}}{\theta_a}e^{-\frac{\Delta\epsilon_{rxn,o}}{k_BT}}\right)\right) \qquad \textbf{[D.2.50]}$$

$$= -4A_{rxn}e^{-\frac{E_{rxn}}{k_BT}}\Gamma_{rxn}^{6}\theta_{aa} = \frac{d\theta_a}{dt}$$

which agrees with the rate equation for *a* species provided in Eq. **D.2.20**.

D.2.2.4 Two-site surface diffusion rate equations

Two-site rate equations for *aa*, *ao*, and *oo* pairs are presented in the following by considering all pertinent diffusive configurations for each site pair. First, recall the un-truncated form of thermodynamically-ideal surface diffusion rate equations

$$\frac{d\theta_{aa}}{dt} = k_{diff}\left(2\theta_{\mathbf{a}oa} + 4\theta_{\substack{a\\ \mathbf{a}o}} - 2\theta_{a\mathbf{a}o} - 4\theta_{\substack{a\\ \mathbf{a}o}}\right) \qquad \textbf{[D.2.51]}$$

$$\frac{d\theta_{ao}}{dt} = k_r\left(\theta_{\mathbf{a}oo} + 2\theta_{\substack{o\\ \mathbf{a}o}} + \theta_{a\mathbf{a}o} + 2\theta_{\substack{a\\ \mathbf{a}o}} - \theta_{\mathbf{a}oa} - 2\theta_{\substack{a\\ \mathbf{a}o}} - \theta_{o\mathbf{a}o} - 2\theta_{\substack{o\\ \mathbf{a}o}}\right) \qquad \textbf{[D.2.52]}$$

$$\frac{d\theta_{oo}}{dt} = k_r\left(2\theta_{o\mathbf{a}o} + 4\theta_{\substack{o\\ \mathbf{a}o}} - 2\theta_{\mathbf{a}oo} - 4\theta_{\substack{o\\ \mathbf{a}o}}\right) \qquad \textbf{[D.2.53]}$$

where the diffusive *a* species is highlighted in red and diffuses to the right in each configuration.

We modify these rate equations by incorporation of lateral interactions dependent on the occupancy of sites neighboring the diffusing *a* species and the vacant site to which the *a* species diffuses.

Each nearest neighbor *j* to the diffusing *a* species carries an energetic contribution

$$\Delta\epsilon_{diff,a+j} = \epsilon_{d^{\ddagger}j} - \epsilon_{aj} \qquad \textbf{[D.2.54]}$$

and each nearest neighbor *j* to the vacant site accepting the diffusing *a* species carries an energetic contribution

$$\Delta\epsilon_{diff,o+j} = \epsilon_{d^{\ddagger}j} - \epsilon_{oj} \qquad \textbf{[D.2.55]}$$

where $d^{\ddagger}$ indicates a site occupied by the diffusion transition state. Note that $\Delta\epsilon_{diff,o+a} \neq \Delta\epsilon_{diff,a+o}$; *the subscript before the + sign indicates whether the pairwise interaction*

is with the diffusion-donating a species or diffusion-accepting o species. We consider $\varepsilon_{d^{\ddagger}_j}$ identical for nearest-neighbor lateral interactions with the diffusion-donating or diffusion-accepting site. Each surface diffusion event also inherently carries a contribution

$$\epsilon_{diff} = \epsilon_{d^{\ddagger}d^{\ddagger}} - \epsilon_{ao} \qquad \textbf{[D.2.56]}$$

which we consider accounted for by E_{diff} *since this energy contribution is intrinsic to the elementary step activation energy barrier.*

The heterogeneity of the diffusive ao configuration significantly increases the number of relevant configurations for each ensemble-specific rate equation. The site occupants neighboring the diffusion-accepting and diffusion-donating site carry distinct energetic contributions because the diffusion-accepting and diffusion-donating sites are distinctly occupied. For example, enumerating all relevant diffusive configurations for the aa ensemble gives

$$\frac{d\theta_{aa}}{dt} = 6A_{diff}e^{-\frac{E_{diff}}{k_BT}}\left[\left(\theta_{\substack{aa\\aaoa\\aa}}e^{-\frac{3\Delta\epsilon_{diff,o+a}+3\Delta\epsilon_{diff,a+a}}{k_BT}}\right.\right.$$

$$+3\theta_{\substack{oa\\aaoa\\aa}}e^{-\frac{3\Delta\epsilon_{diff,o+a}+2\Delta\epsilon_{diff,a+a}+\Delta\epsilon_{diff,a+o}}{k_BT}}$$

$$+\theta_{\substack{oa\\aaoa\\oa}}e^{-\frac{3\Delta\epsilon_{diff,o+a}+\Delta\epsilon_{diff,a+a}+2\Delta\epsilon_{diff,a+o}}{k_BT}}$$

$$\left.+\theta_{\substack{oa\\oaoa\\oa}}e^{-\frac{3\Delta\epsilon_{diff,o+a}+3\Delta\epsilon_{diff,a+o}}{k_BT}}\right)$$

$$+\left(\theta_{\substack{ao\\aaoa\\aa}}e^{-\frac{2\Delta\epsilon_{diff,o+a}+\Delta\epsilon_{diff,o+o}+3\Delta\epsilon_{diff,a+a}}{k_BT}}\right.$$

$$+3\theta_{\substack{oo\\aaoa\\aa}}e^{-\frac{2\Delta\epsilon_{diff,o+a}+\Delta\epsilon_{diff,o+o}+2\Delta\epsilon_{diff,a+a}+\Delta\epsilon_{diff,a+o}}{k_BT}}$$

$$+\theta_{\substack{oo\\aaoa\\oa}}e^{-\frac{2\Delta\epsilon_{diff,o+a}+\Delta\epsilon_{diff,o+o}+\Delta\epsilon_{diff,a+a}+2\Delta\epsilon_{diff,a+o}}{k_BT}}$$

$$\left.\left.+\theta_{\substack{oo\\oaoa\\oa}}e^{-\frac{2\Delta\epsilon_{diff,o+a}+\Delta\epsilon_{diff,o+o}+3\Delta\epsilon_{diff,a+o}}{k_BT}}\right)+\cdots\right] \qquad \textbf{[D.2.57]}$$

which we regard unremunerative to show in full (Eq. **D.2.57** only lists ¼ of all relevant diffusive configurations). Suffice to say, the diffusive events which generate *aa* pairs are of the form ***a****oa* → *o****a****a* and the events which annihilate *aa* pairs are the microscopic reverse events of the form *o****a****a* → ***a****oa*. The diffusive configurations capable of creating *aa* pairs contain lateral interaction contributions from (i) the three nearest neighbors to the diffusing *a* species, and (ii) the three nearest neighbors to the diffusion-accepting *o* species – one of which must be *a*-occupied. The diffusive configurations capable of annihilating *aa* pairs contain lateral interaction contributions from (i) the three nearest neighbors to the

diffusion-accepting *o* species, and (ii) the three nearest neighbors to the diffusing *a* species – one of which must be *a*-occupied. The diffusion rate equation for *aa* pairs is thusly

$$\frac{d\theta_{aa}}{dt} = 6A_{diff}e^{-\frac{E_{diff}}{k_BT}}\theta_{ao}\left[\frac{\theta_{ao}}{\theta_o}e^{-\frac{\Delta\epsilon_{diff,o+a}}{k_BT}}\Gamma^2_{diff,o}\Gamma^3_{diff,a} - \frac{\theta_{aa}}{\theta_a}e^{-\frac{\Delta\epsilon_{diff,a+a}}{k_BT}}\Gamma^3_{diff,o}\Gamma^2_{diff,a}\right] \quad \textbf{[D.2.58]}$$

where

$$\Gamma_{diff,o} = \frac{\theta_{ao}e^{-\frac{\Delta\epsilon_{diff,o+a}}{k_BT}} + \theta_{oo}e^{-\frac{\Delta\epsilon_{diff,o+o}}{k_BT}}}{\theta_o} \quad \textbf{[D.2.59]}$$

$$\Gamma_{diff,a} = \frac{\theta_{aa}e^{-\frac{\Delta\epsilon_{diff,a+a}}{k_BT}} + \theta_{ao}e^{-\frac{\Delta\epsilon_{diff,a+o}}{k_BT}}}{\theta_a} \quad \textbf{[D.2.60]}$$

account for nearest neighbor lateral interactions with the diffusion-accepting and diffusion-donating site, respectively. The first bracketed term in Eq. **D.2.58** represents the diffusive events which generate *aa* pairs and contains (i) θ_{ao}/θ_o to account for the necessity of an *a* species neighboring the diffusion-accepting site, (ii) $e^{-\frac{\Delta\epsilon_{\mathrm{diff,o+a}}}{k_BT}}$ *to account for the interaction energy of the necessary ao pair, (iii)* $\Gamma^2_{\mathrm{diff,o}}$ *to account for the interaction of the diffusion-accepting site with the other two neighboring sites which may have any occupancy, and (iv)* $\Gamma^3_{\mathrm{diff,a}}$ *to account for the interaction of the diffusing a species with the three neighboring sites which may have any occupancy. The second bracketed term in* Eq. **D.2.58** represents the diffusive events which annihilate *aa* pairs and contains (i) θ_{aa}/θ_a to account for the necessity of an *a* species neighboring the diffusion-donating site, (ii) $e^{-\frac{\Delta\epsilon_{\mathrm{diff},a+\mathrm{a}}}{k_BT}}$ *to account for the interaction energy of the necessary aa pair, (iii)* $\Gamma^2_{\mathrm{diff,a}}$ *to account for the interaction of the diffusion-donating site with the*

other two neighboring sites which may have any occupancy, and (iv) $\Gamma^3_{\mathrm{diff,o}}$ *to account for the interaction of the diffusion-accepting site with the three neighboring sites which may have any occupancy.*

The diffusion rate equations for oo and ao pairs are similarly derived and are

$$\frac{d\theta_{oo}}{dt} = 6A_{diff}e^{-\frac{E_{diff}}{k_BT}}\theta_{ao}\left[\frac{\theta_{ao}}{\theta_a}e^{-\frac{\Delta\epsilon_{diff,a+o}}{k_BT}}\Gamma^3_{diff,o}\Gamma^2_{diff,a} - \frac{\theta_{oo}}{\theta_o}e^{-\frac{\Delta\epsilon_{diff,o+o}}{k_BT}}\Gamma^2_{diff,o}\Gamma^3_{diff,a}\right] \quad \textbf{[D.2.61]}$$

and

$$\frac{d\theta_{ao}}{dt} = 3A_{diff}e^{-\frac{E_{diff}}{k_BT}}\theta_{ao}\left[\frac{\theta_{oo}}{\theta_o}e^{-\frac{\Delta\epsilon_{diff,o+o}}{k_BT}}\Gamma^2_{diff,o}\Gamma^3_{diff,a} + \frac{\theta_{aa}}{\theta_a}e^{-\frac{\Delta\epsilon_{diff,a+a}}{k_BT}}\Gamma^3_{diff,o}\Gamma^2_{diff,a} - \frac{\theta_{ao}}{\theta_a}e^{-\frac{\Delta\epsilon_{diff,a+o}}{k_BT}}\Gamma^3_{diff,o}\Gamma^2_{diff,a} - \frac{\theta_{ao}}{\theta_o}e^{-\frac{\Delta\epsilon_{diff,o+a}}{k_BT}}\Gamma^2_{diff,o}\Gamma^3_{diff,a}\right] \quad \textbf{[D.2.62]}$$

We demonstrate the two-site rate equations conform to component rate balance by sum of $d\theta_{aa}/dt$ and $d\theta_{ao}/dt$

$$\frac{d\theta_{aa}}{dt}+\frac{d\theta_{ao}}{dt}=3A_{diff}e^{-\frac{E_{diff}}{k_BT}}\theta_{ao}\left[\frac{\theta_{oo}}{\theta_o}e^{-\frac{\Delta\epsilon_{diff,o+o}}{k_BT}}\Gamma_{diff,o}^2\Gamma_{diff,a}^3\right.$$

$$-\frac{\theta_{aa}}{\theta_a}e^{-\frac{\Delta\epsilon_{diff,a+a}}{k_BT}}\Gamma_{diff,o}^3\Gamma_{diff,a}^2$$

$$-\frac{\theta_{ao}}{\theta_a}e^{-\frac{\Delta\epsilon_{diff,a+o}}{k_BT}}\Gamma_{diff,o}^3\Gamma_{diff,a}^2$$

$$\left.+\frac{\theta_{ao}}{\theta_o}e^{-\frac{\Delta\epsilon_{diff,o+a}}{k_BT}}\Gamma_{diff,o}^2\Gamma_{diff,a}^3\right]$$

$$=3A_{diff}e^{-\frac{E_{diff}}{k_BT}}\theta_{ao}\left[\Gamma_{diff,o}^2\Gamma_{diff,a}^3\cdot\Gamma_{diff,o}-\Gamma_{diff,o}^3\Gamma_{diff,a}^2\right.$$

$$\left.\cdot\Gamma_{diff,a}\right]=0=\frac{d\theta_a}{dt} \qquad \textbf{[D.2.63]}$$

In the following section, we compare the Langmuir-Hinshelwood, QCA, and 1st-order kinetic descriptions in the case of the $A + A \rightarrow A_2$ reaction system with thermodynamically non-ideal adsorbates.

D.2.3 Case Studies I and II with repulsive adsorbate interactions

Table D.7 summarizes the reaction network of the $A + A \rightarrow A_2$ reaction discussed in Case Studies I and II and lists the values of rate constants we consider in this section. Desorption and surface reaction rate constants take the same values as in Case Studies I-II, and adsorption and diffusion rate constants span similar range as in Case Studies I-II. We incorporate thermodynamic non-idealities by accounting for adsorbate-adsorbate interaction between nearest-neighbor *a* surface species which interact with energy ε_{aa}. For the sake of simplicity, we regard transition states and vacant sites as non-interacting – as is commonly assumed (*33–35*). With this approximation, the set of 1st-order rate equations

is greatly simplified; we tabulate 0th- and 1st-order rate equations in Tables D.8 and D.9 respectively

Table D.7: Homogeneous bimolecular catalytic reaction

#	Step	Rate constants
1	$A_{(g)} + o \rightarrow a$	$k_{ads}{}^{*} = 10^{-6} - 10^{6}$
–1	$a \rightarrow A_{(g)} + o$	$k_{des} = 1$
2	$aa \rightarrow oo + A_{2(g)}$	$k_r = 50$
n/a	$ao \rightarrow oa$	$k_{diff} = 0$, 1, or ∞

*k_{ads} is the product of the rate constant of adsorption and the thermodynamic activity (ideally, partial pressure) of $A_{(g)}$.

Table D.8: Thermodynamically non-ideal 0th-order rate equations

Quasi-chemical approximation				
Step	*adsorption*	*desorption*	*reaction*	*diffusion*
Rate	$k_{ads}\theta_o$	$k_{des}\theta_a\Gamma^4$	$k_r\theta_{aa}\Gamma^6$	$k_{diff}\theta_{ao}\Gamma^3$
Ensemble-Specific Stoichiometric Coefficients				
$\boldsymbol{d\theta_a/dt}$	1	– 1	– 4	0
$\boldsymbol{d\theta_o/dt}$	– 1	1	4	0
$\boldsymbol{d\theta_{aa}/dt}$	No explicit rate equations. $\theta_{aa}\theta_{oo}(\theta_{ao})^{-2} = e^{-\epsilon_{aa}/kT}$			
$\boldsymbol{d\theta_{ao}/dt}$				
$\boldsymbol{d\theta_{oo}/dt}$				

Rate equations for each ensemble and each elementary step are constructed by product of the fundamental rate of the step (e.g. $k_{ads}\theta_o$ for $A_{(g)}$ adsorption) and the corresponding ensemble-specific stoichiometric coefficient (e.g. 1 for a for $A_{(g)}$ adsorption). The algebraic constraint for two-site coverages is defined in Eq. **D.2.64**. The interaction parameter Γ is defined in Eq. **D.2.69**.

Table D.9: Thermodynamically non-ideal 1st-order rate equations

1st-order formalism				
Step	*ads.*	*desorption*	*reaction*	*diffusion*
Rate	$k_{ads}\theta_o$	$k_{des}\theta_a\Gamma^4$	$k_r\theta_{aa}\Gamma^6$	$k_{diff}\theta_{ao}\Gamma^3$
Ensemble-Specific Stoichiometric Coefficients				
$\boldsymbol{\frac{d\theta_a}{dt}}$	1	– 1	– 4	0

$\frac{d\theta_o}{dt}$	-1	1	4	0
$\frac{d\theta_{aa}}{dt}$	$\frac{2\theta_{ao}}{\theta_o}$	$-\frac{2\theta_{aa}}{\theta_a}\cdot\frac{e^{\frac{\epsilon_{aa}}{kT}}}{\Gamma}$	$-1-\frac{6\theta_{aa}}{\theta_a}\cdot\frac{e^{\frac{\epsilon_{aa}}{kT}}}{\Gamma}$	$6\left(\frac{\theta_{ao}}{\theta_o}-\frac{\theta_{aa}}{\theta_a}\cdot\frac{e^{\frac{\epsilon_{aa}}{kT}}}{\Gamma}\right)$
$\frac{d\theta_{ao}}{dt}$	$\frac{\theta_{oo}-\theta_{ao}}{\theta_o}$	$\frac{\theta_{aa}e^{\frac{\epsilon_{aa}}{kT}}-\theta_{ao}}{\theta_a}\cdot\frac{1}{\Gamma}$	$3\frac{\theta_{aa}e^{\frac{\epsilon_{aa}}{kT}}-\theta_{ao}}{\theta_a}\cdot\frac{1}{\Gamma}$	$\frac{3\left(\theta_{aa}e^{\frac{\epsilon_{aa}}{kT}}-\theta_{ao}\right)}{\theta_a}\cdot\frac{1}{\Gamma}+\frac{3(\theta_{oo}-\theta_{ao})}{\theta_o}$
$\frac{d\theta_{oo}}{dt}$	$-\frac{2\theta_{oo}}{\theta_o}$	$\frac{2\theta_{ao}}{\theta_a}\cdot\frac{1}{\Gamma}$	$1+\frac{6\theta_{ao}}{\theta_a}\cdot\frac{1}{\Gamma}$	$6\left(\frac{\theta_{ao}}{\theta_a}\cdot\frac{1}{\Gamma}-\frac{\theta_{oo}}{\theta_o}\right)$

Rate equations for each ensemble and each elementary step are constructed by product of the fundamental rate of the step (e.g. $k_{ads}\theta_o$ for $A_{(g)}$ adsorption) and the corresponding ensemble-specific stoichiometric coefficient (e.g. $2\theta_{ao}/\theta_o$ for *aa* for $A_{(g)}$ adsorption). The interaction parameter Γ is defined in Eq. **D.2.69**.

The QCA algebraically constrains the coverage of site pairs in terms of ε_{aa} which is the only non-zero interaction energy if vacant sites and transition states are non-interacting

$$\frac{\theta_{ao}^2}{\theta_{aa}\theta_{oo}} = e^{\epsilon_{aa}/k_BT} \qquad \textbf{[D.2.64]}$$

To evaluate the accuracy of the QCA in cases where surface diffusion is not arbitrarily fast, we define an approach to quasi-chemical equilibrium

$$Z_{QCA} = \frac{e^{\frac{\epsilon_{aa}}{k_BT}}}{\frac{\theta_{ao}^2}{\theta_{aa}\theta_{oo}}} \qquad \textbf{[D.2.65]}$$

which is unity if the QCA is valid and deviates from unity if adsorbate distribution is not chemically-equilibrated.

In Case Studies I and II, for $k_{ads} < 10^{-3}$, $\mu_{ao} = \mu_{oo} = 1$ due to the very low coverages of *a*. Therefore, as $k_{ads} \to 0$, Eq. **D.2.65** becomes

$$\frac{\theta_a^2}{\theta_{aa}} = e^{\epsilon_{aa}/k_BT} = \frac{1}{\mu_{aa}} \qquad \textbf{[D.2.66]}$$

Recall that, as $k_{ads} \to 0$, $A_{(g)}$ adsorption equilibrates and, if adsorbates are immobile, μ_{aa} asymptotically approaches a value of $(1 + 2k_r/k_{des})^{-1} = 1/26$. Therefore, in order to

compare the kinetic descriptions of the QCA, Langmuir-Hinshelwood, and 1st-order models at conditions of quasi-equilibrated adsorption, we choose $\varepsilon_{aa}/k_BT = ln(1 + 2k_r/k_{des})$ *which, if surface diffusion is arbitrarily fast and* $k_{ads} \rightarrow 0$*, will give* $\mu_{aa} = 1/26$ – the same value of μ_{aa} *calculated by the 1st-order model in the case of immobile adsorbates. Engendering isolation of infinitely-mobile a species (i.e.* $\mu_{aa} = 1/26$*) at low coverage therefore requires strong repulsive a–a interactions.* For example, at 500 K, a value of $e^{\epsilon_{aa}/k_BT} = 26 = \mu_{aa}^{-1}$ requires $\varepsilon_{aa} = 13.5$ kJ mol^{-1}.

Considering transition states and vacant sites to be non-interacting, the 1st-order rate equations for *aa* and *ao* are

$$\frac{d\theta_{aa}}{dt} = 2k_{ads}\theta_{ao} - 2k_{des}\theta_{aa}\Gamma^3 e^{\frac{\epsilon_{aa}}{k_BT}} - k_r\theta_{aa}\Gamma^5\left(\Gamma + 6\frac{\theta_{aa}}{\theta_a}e^{\frac{\epsilon_{aa}}{k_BT}}\right) + 6k_{diff}\theta_{ao}\Gamma^2\left(\frac{\theta_{ao}}{\theta_o}\Gamma - \frac{\theta_{aa}}{\theta_a}e^{\frac{\epsilon_{aa}}{k_BT}}\right) \quad \textbf{[D.2.67]}$$

and

$$\frac{d\theta_{ao}}{dt} = k_{ads}(\theta_{oo} - \theta_{ao}) + k_{des}\Gamma^3\left(\theta_{aa}e^{\frac{\epsilon_{aa}}{k_BT}} - \theta_{ao}\right) + 3k_r\theta_{aa}\Gamma^5\left(3\frac{\theta_{aa}}{\theta_a}e^{\frac{\epsilon_{aa}}{k_BT}} - 3\frac{\theta_{ao}}{\theta_a}\right) + 3k_{diff}\theta_{ao}\Gamma^2\left(\frac{\theta_{aa}}{\theta_a}e^{\frac{\epsilon_{aa}}{k_BT}} + \frac{\theta_{oo}}{\theta_o}\Gamma - \frac{\theta_{ao}}{\theta_o}\Gamma - \frac{\theta_{ao}}{\theta_a}\right) \quad \textbf{[D.2.68]}$$

where

$$\Gamma = \frac{\theta_{aa}e^{\frac{\epsilon_{aa}}{k_BT}} + \theta_{ao}}{\theta_a} \quad \textbf{[D.2.69]}$$

captures the kinetic influence of *a–a* nearest-neighbor energetic interactions. Coverages for the three remaining ensembles (i.e. *a*, *o*, and *oo*) are solved for by site balance (i.e. $\theta_a = \theta_{aa} + \theta_{ao}$, $\theta_o = 1 - \theta_a$, and $\theta_{oo} = \theta_o - \theta_{ao}$).

In the following, we compare the predictions of the (i) Langmuir-Hinshelwood formalism and (ii) quasi-chemical approximation with those of the 1st-order model (iii) with and (iv) without adsorbate interactions in the case that adsorbates are immobile, as in Case Study I. Comparing these four kinetic descriptions illustrates and juxtaposes the kinetic consequences of ensemble site requirements, adsorbate mobility, and adsorbate energetic interactions in the context of the $A + A \rightarrow A_2$ reaction.

Figure D.1 shows rates, coverages, and mean-field metrics calculated for each of the four cases with $k_{des} = 1$ and $k_r = 50$. The 1st-order description of immobile interacting and non-interacting adsorbates agrees, respectively, with the QCA and Langmuir-Hinshelwood descriptions for $k_{ads} > 10$ since θ_a becomes sufficiently large to guarantee statistical or chemical equilibration of adsorbate distribution. The choice of $\varepsilon_{aa}/k_BT = ln(1 + 2k_r/k_{des})$ *for interacting-adsorbate models successfully effects agreement in rate (Fig.* D.2.*1(A)) and* μ_{aa} (Fig. D.2.1(C)) in the low coverage regime. If interacting adsorbates are immobile, however, combinatorial and thermodynamic non-idealities compound – resulting in $\mu_{aa} \sim 0.02$ which is roughly half that predicted by the QCA method. Consequently, $A_{2(g)}$ formation rates calculated by the QCA method are roughly half that calculated by the 1st-order formalism with $k_{diff} = 0$.

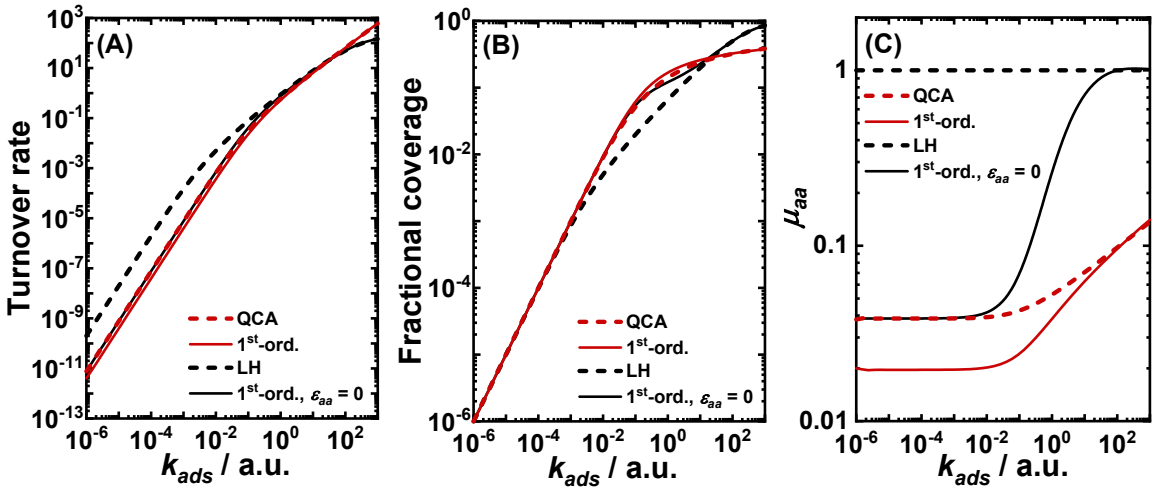

Figure D.1: (A) Turnover rate of $A_{2(g)}$ formation, (B) fractional coverage of a, θ_a, (C) mean-field metric of aa pairs calculated by using the QCA (- - -), 1st-order method with $k_{diff} = 0$, $\varepsilon_{aa}/k_BT = ln(1 + 2k_r/k_{des})$ (—), Langmuir-Hinshelwood formalism (- - -), *and* 1st-order method with $k_{diff} = 0$, $\varepsilon_{aa}/k_BT = 0$ (—). Calculations are of the reaction network in Table D.7 with rate constants $k_{des} = 1$, $k_r = 50$.

Fractional coverages of a agree for all four cases in the low a coverage regime because equilibration of single-site $A_{(g)}$ adsorption is unaffected by thermodynamic or combinatorial non-idealities. For $k_{ads} > 10^{-3}$, however, the four models predict qualitatively different increasing trends in θ_a. Langmuir-Hinshelwood and 1st-order description of immobile, non-interacting adsorbates give different θ_a in the regime of large $|d\mu_{aa}/dk_{ads}|$, as discussed in Case Study I. For $k_{ads} > 10^{-1}$, interacting adsorbate coverages θ_a and θ_{aa} increase weakly because repulsive interactions preponderant on high-coverage surfaces promote (i) desorption and surface reaction events which eliminate a species and (ii) dissuade formation of energetically-unfavorable aa pairs. The distinct high-coverage behavior of repulsively-interacting adsorbates and the compound effect of thermodynamic and combinatorial non-idealities at low coverages profoundly affect $A_{(g)}$ reaction orders and elementary step rate-control as a function of k_{ads}.

Figure D.2 shows reaction orders and degrees of rate control calculated for each of the four cases with k_{des} = 1 and k_r = 50. The 1st-order model, with and without lateral interactions, and QCA method predict quantitatively similar Ψ_A for $k_{ads} < 10^1$ because, in all three cases, $\mu_{aa} < 1$ demand similar replenishment of *aa* by $A_{(g)}$ adsorption. The coverage of *aa* pairs is over-predicted by the Langmuir-Hinshelwood model and, therefore, reaction order in $A_{(g)}$ is underestimated in the moderate coverage regime.

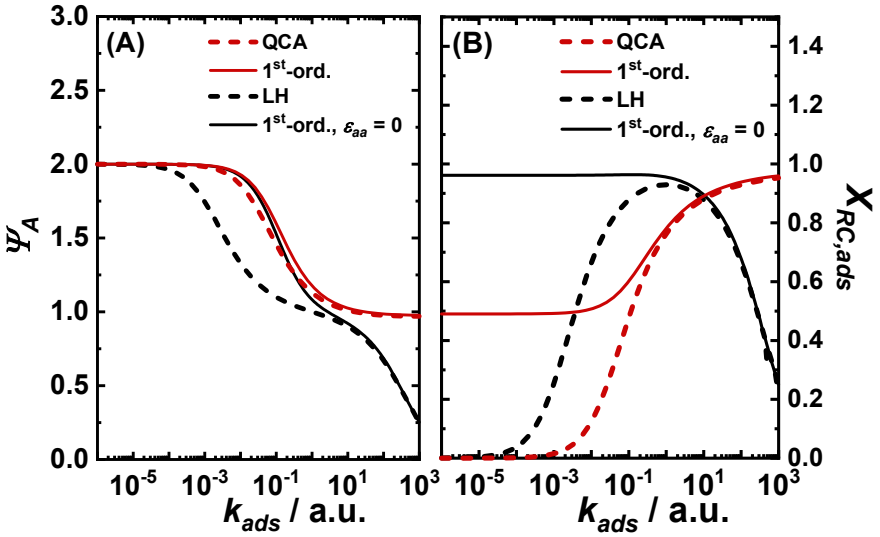

Figure D.2: (A) Reaction order in $A_{(g)}$ and (B) degree of rate control of $A_{(g)}$ adsorption calculated by using the QCA (- - -), 1st-order method with k_{diff} = 0, $\varepsilon_{aa}/k_BT = ln(1 + 2k_r/k_{des})$ (—), *Langmuir-Hinshelwood formalism* (- - -), *and* 1st-order method with k_{diff} = 0, $\varepsilon_{aa}/k_BT = 0$ (—). Calculations are of the reaction network in Table D.7 with rate constants k_{des} = 1, k_r = 50.

Unlike $A_{(g)}$ reaction orders, $X_{RC,ads}$ is profoundly affected by the magnitude of surface diffusion both with and without adsorbate interactions. As discussed in Case Study I, the Langmuir-Hinshelwood and 1st-order models identify antithetical rate-determining steps in the low-coverage regime because the Hinshelwood assumption is ignorant to the isolation of *a* species. Similarly, the QCA incorrectly identifies the surface reaction step to be rate-determining at low coverage (i.e. $X_{RC,r} = 1 - X_{RC,ads} = 1$). In actuality, as the 1st-order model identifies, $X_{RC,r} \sim X_{RC,ads} = ½$ because the dearth of *aa* pairs responsible for rate-

determination of $A_{(g)}$ adsorption in the immobile, non-interacting case is partially assuaged by repulsive *a*–*a* interactions which lower desorption energy barriers and therefore increase the ensemble-specific reversibility $z_{ads,[aa]}$ to shift rate control to surface reaction.

Degree of rate control, however, appear to be the only kinetic descriptor which is significantly affected by immobility of interacting adsorbates. In the following example, we demonstrate that the ostensible insignificance of adsorbate immobility for rate, reaction order, and clustering/isolation behavior is not general and manifests in this particular example because both combinatorial non-idealities and thermodynamic non-idealities bias isolation of *a* adatoms.

D.2.4 Case Studies I and II with attractive adsorbate interactions

We now compare the QCA and 1st-order descriptions of the $A + A \rightarrow A_2$ reaction in the case of *attractive* adsorbate interactions – quantified by $\varepsilon_{aa}/k_BT = -2 < 0$. In order to quantify the effect of surface diffusion rates, we calculate kinetic descriptors using the 1st-order method with $k_{diff} = 0$ and $k_{diff} = k_{des} = 1$ – the condition for which surface diffusion was most kinetically-relevant in Case Study II. Desorption and surface reaction rate constants are the same as in all previous examples.

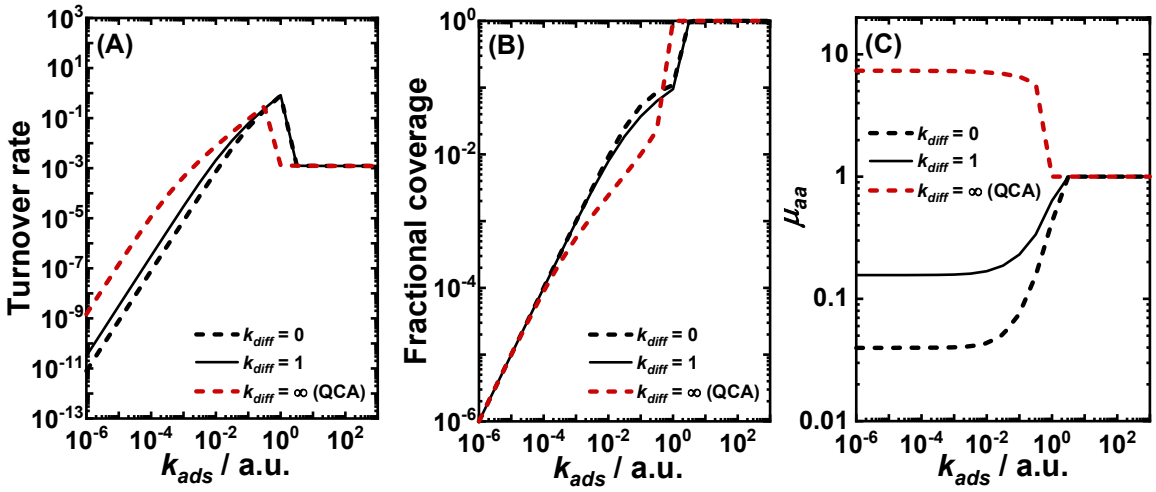

Figure D.3: (A) Turnover rate of $A_{2(g)}$ formation, (B) fractional coverage of a, θ_a, (C) mean-field metric of aa pairs calculated by using the 1st-order method with $k_{diff} = 0$ (- - -) *and* $k_{diff} = 1$ (—) *and the QCA method* (- - -). Calculations are of the reaction network in Table D.7 with rate constants $k_{des} = 1$, $k_r = 50$ and with $\varepsilon_{aa}/k_BT = -2$.

Figure D.3 illustrates the distinct kinetic behavior of immobile ($k_{diff} = 0$), moderately mobile ($k_{diff} = 1$), and infinitely-mobile ($k_{diff} = \infty$) a species with attractive adsorbate interactions. Attractive interactions between nearest-neighbor a–a pairs (i) promotes clustering of a species at all coverages and (ii) induces a kinetic phase transition (KPT) from $\theta_a << 1$ to $\theta_a = 1$ at critical value of $k_{ads} \sim 1$. The propensity of attractive adsorbate interactions to engender islanding of a species results in $\mu_{aa} = e^{-\epsilon_{aa}/k_BT} = e^2 > 1$ for $k_{ads} < 10^{-3}$ if adsorbates are infinitely-mobile (see - - - in Fig. D.3(C)). If a species are immobile ($k_{diff} = 0$) or moderately mobile ($k_{diff} = k_{des} = 1$), combinatorial non-idealities conferred by ensemble site requirements of surface reaction supersede thermodynamic non-idealities and effect isolation of a species ($\mu_{aa} < 1$). Therefore, the isolation of a pairs at low coverages illustrated in Figs. D.1-D.2 and in Case Studies I and II can manifest *even with strong attractive adsorbate interactions*. Surprisingly, combinatorial non-idealities dominate even with ostensibly moderately-fast diffusion rates – as demonstrated by $\mu_{aa} < 1$ in the low a coverage regime for $k_{diff} = k_{des} = 1$. The converse combinatorial non-ideal

effects in the 1st-order and QCA models results in rates and coverages which differ by orders of magnitude (Fig. D.3(A-B) and in disparate reaction orders and degrees of rate control – as shown in Fig. D.4.

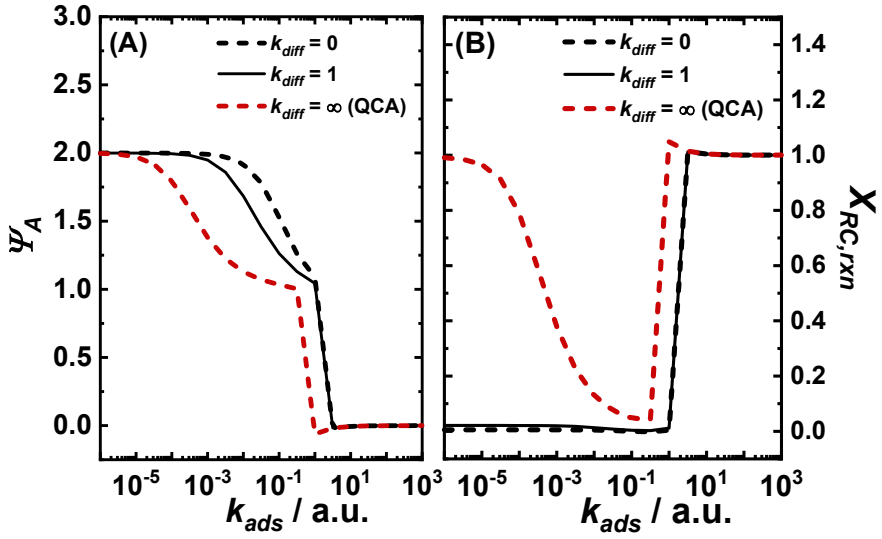

Figure D.4: (A) Reaction order in $A_{(g)}$ and (B) degree of rate control of surface reaction calculated by using the 1st-order method with $k_{diff} = 0$ (- - -) *and* $k_{diff} = 1$ (—) *and the QCA method* (- - -). Calculations are of the reaction network in Table D.7 with rate constants $k_{des} = 1$, $k_r = 50$ and with $\varepsilon_{aa}/k_BT = -2$.

Figure D.4(A) demonstrates that the magnitude of surface diffusion affects (i) the reaction order in $A_{(g)}$ in the moderate coverage regime by as much as ~0.80 and (ii) the identity of the rate-determining step. The implicit infinite-mobility of adsorbates in the QCA method results in an accumulation, rather than a dearth of *aa* pairs. Consequently, (i) $A_{(g)}$ adsorption bears less of a kinetic burden to generate *aa* pairs which are plentiful on a chemically-equilibrated surface and (ii) surface reaction is rate-determining because self-annihilated *aa* pairs are immediately replenished by diffusion. Even if k_{diff} is similar in magnitude to k_{des}, surface diffusion fails to ally isolated *a* species with enough regularity for attractive interactions to effect adsorbate islanding. Therefore, surface reaction is

kinetically-irrelevant for $k_{diff} < 1$ in the low coverage regime and the QCA and 1st-order formalisms identify distinct rate-determining steps.

The antithetical clustering/isolation of *a* species per the QCA and 1st-order formalisms demonstrate the distinct kinetic influences of combinatorial and thermodynamic non-idealities. Depending on elementary step site requirements and rate constants, combinatorial non-idealities may engender isolation ($\mu_{aa} \sim 0.038$ in Case Studies I and II) or clustering ($\mu_{N^*\text{-}N^*} \sim 10^5$ in Case Study III) of low-coverage species; and, depending on the repulsive or attractive nature of energetic interactions, thermodynamic non-idealities may engender isolation ($\varepsilon_{aa}/k_BT > 0$) or clustering ($\varepsilon_{aa}/k_BT < 0$) of surface species. Ensemble-specific rate equations captured by the 1st-order formalism are especially required in cases wherein combinatorial and thermodynamic non-idealities antithetically bias adsorbate distribution.

D.3 Case Study I: $A + A \rightarrow A_2$ with immobile adsorbates

D.3.1 Rank of the 0th- and 1st-order models

We address briefly the relative number of independent equations and site configurations in the 0th- and 1st-order truncation schemes. In the Langmuir-Hinshelwood model, the overall site balance provides the only constraint on site coverages, reducing the number of independent site configurations by one from the total number of site occupants, N. In addition to the N single-site configurations, the 1st-order model considers T_N two-site configurations, where $T_N = \frac{1}{2}N(N+1)$ is the N^{th} triangle number. The number of site constraints (i.e. linearly-independent equations) is $N+1$ since there is an overall site balance and an additional site balance for all N site occupants. The number of independent site configurations is therefore $T_N + N - (N+1) = T_N - 1$. Since the number of independent rate equations per elementary step is equal to the number of independent site configurations, we see that the number of required differential equations in the Langmuir-Hinshelwood model is $O(N)$ and in the 1st-order model is $O(N^2)$.

The number of independent site requirements is not only of importance for computational cost; the rate equation for each independent site configuration is accompanied by a unique rate constant which, in the 1st-order model, is no longer identical to every other appearance of the rate constant in rate equations for other site configurations. The number of independent site configurations therefore determines the number of independent variants of the same rate constant – each of which has a unique reaction sensitivity.

D.3.2 Closed-form rate expressions with quasi-equilibrated adsorption

$A_{(g)}$ adsorption is equilibrated in both the Langmuir-Hinshelwood and 1st-order models if

$$z_{ads} = \frac{k_{des}\theta_a}{k_{ads}\theta_o} = 1 \qquad \textbf{[D.3.1]}$$

as is true in Case Study I for sufficiently low k_{ads}. Eq. **D.3.1** provides an algebraic constraint on θ_a which, in tandem with overall site balance $1 = \theta_a + \theta_o$, gives

$$\theta_a = \frac{K_{ads}}{1 + K_{ads}} \qquad \textbf{[D.3.2]}$$

where $K_{ads} = k_{ads}/k_{des}$ and k_{ads} is the product of the thermodynamic activity of $A_{(g)}$ and the intrinsic adsorption rate constant. The Hinshelwood assumption also algebraically-fixes site-pair coverages, giving $\theta_{aa} = \theta_a^2$. Therefore, in the Langmuir-Hinshelwood model, the rate of $A_{(g)}$ consumption is

$$r = 2k_r\left(\frac{z}{2}\right)\theta_{aa} = 4k_r\frac{K_{ads}^2}{(1 + K_{ads})^2} \qquad \textbf{[D.3.3]}$$

in the regime of equilibrated adsorption. If the surface is bare, $K_{ads}^2 << 1$ and the rate expression is

$$r = 4k_rK_{ads}^2 \qquad \textbf{[D.3.4]}$$

In the 1st-order treatment, the equilibrium condition $k_{ads}(1 - \theta_a) = k_{des}\theta_a$ still holds, but θ_{aa} is no longer incorrectly taken to be equal to θ_a^2. We can determine θ_{aa} by examining its steady-state sum of rate equations

$$\frac{d\theta_{aa}}{dt} = 0 = 2k_{ads}\theta_{ao} - 2k_{des}\theta_{aa} - k_r\theta_{aa}\left(1 + \frac{6\theta_{aa}}{\theta_a}\right) \qquad \textbf{[D.3.5]}$$

By use of the component site balance for a, we substitute $\theta_{ao} = \theta_a - \theta_{aa}$ in Eq. **D.3.5**

$$0 = 2k_{ads}\theta_a - \theta_{aa}(2k_{ads} + 2k_{des}) - k_r\theta_{aa}\left(1 + \frac{6\theta_{aa}}{\theta_a}\right) \qquad \textbf{[D.3.6]}$$

Collecting terms, we find

$$\theta_{aa} = \frac{2k_{ads}\theta_a}{2k_{ads} + 2k_{des} + k_r\left(1 + \frac{6\theta_{aa}}{\theta_a}\right)} \qquad \textbf{[D.3.7]}$$

Writing in terms of K_{ads} gives

$$\theta_{aa} = \frac{K_{ads}}{1 + K_{ads} + \frac{k_r}{2k_{des}}\left(1 + \frac{6\theta_{aa}}{\theta_a}\right)} \cdot \frac{K_{ads}}{1 + K_{ads}} \qquad \textbf{[D.3.8]}$$

and, thusly,

$$r = 4k_r\theta_{aa} = 4k_r \frac{K_{ads}}{1 + K_{ads} + \frac{k_r}{2k_{des}}\left(1 + \frac{6\theta_{aa}}{\theta_a}\right)} \cdot \frac{K_{ads}}{1 + K_{ads}} \qquad \textbf{[D.3.9]}$$

The largest possible value of θ_{aa}/θ_a is unity; therefore, $k_r << {}^2/_7 k_{des}$ is a rigorous criterion for combinatorial ideality if adsorption is quasi-equilibrated. However, in the case of a bare surface (i.e. $K_{ads} << 1$; $\theta_{aa}/\theta_a << 1/6$) and $k_r >> 2k_{des}$, Eq. **D.3.9** becomes

$$r = 8k_{des}K_{ads}^2 = 8k_{ads}K_{ads} \qquad \textbf{[D.3.10]}$$

Eqs. **D.3.4** and **D.3.10** communicate the disparate kinetic descriptions of the Langmuir-Hinshelwood and 1st-order formalism and the provenance of the antithetical rate-determining steps predicted by each.

D.3.3 Ensemble-specific sensitivity, reversibility, and degree of rate control

In Section D.2, we demonstrate that the sensitivities and degree of rate control of each elementary step i are, in fact, a sum of ensemble-specific $s_{i,[j]}$ and $X_{RC,i,[j]}$ for each *independent* ensemble j. We also purport that the existing relationship between elementary step reversibility and sensitivities, $z_i = -s_{-i}/s_i$ is incorrect in the 1st-order model which correctly identifies the distinct reversibilities and sensitivities of each ensemble specific path. Instead, we propose, in Eq. **D.1.11**, that each *ensemble-specific* elementary step reversibility is related to the corresponding sensitivities by $z_{i,[j]} = -s_{-i,[j]}/s_{i,[j]}$. In this

subsection, we demonstrate the veracity of Eq. **D.1.9- D.1.11** and the ostensible violation of Eq. **D.1.5** in the context of the $A + A \rightarrow A_2$ reaction.

Figure D.5 shows ensemble-specific and overall sensitivities and reversibilities for $A_{(g)}$ adsorption calculated by the 1st-order and kMC methods. Figs. D.5(A) and D.5(B) demonstrate that the ratio of ensemble-specific sensitivities does indeed equal $-z_{i,[j]}$, thereby evincing the veracity of Eq. **D.1.11**. Figure D.5(C) demonstrates that the sum of ensemble-specific sensitivities does indeed equal the overall sensitivity – in agreement with the derivation of $s_{i,[j]}$ in Eq. **D.1.9**. Ensemble-specific rate constants are not definable in the kMC method; therefore, ensemble-specific sensitivities and degrees of rate control cannot be calculated – obscuring profound physical insight regarding the kinetic-significance of each ensemble identifiable in the 1st-order formalism.

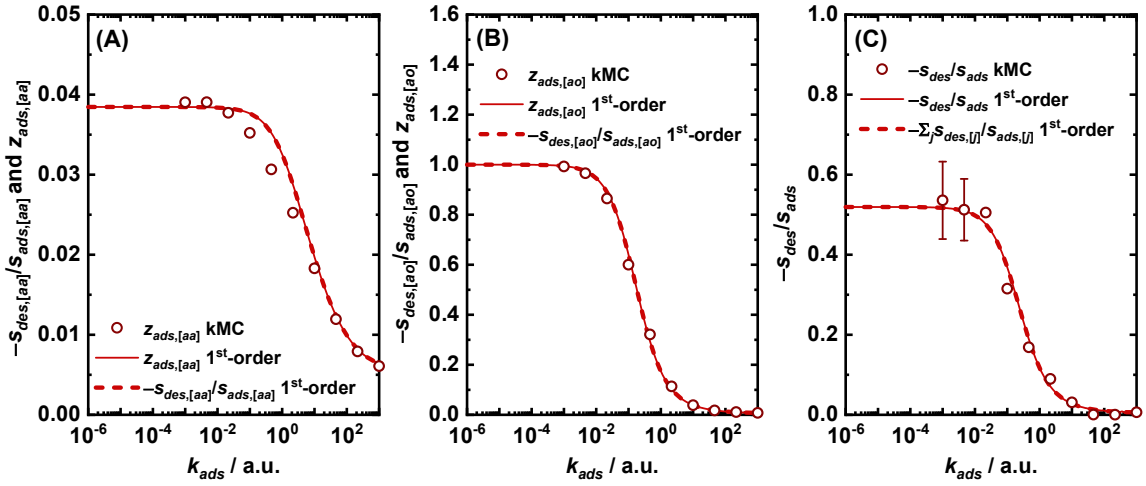

Figure D.5: (A) 1st-order-calculated $A_{(g)}$ adsorption sensitivity ratio (- - -) and 1st-order- and kMC-calculated $A_{(g)}$ adsorption reversibility (—, o) for *aa* site configuration. (B) 1st-order-calculated $A_{(g)}$ adsorption sensitivity ratio (- - -) and 1st-order- and kMC-calculated $A_{(g)}$ adsorption reversibility (—, o) for *ao* site configuration. (C) 1st-order-calculated ratio of sum of $A_{(g)}$ adsorption reverse and forward sensitivities (- - -) and 1st-order- and kMC-calculated $A_{(g)}$ adsorption total sensitivity ratio (—, o). kMC error bars are the standard error of the mean (SEM) and are only shown if larger than the corresponding symbol. Calculations are of the reaction network in Table 5.3 with rate constants $k_{des} = 1$, $k_r = 50$. Distinct $k_{i,[j]}$ are not definable in kMC simulations and therefore distinct $s_{i,[j]}$ are not calculable.

The sum of directional ensemble-specific sensitivities yields the ensemble-specific degree of rate control of the considered elementary step (i.e. $X_{RC,i,[j]} = s_{i,[j]} + s_{-i,[j]}$, as stated in Eq. **D.1.10**). Figure D.6 shows ensemble-specific degrees of rate control for adsorption and surface reaction for both independent ensembles *aa* and *ao* and confirms that the sum of ensemble-specific degrees of rate control is equal to the overall degree of rate control for each elementary step (i.e. $X_{RC,i} = X_{RC,i,[aa]} + X_{RC,i,[ao]}$).

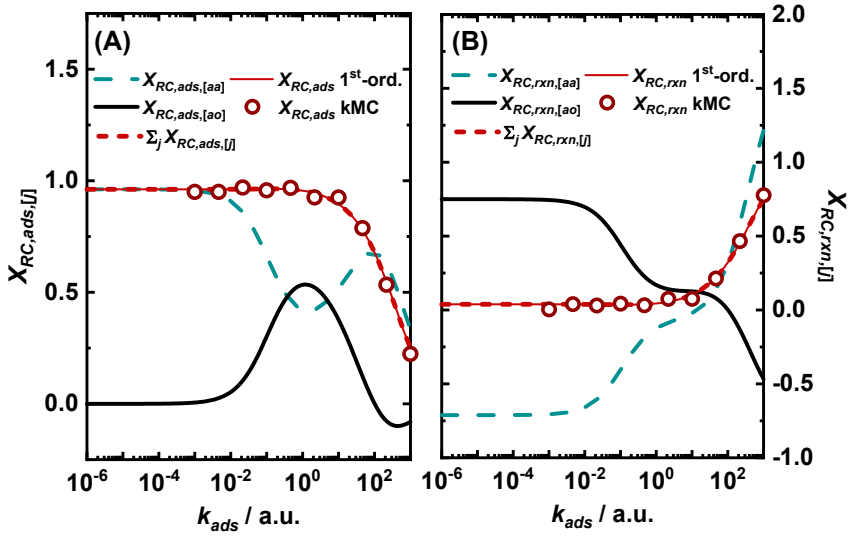

Figure D.6: (A) Ensemble-specific degrees of rate control of $A_{(g)}$ adsorption for *aa* (- -) and *ao* (—) and their sum (- - -) compared to $X_{RC,ads}$ calculated by the kMC (o) and 1st-order (—) methods. (B) Ensemble-specific degrees of rate control of surface reaction for *aa* (- -) and *ao* (—) and their sum (- - -) compared to $X_{RC,rxn}$ calculated by the kMC (o) and 1st-order (—) methods. kMC error bars are the standard error of the mean (SEM) and are only shown if larger than the corresponding symbol. Calculations are of the reaction network in Table 5.3 with rate constants $k_{des} = 1$, $k_r = 50$. Distinct $k_{i,[j]}$ are not definable in kMC simulations and therefore distinct $X_{RC,i,[j]}$ are not calculable.

For $k_{ads} < 10^{-3}$, the rate-determining nature of $A_{(g)}$ adsorption is entirely attributable to the kinetic bottleneck of *aa* pair generation by adsorption (i.e. $X_{RC,ads} = X_{RC,ads,[aa]}$ in Fig. D.6(A)). Interestingly, as k_{ads} increases, the *ao* ensemble contributes a greater fraction of rate-control without appreciable change to $X_{RC,ads}$. We interpret the shift in ensemble-specific $X_{RC,ads,[j]}$ in the range $10^{-2} < k_{ads} < 10^{2}$ as a manifestation of the de-equilibration of

$A_{(g)}$ adsorption which results in $z_{ads,[aa]} \sim z_{ads,[ao]} < 1$ instead of *aa* being the only ensemble which experiences irreversible $A_{(g)}$ adsorption.

Figure D.6(B) confirms $X_{RC,rxn,[aa]} = -X_{RC,rxn,[ao]}$ for $k_{ads} < 10^{-3}$; $X_{RC,rxn,[aa]} < 0$ in this regime because the rapidity of surface reaction is responsible for the dearth of *aa* pairs which limits the formation of $A_{2(g)}$. As rate-control shifts to surface reaction, $X_{RC,rxn,[aa]} \sim X_{RC,rxn}$ because k_{ads} is sufficiently large to replenish *aa* pairs and the kinetically-relevant event is simply the self-annihilation of increasingly preponderant *aa* pairs.

D.4 Case Study II: $A + A \rightarrow A_2$ with adsorbate surface diffusion

From Table 4, the diffusion rate equations for all five ensembles in Case Study II are

$$\frac{d\theta_a}{dt} = 0 \qquad \textbf{[D.4.1]}$$

$$\frac{d\theta_o}{dt} = 0 \qquad \textbf{[D.4.2]}$$

$$\frac{d\theta_{aa}}{dt} = 6k_{diff}\theta_{ao}\left(\frac{\theta_{ao}}{\theta_o} - \frac{\theta_{aa}}{\theta_a}\right) \qquad \textbf{[D.4.3]}$$

$$\frac{d\theta_{oo}}{dt} = 6k_{diff}\theta_{ao}\left(\frac{\theta_{ao}}{\theta_a} - \frac{\theta_{oo}}{\theta_o}\right) \qquad \textbf{[D.4.4]}$$

$$\frac{d\theta_{ao}}{dt} = 3k_{diff}\theta_{ao}\left(\frac{\theta_{oo}}{\theta_o} + \frac{\theta_{aa}}{\theta_a} - \frac{\theta_{ao}}{\theta_o} - \frac{\theta_{ao}}{\theta_a}\right) \qquad \textbf{[D.4.5]}$$

The rate equations for single-site configurations *a* and *o* are zero because surface diffusion cannot change the total coverage of adsorbed species. The non-zero rate equations of multi-site ensembles communicate the propensity of surface diffusion to randomize the surface and bias all mean-field metrics towards unity. Note that, if all $\mu_{ij} = 1$, coverage-dependent stoichiometric coefficients in Eqs. **D.4.3**-**D.4.5** equal zero – indicating the surface has achieved an ergodic state.

In kinetically-relevant regimes of slow or moderately-fast surface diffusion, we are interested in defining a metric which quantifies the approach to randomness, or "statistical equilibrium", for each site ensemble. The definition of ensemble-specific reversibility, or approach to equilibrium, of surface diffusion becomes evident in deriving each of Eqs. **D.4.1-D.4.5** beginning from enumeration of diffusive configurations relevant to each site ensemble.

Let us first consider the microscopic, elementary step events which affect configurations *a* and *o*. Since *a* and *o* are the only site-occupants in this system, both are affected by each diffusion event represented by reversible elementary step

$$ao \rightleftharpoons oa \qquad \textbf{[D.4.6]}$$

which occurs with net rate

$$\begin{aligned} r_{diff} &= \vec{r}_{diff} - \overleftarrow{r}_{diff} \\ &= k_{diff}\theta_{ao} - k_{diff}\theta_{oa} = 0 \end{aligned} \qquad \textbf{[D.4.7]}$$

which is zero, as we expect, because $\theta_{ao} = \theta_{oa}$. From Eq. **D.4.7**, the reversibility of surface diffusion is evidently

$$z_{diff} = \frac{\overleftarrow{r}_{diff}}{\vec{r}_{diff}} = \frac{\theta_{oa}}{\theta_{ao}} = 1 \qquad \textbf{[D.4.8]}$$

indicating surface diffusion is always equilibrated – as expected for an elementary step which, by definition, always occurs with zero net rate. As Eqs. **D.4.3**-**D.4.5** demonstrate, surface diffusion does not always occur with zero net rate with respect to multi-site ensembles; following the same procedure used to derive Eq. **D.4.8**, we now derive ensemble-specific diffusion reversibilities for *aa*, *ao*, and *oo*.

We first consider the microscopic, elementary step diffusion events which affect configuration *aa*. The site pair *aa* can be (i) consumed if the diffusing *a* adatom neighbors another *a* species or (ii) created if the diffusion-accepting vacant site neighbors a non-diffusing *a* adatom. These two directional events are the microscopic reverse of one another, as shown by Eq. **D.4.9** in which the diffusing adatom is highlighted in red.

$$ao\mathit{a} \rightleftharpoons a\mathit{a}o \qquad \textbf{[D.4.9]}$$

All diffusion events which affect *aa* pairs take the form of Eq. **D.4.9**, save for configurational variance. We can now readily derive the net rate and reversibility of

diffusion with respect to *aa* pairs with omission of numeric statistical factors which do not affect reversibility.

$$\begin{aligned} r_{diff,[aa]} &= \vec{r}_{diff,[aa]} - \overleftarrow{r}_{diff,[aa]} \\ &= k_{diff}\theta_{aoa} - k_{diff}\theta_{aao} \\ &= k_{diff}\theta_{ao}\frac{\theta_{ao}}{\theta_o} - k_{diff}\theta_{ao}\frac{\theta_{aa}}{\theta_a} \end{aligned} \qquad \textbf{[D.4.10]}$$

From Eq. **D.4.10**, the reversibility of surface diffusion for *aa* pairs is evidently

$$\begin{aligned} z_{diff,[aa]} &= \frac{\overleftarrow{r}_{diff,[aa]}}{\vec{r}_{diff,[aa]}} = \frac{\frac{\theta_{aa}}{\theta_a}}{\frac{\theta_{ao}}{\theta_o}} \\ &= \frac{\mu_{aa}\theta_a}{\mu_{ao}\theta_a} = \frac{\mu_{aa}}{\mu_{ao}} \end{aligned} \qquad \textbf{[D.4.11]}$$

which explicitly demonstrates that all *a*-relevant mean-field metrics must be unity for surface diffusion to be equilibrated with respect to *aa* pairs. We note that μ_{aa} and μ_{ao} cannot be equal unless both are unity because component site balance constrains $\mu_{aa}\theta_a + \mu_{ao}\theta_o = 1$.

The reversibility of surface diffusion with respect to *ao* and *oo* pairs is derived by an analogous method by which we derive $z_{diff,[aa]}$. The reversible microscopic diffusion step relevant to *oo* pairs is

$$oao \rightleftharpoons ooa \qquad \textbf{[D.4.12]}$$

where, again, the diffusion adatom is highlighted in red. Heterogeneous *ao* pairs are affected by both Eqs. **D.4.9** and **D.4.12**. The choice of direction of Eqs. **D.4.9** and **D.4.12** is, of course, arbitrary; however, we consistently consider the production of homogeneous ensembles as the ensemble-specific forward step so as to bound all reversibilities between

zero and unity – rather than ∞ and unity. From Eqs. **D.4.9** and **D.4.12**, the ensemble-specific diffusion reversibilities of *oo* and *ao* are respectively

$$z_{diff,[oo]} = \frac{\theta_{oo}/\theta_o}{\theta_{ao}/\theta_a} = \frac{\mu_{oo}}{\mu_{ao}} \qquad \textbf{[D.4.13]}$$

$$z_{diff,[ao]} = \frac{\frac{\theta_{oo}}{\theta_o} + \frac{\theta_{aa}}{\theta_a}}{\frac{\theta_{ao}}{\theta_a} + \frac{\theta_{ao}}{\theta_o}} = \frac{\mu_{oo}\theta_o + \mu_{aa}\theta_a}{\mu_{ao}(\theta_o + \theta_a)} = \frac{\mu_{oo}\theta_o + \mu_{aa}\theta_a}{\mu_{ao}} \qquad \textbf{[D.4.14]}$$

which, again, are only rigorously unity if all mean-field metrics are unity; however, if $\theta_o > \theta_a$, the constraint $\mu_{ao}\theta_a + \mu_{oo}\theta_o = 1$ permits both μ_{ao} and μ_{oo} to be very near unity since $\mu_{ao}\theta_a \sim 0$ requires $\mu_{oo} \sim 1$ to satisfy $\mu_{oo}\theta_o \sim 1$.

D.5 Ammonia synthesis on Ru (0001) step sites

We assess the kinetic consequences of combinatorial non-idealities in the industrially-relevant ammonia synthesis reaction using kinetic parameters calculated via density functional theory (DFT) on Ru (0001) step sites, as reported by Logadóttir and Nørskov (*147*). The lattice coordination of (0001) step sites is unclear; we present results calculated on a 2D square lattice, but 1D and hexagonal 2D lattices give similar rates, coverages, reaction orders, and degrees of rate control. In general, lattice coordination is only consequential if adsorbates are interacting – in which case the number of nearest neighbor sites significantly affects reaction energetics. Table D.10 lists the sequence of elementary steps and attendant kinetic parameters for catalytic NH_3 synthesis from N_2 and H_2. Calculation of pre-exponential factors, A, and activation energies, E_A, for -sorption and reaction steps from DFT values (*147*) and transition-state theory (TST) is detailed in the Supporting Information of the recent work of Foley and Bhan (*172*). Activation energies for N^*, H^*, and NH_3^* diffusion are taken from computational (*148*, *149*) and experimental studies (*32*, *145*, *150*). Pre-exponential factors reported in these works (*32*, *145*, *148–150*)

are in the range $10^{12} - 10^{14}$ s^{-1} ; we compute pre-exponential factors of $1.46 \cdot 10^{13}$ s^{-1} for each diffusion step via TST calculations using DFT values from Logadóttir and Nørskov (*147*) and following the work of Foley and Bhan (*172*). We were unable to find calculated or measured values of activation energies for NH^* or NH_2^* diffusion. We therefore estimate the diffusion barriers for NH^* or NH_2^* by linear interpolation of diffusion barriers for N^* and NH_3^* based on the degree of hydrogenation of the diffusing species.

We calculate steady-state coverages and reaction sensitivities of the catalytic sequence in Table D.10 via the Langmuir-Hinshelwood and 1st-order models to determine kinetic significance of combinatorial non-idealities at industrial ammonia synthesis conditions: 200 bar, 20% N_2/60% H_2/20% NH_3, 623 K – 823 K (*231*). 1st-order rate equations are constructed by use of Tables D.1-D.5.

Table D.10: Ammonia synthesis elementary-step reaction sequence on Ru (0001) step sites

	Step	σ	$\vec{A}$ / s^{-1}	$\overleftarrow{A}$ / s^{-1}	$\vec{E}_A$ / eV	$\overleftarrow{E}_A$ / eV
1	$N_{2(g)} + ** \rightleftharpoons 2N^*$	1	$2.39 \cdot 10^4$	$1.46 \cdot 10^{14}$	0.4	1.2
2	$N^* + H^* \rightleftharpoons NH^* + *$	2	$1.46 \cdot 10^{13}$	$1.46 \cdot 10^{13}$	1.1	1.1
3	$NH^* + H^* \rightleftharpoons NH_2^* + *$	2	$1.46 \cdot 10^{13}$	$1.46 \cdot 10^{13}$	1.3	1.46
4	$NH_2^* + H^* \rightleftharpoons NH_3^* + *$	2	$1.46 \cdot 10^{13}$	$1.46 \cdot 10^{13}$	1.2	0.75
5	$NH_3^* \rightleftharpoons * + NH_{3(g)}$	2	$1.46 \cdot 10^{13}$	$2.46 \cdot 10^3$	0.85	0
6	$H_{2(g)} + ** \rightleftharpoons 2H^*$	3	$3.89 \cdot 10^6$	$1.46 \cdot 10^{13}$	0	1.1
7	$N^* + * \rightleftharpoons * + N^*$	n/a	$1.46 \cdot 10^{13}$	$1.46 \cdot 10^{13}$	0.94[a]	0.94[a]
8	$NH^* + * \rightleftharpoons * + NH^*$	n/a	$1.46 \cdot 10^{13}$	$1.46 \cdot 10^{13}$	0.68[d]	0.68[d]
9	$NH_2^* + * \rightleftharpoons * + NH_2^*$	n/a	$1.46 \cdot 10^{13}$	$1.46 \cdot 10^{13}$	0.41[d]	0.41[d]
10	$NH_3^* + * \rightleftharpoons * + NH_3^*$	n/a	$1.46 \cdot 10^{13}$	$1.46 \cdot 10^{13}$	0.15[b]	0.15[b]
11	$H^* + * \rightleftharpoons * + H^*$	n/a	$1.46 \cdot 10^{13}$	$1.46 \cdot 10^{13}$	0.21[c]	0.21[c]

σ is the stoichiometric number, $\vec{A}$ and $\overleftarrow{A}$ are forward and reverse pre-exponential factors, and $\vec{E}_A$ and $\overleftarrow{E}_A$ are forward and reverse activation energies of the corresponding step. [a]Measured by scanning tunnel microscopy on Ru(0001) (*150*) [b]Measured by optical second- harmonic diffraction on Ru(0001) (*32*) [c]Calculated by variational transition state theory with a semiclassical tunneling method (*149*). [d]Activation energy barriers for NH^* and $NH_2{}^*$ diffusion are estimated by linear interpolation of measured N^* and $NH_3{}^*$ activation energies.

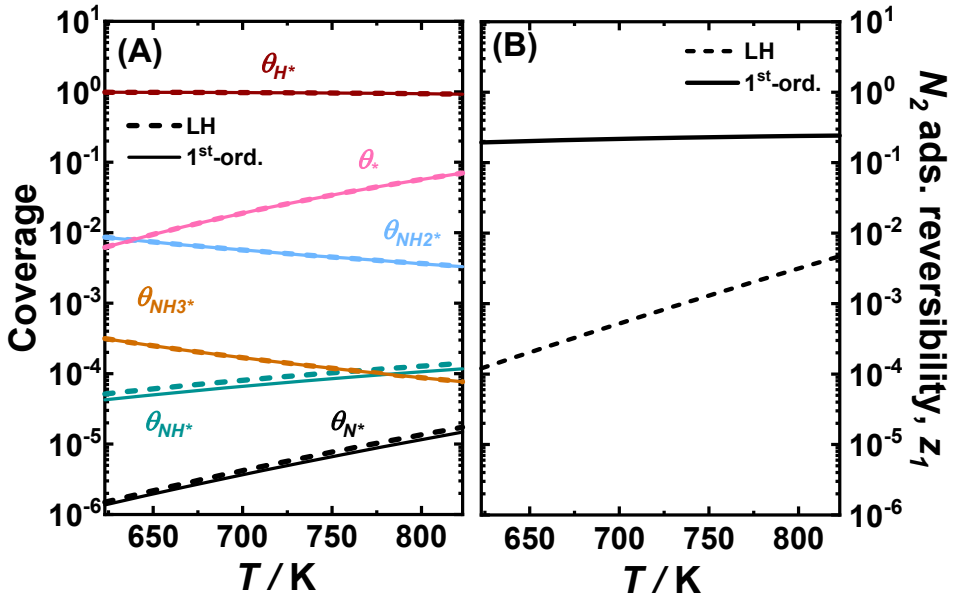

Figure D.7: (A) Fractional coverages θ_{j*} calculated by the Langmuir-Hinshelwood (– –) and 1st-order (—) models. (B) Reversibility of step 1, $N_{2(g)}$ adsorption, calculated by the Langmuir-Hinshelwood (– –) and 1st-order (—) models. Calculations are of the reaction network in Table D.10 at 200 bar total pressure with composition 20% N_2/60% H_2/20% NH_3.

Figure D.7 compares adsorbate coverages and $N_{2(g)}$ adsorption reversibilities calculated by the Langmuir-Hinshelwood and 1st-order models. Both methods predict similar adsorbate coverages (Fig. D.7(A)); however, surface diffusion is insufficiently-fast to randomize the distribution of N^* and NH^* species – resulting in an accumulation of N^*–N^* pairs which enhances the reversibility of $N_{2(g)}$ adsorption by ~2 orders of magnitude (Fig. D.7(B)). Consequently, rate-control shifts to N^* hydrogenation and diffusion which are the only two steps capable of segregating preponderant N^*–N^* pairs. We note that this case study demonstrates that surface diffusion can profoundly affect reaction kinetics even on

highly-covered surfaces so long as at least one low-coverage species is not infinitely-mobile.

E Supporting Information for A generalized Butler-Volmer equation and an equation for Tafel slope applicable at all overpotential

E.1 Derivation of specific results from Eq. 7.32

We demonstrate the utility of a general, microkinetic formulation of transfer coefficient

$$\alpha = \sum_i X_{RC,i} n_i \left(\beta_i + \frac{Z_i}{1 - Z_i} \right) \quad \textbf{[7.32]}$$

by derivation of select case-specific expressions for α directly from Eq. **7.32**.

E.1.1 Proof of Eq. 7.9

Measured Tafel slopes are commonly claimed to reflect the identity of the rate-determining step (rds) based on interpretation per Eq. **7.9**:

$$\alpha = \beta_{rds} n_{rds} + {}^{\gamma}/_{\sigma_{rds}} \quad \textbf{[7.9]}$$

where γ is the number of electrons transferred before the rate-determining step (rds) and β_{rds}, n_{rds}, and σ_{rds} are, respectively, the symmetry factor, number of transferred electrons, and the stoichiometric number of the rds. We contend that Eq. **7.9** is only valid if (i) the rds is irreversible, (ii) all steps preceding the rds are equilibrated, and (iii) the surface is bare. We derive Eq. **7.9** from Eq. **7.32** under these conditions in the following.

We first separate Eq. **7.32** into two terms respectively corresponding to kinetic (β_i) and thermodynamic ($Z_i(1 - Z_i)^{-1}$) contributions to transfer coefficient

$$\alpha = \sum_i X_{RC,i} n_i \beta_i + \sum_i X_{RC,i} n_i \frac{Z_i}{1 - Z_i} \quad \textbf{[E.1]}$$

Since $X_{RC,rds} = 1$ and $X_{RC,i \neq rds} = 0$, the kinetic contribution to α is entirely determined by the rate-determining step

$$\alpha = \beta_{rds} n_{rds} + \sum_i X_{RC,i} n_i \frac{Z_i}{1 - Z_i} \quad \textbf{[E.2]}$$

From Eq. **E.2**, we see that if all non-rate-determining steps were not equilibrated (i.e. if $Z_{i\neq rd} \neq 1$), then the thermodynamic contribution to α would also be entirely determined by the rds. However, if other steps are equilibrated, then $Z_{i\neq rds} = 1$ causes an ostensible pole which must be addressed by recasting the degree of rate control in terms of reaction sensitivity (i.e. by substitution of $X_{RC,i} = s_{+i}(1 - Z_i)$)

$$\alpha = \beta_{rds} n_{rds} + \sum_i s_{+i} n_i Z_i \qquad \textbf{[E.3]}$$

We simplify Eq. **E.3** by recognizing that (i) $Z_{rds} = 0$ since the rate-determining step is irreversible, (ii) $Z_{i<rds} = 1$ because all steps preceding the rds are equilibrated, and (ii) $s_{+i>rd} = 0$ because forward half-steps succeeding the irreversible rds are kinetically-irrelevant. Therefore, Eq. **E.3** becomes

$$\alpha = \beta_{rds} n_{rds} + \sum_{i<rds} s_{+i} n_i \qquad \textbf{[E.4]}$$

demonstrating that the thermodynamic contribution to α is entirely determined by the steps preceding the rate-determining step. This thermodynamic term is re-expressed in exclusive terms of reaction stoichiometry by evoking the condition that the surface is bare — implying that the thermodynamic degree of rate control of all intermediates is zero (i.e. $X_{TRC,m^*} = 0$ for surface intermediates m^* between the first step and the rate-determining step). Dumesic and coworkers (*85*) have proven that the condition $X_{TRC,m^*} = 0$ confers a constraint on forward reaction sensitivities, s_{+i}, in terms of reaction stoichiometry

$$\frac{s_{+i}}{s_{+(i+1)}} = \frac{\sigma_i}{\sigma_{i+1}} \qquad \textbf{[E.5]}$$

which is crucial to recasting $\sum_{i<rds} s_{+i<rd}\ n_i$ (Eq. **E.4**) as γ/σ_{rds} (Eq. **7.9**).

We begin by considering Eq. **E.5** for the case of $i = rds - 1$ (i.e. the step before the rate-determining step) to find

$$\frac{s_{+(rds-1)}}{s_{+rds}} = \frac{\sigma_{rds-1}}{\sigma_{rds}} \qquad \textbf{[E.6]}$$

which is simplified by recognizing $s_{+rds} = X_{RC,rds}(1 - Z_{rds})^{-1} = 1$, giving

$$s_{+(rds-1)} = \frac{\sigma_{rds-1}}{\sigma_{rds}} \qquad \textbf{[E.7]}$$

Now, applying Eq. **E.5** to $i = rds - 2$, we have

$$s_{+(rds-2)} = s_{+(rds-1)} \times \frac{\sigma_{rds-2}}{\sigma_{rds-1}} \qquad \textbf{[E.8]}$$

which, after substitution of Eq. **E.7** for $s_{+(rds-1)}$ is

$$s_{+(rds-2)} = \frac{\sigma_{rds-2}}{\sigma_{rds}} \qquad \textbf{[E.9]}$$

entirely analogously to Eq. **E.7**. Indeed, repeating this procedure indefinitely demonstrates that

$$s_{+i} = \frac{\sigma_i}{\sigma_{rds}} \qquad \textbf{[E.9]}$$

for all $i < rds$. Substituting Eq. **E.9** into Eq. **E.4** gives

$$\alpha = \beta_{rds} n_{rds} + \frac{\sum_{i<rds} \sigma_i n_i}{\sigma_{rds}} \qquad \textbf{[E.10]}$$

which is identical to Eq. **9** recognizing that

$$\gamma = \sum_{i<rds} \sigma_i n_i \qquad \textbf{[E.11]}$$

which is the total number of electrons transferred before the rate-determining step. The derivation of Eq. **E.10** directly from Eq. **7.32** is, we contend, further justification of the felicity of the general formulation of α to formalize and re-interpret mechanistic and kinetic understanding of composite electrochemical reactions.

E.1.2 Disproof of Eq. 7.9 for non-equilibrated kinetically-irrelevant steps

The derivation of Eq. **7.9**, identically Eq. **E.10**, in Section E.1.1 is only valid if kinetically-irrelevant steps are equilibrated. If steps preceding the rate-determining step are not equilibrated, then the specific formulation of the transfer coefficient is entirely different. We derive this distinct formulation of α and demonstrate the invalidity of Eq. **7.9** by first returning to Eq. **E.2**:

$$\alpha = \beta_{rds} n_{rds} + \sum_i X_{RC,i} n_i \frac{Z_i}{1 - Z_i} \qquad \textbf{[E.2]}$$

If $Z_i \neq 1$, then there exists no pole in the final term of Eq. **E.2**, and kinetic degrees of rate control can be directly substituted. Since there is a sole rate-determining step, $X_{RC,rds} = 1$ and $X_{RC,i \neq rds} = 0$. Therefore, Eq. **E.2** reduces

$$\alpha = \left(\beta_{rds} + \frac{Z_{rds}}{1 - Z_{rds}}\right) n_{rds} \qquad \textbf{[E.12]}$$

which is the general formulation of α (Eq. **7.32**) with a single non-zero term from $i = rds$. Eq. **E.12** is evidently distinct to Eq. **7.9** and demonstrates that the thermodynamic/stoichiometric contributions to the transfer coefficient are fundamentally different depending on the reversibility of kinetically-irrelevant steps. Identification of a sole rate-determining step is therefore insufficient to determine the functional form of the transfer coefficient. The transfer coefficient, and Tafel slope, are functions of both the (β_i) and thermodynamic ($Z_i(1 - Z_i)^{-1}$) contributions of each step; we therefore caution against the association of kinetic-irrelevance ($X_{RC,i} = 0$) and equilibration ($Z_i = 1$) of elementary steps — these conditions are distinct and disparately impact α.

E.2 Details and derivations for Case Study I

We provide derivations for closed-form expressions of surface coverages, elementary step reversibilities, and kinetic degrees of rate control for the HOR mechanism in Case Study I.

E.2.1 Surface coverages in Case Study I

Steady-state surface coverages are derived by examination of the PSSH condition for each surface species, H^* and $*$. Since surface coverages are constrained by site balance, $\theta_* = 1 - \theta_{H^*}$, we provide only derivation of the closed-form expression for θ_{H^*}. The PSSH condition for hydrogen adatoms is

$$\frac{d\theta_{H^*}}{dt} = 0 = r_{+1} - r_{-1} - r_{+2} + r_{-2} \quad \textbf{[E.13]}$$

In terms of rate constants, fluid-phase activities, and surface coverages, Eq. **E.13** is

$$0 = k_{+1}a_{H_2}a_{OH^-}\theta_* - k_{-1}a_{H_2O}\theta_{H^*} - k_{+2}a_{OH^-}\theta_{H^*} + k_{-2}a_{H_2O}\theta_* \quad \textbf{[E.14]}$$

Substituting $\theta_* = 1 - \theta_{H^*}$, we have

$$0 = k_{+1}a_{H_2}a_{OH^-}(1 - \theta_{H^*}) - k_{-1}a_{H_2O}\theta_{H^*} - k_{+2}a_{OH^-}\theta_{H^*} + k_{-2}a_{H_2O}(1 - \theta_{H^*}) \quad \textbf{[E.15]}$$

which, after rearrangement, gives

$$\theta_{H^*} = \frac{k_{+1}a_{H_2}a_{OH^-} + k_{-2}a_{H_2O}}{k_{+1}a_{OH^-}a_{H_2} + k_{-1}a_{H_2O} + k_{+2}a_{OH^-} + k_{-2}a_{H_2O}} \quad \textbf{[E.16]}$$

which is the closed-form expression for the steady-state coverage of hydrogen adatoms. Correspondingly, $\theta_* = 1 - \theta_{H^*}$ is

$$\theta_* = \frac{k_{-1}a_{H_2O} + k_{+2}a_{OH^-}}{k_{+1}a_{OH^-}a_{H_2} + k_{-1}a_{H_2O} + k_{+2}a_{OH^-} + k_{-2}a_{H_2O}} \quad \textbf{[E.17]}$$

E.2.2 Elementary step reversibilities in Case Study I

The reversibilities of step 1 and 2 in Case Study I are facilely determined by substitution of the closed-form expressions for surface coverage (Eqs. **E.16-E.17**) into the definition of reversibility:

$$Z_1 \equiv \frac{r_{-1}}{r_{+1}} = \frac{k_{-1}a_{H_2O}\theta_{H^*}}{k_{+1}a_{H_2}a_{OH^-}\theta_*} \quad \textbf{[E.18]}$$

and

$$Z_2 \equiv \frac{r_{-2}}{r_{+2}} = \frac{k_{-2}a_{H_2O}\theta_*}{k_{+2}a_{OH^-}\theta_{H^*}} \quad \textbf{[E.19]}$$

Substituting surface coverages, the reversibilities are

$$Z_1 = \frac{k_{-1}a_{H_2O}\left(k_{+1}a_{H_2}a_{OH^-} + k_{-2}a_{H_2O}\right)}{k_{+1}a_{H_2}a_{OH^-}\left(k_{-1}a_{H_2O} + k_{+2}a_{OH^-}\right)} \quad \textbf{[E.20]}$$

and

$$Z_2 = \frac{k_{-2}a_{H_2O}\left(k_{-1}a_{H_2O} + k_{+2}a_{OH^-}\right)}{k_{+2}a_{OH^-}\left(k_{+1}a_{H_2}a_{OH^-} + k_{-2}a_{H_2O}\right)} \quad \textbf{[E.21]}$$

E.2.3 Degrees of rate control in Case Study I

Kinetic degrees of rate control of step 1 and 2 in Case Study I are derived by application of the derivative definition of $X_{RC,i}$ (Eq. **7.13**) to the closed-form expression for the rate of HOR (Eq. **7.38**)

$$\begin{aligned} X_{RC,1} &\equiv \left(\frac{\partial \ln r}{\partial \ln k_{+1}}\right)_{K_1,k_{+2},k_{-2}} \\ &= \frac{k_{+1}}{r}\left(\frac{\partial}{\partial k_{+1}}\left[\frac{k_{+1}k_{+2} - k_{-1}k_{-2}}{k_{+1} + k_{-1} + k_{+2} + k_{-2}}\right]\right)_{K_1,k_{+2},k_{-2}} \end{aligned} \quad \textbf{[E.22]}$$

where all fluid-phase activities are unity and $X_{RC,2} = 1 - X_{RC,1}$ is not shown in detail. In the irreversible forward/anodic regime, reverse/cathodic half-step rate constants are negligible and Eqs. **E.22** simplifies to

$$X_{RC,1} = \frac{k_{+1} + k_{+2}}{k_{+2}} \left(\frac{\partial}{\partial k_{+1}} \left[\frac{k_{+1} k_{+2}}{k_{+1} + k_{+2}} \right] \right)_{K_1, k_{+2}, k_{-2}} \quad \textbf{[E.23]}$$

Evaluating the derivative in Eq. **E.23**,

$$X_{RC,1} = \frac{k_{+1} + k_{+2}}{k_{+2}} \left(\frac{(k_{+1} + k_{+2}) k_{+2} - k_{+1} k_{+2}}{(k_{+1} + k_{+2})^2} \right) \quad \textbf{[E.24]}$$

which, after simplification, is

$$X_{RC,1} = \frac{k_{+2}}{k_{+1} + k_{+2}} \quad \textbf{[E.25]}$$

identically to Eq. **7.40**. From Eq. **E.25**, $X_{RC,2} = 1 - X_{RC,1}$ is

$$X_{RC,2} = \frac{k_{+1}}{k_{+1} + k_{+2}} \quad \textbf{[E.26]}$$

identically to Eq. **7.41**.

E.3 Unidirectional TST rate functions

We derive TST rate functions for the overall forward/anodic and reverse/cathodic reactions by an identical procedure to formulation of r_{TST} using definitions of unidirectional sensitivities

$$\vec{s}_{\pm i} \equiv \left(\frac{\partial \ln \vec{r}}{\partial \ln r_{\pm i}} \right)_{r_{\mp i}, r_{\pm j}} = \left(\frac{\partial \ln \vec{r}}{\partial \ln k_{\pm i}} \right)_{k_{\mp i}, k_{\pm j}} \quad \textbf{[E.27]}$$

and

$$\overleftarrow{s}_{\pm i} \equiv \left(\frac{\partial \ln \overleftarrow{r}}{\partial \ln r_{\pm i}} \right)_{r_{\mp i}, r_{\pm j}} = \left(\frac{\partial \ln \overleftarrow{r}}{\partial \ln k_{\pm i}} \right)_{k_{\mp i}, k_{\pm j}} \quad \textbf{[E.28]}$$

With the definition of unidirectional reaction sensitivity in-hand, we approximate the forward ($\vec{r}$) and reverse ($\overleftarrow{r}$) reaction rate by Taylor expansion about a steady-state reaction condition $\boldsymbol{X}$. In the following, we present only the derivation of $\vec{r}_{TST}$ — derivation of $\overleftarrow{r}_{TST}$

follows an entirely analogous procedure with each equation identical upon exchange of '$\rightarrow$' and '$\leftarrow$'. The first-order Taylor expansion of $\vec{r}$ about $\boldsymbol{X}$ is

$$ln\,\vec{r} \approx ln\,\vec{r}_{TST} \equiv ln\,\vec{r}|_{\boldsymbol{X}} + \sum_{\pm i}\left(\frac{\partial\, ln\,\vec{r}}{\partial\, ln\, r_{\pm i}}\right)_{r_{\mp i}, r_{\pm j}} \left(ln\, r_{\pm i} - ln\, r_{\pm i}\big|_{\boldsymbol{X}}\right) \qquad \textbf{[E.29]}$$

We simply by substituting the definition of forward reaction sensitivity (Eq. **E.27**) and separating vector ($\ln r_{\pm i}$) and scalar ($\ln r_{\pm i}\big|_{\boldsymbol{X}}$) terms

$$ln\,\vec{r}_{TST} = ln\,\vec{r}|_{\boldsymbol{X}} + \sum_{\pm i}\vec{s}_{\pm i}\, ln\, r_{\pm i} - \sum_{\pm i}\vec{s}_{\pm i}\, ln\, r_{\pm i}\big|_{\boldsymbol{X}} \qquad \textbf{[E.30]}$$

which, after exponentiation, is

$$\vec{r}_{TST} = \vec{r}|_{\boldsymbol{X}} \times \prod_{\pm i} r_{\pm i}^{\vec{s}_{\pm i}} \times \left(\prod_{\pm i} r_{\pm i}^{\vec{s}_{\pm i}}\Big|_{\boldsymbol{X}}\right)^{-1} \qquad \textbf{[E.31]}$$

Akin to the formulation of r_{TST}, the collection of scalar terms into a single parameter reveals that the forward rate is a sensitivity-weighted geometric average of the rates of all half-steps

$$\vec{r}_{TST} = \vec{\kappa}_{app} \prod_{\pm i} r_{\pm i}^{\vec{s}_{\pm i}} \qquad \textbf{[E.32]}$$

where $\vec{\kappa}_{app} = \vec{r}|_{\boldsymbol{X}}\left(\prod_{\pm i} r_{\pm i}^{\vec{s}_{\pm i}}\Big|_{\boldsymbol{X}}\right)^{-1}$ is a scalar quantity less interpretable than κ_{app} — the apparent TST transmission coefficient of the composite reaction. We reserve physical interpretation of $\vec{\kappa}_{app}$ and $\overleftarrow{\kappa}_{app}$ for a subsequent investigation with particular focus on unidirectional rates of electrochemical reactions.

Expression of $\vec{r}_{TST}$ in terms of $r_{\pm i}$ facilitates the derivation of Eq. **7.43** — the formulation of forward reaction rate in a TST-form analogous to that for a forward half-step. Substitution of half-step TST rates per Eqs. **7.21** and **7.22** into Eq. **E.32** yields

$$\vec{r}_{TST} = \vec{\kappa}_{app} \frac{k_B T}{h} e^{-\sum \vec{s}_{\pm i}\left(G^0_{TS,i} + \sum_j \nu_{\pm ij} G^0_j - \alpha_{\pm i} e_0 (E - E_{ref})\right)/k_B T} \prod_j a_j^{-\sum \vec{s}_{\pm i} \nu_{\pm ij}} \quad \textbf{[E.33]}$$

which is simplified by substituting (i) unidirectional degrees of rate control defined recently by Foley and Bhan (*172*)

$$\vec{X}_{RC,i} \equiv \left(\frac{\partial \ln \vec{r}}{\partial (-G^0_{TS,i}/k_B T)} \right)_{G^0_{TS,j \neq i}} = \vec{s}_{+i} + \vec{s}_{-i} \quad \textbf{[E.34]}$$

and

$$\vec{X}_{TRC,j} \equiv \left(\frac{\partial \ln \vec{r}}{\partial (-G^0_j/k_B T)} \right)_{G^0_{k \neq j}} = \sum_{\pm i} \vec{s}_{\pm i} \nu_{\pm ij} \quad \textbf{[E.35]}$$

and (ii) the definition of forward transfer coefficient

$$\vec{\alpha} \equiv \sum \vec{s}_{\pm i} \, \alpha_{\pm i} = \alpha_a \quad \textbf{[E.36]}$$

to give

$$\vec{r}_{TST} = \vec{\kappa}_{app} \frac{k_B T}{h} e^{-\frac{\left(\sum \vec{X}_{RC,i} G^0_{TS,i} + \sum \vec{X}_{TRC,j} G^0_j\right)}{k_B T}} e^{\frac{\sum \vec{\alpha} e_0 (E - E_{ref})}{k_B T}} \prod_j a_j^{-\vec{X}_{TRC,j}} \quad \textbf{[E.37]}$$

where the apparent rate-controlling transition state and initial state for the *forward* reaction path are $\vec{G}^0_{TS,app} = \sum \vec{X}_{RC,i} \, G^0_{TS,i}$ and $\vec{G}^0_{IS,app} = -\sum \vec{X}_{TRC,j} \, G^0_j$.

E.4 Microscopic reversibility of composite electrochemical reactions

In Section 7.4.4 we detail the formulation of $r_{BV-TS} = \vec{r}_{TST} - \overleftarrow{r}_{TST}$ under the condition of *stoichiometric regularity* (i.e. that $\sigma_i = 1$ for all steps i) which permits the extension of the principle of microscopic reversibility beyond on the scope of an elementary step. In this section, we reproduce the construction of r_{BV-} more generally and in further mathematical detail.

We first elaborate upon the definition of Z_{eff} in Eq. **7.48** by expression of Z_{eff} in terms of the more familiar and experimentally-measurable overall reversibility of reaction

$$Z_{ov} \equiv \prod_i Z_i^{\sigma_i} \qquad \textbf{[E.38]}$$

Crucially, Z_{ov} is not generally equal to

$$Z_{eff} \equiv \prod_i Z_i \qquad \textbf{[E.39]}$$

which we regard the more pertinent thermodynamic descriptor of a composite reaction because $Z_{eff} = \overleftarrow{r}/\vec{r}$ intimately connects reaction thermodynamics and kinetics. Z_{ov} and Z_{eff} are relatable in terms of the affinity-averaged stoichiometric number

$$\bar{\sigma} \equiv \frac{\sum_i A_i \sigma_i}{\sum_i A_i} \qquad \textbf{[E.40]}$$

where the affinity of step i is

$$A_i \equiv -\Delta G_i + n_i e_0 \eta \qquad \textbf{[E.41]}$$

where ΔG_i is the chemical free energy change of step i. For a step irreversible in the forward/anodic direction, $A_i = \infty$; for a step irreversible in the reverse/cathodic direction, $A_i = -\infty$; and, for an equilibrated step $A_i = 0$. We therefore see that, if there exists a sole, rate-determining step away from equilibrium, $\bar{\sigma} = \sigma_{rds}$. In this sense definition of $\bar{\sigma}$ generalizes the concept of the stoichiometric number of the rate-determining step and affords a rigorous relationship between Z_{ov} and Z_{eff}:

$$Z_{eff} = Z_{ov}^{1/\bar{\sigma}} \qquad \textbf{[E.42]}$$

which recasts Z_{eff} in explicit terms of the measurable deviation of the reaction from thermodynamic equilibrium, $A = -\Delta G + n e_0 \eta$.

From Eq. **E.42**, we can now more generally state Eq. **7.49** as

$$\frac{\overleftarrow{r}_{TST}}{\vec{r}_{TST}} = Z_{eff} = \left(\frac{\prod_j a_j^{\nu_j}}{exp\left(-\frac{\Delta G^0 - ne_0\eta}{k_B T}\right)} \right)^{1/\bar{\sigma}} \quad \textbf{[E.43]}$$

accounting for the affinity-averaged stoichiometric number, $\bar{\sigma}$, no longer assumed to be unequivocally unity per the condition of $\sigma_i = 1$ for all i. The inclusion of $\bar{\sigma}$, however, confers a functional path-dependence to the right-hand-side of Eq. **E.43**. That is to say that $\bar{\sigma}$ is, in general, a function of the kinetic- and thermodynamic-relevance of each constituent elementary step and therefore is not a purely thermodynamic, path-independent entity in the same fashion as Z_{ov}. Essentially, for Z_{eff} to be a purely thermodynamic entity, akin to Z_{ov}, the relationship between Z_{eff} and Z_{ov} must be scalar. That is to say that $\bar{\sigma}$ must be a well-defined number with no local functional dependence (i.e. all derivatives of $\bar{\sigma}$, for example $\partial\bar{\sigma}/\partial\eta$, are zero). Foley and Bhan (*172*) have recently identified one condition wherein $\bar{\sigma}$ is a scalar: the case of entire equilibrium, for which $Z_{eff} = Z_{ov} = 1 = Z_i$ for all i. We identify two further conditions: (i) the case of stoichiometric regularity, for which $\bar{\sigma}$ is unequivocally unity because $\sigma_i = 1$ for all i and (ii) the case of a single non-equilibrated, rate-determining step, for which Eq. **E.40** collapses to $\bar{\sigma} = \sigma_{rd}$.

We refer to $\bar{\sigma}$ under any of these three cases as $\bar{\sigma}_{MR}$ — the scalar, functionally-independent affinity-averaged stoichiometric coefficient of a composite reaction to which the principle of microscopic reversibility can be applied. With $\bar{\sigma} = \bar{\sigma}_{MR}$, the right-hand-side of Eq. **E.43** is purely thermodynamic — as described for Eq. **7.49**. Relationships between forward, reverse, and net microkinetic descriptors prescribed by the principle of microscopic reversibility can now be derived by substitution of the full functional forms of $\vec{r}_{TST}$ and $\overleftarrow{r}_{TST}$ into Eq. **E.43**

$$\frac{\overleftarrow{\kappa}_{app}}{\vec{\kappa}_{app}} exp\left(-\frac{\sum_i\left(\overleftarrow{X}_{RC,i}-\vec{X}_{RC,i}\right)G^0_{TS,i}+\sum_j\left(\overleftarrow{X}_{TRC,j}-\vec{X}_{TRC,j}\right)G^0_j-(\overleftarrow{\alpha}-\vec{\alpha})e_0\eta}{k_BT}\right) \quad \textbf{[E.44}$$

$$\times\prod_j a_j^{-\left(\overleftarrow{X}_{TRC,j}-\vec{X}_{TRC,j}\right)}=\left(\frac{\prod_j a_j^{\nu_j}}{exp\left(-\frac{\Delta G^0-ne_0\eta}{k_BT}\right)}\right)^{1/\bar{\sigma}_{MR}} \quad \textbf{]}$$

and equation of the functional dependencies of the left-hand and right-hand sides of Eq. **E.44**. For example, the right-hand-side of Eq. **E.44** has no dependence on the standard state free energies of transition states or intermediates. Therefore, the terms multiplying $G^0_{TS,i}$ and G^0_m for intermediates m must be zero, implying

$$\vec{X}_{RC,i}=\overleftarrow{X}_{RC,i} \quad \textbf{[E.45]}$$

$$\vec{X}_{TRC,m}=\overleftarrow{X}_{TRC,m} \quad for\ intermediates\ m \quad \textbf{[E.46]}$$

The functional dependence of the right-hand side on the activity of reactants and products k is determined by the exponent $\nu_k/\bar{\sigma}_{MR}$ and the dependence of the left-hand-side on the activity of reactants and products is determined by the exponent $-\left(\overleftarrow{X}_{TRC,k}-\vec{X}_{TRC,k}\right)$. Therefore,

$$\vec{X}_{TRC,k}\ -\ \overleftarrow{X}_{TRC,k}=\frac{\nu_k}{\bar{\sigma}_{MR}} \quad for\ reactants\ and\ products\ k \quad \textbf{[E.47]}$$

Similarly, equation of the functional dependence of the left- and right-hand sides of Eq. **E.44** on overpotential implies

$$\vec{\alpha}\ -\overleftarrow{\alpha}=\frac{n}{\bar{\sigma}_{MR}} \quad \textbf{[E.48]}$$

which is identical to Eq. **7.10** with $\bar{\sigma}_{MR}=\sigma_{rds}$ for the case of a single non-equilibrated, rate-determining step. Eqs. **E.45**-**E.48** are the mathematical manifestations of the principle

of microscopic reversibility applied to an appropriate composite electrochemical reaction and enable formulation of r_{BV-TST} for any condition that ensures $\bar{\sigma} = \bar{\sigma}_{MR}$.

Indeed, evaluation $\vec{r}_{TST} - \overleftarrow{r}_{TST}$ for any of the conditions which ensure $\bar{\sigma} = \bar{\sigma}_{MR}$ gives an identical formulation of the generalized Butler-Volmer equation

$$r_{BV-TST} = k_{BV-TST}\left[e^{\frac{\vec{\alpha}e_0\eta}{k_BT}}e^{-\frac{\sum_k \vec{X}_{TRC,k}G_k}{k_BT}} - e^{\frac{\overleftarrow{\alpha}e_0\eta}{k_BT}}e^{-\frac{\sum_j \overleftarrow{X}_{TRC,k}G_k}{k_BT}}\right] \quad \textbf{[54]}$$

where $G_k = G_k^0 + k_BT\ln(a_k)$ and the Butler-Volmer rate constant is

$$k_{BV-TST} = \vec{\kappa}_{app}\frac{k_BT}{h}e^{-\frac{\sum_i X_{RC,i}G_{TS,i}^0}{k_BT}}e^{-\frac{\sum_m X_{TRC,m}G_m}{k_BT}} \quad \textbf{[55]}$$

where

$$\vec{\kappa}_{app} = \overleftarrow{\kappa}_{app} \quad \textbf{[E.49]}$$

since the right-hand-side of Eq. **E.44** does not depend on $\vec{\kappa}_{app}$ or $\overleftarrow{\kappa}_{app}$.

E.5 Details for Case Study II

Case Study II in Section 7.4.1 details the fidelity of unidirectional kinetic descriptors (e.g. $\overrightarrow{\Psi}_{H_2}$) for mechanistic study of reversible electrochemical reactions near equilibrium (i.e. $0.1 < Z_{eff} < 10$). We provide comparison of unidirectional (e.g. α_a and $\overrightarrow{\Psi}_{H_2}$) to net (e.g. α and Ψ_{H_2}) descriptors in Figure E.1 to reinforce our contention that unidirectional descriptors are more suitable for physical interpretation at reversible conditions. Figure E.1 demonstrates the divergent behavior of α and Ψ_{H_2} near equilibrium which renders these conventional kinetic descriptors unsuitable for mechanistic interpretation. Rather, at reversible conditions, forward/anodic descriptors α_a and $\overrightarrow{\Psi}_{H_2}$ take more familiar, interpretable values which straightforwardly communicate the identity of rate-determining steps and influence of a_{H_2} on reaction kinetics — as is detailed in Section 7.4.1.

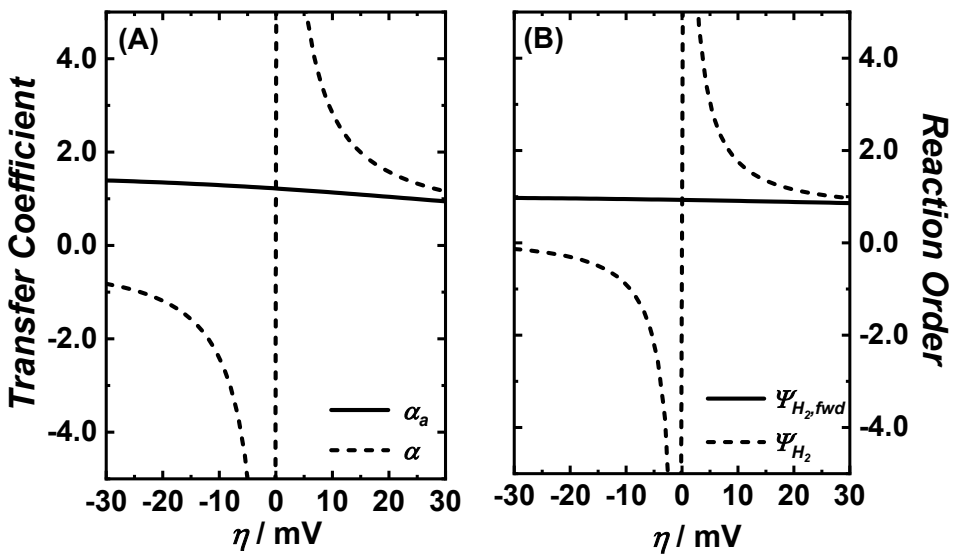

Figure E.1: (A) Forward/anodic transfer coefficient ($\boldsymbol{\alpha_a}$) and net transfer coefficient ($\boldsymbol{\alpha}$). (B) Forward/anodic reaction order in $\boldsymbol{H_2}$ ($\boldsymbol{\Psi_{H_2,fwd} = \vec{\Psi}_{H_2}}$) and net reaction order in $\boldsymbol{H_2}$ ($\boldsymbol{\Psi_{H_2}}$).